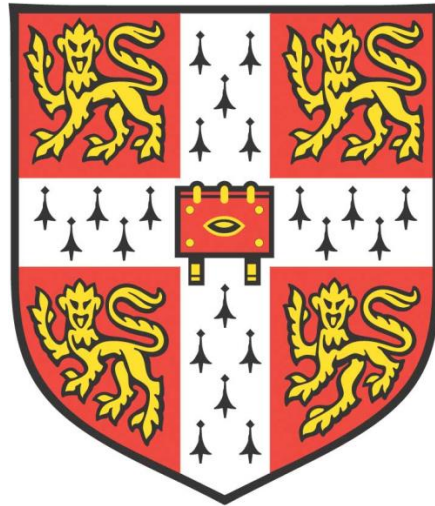


*Biochemical Sensing using Siloxane  
Polymer Waveguides*



**Gergely Zsigmond Racz**  
**Sidney Sussex College**  
**May 2018**

**Centre for Advanced Photonics and Electronics**  
**Department of Engineering**  
**University of Cambridge**

**This dissertation is submitted in accordance with the requirements for the degree  
of Doctor of Philosophy**



*Uxori carissimae et parentis meis*

## DECLARATION

This dissertation is the result of my own work and includes nothing, which is the outcome of work done in collaboration except where specifically indicated in the text. It has not been previously submitted, in part or whole, to any university or institution for any degree, diploma, or other qualification.

In accordance with the Department of Engineering guidelines, this thesis is does not exceed 65,000 words, and it contains less than 150 figures.

Signed: \_\_\_\_\_

Date: \_\_\_\_\_

Gergely Zsigmond Racz, MEng, MRes

## ABSTRACT

The objective of this work presented here is to extend the capabilities of siloxane waveguide technology in the field of biochemical sensing. Recent advances in the integration of polymeric optical waveguides with electronics onto standard printed circuit boards (PCBs) allow the formation of cost-effective lab-on-a-chip modules suitable for mass production. This technology has been primarily designed for on-board data communication. The focus of this research is to investigate the possibility of realising a siloxane polymer based lab-on-chip sensor.

Different siloxane-polymer-based optical waveguide sensor structures have been designed and analysed from the aspect of biochemical sensing. An evanescent-wave absorption sensor based on mode-selective asymmetric waveguide junctions is proposed for the first time. The device mitigates the common optical effect of spurious response in absorption sensors due to the analyte transport fluid.

Head injury is the leading cause of death in the population of people under 40 years. Currently, 3 out of 5 deaths in emergency rooms are due to severe brain injuries in the developed world. Researchers at the Neurosciences Critical Care Unit (NCCU) at Addenbrooke's Hospital have managed to correlate biochemical changes with the severeness of the injury and the likelihood of patient recovery. Considerable progress has been made to develop a lab-on-chip sensor capable of continuously monitoring glucose, lactate and pyruvate concentrations in the brain fluid, hence the contribution to the current trend in the advancement of portable lab-on-chip technologies for the deployment of point-of-care diagnostic tools. A novel recognition layer has been developed based on porphyrin in combination with glucose, lactate and pyruvate oxidase for measuring all the analytes, enabling fast and reversible chemical reactions to be monitored by optical interrogation. The operational wavelength of the developed recognition layer is 425nm, which required the formation of polymer features that were beyond the fabrication capabilities at the time. Through considerable process development and the adoption of nanoimprinting lithography, siloxane polymer based optical waveguides were fabricated allowing the realisation of highly sensitive optical sensors. Based on the results that are presented here, it can be concluded the functionalization of siloxane polymer waveguide have a potential for realising biochemical sensors in the future. The new fabrication technique will allow the formation of more robust and complex lab-on-chip sensors based on this material.

## LIST OF PUBLICATIONS

- [1] G. Racz, N. Bamiedakis, R. Penty, “Mode-selective optical sensing using asymmetric waveguide junctions”, *Sensors and Actuators: A, Physical*, vol. 233, pp. 91–971, 2015.
- [2] G. Racz, N. Bamiedakis, R. Penty, “Mode-selective sensing based on asymmetric waveguide junctions”, *Advanced Photonic Congress*, Conference paper, 2014.

## ACKNOWLEDGEMENTS

I would like to express my appreciation for the support and guidance of my supervisor Prof. Richard Penty and my advisor Prof. Ian White. Their vision and insightful questions along with their extensive knowledge have been of great value. I am also grateful to my fellow group members at the Photonic Research Group, who have helped me. Particularly, Dr. Nikos Bamiedakis and Adrian Wonfor, whom have demonstrated considerable patience helping me in the lab with the practical work. Moreover, I would like to thank Dr. Malik Qasim, who was my chemistry advisor and provided an expert knowledge that was essential to carry out this work. CMMPE. Also, I would like to express my gratitude to the EPSRC and CDT for Photonic Systems Development for supporting me along these years as well as the Engineering Department who provided the research grant for the sensor development.

Last but not least, I would like to thank my dearest wife who supported me during these years. Her unconditional love has kept me going during the difficult times.

## TABLE OF CONTENT

<b>CHAPTER 1 - INTRODUCTION .....</b>	<b>1</b>
1.1 EMERGENCE OF LAB-ON-CHIP TECHNOLOGIES .....	1
1.2 BRAIN FLUID SENSOR PROJECT FOR TRAUMATIC BRAIN INJURY ANALYSIS .....	2
1.3 SILOXANE WAVEGUIDE TECHNOLOGY FOR SENSING .....	4
1.4 NOVELTY OF WORK .....	5
1.5 AIMS AND SYNOPSIS OF THIS THESIS .....	6
1.6 REFERENCES .....	8
<b>CHAPTER 2 – OPTICAL SENSING TECHNIQUES.....</b>	<b>10</b>
2.1 INTRODUCTION .....	10
2.2 FUNDAMENTAL OPTICAL TRANSDUCTION MECHANISMS .....	13
2.3 OPTICAL WAVEGUIDE THEORY .....	18
2.4 OPTICAL WAVEGUIDES STRUCTURES FOR SENSING .....	24
2.5 CONCLUSION .....	30
2.6 REFERENCES .....	31
<b>CHAPTER 3 -OPTICAL WAVEGUIDES BASED ON SILOXANE POLYMER FOR SENSING APPLICATIONS.....</b>	<b>33</b>
3.1 INTRODUCTION .....	33
3.2 SILOXANE POLYMER-BASED OPTICAL WAVEGUIDE STRUCTURES FOR BIOCHEMICAL SENSING.....	38
3.2.1 <i>Waveguide design</i> .....	39
3.2.2 <i>Optical field localisation for sensitivity enhancement</i> .....	45
3.3 CONCLUSION .....	51
3.4 REFERENCES .....	53
<b>CHAPTER 4- ADVANCED OPTICAL INTERROGATION TECHNIQUE BASED ON MODE DUPLEX SENSING .....</b>	<b>56</b>
4.1 INTRODUCTION .....	56
4.2 ASYMMETRIC Y-JUNCTIONS .....	57
4.2.1 <i>Types of Y-Junctions</i> .....	57
4.2.2 <i>Design of asymmetric Y-junctions and simulation results</i> .....	61
4.2.3 <i>Fabrication sensitivity</i> .....	72

## Chapter 1 - Introduction

4.3 MODE SELECTIVE SENSOR BASED OF ASYMMETRIC Y-JUNCTIONS .....	74
4.3.1 <i>Sensor operation</i> .....	75
4.3.2 <i>Sensitivity analysis</i> .....	76
4.3.3 <i>Modal Injection effects on sensor performance</i> .....	83
4.4 CONCLUSION .....	86
4.5 REFERENCES .....	87
<b>CHAPTER 5 – DEVICE FABRICATION AND EXPERIMENTAL RESULTS...90</b>	
5.1 INTRODUCTION .....	90
5.2 STANDARD FABRICATION TECHNOLOGY FOR SILOXANE WAVEGUIDES BASED ON UV PHOTOLITHOGRAPHY .....	94
5.3 NANO-IMPRINT LITHOGRAPHY .....	99
<i>Master Fabrication</i> .....	101
<i>Siloxane polymer waveguide measurements</i> .....	119
5.4 INVESTIGATION OF SILOXANE POLYMER WAVEGUIDE TECHNOLOGY FOR BRAIN FLUID ANALYSIS .....	121
<i>Introduction to Porphyrins</i> .....	123
<i>Deposition techniques</i> .....	125
<i>Recognition layer development</i> .....	129
5.4.4 <i>Waveguide Measurements</i> .....	146
5.5 CONCLUSION .....	154
5.6 REFERENCES .....	156
<b>CHAPTER 6 - APPENDIX .....</b>	<b>161</b>
6.1 REVIEW OF OPTICAL SENSING TECHNIQUES FOR BRAIN MICRODIALYSIS .....	161
6.1.1 <i>Glucose Sensing Review</i> .....	162
6.1.2 <i>Lactate Sensing Review</i> .....	175
6.1.3 <i>Pyruvate Sensing</i> .....	178
6.2 REFERENCES .....	180

# LIST OF FIGURES

<p>FIGURE 1.1 (A) MAGNETIC RESONANCE IMAGE (MRI) SHOWING THE BRAIN OF A HEAD INJURY PATIENT WITH A MICRODIALYSIS CATHETER TUBE IN POSITION, THE TIP INDICATED BY AN ARROW (YELLOW). SCALE BARS (GREEN) SHOW CENTIMETRE DIVISIONS. (MRI TECHNICAL DETAILS: 3D MP—RAGE SEQUENCE, AT 3 TESLA). IMAGE IS COURTESY OF THE WOLFSON BRAIN IMAGING CENTRE (UNIVERSITY OF CAMBRIDGE). (B) SCHEMATIC DIAGRAM SHOWING THE PRINCIPLES OF MICRODIALYSIS. BLOOD CAPILLARIES SUPPLY GLUCOSE AS A SOURCE OF ENERGY FOR THE BRAIN CELLS, WHICH METABOLISE IT. SOME OF THE PRODUCTS (METABOLITES), INCLUDING LACTATE AND PYRUVATE, EMERGE FROM THE CELLS INTO THE BRAIN’S EXTRACELLULAR FLUID AND ARE COLLECTED BY THE MICRODIALYSIS CATHETER TUBE [1.12].</p>	3
<p>FIGURE 1.2. – SCHEMATIC OF LAYOUT OF THE ELECTRO-OPTIC PCB-INTEGRATED OPTICAL BIOSENSOR – . (A) PLANAR VIEW OF (A) TOP AND (B) BOTTOM BOARD SIDES [1.14].</p>	4
<p>FIGURE 2.1 - BIOSENSING MECHANISM</p>	11
<p>FIGURE 2.2 - ANTIBODY-ANTIGEN INTERACTION [2.2]</p>	12
<p>FIGURE 2.3. – LIGHT INCIDENT ON AN ABSORBING MATERIAL WITH INTENSITY <math>I_x</math>, THICKNESS OF <math>x</math> AND CROSS SECTION OF <math>A</math>.</p>	13
<p>FIGURE 2.4 – SCHEMATIC OF DIFFERENT SENSOR ARCHITECTURES (A) GUIDED WAVE SENSOR (B,C) EVANESCENT WAVE SENSOR (D) OPTRODE SENSOR</p>	15
<p>FIGURE 2.5 - JABLONSKII DIAGRAM [2.2]</p>	16
<p>FIG. 2.6 - RAMAN SCATTERING MECHANISM (A) RAMAN STOKES SCATTERING (B) RAMAN ANTI-STOKES SCATTERING [2.2]</p>	17
<p>FIGURE 2.7 – OPTICAL WAVEGUIDE STRUCTURE FOR MULTIMODE BEHAVIOUR, LIGHT IS CONFINED WITH THE CORE DUE TO TOTAL INTERNAL REFLECTION ON BOTH INTERFACES</p>	18
<p>FIGURE 2.8 – TWO DIELECTRIC MEDIA WITH REFRACTIVE INDEX <math>n_1, n_2</math> AND AN INCIDENT WAVE WITH ANGLE <math>\phi_1</math></p>	19
<p>FIGURE 2.9 – DIFFERENT METHODS OF LIGHT COUPLING</p>	26
<p>FIGURE 2.10. – ARROW STRUCTURE</p>	27
<p>FIGURE 2.11. - HOLLOW WAVEGUIDE STRUCTURE</p>	29
<p>FIGURE 2.12 - HOLLOW WAVEGUIDE STRUCTURE</p>	29
<p>FIGURE 3.1 - LOSS VS WAVELENGTH SPECTRUM FOR SILOXANE POLYMER MATERIAL FROM 400NM-1600NM [3.16]</p>	36
<p>FIGURE 3.2 - MICROSCOPE IMAGES OF FABRICATED WAVEGUIDES WITHOUT TOP CLADDING, (A) CROSSINGS, (B) Y-SPLITTERS AND (C) STRAIGHT WAVEGUIDES [3.16]</p>	38
<p>FIGURE 3.3- EFFECTIVE INDEX CALCULATIONS FOR MODES EMERGING (FROM CLADDING RI) AS WAVEGUIDE DIMENSIONS INCREASED</p>	40
<p>FIGURE 3.4 – FIELD PROFILE IMAGES IN THE WAVEGUIDE CROSS SECTION FOR <math>TE_1</math> AND <math>TE_2</math> MODES</p>	41
<p>FIGURE 3.5 – THEORETICAL SENSITIVITY OF WAVEGUIDE TO SENSING LAYER REFRACTIVE INDEX CHANGE FOR MULTIPLE MODES AS FUNCTION OF WAVEGUIDE THICKNESS, <math>n_{CORE}=1.52</math>, <math>n_s=1.33</math> AT 675NM WAVELENGTH [3.23]</p>	42
<p>FIGURE 3.7 – SYMMETRIC AND UNCLAD WAVEGUIDE STRUCTURES</p>	45
<p>FIGURE 3.8 – SCHEMATIC SHOWING THE REFRACTIVE INDEX PROFILE OF THE COUPLING (A) AND SENDING SECTION WITH THE LIGHT PROPAGATING THROUGH THE STRUCTURE AND (B) ITS EFFECT ON FIELD PROFILE</p>	46
<p>FIGURE 3.9. – STRUCTURE OF METAL-CLADDED LEAKY WAVEGUIDES</p>	46
<p>FIGURE 3.10 – SIMULATION RESULTS SHOWING HOW CORE CONFINEMENT INCREASE (A) WITH <math>Ta_2O_5</math> AND ITS (B) CORRESPONDING OPTICAL FIELD SHIFT AT 0 AND 15NM</p>	47

# Chapter 1 - Introduction

FIGURE 3.11 – SIMULATION RESULTS SHOWING HOW OPTICAL POWER ABSORPTION (NORMALISED) CHANGES WITH GLUCOSE CONCENTRATION INCREASE AT DIFFERENT $Ta_2O_5$ THICKNESS .....	50
FIGURE 3.12 – SENSOR SENSITIVITY OPTIMISATION FOR $Ta_2O_5$ THICKNESS FOR TE1 AND TE2 MODES AT 1MM GLUCOSE CONCENTRATION .....	50
FIGURE 3.13 – SENSOR SENSITIVITY DEPENDENCE ON PORPHYRIN-BASED RECOGNITION LAYER THICKNESS AT 16NM OF $Ta_2O_5$ AT 1MM GLUCOSE CONCENTRATION .....	51
FIGURE 4.1 - (A) FORWARD AND (B) BACKWARD MODAL PROPAGATION THROUGH A SYMMETRIC, SINGLE-MODE Y-JUNCTION [4.13.] .....	57
FIGURE 4.2 – EVOLUTION OF THE SECOND MODE INTO THE ARMS OF A FEW MODE SYMMETRIC JUNCTION [4.13] .....	58
FIGURE 4.3 - EVOLUTION OF (A) THE THIRD MODE AND (B) THE FOURTH MODE, FROM THE STEM THROUGH A FEW-MODE Y-JUNCTION [4.13] .....	59
FIGURE 4.4 – EVOLUTION OF 2 <sup>ND</sup> MODE IN ARM A THROUGH A TWO MODE Y-JUNCTION [4.13] .....	60
FIGURE 4.5 – EVOLUTION OF FM MODES BETWEEN (A) THE WIDER ARM AND (B) THE NARROWER ARM OF A ASYMMETRIC SINGLE MODE JUNCTION [4.13] .....	60
FIGURE 4.6 - EVOLUTION OF (A) THE FM AND (B) THE SECOND (FIRST-ODD) MODE BETWEEN THE STEM AND ARMS A AND B OF THE ASYMMETRIC TWO-MODE Y-JUNCTION, RESPECTIVELY [4.13] .....	61
FIGURE 4.7 – 2 ARM ASYMMETRIC WAVEGUIDE JUNCTION STRUCTURE .....	62
FIGURE 4.8 – N-STEM ASYMMETRIC Y-JUNCTION [4.13].....	63
FIGURE 4.9 – MODES REPRESENTED IN FIMMPROP WITHIN THE WAVEGUIDE SECTION.....	65
FIGURE 4.10 – ASYMMETRIC WAVEGUIDE JUNCTION (A) SCHEMATIC IN FIMMPROP AND IT CORRESPONDING (B) WAVEGUIDE CROSS SECTIONS. ....	65
FIGURE 4.11 – NUMERICAL APPROXIMATIONS FOR (A) MODAL EFFECTIVE INDICES AT THE SINGLE MODE SECTION AS THE WAVEGUIDE SEPARATION IS INCREASED AND (B) MINIMUM JUNCTION LENGTH FOR MAXIMUM COUPLING COEFFICIENT FOR S-FUNCTION SHAPED ARMS. ....	66
FIGURE 4.12 – MODE COUPLING EFFICIENCIES TO THE SINGLE MODE ARMS AS THE RATIO OF SINGLE MODE ARMS ( $W_1, W_2$ ) CHANGE IN RESPECT TO TOTAL ARM WIDTH ( $W$ ).....	67
FIGURE 4.13 - INTENSITY FIELD PROFILE OF THE JUNCTIONS (TOP VIEW) AT DIFFERENT LEVEL OF ASYMMETRY. ....	68
FIGURE 4.14 MODE SORTING Y-JUNCTIONS FOR: (A) A 2-MODED AND (B) A 3- MODED DEVICE AS WELL AS (C) A 4-MODED DEVICE EMPLOYING CASCADED 2-ARM JUNCTIONS.....	68
FIGURE 4.15 – NUMERICAL CALCULATION SHOWING HOW THE DISTRIBUTION OF TOTAL WIDTH ( $W$ ) BETWEEN THE ARM WIDTHS EFFECT THE COUPLING EFFICIENCY .....	69
FIGURE 4.16 – FIELD INTENSITY PROFILES FOR TE MODES AT DIFFERENT INPUT MODE EXCITATION .....	70
FIGURE 4.17 – SCHEMATIC STRUCTURE (TOP VIEW) OF CASCADED ASYMMETRIC JUNCTION MODEL IN FIMMPROP .....	70
FIGURE 4.18 – NUMERICAL CALCULATION SHOWING THE MODAL COUPLING EFFICIENCY CHANGES IN THE 4 TO 2 MODE SORTER JUNCTION AT DIFFERENT OUTPUT ARM WIDTHS.....	71
FIGURE 4.19 -FIELD INTENSITY PROFILES FOR TE MODES AT DIFFERENT INPUT MODE EXCITATIONS.....	72
FIGURE 4.20 – STRUCTURE DIMENSION INCREMENT BY $\Delta$ .....	73
FIG. 4.21– SUMMARY OF FABRICATION SENSITIVITY ANALYSIS, WHERE MODE COUPLING EFFICIENCY CHANGES WITH ARM WIDTHS FOR EACH DEVICE.....	73

## Chapter 1 - Introduction

FIG. 4.22 – ILLUSTRATION OF THE PROBLEM REGARDING THE OPTIMISATION OF SENSING LAYER, EVANESCENT FIELD PENETRATION AND INTERFERENCE BETWEEN TARGET ANALYTE (RED DOTS) AND OTHER ABSORBING CHEMICAL SPECIES (PURPLE TRIANGLES) FOR BOTH (A) MEMBRANE WITH RELATIVELY LARGE THICKNESS ( $\sim 1 \mu\text{m}$ ) AND (B) MONOLAYER WITH DEPTH OF ORDER 10S OF NANOMETRES .....	75
FIGURE 4.23 – SCHEMATIC OF THE PROPOSED OPTICAL WAVEGUIDE SENSOR: (A) PLANAR VIEW AND (B) TOP VIEW, AND CROSS SECTION OF THE DEVICE AT ITS DIFFERENT SEGMENTS: (C) MULTIMODE INPUT SECTION, (D) SENSING SECTION AND (E) OUTPUT SECTION.....	76
FIG. 4.24 MODE SENSITIVITY FOR ABSORPTION CHANGES IN (A) THE SENSING LAYER AND (B) THE OUTER MEDIUM FOR EACH MODE.	77
FIG. 4.25 RELATIVE ERROR IN THE ESTIMATION OF THE SENSING LAYER ABSORPTION $\alpha m$ OBTAINED WITH THE PROPOSED MODE SELECTIVE SENSOR AS A FUNCTION OF THE SPURIOUS ABSORPTION OF THE OUTER MEDIUM FOR A RANGE OF SENSING LAYER THICKNESSES.....	80
FIGURE 4.26 RELATIVE ERROR IN THE ESTIMATION OF THE SENSING LAYER ABSORPTION $\alpha m$ FOR DIFFERENT ABSORPTION MULTIPLIERS OF THE OUTER MEDIUM FOR THE MULTIMODE WAVEGUIDE WITHOUT THE USE OF ASYMMETRIC JUNCTIONS (STRUCTURE (B) AND CROSS SECTION (C-D)). .....	81
FIGURE 4.27 RELATIVE ERROR IN THE ESTIMATION OF THE SENSING LAYER ABSORPTION $\alpha$ FOR DIFFERENT ABSORPTION MULTIPLIERS OF THE OUTER MEDIUM FOR THE THREE DIFFERENT MODE-SELECTIVE SENSORS. ....	82
FIGURE 4.28 – RELATIVE ERROR IN THE ESTIMATION OF THE OUTER MEDIUM ABSORPTION $\beta$ OBTAINED WITH THE PROPOSED MODE SELECTIVE SENSOR FOR A DIFFERENT NUMBER OF INTERROGATING MODES IN THE DEVICE. ....	83
FIGURE 4.29 – MISALIGNMENT TOLERANCE OF A 2-ARM JUNCTION WITH (A) $5 \mu\text{m}$ AND (B) $62.5 \mu\text{m}$ COUPLING CORE WIDTH.....	84
FIGURE 4.30 – MODE SORTING PERFORMANCE OF A 2-ARM JUNCTION SENSOR WITH A $5 \times 2$ .....	85
MISALIGNMENT TOLERANCE EFFECTS THE MEASUREMENT ACCURACY AS THE MODAL EXCITATION CHANGES. FIG 4.31 SHOWS THE CONCENTRATION ESTIMATION ON 2 MODED SENSOR FOR DIFFERENT COUPLING CORE WIDTHS AND ITS MISALIGNMENT PERFORMANCE. THE USE OF LARGE MULTIMODE FIBRES ARE IMPORTANT IN ORDER TO EXCITE THE MODES APPROPRIATELY AS WELL AS ACHIEVING RELAXED MISALIGNMENT TOLERANCE.....	85
FIGURE 4.31. - RELATIVE ERROR IN THE ESTIMATION OF THE SENSING LAYER ABSORPTION $\alpha$ FOR DIFFERENT ABSORPTION MULTIPLIERS OF THE OUTER MEDIUM AS A FUNCTION OF FIBRE OFFSET, (A) $5 \mu\text{m}$ AND (B) $62.5 \mu\text{m}$ COUPLING CORE WIDTH.....	86
FIGURE 5.2 – FABRICATION PROCESS NON-IDEALITIES AFFECTING THE CORE CROSS SECTION.....	97
FIGURE 5.3 – SIZE COMPARISON OF STANDARD LARGE CORE STRUCTURE WITH SINGLE MODE AT 1550 FOR (A) $50 \mu\text{m}$ AND (B) $20 \mu\text{m}$ OF PROXIMITY GAP. [5.8].....	97
FIGURE 5.4 – DIRECTIONAL COUPLERS FABRICATED BY YING HAO ILLUSTRATING THE FABRICATION LIMITATION FOR FEATURES BELOW $10 \mu\text{m}$ FOR 3DB COUPLERS [5.8] .....	98
FIGURE 5.5 – MICROSCOPE IMAGE OF SILOXANE BASED MICROFLUIDIC WELLS OVER AN ARRAY OF OPTICAL WAVEGUIDE CORES MADE FOR BRAIN FLUID ANALYSER PROJECT.....	98
FIGURE 5.6 – PROCESS OF FABRICATING SILOXANE POLYMER WAVEGUIDES USING NANO-IMPRINT LITHOGRAPHY .....	99
FIGURE 5.7 – COMPARISON BETWEEN (A) THERMAL AND (B) UV NIL TECHNIQUES ILLUSTRATING THE LATTER DOES NOT REQUIRE HIGH PRESSURE OR ELEVATED TEMPERATURE [5.16] .....	100
FIGURE 5.8. – PRINCIPLE OF DEEP REACTIVE ION ETCHING PROCESS [5.18].....	101
FIGURE 5.9. – SEM IMAGE SHOWING ROUGH CAKE LAYERED SIDEWALL.....	102

# Chapter 1 - Introduction

FIGURE 5.10 – SILICON TRENCH FABRICATION USING STANDARD BOSCH RECIPE (A) AND THE FABRICATED SAMPLE (B) .....	103
FIGURE 5.11 – SILICON MASTER STAMP FABRICATION BASED ON (1-2) ELECTRON BEAM LITHOGRAPHY USING UV3 RESIST FOLLOWED BY HARD MASK DEPOSITION (ALUMINIUM) THEN (4) LIFT-OFF AND (5) DEEP REACTIVE ION ETCHING. ....	104
FIGURE 5.12 – SIDEWALL QUALITY OPTIMISATION BY ADJUSTING FLOW RATE (A,B) AND PULSE TIME (C,D).....	105
FIGURE 5.13 – SINGLE MODE OPTICAL WAVEGUIDE FEATURES PATTERNED ON SILICON SUBSTRATE, (A) CROSS SECTION VIEW, (B) SIDEVIEW .....	107
FIGURE 5.14 – MICROSCOPE IMAGES OF DAMAGED ASYMMETRIC Y-JUNCTIONS PATTERNS ON SILICON, (A) BROKEN ARM AT THE TIP OF THE JUNCTION, (B) RESULTING DAMAGED WAVEGUIDE JUNCTION ARRAY.....	107
FIGURE 5.15 – SEM IMAGES OF ASYMMETRIC Y-JUNCTIONS PATTERNED INTO SILICON SUBSTRATE, (A) TIP OF THE JUNCTION, (B) ROUGH WAVEGUIDE EDGES.....	108
FIGURE 5.16 – SCHEMATICS OF POLYMER WAVEGUIDE FABRICATION BASED ON NIL USING ETFE REPLICA MOULD .....	109
FIGURE 5.17 – SILICON TO ETFE PATTERN TRANSFER BASED ON THERMAL NIL PROCESS .....	110
FIGURE 5.18 – WAVEGUIDE FEATURE TRANSFER FROM (A) SILICON TO (B) ETFE THIN FILM.....	111
FIGURE 5.19 – REPLICA MOULD PROCESS DEVELOPMENT SHOWCASING (A) BEFORE AND (B) AFTER IMAGES.....	111
FIGURE 5.20 – IMPRINTING PROCESS BY MASK ALIGNER .....	112
FIGURE 5.21 – IMPRINTING PROCESS DEVELOPMENT, (A) GAS BUBBLES DUE TO NON-IDEAL CURING, (B) SHORTER CURING TIME, (C) FULLY DEVELOPED SAMPLE AFTER VACUUM TREATMENT .....	113
FIGURE 5.22 – INTENSITY FIELD PROFILE OF SILOXANE WAVEGUIDE CORE FABRICATED BY UV NIL USING A MASK ALIGNER (MJB4) INDICATING LARGE RESIDUAL LAYER .....	114
FIGURE 5.23 – ETFE TO SILOXANE POLYMER IMPRINTING PROCESS.....	114
FIGURE 5.25 – MICROSCOPE IMAGES (TOP VIEW) OF THE WAVEGUIDES (A-C) FOLLOWING THE STANDARD DICING PROCEDURE USING MICRORACE SERIES 3 DICING SAW. ....	118
FIGURE 5.26 – MICROSCOPE IMAGES SHOWING THE POLYMER WAVEGUIDE SAMPLES CLEAVED BY HAND USING A DIAMOND CUTTER. ....	118
FIGURE 5.27 – EXPERIMENTAL SETUP FOR INTENSITY PROFILE MEASUREMENT .....	119
FIGURE 5.28 – INTENSITY FIELD PROFILE OF (A) 2.5x3 AND (B) 3x3 $\mu\text{m}$ SILOXANE RIDGE WAVEGUIDE CAPTURED ON A CCD CAMERA AT 50X MAGNIFICATION.....	120
FIGURE 5.29 – NEARFIELD 3D INTENSITY PLOT OF THE LIGHT INTENSITY CAPTURED AT THE END FACET OF SINGLE MODE WAVEGUIDE .....	120
FIGURE 5.30 – WAVEGUIDE TRANSMISSION MEASUREMENT FOR AN ARRAY OF SILOXANE WAVEGUIDE (2.5-5 $\mu\text{m}$ WIDE AND 3 $\mu\text{m}$ HIGH) .....	121
FIGURE 5.31 – MOLECULAR STRUCTURE OF PORPHYRIN, WHERE THE METAL IN THE CENTRE ACTS AS A HOST FOR ANY OF THE D-BLOCK ELEMENTS [5.25]. ....	123
FIGURE 5.32 TWO STEP REACTION MECHANISM OF ZNTPP TO NO <sub>2</sub> [5.24]. ....	124
FIGURE 5.33. – ABSORPTION SPECTRUM OF PORPHYRIN .....	125
FIGURE 5.34 – SEM IMAGES OF (A) SPIN COATING (B) VE (C) GDS FILMS OF CoTPP [5.38] .....	128
FIGURE 5.35 UV-VIS ABSORPTION SPECTRUM OF PORPHYRIN THIN FILM DEPOSITED BY SPIN COATING VACUUM EVAPORATION AND GLOW-DISCHARGE SUBLIMATION [5.38] .....	129

## Chapter 1 - Introduction

FIGURE 5.36 ABSORBANCE SPECTRA OF (A) BEFORE (1) AND AFTER EXPOSURE (2) TO 50MG/DL GLUCOSE SOLUTION. THE DYNAMIC RANGE OF GOD-4 COMPLEX IS SHOWN ON (B) [5.21] .....	130
FIGURE 5.37 - SCHEMATIC OF THE OPTICAL SYSTEM FOR HP 8453 UV-VISIBLE SPECTROMETER.....	131
FIGURE 5.38 – MEASURED OPTICAL ABSORPTION SPECTRUM OF THE CTPP4 SOLUTION .....	132
FIGURE 5.39 – EVOLUTION OF CTPP4-GOX COMPLEX IN THE OPTICAL SPECTRUM AS IT REACTS WITH 20MM/L OF GLUCOSE.....	133
FIGURE 5.40 – CHANGE IN REACTION TIME AS A FUNCTION OF GLUCOSE CONCENTRATION .....	134
FIGURE 5.41 – EVOLUTION OF CTPP4-GOX COMPLEX IN THE OPTICAL SPECTRUM AS IT REACTS WITH 20MM/L OF GLUCOSE, WHILE NOT REACTING TO THE OTHER SUBSTANCES .....	135
FIGURE 5.42 – MULTI-LAYERED RECOGNITION LAYER ILLUSTRATING THE BINDING REACTION WITH GLUCOSE MOLECULES AND THE USE OF A PHOSPHATE BUFFER FOR REACTION REVERSAL.....	137
FIGURE 5.44 – CTPP4-POX COMPOUND REACTION WHEN 0.1MM OF PYRUVATE APPLIED AND REVERSED WHEN 25MM/L PHOSPHATE BUFFER WAS APPLIED.....	138
FIGURE 5.45 – CTPP4 DEPOSITED ONTO (1) SILOXANE POLYMER WAVEGUIDE SAMPLES (2) AFTER EXPOSITION TO PHOSPHATE BUFFER AT 50MM/L CONCENTRATION .....	139
FIGURE 5.46 – SCHEMATIC DIAGRAMS OF GRAPHENE STRUCTURES IN 0D,1D AND 3D [5.46] .....	141
FIGURE 5.47 – SCHEMATIC REPRESENTATION OF COVALENTLY BONDED GO AND TPP [5.48].....	142
FIGURE 5.48– SCHEMATIC DESCRIBING THE DEPOSITION OF GRAPHENE OXIDE ON SILOXANE POLYMER COATED GLASS SUBSTRATE, (1) IMPRINTING, (2) UV EXPOSURE, (3) ETFE PEEL OFF AND COPPER ETCHING, (4) WATER TREATMENT.....	143
FIGURE 5.49 – IMAGES OF THE GO-CTPP4 LAYER DEPOSITED ONTO A (A) SILOXANE POLYMER COATED GLASS SLIDE AND ITS SURFACE IMAGE SHOWN ON MICROSCOPE (B) .....	144
FIGURE 5.50 – SCHEMATIC SHOWING THE (A) HYBRID GO-CTPP4 LAYER WITH THE PDMS (2 $\mu$ L) WELL ATTACHED, (B) PHOTO OF THE TEST SAMPLE .....	145
FIGURE 5.51 – ABSORPTION SPECTRUM OF SILOXANE POLYMER SAMPLE FUNCTIONALISED WITH CTPP4-GOX AND EXPOSED TO ARTIFICIAL BRAIN FLUID CONTAINING 5MM/L OF GLUCOSE .....	146
FIGURE 5.52 – INVERTED WAVEGUIDE PATTERN FORMED BY DIRECT IMPRINTING.....	147
FIGURE 5.53 – MICROSCOPE IMAGES SHOWING THE WAVEGUIDE ARRAY AFTER THE GRAPHENE TRANSFER TRIALS BY (A) IMPRINTING PMMA RESULTING IN A RESIDUAL LAYER (SHADED AREA) AND THE STANDARD PROCESS, (B) UNBONDED GRAPHENE WASHED AWAY .....	148
FIGURE 5.54– CTPP4-GOX RECOGNITION LAYER STRUCTURE DEPOSITED ON THE WAVEGUIDE CORE AND INTERROGATED EVANESCENTLY .....	149
FIGURE 5.55 – FABRICATED HIGH QUALITY SILOXANE WAVEGUIDE ARRAYS (2.5-5 $\mu$ M WIDE AND 3 $\mu$ M HIGH) (B) WITH MICROFLUIDIC WELL (A) FORMED BY THE PATTERNED CLADDING.....	149
FIGURE 5.56 – EXPERIMENTAL SETUP (A) OF OPTICAL LAB-ON-CHIP SENSING WITH SENSING LAYER, OPTICAL WAVEGUIDE SENSOR AND MICROFLUIDIC CHANNELS ATTACHED, (B) IMAGE OF SENSOR UNIT DURING MEASUREMENT WITH INLET TUBES PUMPING FLUIDS INTO THE MICROFLUIDIC CHAMBER.....	151
FIGURE 5.57 – OPTICAL SENSING EXPERIMENT WITH GLUCOSE AT 10MM/L CONCENTRATION (NOISE .....	153

## LIST OF TABLES

TABLE 3.1. – SUMMARY OF DIFFERENT OPTICAL WAVEGUIDE MATERIALS. [3.9.] .....	35
TABLE 3.2- SIMULATION RESULTS COMPARING ORMOCORE AND SILOXANE POLYMER MATERIALS IN TERMS OF LIGHT CONFINEMENT AND PENETRATION IN SENSING LAYER.....	44
TABLE 3.3. – CALCULATED MODAL ABSORPTION PARAMETERS AND THEIR RELATIONSHIP WITH CONFINEMENT .....	49
TABLE 5.1. – SUMMARY OF DIFFERENT FABRICATION METHODS .....	93
TABLE 5.2 - STANDARD BOSCH RECIPE.....	102
TABLE 5.3 – DRIE ETCHING RECIPE.....	106
TABLE 5.4 – MEASURED ABSORPTION [AU] AT DIFFERENT PEAKS WITH TIME, RESOLUTION 0.0002 AU AND ACCURACY OF 0.005 AU .....	133
TABLE 5.5 – REACTION TIME CHANGES WITH CTPP4/GOX RATIO.....	134
TABLE 5.7 – ABSORPTION CHANGE [AU] OF CTPP4-LOX COMPOUND AT 420NM FOR 0.1MM OF LACTATE.....	138
TABLE 5.8 – ABSORPTION CHANGE OF CTPP4-POX COMPOUND AT 420NM FOR 0.1MM/L OF PYRUVATE.....	138
TABLE 5.9 – LIST OF COMPONENTS IN THE ANALYTE UNDER TEST .....	145
TABLE 5.10 ABSORPTION CHANGE OF CTPP4-GOX FUNCTIONALISED ON SILOXANE POLYMER AT 420NM .....	146
TABLE 7.1 – SUMMARY OF THE DIFFERENT RECOGNITION METHODS .....	164
TABLE 7.2. – SUMMARY OF ABSORPTION BASED GLUCOSE SENSOR.....	166
TABLE 7.3 – SUMMARY OF FLUORESCENCE BASED GLUCOSE SENSORS .....	169
TABLE 7.4. – SUMMARY OF INTERFEROMETRIC GLUCOSE SENSORS .....	174
TABLE 7.5. – SUMMARY OF OPTICAL LACTATE SENSORS .....	176
TABLE 7.6 – SUMMARY OF OPTICAL PYRUVATE SENSORS .....	179

## LIST OF ABBREVIATIONS AND ACRONYMS

NA	Numerical aperture
SMF	Single mode fiber
MMF	Multimode fiber
SOI	Silicon on insulator
VCSEL	Vertical cavity surface emitting laser
NCCU	Neurosciences Critical Care Unit
GOX/LOX/POX	Glucose, lactate, pyruvate oxidase
CTPP <sub>4</sub>	Meso-tetra(4-carboxyphenyl)porphine
GO	Graphene oxide
VIS	Visible spectrum
UV	Ultra-violet
TBI	Traumatic brain injury
SAM	Self assembled monolayer
GDS	Glow discharge sublimation
DRIE	Deep reactive ion etching
EBL	Electron beam lithography
ETFE	Ethylene tetrafluoroethylene
NIL	Nanoimprinting lithography
MZM	Mach-Zehnder modulator
UV VIS	Ultraviolet visible spectroscopy
SEM	Scanning electron microscopy
GOD	Glucose oxidase
FAD	Flavin adenine dinucleotide
FLU	Fluorescence
FIA	Flow injection analysis
SWNIR	Shortwave Near Infrared

# Chapter 1 - Introduction

## 1.1 Emergence of lab-on-chip technologies

Over the last 30 years, two major product revolutions have taken place due to the growth of the optoelectronics and fiber-optic communications industries. The optoelectronics industry have produced several ground breaking products such as compact disk players, laser printers, bar code scanners, and laser pointers. The optical communication industry has revolutionized the telecommunication industry by providing higher performance, more reliable telecommunication links and increased bandwidth. This revolution has mainly been driven by the ever increasing demand for internet traffic, which also led to new innovation in short link data communications such as chip to chip and board to board interconnections. The current state-of-art technologies are pushing towards the limits of the maximum transmission capacity for optical transmission. In parallel with these developments, fibre-optic sensor technologies have rapidly proliferated as several optical components, techniques and algorithms used in the fibre-optic communications can be used for optical sensing.

Optical sensing technologies have made great progress owing to several advantages over their electronic counterparts due the high sensitivity and immunity to electromagnetic interference [1.1]. Optical sensors have rapidly gained popularity in biochemical sensors application as they can provide some ideal characteristics [1.2-4], such as the possibility of using spectral measurement, miniaturisation, remote sensing over long distances and the use of self-referencing without any electrical.

In the 80's only a limited number of groups were publishing data on optical sensors with integrated biorecognition layers [1.5-8] and microfluidics. The possibility of moving a biochemical sensor off the optical bench was still a long term goal mainly owing to the bulky expensive optics that was available at the time. However recent advances in nanofabrication, along with growing appreciation of potential benefits of photonics and microfluidics have provided a powerful tool for integrating several subsystems into one

chip. Lab-on-chip (LOC) technologies have a tremendous potential in a wide range of applications in healthcare, environmental monitoring, food quality control and in global health in general. Since the modern inception of microfluidic technologies, the use in biomedical sensing has been perceived as one of the most powerful potential applications of this technology. By taking advantage of their small size, low volume requirements for samples and rapid analysis, LOC technologies have started to emerge in remote settings as a result of developments in integrating fluid actuation, sample pre- and post-treatment as well as signal detection and analysis [1.9]. Extensive research has begun in this field as both academia and industry have realised the future impact of this technology on important issues such as global health and point of care diagnostics. For example, developing and third-world countries are in great need of low-cost health related technologies specifically in healthcare diagnostics. Given the discussed technological advances and growing demand for low cost optical lab-on-chip sensors, this work has focused on investigating the possible application of Siloxane waveguide technology for biochemical sensing applications.

### 1.2 Brain fluid sensor project for traumatic brain injury analysis

Head injury is one of the leading cause of death in the under-40 population in the developed world [1.10]. In terms of population statistics, in the UK every year 1,500 per 100,000 of the population (total 900,000) attend emergency departments with a head injury, 6–10 out of 100,000 die from traumatic brain injury (TBI). Moreover, an estimated 1.2 million people live with some level of TBI-related disability in the UK, which has profound socio-economic consequences, as the prevalence is particularly high among children and young to middle-aged adults. While many individuals have good outcomes, others experience varying degrees of disability, which are often life-long, with consequent demands on carers and resources.

Monitoring of changes in the cerebral biochemistry by microdialysis is a promising technique that has enhance our understanding of the pathophysiology of brain injury [1.11]. Brain chemistry can be monitored by means of inserting fine semi-permeable catheters into the brain, a technique called microdialysis. A recent study by Researchers at the Neurosciences Critical Care Unit (NCCU) at Addenbrooke's Hospital has recognised that the characteristic of adverse metabolism if the microdialysate lactate-to-pyruvate ratio is above 25, which is

## Chapter 1 - Introduction

associated with poor outcome. This marker has been proven to be an essential factor and can serve as a clear indicator for the severeness of the injury. However there are several technological and practical limitations.

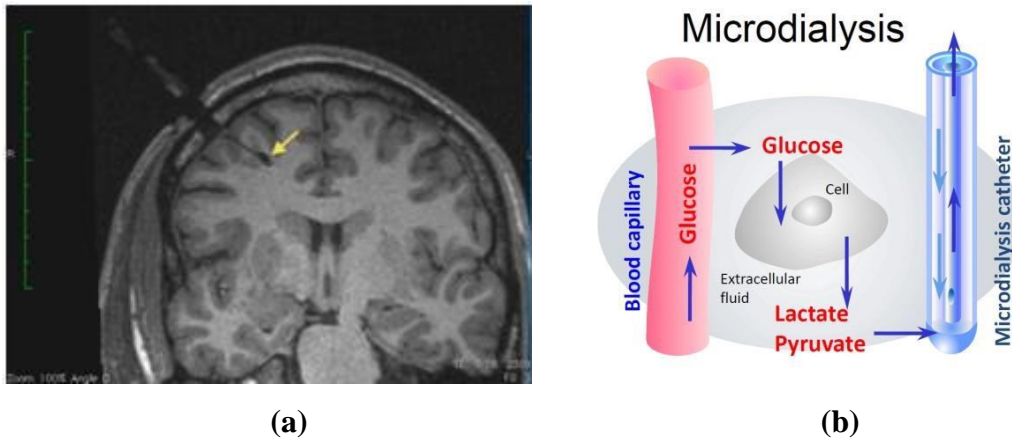


Figure 1.1 (a) Magnetic resonance image (MRI) showing the brain of a head injury patient with a microdialysis catheter tube in position, the tip indicated by an arrow (yellow). Scale bars (green) show centimetre divisions. (MRI technical details: 3D MP—RAGE sequence, at 3 Tesla). Image is courtesy of the Wolfson Brain Imaging Centre (University of Cambridge). (b) Schematic diagram showing the principles of microdialysis. Blood capillaries supply glucose as a source of energy for the brain cells, which metabolise it. Some of the products (metabolites), including lactate and pyruvate, emerge from the cells into the brain's extracellular fluid and are collected by the microdialysis catheter tube [1.12].

Brain microdialysates are inherently very small volumes (typically 18  $\mu\text{L}/\text{h}$ ), and are technologically demanding to analyse. Glucose, lactate and pyruvate are currently measured at the bedside with commercially available analysers using enzymatic colorimetric “wet chemistry”. However, these analysers cannot monitor continuously, because they are designed for microdialysates collected in micro-vials on the outlet of the microdialysis catheter, with micro-vials changed manually (typically hourly) by a nurse and transferred to the bedside analyser. These analysers are expensive to purchase, maintain (servicing costs) and operate (reagent costs), and are demanding on staff time, training and expertise. The only commercially available clinical microdialysis analyser is currently the ISCUSflex (M Dialysis AB, Stockholm, Sweden), which costs £38,947. Service maintenance costs are currently £2865 per annum, and reagents sufficient for several days £177.

Design of a more cost-effective, robust, compact, user-friendly and continuous monitoring device, using a sensor that could be connected directly to the outlet of the microdialysis

catheter would thus be highly desirable and would significantly improve the quality of the patient diagnosis as well as expand the research capabilities of these centres.

Our on-going research aims to develop a sensor for the continuous real-time measurement of glucose, lactate and pyruvate concentrations in brain microdialysates from head injury patients in the Neurosciences Critical Care Unit (NCCU) at Addenbrooke's Hospital. Initial work has identified the potential of developing low-cost bio-medical polymeric optical sensors using polymer waveguide technology suitable for use in clinical environments. These sensors need to be compatible with microdialysis fluid flow. Typically we use a flow rate of 0.3  $\mu\text{l}/\text{min}$  (18  $\mu\text{l}/\text{h}$ ), though flow rates in the range 0.1 – 5  $\mu\text{l}/\text{min}$  are possible with current technology.

### 1.3 Siloxane waveguide technology for sensing

Recent advances in the integration of polymeric optical waveguides with electronics onto standard printed circuit boards (PCBs) allow the development of cost-effective lab-on-a-chip modules suitable for mass production. Advantages of Siloxane polymers are low cost and stable optical properties even under thermal and mechanical stresses and exposure to humidity. Other advantages include low power consumption, compatibility with the existing PCB technology standards, and facility for extension of an integrated radio frequency subsystem for remote monitoring. Extensive research has been done with this technology in order to create high capacity optical interconnect. Most recently, a passive optical backplane based on a novel meshed waveguide structure demonstrated the potential for one terabit per second capacity [1.13].

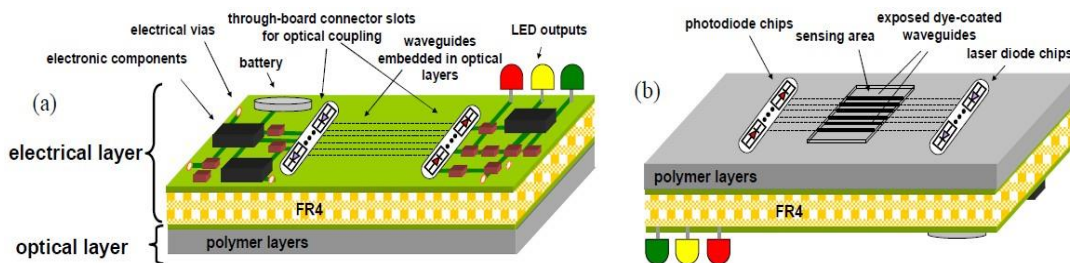


Figure 1.2. – Schematic of layout of the electro-optic PCB-integrated optical biosensor – . (a) Planar view of (a) top and (b) bottom board sides [1.14].

## Chapter 1 - Introduction

Siloxane polymer based optical waveguides have not been used solely for interconnect technology. The first siloxane based sensor was an ammonia gas sensor (Fig. 1.2.) formed directly onto a PCB and achieved reversible and repeatable detection [1.14]. The gas sensor showed good operation with projected sensitivity of at least 700 ppm for a BCP coated waveguides in operating wavelength of 635nm.

Developing robust and mass producible sensors using such waveguides technology is challenging as most recognition layers require optical interrogation in the visible wavelength. Generally, highly sensitive single mode optical waveguides operating at visible light wavelength are around or below

1 $\mu$ m, which results in high coupling losses and limited number of fabrication options. The industry standard fabrication process is UV photolithography, which is not recommended with feature sizes below 2  $\mu$ m. One key advantage of the siloxane material is its small refractive index difference between the core and the cladding materials allowing larger optical structures to be realized as well as the potential to extended evanescent field penetration into the sensing medium. The aforementioned gas sensor is made of an array of 50 x50  $\mu$ m multimode waveguides, which were originally designed for on-board interconnect technology. Large core waveguides provide relaxed fabrication tolerances and better light coupling efficiencies; however, as will be explained later in this thesis at the expense of sensor sensitivity.

### 1.4 Novelty of work

A variety of optical waveguide structures are analysed from the aspect of biochemical sensing. Based on sensitivity analysis of composite optical waveguide structures, it was concluded that it is a great solution in compensating water effects near the sensing layer. A thin high index Ta<sub>2</sub>O<sub>5</sub> layer (RI=2.16) can be used to compensate the abrupt refractive index profile shift present at the sensing layer region due to water molecules. Moreover, optical field confinement in sensing layer can be enhanced by careful adjustment of Ta<sub>2</sub>O<sub>5</sub> layer thickness reaching up to 30 percent.

A novel method of optical interrogation is presented based on a mode selective optical sensing. Asymmetric Y-junctions are used in multimode evanescent-wave absorption sensors in order to overcome the spurious effects due to absorption changes in the outer medium (analyte carrying microfluidics) and improve their operation and reliability. The proposed sensor device maintains the fundamental simplicity of multimode absorption sensors while

overcoming this common issue with such devices [1.15]. A short overview of Y-junction theory is provided, where the design of the proposed waveguide sensor is presented and its operating principle is described (Section 5.3). Simulation results are reported in Chapter 4.6 demonstrating that the device can efficiently detect the analyte of interest with an accuracy better than 95 %, even in the case of a highly-absorbing outer medium with an absorption 80 times greater than that of the sensing layer.

A novel recognition layer has been developed for determination of glucose, lactate and pyruvate concentrations in brain fluid. The development started by showing that the CTPP4-GOD complex can be used to detect all three analytes. An appropriate deposition technique has been developed based on solvent casting in order to create a thin film required for reliable reversible operation. Although, the recognition layer indicated reversible reaction on glass slides, it only showed limited reversibility on siloxane polymer-based samples. Recognition layer was further enhanced by the addition of graphene oxide layer, serving as a new substrate. It allowed easier and faster deposition with high surface quality. Optical waveguide experiments were carried out, where strong opto-chemical reaction was achieved, as it is discussed in Chapter 5.

A novel fabrication technique for siloxane polymer waveguides has been developed allowing 30nm resolution. Both Thermal and UV Nanoimprinting lithography has been investigated for fabricating photonic lab-on-chip sensors. The fabrication process involved the development of our own master stamp patterning process based on Electron Beam Lithography and Deep Reactive Ion Etching.

### 1.5 Aims and synopsis of this thesis

The aim of this thesis is to investigate the design, manufacture and testing of a siloxane polymer waveguide-based lab-on-chip sensor for the purpose of analysing brain microdialysates. This waveguide technology has been primarily designed for on-board data communication. However the focus of this research is to investigate the possibility of realizing a siloxane polymer based lab- on-chip sensor capable of continuously monitoring glucose lactate and pyruvate concentrations in brain fluids, thus contributing to the current trend in the advancement of portable lab-on-chip technologies for the deployment of point-of-care diagnostic tools for medical practitioners.

**Chapter 1** provides a brief overview of the technologies that led to the advent of lab-

## Chapter 1 - Introduction

on-chip technologies. The second part of the introduction summarizes the motivation and the future application behind this research. Moreover, it illustrates the demand by medical practitioners for the development of such technology for point of care clinical diagnosis. The final part of the introduction outlines the main features and key attributes of siloxane polymer waveguide technology for sensing applications.

**Chapter 2** reviews some of the state-of-art optical sensing technologies as well as introducing the reader to the fundamental theory.

**Chapter 3** summarizes the design and modelling work that was carried out for the development of single mode waveguide structures and other novel sensor structures.

**Chapter 4** provides a detailed overview of the fundamentals of waveguide Y-junctions and mode duplex optical transmission. A novel sensor architecture is proposed in this work, where asymmetric Y-junction are used for mode selective sensing. Though a similar mode-sorting technique has been previously proposed [1.16-18], it is the first time it is being proposed for sensing applications.

**Chapter 5** reviews the state-of-art fabrication techniques available for polymer integrated optics primarily focusing on an emerging technology called Nano-imprinting Lithography and compares it with the standard UV approach. Experimental results are provided for both techniques and illustrate their limitations. These fabrication techniques are compared on the basis of single mode waveguide fabrication, the related experimental results and characterisations are also discussed. The last part of Chapter 5 summarizes the experimental results of a novel Brain fluid analyzer and its characteristics as well as the used microfluidics. The reader is guided through the different development phases of a novel recognition layer, including a short overview of graphene material and the corresponding experimental results.

**Chapter 6** concludes the thesis by summarising the results and its achievements.

**Appendix** summarizes a comprehensive literature review that aimed to provide a snapshot of currently existing technologies and tested biochemical reactions that can be used for sensing the three aforementioned biomolecules. At the end of this chapter, there is a final review helping the reader understand the reason why certain research directions and goals were set.

## 1.6 References

- 1.1 Naseer Sabri, S A Aljunid, M S Salim, R B Ahmad, R Kamaruddin, "Toward Optical Sensors: Review and Applications", *Journal of Physics: Conference Series* 423, 2013.
- 1.2 R. A. Potyrailo, S. E. Hobbs, G. M. Hieftje, "Optical waveguide sensors in analytical chemistry: today's instrumentation, applications and trends for future development", *Fresenius J. Analytical Chemistry*. vol. 362 , pp. 349-373 , 1998.
- 1.3 G. Gauglitz, "Opto-Chemical and Opto-Immuno Sensors", *Sensors Technology*, vol. 1 Issue 1., 1996.
- 1.4 F. S. Ligler, C. A. R. Taitt, "Optical biosensor: present and future", First Edition, Elsevier, 2002.
- 1.5 Peterson JJ, Vurek GG, "Fiber-optic sensors for biomedical applications", *Science* vol. 224, pp. 123–127, 1984.
- 1.6 Buck, R. P., Hatfield, W. E., Uman, M., Bowden, E. F., "Biosensor Technology: Fundamentals and Applications", CRC Press, pp 209-390 ,1990;
- 1.7 Wise, D. L., Wingard, L. B., Eds. "Biosensors with Fiberoptics", Humana Press, 1st Edition, 1991.
- 1.8 Wolfbeis, O. S., Ed. Fiber, "Optic Chemical Sensors and Biosensors", CRC Press, 1st Edition, 1991.
- 1.9 Curtis D. Chin, Vincent Linder and Samuel K. Sia, "Lab-on-a-chip devices for global health: Past studies and future opportunities", *Lab Chip*, vol. 7, pp 41–57, 2007.
- 1.10 D. J. Thurman, C. Alverson, Doug Browne, K. A. Dunn, J. Guerrero, R. Johnson, V. Johnson, J. Langlois, D. Pilkey, J. E. Sniezek, S. Toal, "Traumatic Brain Injury in the United States: A Report to Congress", National Center for Injury Prevention and Control, 1999.
- 1.11 I. Timofeev, K. L. H. Carpenter, J. Nortje, P. G. Al-Rawi, M. T. O'Connell, M. Czosnyka, P. Smielewski, J. D. Pickard, D. Menon, P. J. Kirkpatrick, A. K. Gupta and Peter J. Hutchinson, "Cerebral extracellular chemistry and outcome following traumatic brain injury: a microdialysis study of 223 patients", Division of Neurosurgery, Department of Clinical Neurosciences, University of Cambridge, Addenbrooke's Hospital, Cambridge, Oxford University Press, 2010.
- 1.12 K. Carpenter, I. Jalloh, C. N. Gallagher, P. Grice, D. J. Howe, A. Mason, I. Timofeev, A. Helmy, M. P. Murphy, D. K. Menon, P. J. Kirkpatrick, T. A. Carpenter, G. R. Sutherland,

## Chapter 1 - Introduction

- J. D. Pickard, P. J. Huchinson, “C-labelled microdialysis studies of cerebral metabolism in TBI patients”, *European Journal of Pharmaceutical Sciences*, vol. 57, pp. 87-97, 2014
- 1.13 J. Beals, N. Bamiedakis, A. Wonfor, R. V. Penty, “A terabit capacity polymer optical backplane based on novel meshed waveguide architecture”, *Appl. Phys. A*, vol 95., pp 983- 988, 2009.
- 1.14 N. Bamiedakis et al., “Low-cost PCB-integrated Polymer Waveguide Sensor for Gas Detection”, *Conference Paper on Lasers and Electro-Optics (CLEO)*, 2011.
- 1.15 Stewart, B. Culshaw, “Optical waveguide modelling and design for evanescent field chemical sensors,” *Optical and Quantum Electronics*, vol. 26, 1993.
- 1.16 M. Izutsu, Y. Nakai, and T. Sueta, “Operation mechanism of the single-mode optical-waveguide-Y junction,” *Optics Letters*, vol. 7, no. 3, pp. 136–138, 1982.
- 1.17 J. D. Love and N. Riesen, “Single-, few-, and multimode Y-junctions,” *J. Lightwave Technology*, vol. 30, pp. 304–309, 2012.
- 1.18 N. Riesen, J.D. Love, and J.W. Arkwright, “Few-mode elliptical core fiber data transmission,” *IEEE Photonics Technology Letters*, vol 24, pp. 344–346, 2012.

# Chapter 2 – Optical sensing techniques

## 2.1 Introduction

The purpose of a sensor in any system is to translate the physical, chemical or biological information into an electrical or optical signal. Biochemical sensors are usually used to determine the concentration of chemical or biological analytes in an aqueous environment. These sensors can be used in various applications, such as food quality control, wellness monitoring, and pathogen sensing or clinical diagnostics. The purpose of this chapter is to provide an overview of current and emerging optical sensing technologies and introduce some of the fundamental concepts.

The general definition of chemical sensors by Wolfbeis (1990) states “Chemical sensors are small-sized devices comprising of a recognition element, a transduction element and a signal processor capable of continuously and reversibly reporting a chemical concentration” [2.1]. There are several key attributes which make a sensor complete such as adequate sensitivity, broad dynamic range, low-cost, small size, electrical output, good signal to noise-ratio, simple fabrication, robustness, high selectivity and suitability for mass production. A few important attributes are described in detail.

Sensitivity is usually defined as the lowest level of concentration that can be detected in the sensing environment. In order to determine the required dynamic range, it is important to find the range of concentration at which the target complex is present in the sensing medium. As an example, the normal physiological range in brain fluid for glucose is 0.1-6mM, while it is 0.1-12 mM for lactate and 0.01-1mM for pyruvate. As will be discussed later in this chapter, it is clearly important for the available design options for both the recognition layer and the optical sensor system. In other chemical sensors such as environmental monitoring of toxic agents, it is only necessary to determine if the concentration reaches an alarming level.

Selectivity is usually defined by the ability to differentiate between the target chemical compounds and other interferents. In some cases, there are dozens of other molecules present

in the medium that can interfere with the sensing mechanism, which often lead to errors in the concentration determination.

Reversibility and reusability are essential for many everyday applications. An ideal sensor is required to be able to respond dynamically to changes in the analyte concentration, preferably over a long period of time without interruptions.

The robustness of a sensor is defined by its ability to perform its function in a wide variety of conditions. Sensor operation may be altered in a different ambient environment. As an example: chemical compounds (reagents) are often more temperature dependent than other subsystems. A few degree change in temperature can lead to a different level of optical reaction as well as change the required driving condition of the light source. Other variables such as humidity, pressure or exposure to different aromatic compounds in the air can also be factors.

For a point-of-care clinical diagnostic tool, low-cost and portability are important design considerations as there can be dozen of patients a day accepted to a clinic every day in different departments. The fabrication technology can define the cost and the ease of mass production. As an example, designs that can be fabricated by standard UV photolithography will cost a fraction of those that require electron-beam lithography. Using optical technique – which require simple and low cost light sources and detectors – is usually easier to transfer to industry and therefore have the potential to make an actual positive impact on the work of medical practitioners.

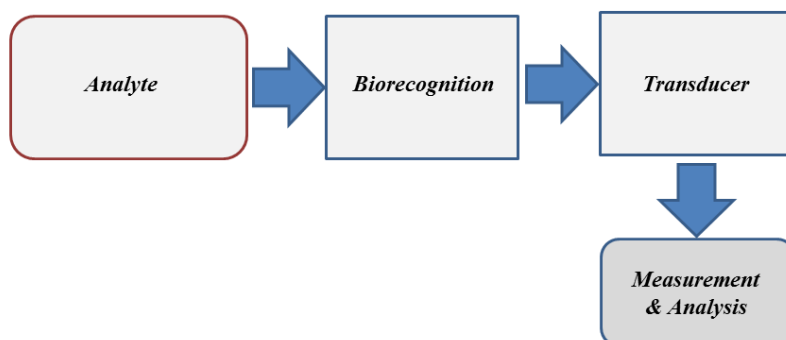


Figure 2.1 - Biosensing Mechanism

A biosensor comprise three main parts (Fig 2.1): a biorecognition element, transducer and measurement & analysis. Biorecognition is made of bioreceptors that are responsible for capturing or binding the target molecule. In the moment of the molecular binding, a sensing effect takes place, which can be measured from electrical, mechanical or optical changes. The signal triggering molecule binding to a sensing site is called the ligand. Generally, the sensor selectivity of a sensor is defined at this stage. The ratio of the triggered signal strength and the minimum number of required molecules defines the sensitivity and resolution of the sensor.

The point at which the signal shows no further change with increasing analyte concentration defines the dynamic range of the sensor.

The most widely used bio recognition elements are based on antibody-antigen, enzymatic, nucleic-acid or cellular interactions [2.2]. Antibodies (also called immunoglobulins) are complex biomolecules made of various amino acids arranged in a characteristic Y-shape as shown on Fig. 2.1. The specific target molecule (antigen) is captured by the antibody with high selectivity – due to their complementary molecular structure – and forms a strong bond. This bonding reaction is very rapid and stable. However, it is usually limited by a reasonable lifetime. Antigen-antibody reaction is capable of detecting very small amounts of target molecules, even in a highly contested environment where several other biochemical compounds are present.

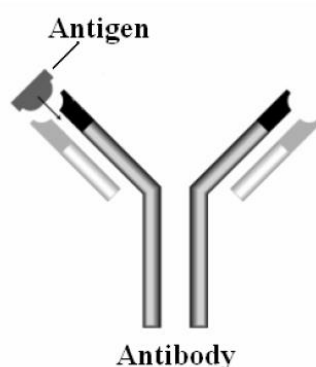


Figure 2.2 - Antibody-antigen Interaction [2.2]

Enzyme based recognition is also powerful as it possesses the ability to amplify the detection mechanism. As result of this catalytic activity, the permitted minimum detection limit can be enhanced compared to other techniques, making it a commonly used recognition element. Although, this reaction can be denaturised, therefore leading to disassociating into subcomponents, which can lead to an unstable reaction or no reaction at all.

DNA sensors often use DNA/RNA hybridization, where the biorecognition mechanism exploit the complementarities of the nucleotide pairs such as cystosine (C)-guanune(G), adenine(A)-thymine(T).

The transduction mechanism of the triggered signal refers to the conversion of detection (also called interrogation) event to detectable signal. There are a wide variety of transduction methods from electro-chemical, mass-based to mechanical. The last process of the sensing mechanism is the measurement and analysis, where the transduced signal is recorded and interpreted as the quantity of biomolecular activity.

## 2.2 Fundamental Optical Transduction Mechanisms

### Optical Absorption

Light incident on a material may or may not be absorbed by the material. The probability of that light is absorbed is related to the cross section ( $\sigma$ ). This cross section is an effective area of the atom or molecule (Fig. 2.3). Consider a light incident on a material (molecular concentration of  $C$ , [ $\text{cm}^{-3}$ ]). The number of molecules illuminated by light intensity ( $I_x$ ) is  $C \cdot A \cdot dx$ . The total effective area that the molecule presents is  $\sigma \cdot C \cdot A \cdot dx$ . The probability of light being absorbed or scattered out of the beam in thickness  $dx$  is:

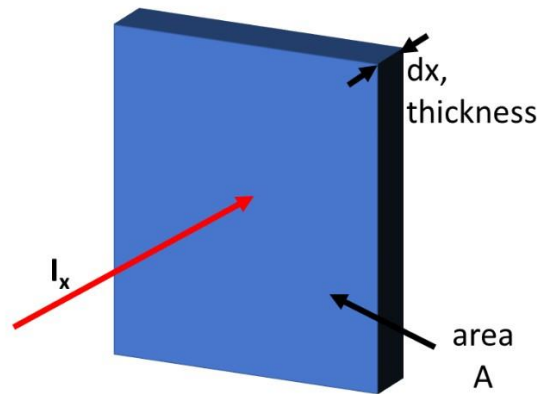


Figure 2.3. – Light incident on an absorbing material with intensity  $I_x$ , thickness of  $x$  and cross section of  $A$

$$-\frac{dI_x}{I_x} = \frac{\sigma C A}{A} dx \quad (2.1)$$

Where,  $dI_x$  is the change in intensity across  $dx$

Beer-Lambert Law, by integrating both sides of the equation:

$$\int_0^I \frac{dI_x}{I_x} = - \int_0^I \sigma C dx \quad (2.2)$$

$$\ln(I) - \ln(I_0) = \ln\left(\frac{I}{I_0}\right) = -\sigma C x \quad (2.3)$$

$$I = I_0 e^{-\sigma C x} = I_0 e^{-\alpha x} \quad (2.4)$$

Where  $\alpha$  is the linear absorption coefficient of which if scattering effects are ignored is the same as the absorption attenuation coefficient. As a result of Beer-Lambert law, light intensity decreases exponentially with depth ( $x$ ) in material. Linear absorption coefficient is expressed in  $\text{cm}^{-1}$  and wavelength dependent, therefore the law becomes:

$$I_{(\lambda)} = I_0 e^{-\alpha_{(\lambda)} x} \quad (2.3)$$

Absorbance is defined as,

$$A = \log\left(\frac{I_0(\lambda)}{I_{(\lambda)}}\right) = \log\left(\frac{I_0(\lambda)}{I_{(\lambda)} e^{-\alpha x}}\right) = \log(e^{\alpha x}) \quad (2.4)$$

$$A = \alpha x \log(e) = 0.434 \alpha x \quad (2.5)$$

Which includes both absorption and scattering.

$$A = 0.434 \alpha C x \quad (2.6)$$

Total absorbance over a multi layered material can be described as:

$$A_{total} = A_1 + A_2 + A_3 + \dots + A_n \quad (2.7)$$

$$A_{total} = \alpha_1 C_1 x_1 + \alpha_2 C_2 x_2 + \alpha_3 C_3 x_3 + \dots + \alpha_n C_n x_n \quad (2.8)$$

By measuring the absorbance of the solution, the concentration of the bioanalyte can be estimated in any aqueous solution.

There are a number of different strategies for designing an absorption-based optical biosensor. One way is to detect the light absorption directly – which relies on tracking the changes in the optical absorption lines or bands at a convenient wavelength – which is linearly proportional to the concentration. Indirect absorption is another way, where a secondary reagent is used to mediate the sensing, e.g pH sensors use an indicator dye whose colour/absorption characteristics change as a function of pH.

There are several different design approaches (Fig. 2.4) for biosensors in terms of light-matter interaction, which are the same for both fibre optics and waveguides.

- **Guided Wave Approach:** The fibre or waveguide is only used to convey the light to and from the spectroscopic cell (Fig 2.4a-b), and therefore take no direct part in the sensing mechanism [2.3]. Light scattering is high ultimately

limiting the achievable sensitivity of the sensor.

- **Evanescent Wave Approach:** The fibre or waveguide itself forms a sensing element, by using its evanescent field extending from the core to interact with the analyte that is immobilised on the top of the core or cladding layer [2.4-5] as shown on Fig. 2.4b-c.
- **Optrode Approach:** The fibre or waveguide has an indicator dye attached to the fibre tip, which are called optrodes as shown on Fig. 2.4d and in [2.6]. The tip of the fibre is surrounded by a microfluidic well delivering the analyte fluid to the sensing or recognition layer.

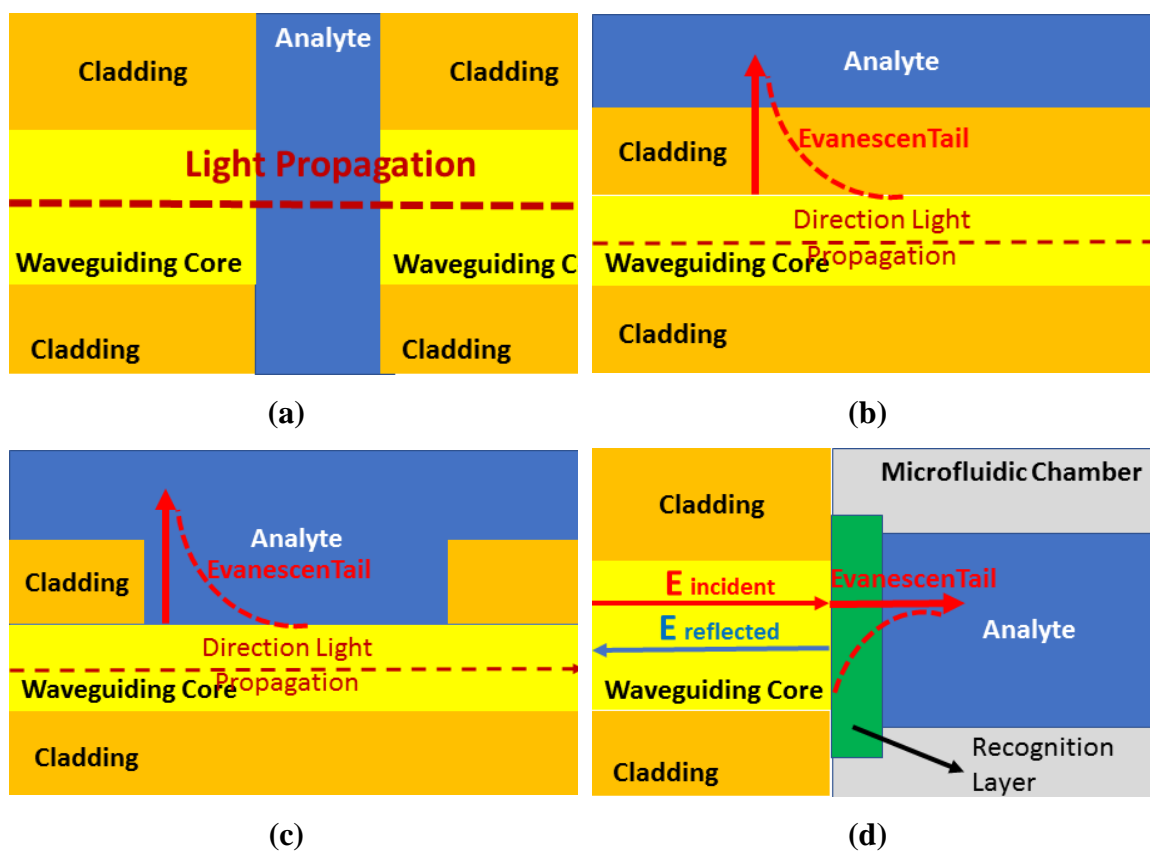


Figure 2.4 – Schematic of different sensor architectures (a) Guided Wave Sensor (b,c) Evanescent Wave Sensor (d) Optrode Sensor

### Fluorescence

Fluorescence phenomena are related to an energetic transition from an excited state to a lower energy level resulting in photon emission. The process can be best understood by the Jablonskii diagram shown in Fig. 2.5. In this diagram,  $S_0, \dots, S_n$  and  $T_1, \dots, T_m$  represent the electronic energy levels of a molecule ( $S_1, \dots, S_n$  are excited singlet states and  $T_1, \dots, T_m$

are excited triplet states). At equilibrium, molecules have the lowest possible energy level  $S_0$  [2.2].

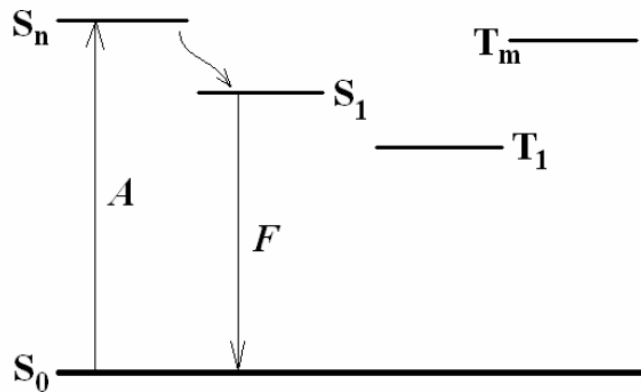


Figure 2.5 - Jablonskii diagram [2.2]

Molecular transitions occur to an excited state by optical absorption. Following the absorption, the resultant energy level is dictated by the wavelength of the incident radiation, and hence the incident photon energy.

The intensity of the absorption (number of ground state molecules promoted to the electronic excited state) depends on the intensity of the excitation radiation (number of photons) and the probability of the transition with photons of the particular energy used. Molecular relaxation can result from an emission of a photon without any change in spin multiplicity (from singlet state to another singlet state), this process is called fluorescence. The wavelength at which the photon is emitted depends on the energy lost by the molecule in the relaxation process. The concentration of the target analyte can be determined by monitoring either the fluorescence intensity or lifetime [2.6- 7].

### Surface Plasmon Resonance

Surface electromagnetic waves that propagate in a direction parallel to the metal/dielectric interface are usually called surface plasmon polaritons (SPPs). Alternatively, they are also called surface plasmon waves (SPWs) as they propagate along the interface as a wave. SPW occur when the frequency of the light matches the natural frequency of oscillating surface electrons. These oscillations are highly sensitive to changes in any sensing event on the surface, such as adsorption or binding of molecules. The surface wave propagates exactly on the metal/dielectric interface, which can be either be with air or with an aqueous medium carrying the target analyte. When this phenomena occurs in a nanoscale

structure, such as metal particles or nanoantenna, it is called localised surface plasmon resonance (LSPR). These waves do not propagate as regular waves, as the SPR wave is a TM-polarized wave, where the magnetic vector is perpendicular to SPW propagation direction and parallel to the interface plane. When this wave interacts with the analyte, a phase change is introduced, which can be a measure of analyte concentration.

### Raman Scattering

Raman spectroscopy is a technique where laser light interacts with molecular vibrations, phonons or other excitations in the system, resulting in a shift of photon energy. As a result of this shift, an energy exchange occurs between the photons and scattering molecules. As a result of Rayleigh (or elastic) scattering, there is a change to the incident photon energy after collision. The scattered photon retains the identical frequency as the incident photon (Fig. 2.6). In Raman (or inelastic) scattering, the energy is transferred from the molecule to the photon or vice versa. Raman to Stokes scattering occurs when the scattered photon has less energy than the incident photon. When the scattered photon has more energy than the incident photon, the process is called Raman to anti-Stokes scattering.

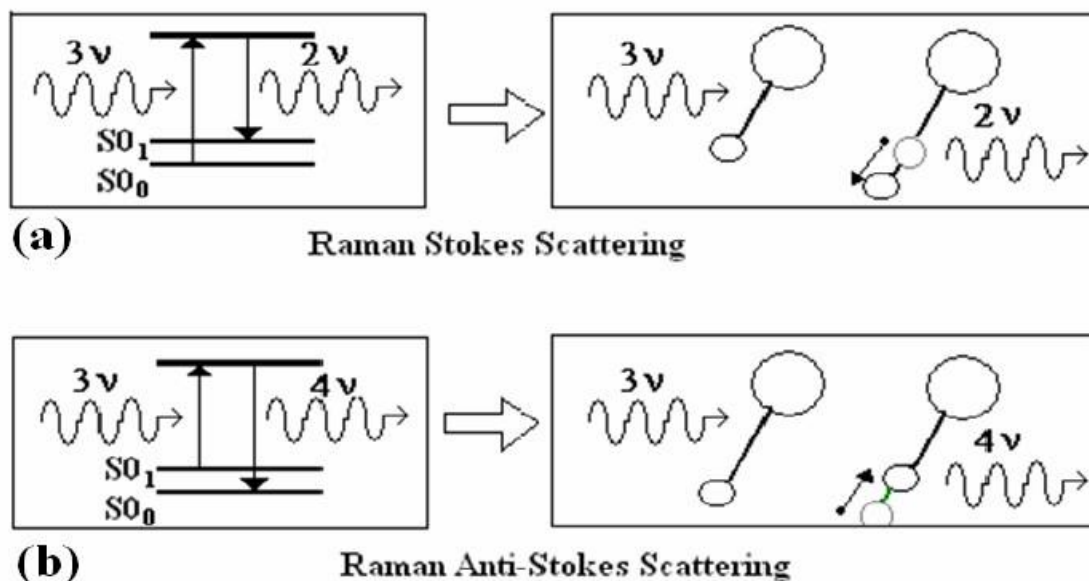


Fig. 2.6 - Raman scattering Mechanism (a) Raman Stokes scattering (b) Raman Anti-Stokes scattering [2.2]

Raman signals are usually weak and require a powerful light source and sensitive detector for this reaction to be detected. As a result, it is difficult to adopt this technology for cost effective integrated sensor design for mass market applications, and therefore it is outside of the scope of this thesis. An interesting advantage of this process is – while only a limited number of molecules contribute to tissues fluorescence – most biological molecules

are Raman active and therefore able to overcome the limitations of fluorescence.

### Effective index change in guiding structures

By using optical wave guiding structures, sensing events can be monitored by correlating the analyte concentration with a phase shift in the propagating optical waveguide mode. There are two different ways to sense the binding event. First by monitoring the change in adlayer formation (thickness) as the molecules bind to the recognition layer from a gaseous or liquid medium. The other method is to measure the refractive index change of the homogeneous liquid that serves as the waveguide cover. The change of the effective refractive index of the propagating mode into the guiding layer can be easily correlated with the change in analyte concentration. This optical sensing principle will be discussed in Chapter 3.

## 2.3 Optical Waveguide Theory

A brief overview is required in order to understand the design process of the sensors described in the later chapters. A dielectric or optical waveguide has the capability of confining light within its structure. The most well-known structure such as this is the optical fibre. However in integrated optics, planar optical waveguides are used. These optical waveguide structures allow compact lab on chip sensors to be formed, integrated with microfluidics and the biorecognition layer. Fig 2.7 shows the basic structure of a 3 layered slab waveguide structure consisting of a guiding core, substrate and a cover (or cladding) layer.

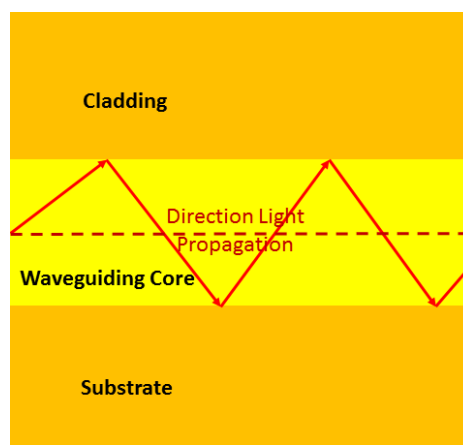


Figure 2.7 – Optical waveguide structure for multimode behaviour, light is confined within the core due to total internal reflection on both interfaces

The core layer can be a few hundred nanometres to several millimetres thick with a refractive index higher than the surrounding medium. In the following derivations, all the dielectric medias are assumed to be ideal, and thus homogeneous, isotropic and loss free.

Light propagating within the core layer is confined by the law of total internal reflection. Considering two media with refractive indices ( $n_1$  and  $n_2$ ), with a monochromatic light beam incident at an angle  $\phi_1$  between the wave normal and  $z$  is partially reflected at the same angle  $\phi_1$  and partially refracted into the adjacent medium at  $\phi_2$  as shown on Fig. 2.8.

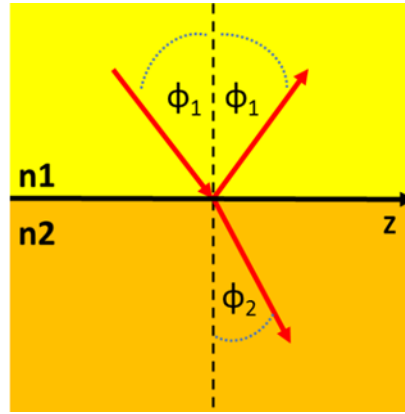


Figure 2.8 – Two dielectric media with refractive index  $n_1, n_2$  and an incident wave with angle  $\phi_1$

The angle of  $\phi_2$  of the refracted wave is given by Snell's law:

$$n_1 \sin(\phi_1) = n_2 \sin(\phi_2) \quad (2.9)$$

The amplitude of the refracted and reflected wave depend on the angle of incident and the polarisation of the incident light. These amplitudes can be calculated by using the reflection and refraction coefficients given by Fresnel formulas for each polarisation ( $\sigma$ ).

$$\rho_\sigma = \frac{n_1 \sin(\phi_1) - n_2 \sin(\phi_2)}{n_1 \sin(\phi_1) + n_2 \sin(\phi_2)} \quad (2.10)$$

$$\rho_\sigma = \frac{n_1 \sin(\phi_1) - n_1 \sqrt{n_2^2 - n_1^2 \sin^2(\phi_1)}}{n_1 \sin(\phi_1) + n_1 \sqrt{n_2^2 - n_1^2 \sin^2(\phi_1)}} \quad (2.11)$$

$$\tau_\sigma = 1 - \frac{\sin(\phi_1 - \phi_2)}{\sin(\phi_1 + \phi_2)} \quad (2.12)$$

Where  $\rho$  is the reflection coefficient and  $\tau$  the transmission coefficient for electrical field. For  $\pi$ -polarisation, where the magnetic field is perpendicular to the plane of incidence the transmission coefficient can be described as:

$$\rho_\pi = \frac{n_2 \cos(\phi_1) - n_1 \cos(\phi_2)}{n_2 \cos(\phi_1) + n_1 \cos(\phi_2)} \quad (2.13)$$

$$\rho_{\pi} = \frac{n_2^2 \cos(\varphi_1) - n_1 \sqrt{n_2^2 - n_1^2 \sin^2(\varphi_1)}}{n_2^2 \cos(\varphi_1) + n_1 \sqrt{n_2^2 - n_1^2 \sin^2(\varphi_1)}} \quad (2.14)$$

$$\tau_{\pi} = \left(1 - \frac{\tan(\varphi_1 - \varphi_2)}{\tan(\varphi_1 + \varphi_2)}\right) * \frac{\cos \varphi_1}{\cos \varphi_2} \quad (2.15)$$

The critical angle ( $\varphi_c$ ) can be given by:

$$\sin \varphi_c = \frac{n_2}{n_1} \quad (2.16)$$

Until the incident angle is less than the critical angle only partial reflection occurs and  $\sigma$  remains real valued. When the incident angle is greater than the critical angle total reflection occurs with complex valued  $\sigma$ . In the medium with the lower refractive index a propagating wave is generated which is attenuated exponentially in  $z$  direction. This attenuated wave is called evanescent field and can be described by the following expression called decay factor:

$$e^{-\frac{2\pi}{\lambda_0} \sqrt{n_1^2 \sin^2(\varphi_1) - n_2^2} z} \quad (2.17)$$

Where  $\lambda_0$  is the wavelength in vacuum.

The properties of evanescent field will be discussed in the later chapters.

In addition, the incident wave following the reflection will be phase shifted by

$$\tan \varphi_{\sigma} = \frac{2 \sqrt{n_1^2 \sin^2(\varphi_1) - n_2^2}}{n_1 \cos(\varphi_1)} \quad (2.18)$$

$$\tan \varphi_{\pi} = \frac{n_1^2}{n_2^2} \frac{\sqrt{n_1^2 \sin^2(\varphi_1) - n_2^2}}{n_1 \cos(\varphi_1)} \quad (2.19)$$

For  $\sigma$  and  $\pi$  respectively. Introducing the effective index, specifying the phase velocity of guided light with:

$$n_{eff} = n_1 \sin \varphi_1 \quad (2.20)$$

For  $\sigma$ , this can be written as:

$$\varphi_{\sigma} = 2 \arctan \sqrt{\frac{n_{eff}^2 - n_2^2}{n_1^2 - n_{eff}^2}} \quad (2.21)$$

In the case of a planar waveguide, where the refractive index of the core is greater than both the substrate and cladding, there may be two critical angles at each interfaces. When the incident angle is greater than the critical angle, the light is confined within the core media due to total internal reflection at both interfaces as illustrated on Fig. 2.7.

Maxwell's Equations

Electrical and magnetic fields propagating within a dielectric media can be described by the well-known Maxwell's equations. In optics, the special case of charge and current-free media is considered and therefore the equations can be expressed as:

$$\vec{\nabla} \times \vec{E} = -\mu \frac{\partial \vec{H}}{\partial t} \quad (2.22)$$

$$\vec{\nabla} \times \vec{H} = \frac{\partial \vec{D}}{\partial t} \quad (2.23)$$

$$\vec{\nabla} \cdot \vec{D} = 0 \quad (2.24)$$

$$\vec{\nabla} \cdot (\mu \vec{H}) = 0 \quad (2.25)$$

Where,

$\mu$  – magnetic permittivity

$\vec{E}$  – electric field

$\vec{H}$  – magnetic field

$\vec{D}$  – electric displacement

$\epsilon$  – permittivity

From these equations, the basic wave equations can be derived that is one of the most fundamental theorem of wave optics. The vectorial multiplication of eq.2.20-21 with  $\vec{\nabla}$  and using the identity  $\vec{\nabla} \times \vec{\nabla} \times \vec{E} = \vec{\nabla}(\vec{\nabla} \cdot \vec{E}) - \vec{\nabla}^2 \vec{E}$  as well as  $\vec{\nabla} \cdot \vec{E} = 0$  yields the wave equations for the electrical and magnetic field:

$$\Delta \vec{E} = \frac{1}{c^2} \frac{\partial^2 \vec{E}}{\partial t^2} \quad (2.26)$$

$$\Delta \vec{H} = \frac{1}{c^2} \frac{\partial^2 \vec{H}}{\partial t^2} \quad (2.27)$$

With  $\Delta = \vec{\nabla} \cdot \vec{\nabla}$  and  $c^2 = (\mu\epsilon)^{-1}$

In optical applications, the travelling waves passing through different interfaces having different dielectric constants ( $\epsilon_r^1, \epsilon_r^2$ ). From Maxwell's equations, it can also be derived that at the interface the tangential components of the electric and magnetic field have to be continuous:

$$E_t^{(1)} = E_t^{(2)} \quad (2.28)$$

$$H_t^{(1)} = H_t^{(2)} \quad (2.29)$$

Components normal to both fields are discontinuous at the interface, whereas the normal components of  $eE$  (electric displacement) and  $\mu H$  have to be continuous.

$$\epsilon_0 \epsilon_r^{(1)} E_t^{(1)} = \epsilon_0 \epsilon_r^{(2)} E_t^{(2)} \quad (2.29)$$

$$\mu_0 \mu_r^{(2)} H_t^{(1)} = \mu_0 \mu_r^{(2)} H_t^{(2)} \quad (2.30)$$

With permittivity  $\epsilon = \epsilon_0 \epsilon_r$  ( $\epsilon_0$  – permittivity of vacuum) and the permeability  $\mu = \mu_0 \mu_r$  ( $\mu_0$  – permeability of free space and  $\mu_r$  the relative permeability of the medium, which is dielectric waveguide is usually assumed to be unity).

As a subset solution to the Maxwell's equations the fields within a optical waveguiding medium can be expressed as a harmonic wave with the form:

$$A_t = A_0 e^{j\omega_0 t} \quad (2.31)$$

Where,  $\omega_0 = 2\pi/\lambda_0$  is the angular frequency. By introducing 2.24 to 2.20 and 2.21 yields:

$$\vec{\nabla} \times \vec{E} = -j \omega_0 \mu_0 \vec{H} \quad (2.32)$$

$$\vec{\nabla} \times \vec{H} = j \omega_0 \epsilon \vec{E} \quad (2.33)$$

For planar optical waveguides where  $z$  is the direction of propagation, each solution can be described by:

$$A_{(x,y,z)} = A_{(x,y)} e^{j\beta_{eff} z} \quad (2.34)$$

Where,  $\beta_{eff} = \frac{2\pi}{\lambda} n_{eff} \sin(\varphi_1)$  being the propagation constant of a particular mode with effective index  $n_{eff}$ . By substituting 2.32 into 2.27 and 2.31 and separating  $x, y$  any  $z$  gives the following relations:

$$\frac{\partial E_z}{\partial y} + j\beta E_y = -j \omega_0 \mu H_x \quad (2.35)$$

$$\frac{\partial E_z}{\partial x} + j\beta E_x = -j \omega_0 \mu H_y \quad (2.36)$$

$$\frac{\partial E_y}{\partial x} + \frac{j\beta E_x}{\partial y} = -j \omega_0 \mu H_z \quad (2.37)$$

$$\frac{\partial H_z}{\partial y} + j\beta H_y = -j \omega_0 \epsilon E_x \quad (2.38)$$

$$\frac{\partial H_z}{\partial x} + j\beta H_x = -j \omega_0 \epsilon E_y \quad (2.39)$$

$$\frac{\partial H_y}{\partial x} + \frac{j\beta H_x}{\partial y} = -j \omega_0 \epsilon E_z \quad (2.40)$$

As it was discussed before and illustrated on Fig. 2.6, the light travelling within the core is confined in  $x$  direction while propagated in the  $z$  direction. In the  $y$  direction, it is assumed to extend infinitely, leaving  $\frac{\partial}{\partial y} = 0$ , because the electric and magnetic field

supported by the waveguide do not depend on this direction.

### Waveguide Modes

A guided light satisfying the condition that it reproduces itself after at least two reflections is called eigenmodes or simply waveguide mode [2.8]. The mode equation for three-layered planar waveguide can be expressed as [2.9].

$$2 k d \sqrt{n_c^2 - n_{eff}^2} + \varphi_c + \varphi_s = 2 \pi m \quad (2.41)$$

These are two types of modes that are distinguished with a planar waveguide: transverse electric (TE) and transverse magnetic (TM). The TE mode only allows electric fields perpendicular to the direction of propagation ( $E_z = 0$ ), whereas for TM a similar condition with no  $H_z$  component. By applying this condition to 2.35-40 the equations become>

For TE modes:

$$\beta E_y = -j \omega_0 \mu H_x \quad (2.42)$$

$$\frac{\partial E_z}{\partial x} = -j \omega_0 \mu H_z \quad (2.43)$$

$$\frac{\partial H_z}{\partial x} + j\beta H_x = -j \omega_0 \varepsilon E_y \quad (2.44)$$

For TM modes:

$$\frac{\partial E_z}{\partial x} + j\beta E_x = -j \omega_0 \mu H_y \quad (2.45)$$

$$j\beta H_y = -j \omega_0 \varepsilon E_x \quad (2.46)$$

$$\frac{\partial H_y}{\partial x} = -j \omega_0 \varepsilon E_z \quad (2.47)$$

If the wave vector is introduced as  $k=2 \pi /\lambda$ , the propagation constant  $\beta$  becomes bounded by the following condition for guided modes:

$$k n_{cover}, k n_{clad} \leq \beta \leq k n_{core} \quad (2.48)$$

The solution satisfying this boundary condition are therefore for TE:

$$E_y = A e^{-\gamma x} \quad x \geq 0 \quad (2.48)$$

$$E_y = A(\cos(\delta x) - \frac{\gamma}{\delta} \sin(\delta x)) \quad 0 \geq x \geq -d \quad (2.50)$$

$$E_y = A \left( \cos(\delta x) - \frac{\gamma}{\delta} \sin(\delta x) \right) e^{\alpha(x+h)} \quad -d \geq x \quad (2.51)$$

Boundary conditions for TM:

$$H_y = A e^{-\gamma y} \quad x \geq 0 \quad (2.48)$$

$$H_y = A(\cos(\delta x) - \left(\frac{n_{cover}}{n_{clad}}\right)^2 \frac{\gamma}{\delta} \sin(\delta x)) \quad 0 \geq x \geq -d \quad (2.50)$$

$$H_y = A \left( \cos(\delta h) - \left( \frac{n_{cover}}{n_{clad}} \right)^2 \frac{\gamma}{\delta} \sin(\delta h) \right) e^{\alpha(x+h)} \quad -d \geq x \quad (2.51)$$

Where A is an arbitrary constant and

$$\alpha = \sqrt{\beta^2 - k^2 n_{clad}^2} \quad (2.52)$$

$$\gamma = \sqrt{\beta^2 - k^2 n_{cover}^2} \quad (2.53)$$

$$\delta = \sqrt{k^2 n_{core}^2 - \beta^2} \quad (2.54)$$

Based on these equations the eigenvalue equation can be determined as:

$$\tan(\delta d - v\pi) = \frac{\delta(r_c \gamma + r_s \gamma)}{\delta^2 - r_c r_s \gamma \alpha} \quad (2.58)$$

Where  $r_{c,s}=1$  for TE modes and  $\left( \frac{n_{cover}}{n_{clad}} \right)^2$  for TM modes.

In Chapter 3, an example waveguide design discussed specifically for siloxane polymer.

## 2.4 Optical Waveguides Structures for Sensing

Guided-wave optics has made significant advances in the last few decades due to the high demand for miniaturization in the optoelectronic and semiconductor industry. Optical interrogation and sensing principles have been established. This section introduces the reader to the main concepts of different integrated waveguide sensors.

The main benefits of the waveguide approach are high sensitivity, scalability, compactness and compatibility with current PCB manufacturing processes. Several LOC technologies can be integrated onto waveguide based sensor designs incorporating microfluidics, light sources and detectors as well as on-board signal processing. Waveguide structures can be categorized into the following three main types:

Slab waveguides were the first to be introduced at the advent of guided-wave optics. Optical propagation is based on simple planar geometry and allows simple analytical solutions for designs and sensitivity analysis as they can be easily modelled by a three-layer system. The main advantages being of this planar structure include easier fabrication and larger sensing area. Moreover, the light is only confined in one direction.

Rectangular waveguides are defined in terms of cross section and are also called strip or channel waveguides. There are a few variations of this type, based on how it is etched out of the substrate (ridge or buried). The main advantage of rectangular shaped waveguides is the higher confinement of light in the core and optical path length optimisation, which allows

more advanced optical interrogating structures to be realised, such as interferometers or resonators. Due to the more complex geometry of the waveguide, approximations have to be used to design and simulate, which can be complex and inaccurate.

Circular waveguides, most commonly in the form of optical fibre, are the most used guiding structure for optical communications. The biggest advantage of optical fibres for sensing applications is their capability to be used as an optrode (or probe). Usually one end of the fibre is used as the sensing site, which can be inserted into the sensing medium in in-situ or in-vivo configurations. The deposition of the recognition layer is very easy as the cladding can be just peeled off from the core.

Coupling light into these optical structures can be cumbersome and usually results in one of the greatest optical power losses in the system. The wavenumber of the wave guiding structure along the direction of propagation is called the propagation constant, which is generally larger than the wavenumber of light that propagates in vacuum or air. The ability to couple light from air into the waveguide is dependent on matching the wavenumbers of light in the two different media. There are four main techniques to achieve this process as illustrated on Fig. 2.9.

- Gratings can be fabricated on the top of the surface which adds a grating vector to the light wave and therefore matches the wave vectors in the waveguide [2.10].
- Integrated 45° mirrors can be fabricated by different methods from laser ablation [2.11] to laser writing [2.12] with losses as low as 0.3-0.8dB/ mirror. Mirrors can be used for both in- and out-of-plane coupling with great efficiency. However they are prone to surface roughness and non-optimum angles, which can lead to serious performance degradation. Air exposed mirrors are also affected by moisture in the air, which can affect the reflectivity of the mirror. Metallization of the mirror is preferred [2.13-14] as it can increase the reflectivity of the mirrors.
- A prism can also be used to couple light into planar waveguides. However, they tend to be bulky and therefore are not favourable for highly integrated designs. A prism with a higher refractive index compared to air is placed close to the waveguide surface with a thin air gap (0.5-1µm) in between. The light undergoes total internal reflection in the prism at the angle larger than the critical angle. The transverse field distribution extends outside the prism and decays exponentially in the air gap. When the thickness and interaction length of the air gap are appropriate, wavenumber matching occurs. The same operation can be reversed coupling light out from the planar waveguide to free space.

- End-fire-coupling is a technique where the light is coupled by directly focusing the beam at one end of the waveguide. Lensed optical fibres are usually used in order to efficiently couple light in at one end and multimode fibre to output couple at the other.

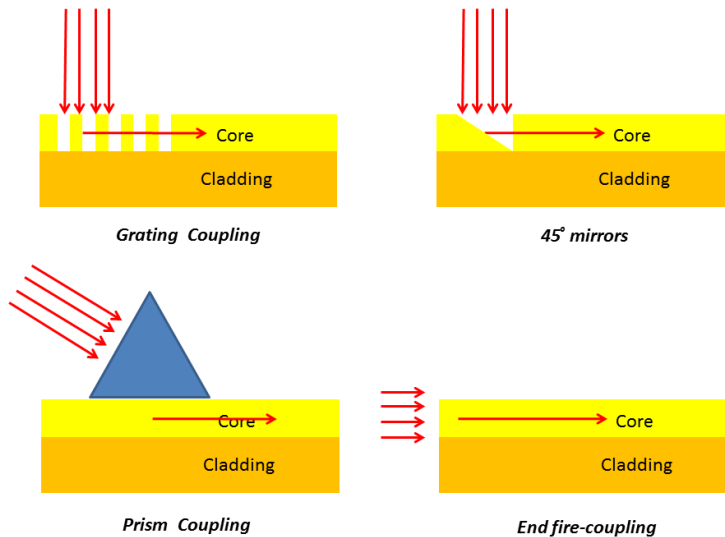


Figure 2.9 – Different methods of light coupling

### **Evanescent Field Sensing**

Waveguides are used to confine optical power and provide directional propagation governed by Total Internal Reflection. Although the light is confined, there is a part of it that extends outside of the wave guiding core into the outer medium. As it travels at the interface it interfaces with the outer environment. This phenomenon has been characterised by Tiefenhaler and Lukosz [2.9]. The evanescent field decays exponentially normal to the direction of propagation into the cover medium, thereby making the propagating light within the core sensitive to changes in refractive index and absorption changes of the cover layer. The cover layer can be a recognition layer allowing selective binding of target molecules or a bulk chemical compound.

which is normally an uncladded section of the waveguide covered in a recognition layer. Typically the evanescent field depth is between 100-500nm, which is a limiting factor for evanescent field wave sensors in terms of the type of target molecules as well as sensor sensitivity.

This sensing technique is suitable for analysing ultrathin recognition layer thicknesses below the interrogating wavelength. Both absorption of the bulk material in the cover medium and refractive index changes can be monitored. Adsorption/binding of a target molecule results in phase velocity changes of the guided mode in the waveguide.

$$v_p = \frac{c}{n_{eff}} \quad (2.59)$$

$$n_{eff} = n_{eff}(\lambda, n_c, n_{cl}, n_s, t_{ad}, d, \text{polarisation}) \quad (2.60)$$

The sensitivity of the measurement of the physical or chemical quantity present in the cover layer depends on the strength and distribution of power in the waveguide layers. In general, the design task is to optimise the waveguide design to maximise the sensitivity of the quantity to be measured. Evanescent field sensors are an actively researched area and there are several novel waveguide structures available, a few of which are briefly explained below. More sensitivity analysis and design examples for siloxane polymer waveguide technology will be discussed in Chapter 3.2.1 in detail.

#### **Anti-resonant reflecting optical waveguides**

The anti-resonant reflecting optical waveguide (ARROW) is a five layer guiding structure (Fig. 2,10) where light confinement is achieved by total internal reflection at the cover/recognition layer interface and anti-resonant reflection (99.99%) below the core due to the presence of the double cladding layers.

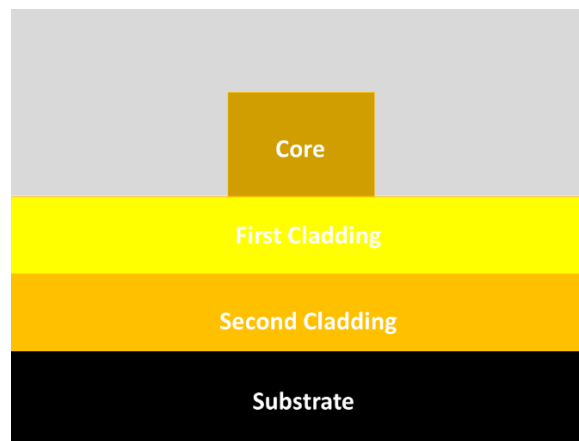


Figure 2.10. – ARROW Structure

This leaky waveguide structure is based on virtual mono mode behaviour. Higher order modes are filtered out by loss discrimination due to the low reflectivity assured to these modes by the two cladding layers. The refractive indices and cladding thicknesses have to be accurately designed for the operational wavelength in order to provide high reflectivity and guiding capabilities. These structures have been realized using both silicon and polymer materials.

There are several benefits of using ARROW waveguides, such as larger permitted dimensions (micro instead of nano meters), and therefore better light coupling efficiency is possible. Better optical light confinement in the low index material is possible providing higher sensitivities. Thus, it is an attractive choice for sensing applications [2.13-15]. More advanced structures can be realised such as Mach-Zehnder interferometers [2.16].

### **Metal Clad Leaky Waveguides**

Metal-Cladding Leaky Waveguides (MCLWs) are four-layer waveguides – composed of a light guiding core with a cladding and a thin metal layer sandwiched between the two dielectric layer. This structure has also attracted considerable attention due to the enhancement of sensing capabilities with respect to traditional waveguides based on high index guiding films. Similar to normal planar optical waveguides, the light is confined by TIR at the core cladding interface. However, at the core-metal interface Normal Reflection (NR) occurs. As a result, modes propagating into the structure are not truly guided and are called “leaky modes” [2.18]. The main benefit of using this structure is the enhancement to the evanescent penetration into the fluidic medium which normally has refractive index around 1.33 for a water based carrier fluid. It is possible to maximise the penetration depth of the guided mode within the recognition layer, with a resulting higher light analyte interaction and therefore better sensitivity. On the other hand – as a result of the NR – it also results in high losses, which limits the interaction length of the sensor.

### **Hollow Waveguides**

Hollow waveguides allow optical power confinement within the solution to be analysed in the waveguide core, which is made of the low-index liquid containing the analyte. The liquid core with a refractive index of 1.33 guides the light between two carefully designed cladding layers designed to produce the necessary anti-resonant reflection. This structure shown on Fig 2.11 allows maximum excellent light matter interaction – as the light confinement in the target medium is 100 percent. One example of this type of sensor is in [2.19].

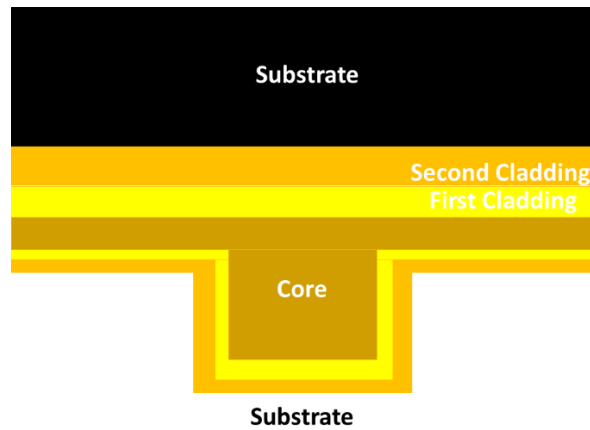


Figure 2.11. - Hollow waveguide structure

### Slot Waveguides

The sensitivity of the waveguide sensor is highly dependent on the amount of light (confinement) in the sensing medium. Recently slot waveguide structures have been a relatively new and highly researched area. The structure is made of two strips of high refractive index material separated by a slot (Fig. 2.12). It supports a single quasi-transverse electric (TE) mode, highly confined in the low index submicrometer gap between the two strips [2.20-21]. This structure is highly sensitive to interactions taking place in the slot region, where the analyte transport fluid is situated. The wave guiding structures are designed to support single-mode behaviour. The sensitivity can be further enhanced by the addition of multiple slots [2.20].

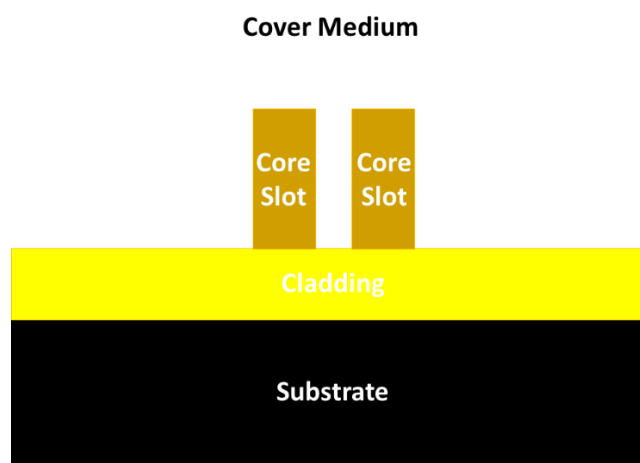


Figure 2.12 - Hollow waveguide structure

The main disadvantage of a using slot structure is the high cost of development and fabrication, as it can be only carried out by electron beam lithography. Moreover, the waveguide dimensions are in the nanometer range resulting in a very high coupling loss, which is a great practical issue in the case of a low cost lab-on-chip sensor development. This structure – as all the previously mentioned – can also be used for more advanced optical interrogation, such as microring resonators or interferometry [2.22], which will be discussed later.

## 2.5 Conclusion

This chapter has provided a brief overview of different optical transduction mechanisms. Fundamental optical concepts have been overviewed, and then their potentials and limitations for lab-on-chip applications. A lot of the mentioned sensor designs were based on high refractive index materials from group IV semiconductor materials such as silicon. Group III-IV material-based sensors have been played a major role in the development of integrated photonic sensor systems. It is mainly due to their high optical confinement and extremely small dimensions allowing highly sensitive and compact devices to be realised. However, the low index materials based on polymer materials are becoming an attractive choice due to their low production and development cost as well as favourable loss characteristics compared to silicon in the visible optical range. Low index materials also provide higher chemical flexibility as they can be easily functionalised for different binding agents. Fabricating materials and structures based on polymers are cheaper and more available than their silicon counterparts as simple photolithography and nano-imprinting can be used with matching accuracy. Not to mention the fact that polymer materials are more environmentally friendly and require smaller efforts in their disposal.

## 2.6 References

- 2.1.O. S. Wolfbeis, “Chemical Sensors – survey and trends”, *Journal of Analytical Chemistry*, vol. 337, pp. 522-527., 1990.
- 2.2.V. M. N. Passaro, F. Dell’Olio, B. Casamassima, F. De Leonardis, “Guided-Wave Optical Biosensors”, *Sensors*, vol. 7, pp. 508-536, 2007.
- 2.3.R. Irawan, Y.H. Cheng, W.M. Ng, M.M. Aung, I.K. Lao, V. “Polymer waveguide sensor for early diagnostic and wellness monitoring”, *Biosensors and Bioelectronics*, vol. 26 , pp. 3666– 3669, 2011.
- 2.4. K. Matsumoto, H. Minamitani, K. Kim, T. Yamamoto, K. Sasaki, “Characteristics of optical waveguide type glucose sensor”, *Conference paper, IEEE 19<sup>th</sup> Annual Conference*, 1997.
- 2.5. R. Zou, B. Chen, H. Wang, X. Hu, M. Iso, “Glucose sensor based on planar optical waveguide”, *Bioinformatics and Biomedical Engineering, The 1st International Conference*, 2007.
- 2.6. Paola De Luca , Maria Lepore , Marianna Portaccio , Rosario Esposito , Sergio Rossi , Umberto Bencivenga and Damiano Gustavo Mita, “Glucose determination by means of steady-state and time-course UV fluorescence in free or immobilized Glucose Oxidase”, *Sensors* , vol. 7, pp. 2612-2625, 2007.
- 2.7.F. Wang , F. Schubert, H. Rinneberg, “A fluorometric rate assay of hydrogen peroxide using immobilized peroxidase with a fibre-optic detector”, *Sensors and Actuators B*, vol. 28, 1995.
- 2.8.B. E.A. Saleh, M. C. Teich, “Fundamentals of Photonics”, *John Wiley & Sons Inc.*, 2<sup>nd</sup> Edition, 1991.
- 2.9.K. Tiefenthaler, W. Lukosz, “Sensitivity of grating couplers as integrated-optical chemical sensors”, *Journal of Optical Soc. Am.*, vol. 6, no. 2, pp. 209-221, 1989
- 2.10. D. Vermeulen, S. Selvaraja, P. Verheyen, G. Lepage, W. Bogaerts, P. Absil, D. Van Thourhout, and G. Roelkens , “High-efficiency fiber-to-chip grating couplers realized using an advanced CMOS-compatible Silicon-On-Insulator platform”, *Optics Express*, vol. 18, issue 17, pp. 18278-18283, 2010.
- 2.11. N. Hendrick, “Tolerance analysis for multilayer optical interconnections integrated on a printed circuit board”, *JLT*, vol. 25., pp. 2395-2401, 2007.
- 2.12. McCarthy, “Fabrication and characterisation of direct laser-written multimode polymer waveguides with out-of-plane turning mirrors”, *Conference on Lasers*

- and Electro-Optics Europe, pp. 477, 2005.
- 2.13. L. Glebov, “Optical interconnect modules with fully integrated reflector mirrors”, *IEEE Photonics Technology Letters*, vol. 17, pp. 1540-1542, 2005.
  - 2.14. Prieto F. Llobera, A., Jimenez, D., Domenguez, C, Calle, A., Lechuga, L. M., “Design and Analysis of Silicon Antiresonant Reflecting Optical Waveguides for Evanescent Field Sensor”, *JLT*, vol.1. 18, pp. 966-972, 2000.
  - 2.15. Prieto F., Lechuga, L.M.m Calle, A., Llobera, A. Dominguez, C. “Optimized Silicon Antiresonant Reflecting Optical Waveguides for Sensing Applications”, *JLT*, vol. 19, pp. 75- 83, 2001.
  - 2.16. Benaissa, K., Nathan, A. “Silicon anti-resonant reflecting optical waveguides for sensor applications”, *Sens. And Actuators B.*, Vol. 65, pp. 33-44, 1998.
  - 2.17. Prieto, F.; Sepulveda, B.; Calle, A.; Llobera, A.; Dominguez, C.; Lechuga, L. M. “Integrated Mach-Zehnder interferometer based on ARROW structures for biosensor applications”, *Sens. Actuators B*, vol. 92, pp. 151-158., 2003.
  - 2.18. M. Zourob, N. J. Goddard, *Biosensors and Bioelectronics*, “Metal clad leaky waveguides for chemical and biosensing applications”, *Biosensors and Bioelectronics* vol. 20, pp. 1718– 1727., 2007.
  - 2.19. Campopiano, S.; Bernini, R.; Zeni, L.; Sarro, P. M.; “Microfluidic sensor based on integrated optical hollow waveguides”, *Optics Letters*, Vol. 29, pp. 1894-1896. 2009.
  - 2.20. Haishan Sun, Antao Chen, Larry R. Dalton, “Enhanced Evanescent Confinement in Multiple-Slot Waveguides and Its Application in Biochemical Sensing”, *IEEE Photonics Journal*, vol. 1, pp. 47-57, 2009.
  - 2.21. V. R. Almeida, Q. Xu, C. A. Barrios, and M. Lipson, “Guiding and confining light in void nanostructure, *Opt. Lett.*, vol. 29, no. 11, pp. 1209–1211, 2004.
  - 2.22. Q. Xu, V. R. Almeida, R. R. Panepucci, and M. Lipson, “Experimental demonstration of guiding and confining light in nanometer-size low-refractive-index material, *Opt. Lett.*, vol. 29, no. 14, pp. 1626–1628, 2004.

# Chapter 3 -Optical waveguides based on siloxane polymer for sensing applications

## 3.1 Introduction

The research carried out by the Photonics group in the Engineering Department has included the integration of polymer optical waveguides with electronics onto standard printed circuit boards (PCBs) for the formation of cost-effective high-speed board-level optical interconnects. The work in board-level polymer waveguide technologies has demonstrated the potential to produce cost-effective electro-optic (EO) PCBs using conventional manufacturing methods of the electronics industry. Proof-of-principle PCB-integrated optical units have been fabricated onto low-cost FR4 substrates exhibiting excellent optical transmission characteristics and achieving high-speed on-board optical interconnection [3.1-2]. The further integration of sensing elements onto such electro-optic (EO) PCBs can enable the formation of low-cost PCB-integrated optical sensor modules suitable for large-scale manufacturing.

Research work has been recently carried out in collaboration with the Chemistry Department at Cambridge towards the development of a PCB-integrated optical gas sensor based on the polymer waveguide technology. As a proof-of-principle demonstrator, an NH<sub>3</sub> optical sensor has been produced on low-cost substrates achieving detection sensitivity of 30 ppm [3.3]. The potential to sense multiple analytes from a single device has also been demonstrated. The aim of this work summarised in this thesis is further applying this technology in bio-medical sensing applications by developing low-cost polymeric optical sensors suitable for use in clinical environments. In this chapter, a brief overview of the siloxane polymer-based waveguide technology is presented introducing the features of the polymer material.

Followed by a design and sensitivity analysis of the key sensing waveguide structures that can be used for porphyrin-based recognition layer interrogation.

### **Overview of siloxane polymer-based waveguide technology**

The ever-increasing demand for short optical transmission links in modern communication systems was the main drive for developing optical interconnects. This demand is mainly driven by companies specialised in storage area networks, supercomputing networks and data centres. The idea of replacing the conventional copper-based interconnections with optics was first proposed in 1984 by Goodman et. Al. [3.4]. Since then a large amount of research has been done proposing the deployment of optical interconnects within electronic circuits. [3.5-8.] It is now well established that optics promises a great solution that offers the following important advantages over the electric counterparts.

Advantages include:

- Larger Bandwidth
- Lower Power Consumption
- Better Crosstalk Performance
- Higher Interconnection Density
- Better Scalability

The recent advancement in board level optical communication, including chip to chip interconnection using hybrid electro-optic printed circuit boards, paved the way for advanced integrated optoelectronic devices in both communication and sensing.

Electro-optical integration requires the use of compatible materials, waveguides and other subsystems with existing PCB fabrication technologies. The summary of the requirements for such integration are as follows:

- Reliable low-cost materials compatible with the existing PCB technology standards
- High-speed, low-power and low-cost optoelectronic components
- Simple and cost-effective coupling and packaging schemes

There are a wide range of optical waveguide materials available, including silicon (Si), silica (SiO<sub>2</sub>), lithium niobate (LiNbO<sub>3</sub>), III-V Group Semiconductors such as indium phosphide (InP), Gallium Arsenide (GaAs) and of course polymers. The properties of these materials are summarised in the table below.

Table 3.1. – Summary of different optical waveguide materials. [3.9.]

Material	Propagation Loss (dB/m)	Ease of Fabrication	Cost
Silicon (Si)	0.1	Medium	Medium
Silica (SiO <sub>2</sub> )	0.1	Medium	Medium
Lithium Niobate (LiNbO <sub>3</sub> )	0.5	Hard	High
Indium Phosphide (InP) multistep processes	3	Hard	High
Gallium Arsenide (GaAs)	0.5	Hard	High
Optical Polymers	0.1	Easy	Low

Silica and Silicon are the most widely used materials for planar lightwave circuits due to their advantage of having a refractive index perfectly matched to silica fibre and as well as low propagation loss. However, the fabrication process is more complex and expensive than polymers. Lithium niobate and III-V group semiconductor materials have been extensively researched. However, these materials have high propagation loss (Table 3.1), and both of them involve expensive and highly complex fabrication procedures. Optical polymer materials can be chemically engineered to exhibit favourable optical properties, such as low birefringence and absorption loss at the wavelength of interest. One of the most appealing aspects of polymers is their low cost and stable optical properties even under thermal and mechanical stresses and exposure to humidity [3.10.]. All these characteristics make polymer an ideal candidate for the future integrated optical devices.

### **Type of polymers**

The quality of optical polymer materials have seen significant improvement in controlling of the optical and thermal characteristics of the material. Optical polymers have proven to exhibit excellent performance in demanding environments and *low propagation losses* (0.1 dB/cm) [3.11] There are several examples of polymer-based sensors in Chapter 2.2 proving the great versatility of this material. The most commonly used polymers are SU-8 [3.12], fluorinated polyimide [3.13], benzocyclobulene [3.14], polymethylmethacrylate (PMMA) [3.15]. The majority of the polymers used in photosensitive patterning are epoxies, acrylates, polyimides and siloxanes, which are

suitable for photolithographic fabrication methods. More information about the different fabrication methods are in the next section.

One of the key attributes of optical polymers is low intrinsic loss, which is an important factor as device dimensions start to increase (e.g. above 1-2 meters in optical backplane applications). Intrinsic loss also determines the optical power attenuation, which effects the link budget from the sensing point of view, an ideal handheld device need a long battery life and therefore requires low power consumption. As a result, the transmitting medium has to be optically as transparent as possible at the wavelength of interest.

Intrinsic loss can be divided into absorption and scattering losses. The first can be attributed to electronic and vibrational absorption due to molecular vibrations and fundamental electron excitation. By carefully designing the molecular structure of the material, it is possible to tailor the absorption spectrum to the wavelength of interest. For example, by adding hydrogen atoms by halogen atoms in acrylate materials (e.g. PMMA) absorption around 1550 nm can be significantly reduced. Scattering losses are caused by density fluctuations, compositional inhomogenities and induced stresses. However, these are typically very low in polymers [3.16]. Siloxane material exhibits very low optical absorption in the visible part of the optical spectrum (Fig. 3.1). Most of the aforementioned recognition layers that were discussed are reactive in the visible range, which make this particular material a good candidate for optical sensing.

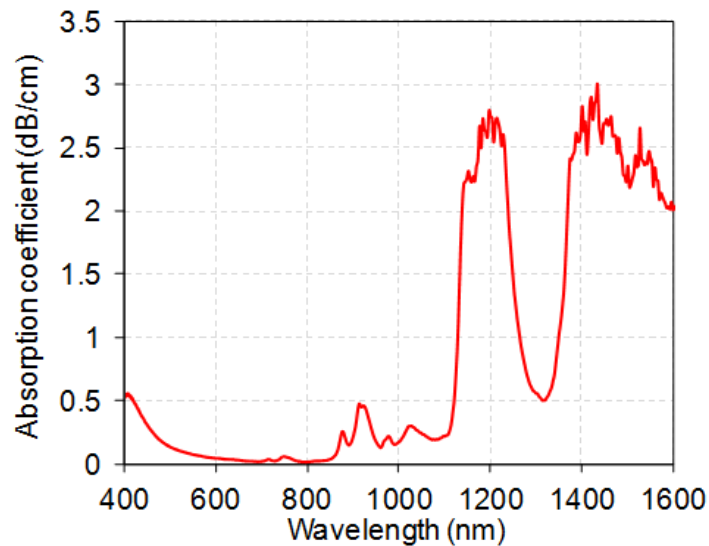


Figure 3.1 - Loss vs Wavelength Spectrum for siloxane polymer material from 400nm-1600nm [3.16]

In order to ensure polarisation insensitivity (polarisation dependent loss) and birefringence in the optical layer. It is important to minimise the birefringence of the material and changes in the in

molecular orientation during manufacturing or induced material stress due to mismatched of the thermal expansion coefficient between different layers can affect it. However, it can be minimised through careful design of material composition. Fortunately, polymers usually have very low birefringence ( $< 10^{-5}$ ) [3.17].

The refractive indices of the optical polymers are usually between 1.2 and 2. It is also possible to tune the refractive index of the polymer by blending and copolymerising different organic groups and carefully selecting their mixture ratio [3.17]

Good resilience to high temperature changes is also a vital property of the material in order to ensure the compatibility of the technology processes of the conventional PCBs and long-term reliability. In the case of OE PCBs, it is essential that the material is capable of maintaining its optical characteristics during such as soldering ( $250^{\circ}\text{C}$ ) and lamination ( $180^{\circ}\text{C}$ ) in the PCB manufacturing process. Moreover, a high degree of process ability and manufacturability is also required for PCB integration, such as adhesion, dicing, etching and coating.

### **Waveguide Components**

Ever since researchers began to show interest in the polymer waveguide technology in the early 90's, several different fundamental components have been developed. This chapter will give a short overview of basic active and passive components.

#### **Active Components**

There is an increasing demand for on-board optical links creating a necessity for active optoelectronic components. These components need to be low powered, high-bandwidth and low cost, while allowing high density integration on the conventional printed circuit boards. The most commonly used laser sources are VCSELs due to their low threshold current, high modulation bandwidth and wide operating temperature range ( $-55^{\circ}\text{C}$  to  $+125^{\circ}\text{C}$ ). Most VCSEL-s operate within the data communication windows at 850nm, 950nm for polymer fibre optical links. Thanks to its maturity, and low cost it is widely used in the industry. [3.1-2, 3.6] In sensing, it is more difficult the find a reliable low cost high power source due to fact that these applications often require to operate at shorter wavelengths. In most of the cases they used light emitting diodes.

For light detection, PIN photodiodes and metal-semiconductor photodetectors (MSM) are the most widely used components [3.18] The detector needs to be carefully chosen based on the desired application considering sensitivity, operating wavelength, waveguide dimensions and the light coupling scheme employed.

#### **Passive Components**

Different components capable of providing the same functionality as electric wiring technologies are the key goal for this technology. [19] Efficient and simple implementation of point to point

and point to multipoint optical connections are the most fundamental requirements and these include bends, crossing, signal splitters and combiners.

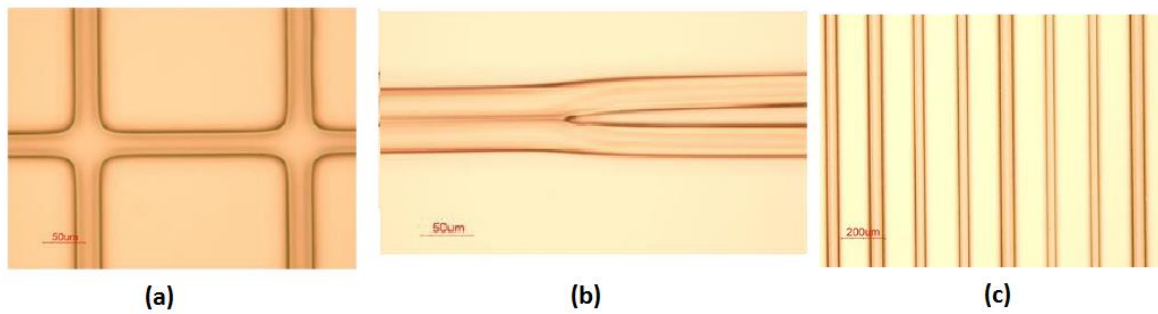


Figure 3.2 - Microscope images of fabricated waveguides without top cladding, (a) crossings, (b) Y-splitters and (c) straight waveguides [3.16]

Fig 3.2 illustrates a few fundamental components, such as  $90^{\circ}$  crossings, which has an important role in on-board optical links, where the density of integration is very high. The aim is to minimise the cross talk and the loss. Crossing loss is a result of strong diffraction of the guided mode at the intersections when incident light in one waveguide comes to the point of the intersection region and diffracts into the crossing waveguide crossing or into radiation modes [3.6]. In [3.7], a multimode polymer waveguide crossing was implemented with loss as low as 0.02dB per  $90^{\circ}$  degree crossing.

Splitters and combiners are often used in integrated optics for various different purpose such as power or mode division. Power splitters are usually composed of symmetrical Y-branches composed of two identical regions with a small divergence angle between them. The most important aim is to minimise the radiation loss, which can be done by minimising the branching angle and increasing the length. Some work has been done with multimode 1x4 and 1x8 power splitters and combiners with excess losses as low as 0.11 dB. [3.20] There is a more detailed discussion about symmetric and asymmetric waveguide junctions in Chapter 4. These simple structures can be used to realise more advanced interrogating techniques such as interferometers, which have seen widespread adoption in both optical communications and biochemical sensing.

### 3.2 Siloxane polymer-based optical waveguide structures for biochemical sensing

Optical planar waveguides are widely used for chemical and biological sensing (several examples were discussed in Chapter 2). Different structures have been developed aiming to enhance the sensitivity of the optical interrogation. Several different structures have been investigated to be

used in conjunction with the Dow Corning siloxane polymer material at a standard sensing wavelength window of 420 nm. This chapter summarises the design process for single mode siloxane waveguides in detail. Moreover, it investigates how evanescent field localisation techniques can enhance the sensitivity. The waveguides structures were designed using FIMMWAVE software, where various mode solving techniques are available. Effective index approximation [3.21] was used due to its speed and ability to solve both real and complex refractive index profiles. Both two and three-dimensional structures can be modelled using FIMMWAVE/FIMMPROP and the results were analysed in MATLAB. Three dimensional structures were modelled using a built-in bidirectional eigen-mode expansion method in FIMMWAVE. One of the main focus of this thesis is to investigate the applicability of Siloxane polymer-based waveguide sensors for the use of brain microdialysis. ISCUSflex – which is the industry standard microdialysis instrument — uses Quinoneimine dye, which is an irreversible dye used for brain microdialysis having an absorption maximum at 530 nm. Alternative recognition elements and sensor technologies are discussed in the Appendix. As it is discussed in Chapter 5.4 our choice of recognition material is porphyrin, where the operational wavelength is 420 nm. At this wavelength, the refractive index of the siloxane material 1.55333 and 1.55033 for the core and cladding respectively.

### 3.2.1 Waveguide design

A key step in designing siloxane polymer-based waveguide sensor is to define the cut-off dimensions. If the dimensions are greater than cut-off the waveguide becomes multi moded. In general, single mode interrogation yields better sensitivity and stability for two main reasons. The overall sensitivity is dependent on modal distribution, and therefore it will be dependent on fibre-waveguide launching conditions. Moreover, different modes will have different penetration depths into the recognition layer, experiencing different modal absorption. As a result, the modal sensitivity will be highly dependent on recognition layer thickness as well, which might be difficult to control. However, there are some cases, where few-moded operation is beneficial. This issue will be discussed in detail in Chapter 4, where a novel sensor architecture is proposed in order to overcome this effect.

Numerical calculations were performed using a mode solver (in FIMMWAVE) in order to find the effective indices of the modes inside the waveguides. The fundamentals of these calculations were introduced in Chapter 2.3 such as the eigenmode equation 2.55-2.58. Fig 3.3 shows the emergence of optical modes in the siloxane based optical waveguide as the square cross section of the waveguide is increased.

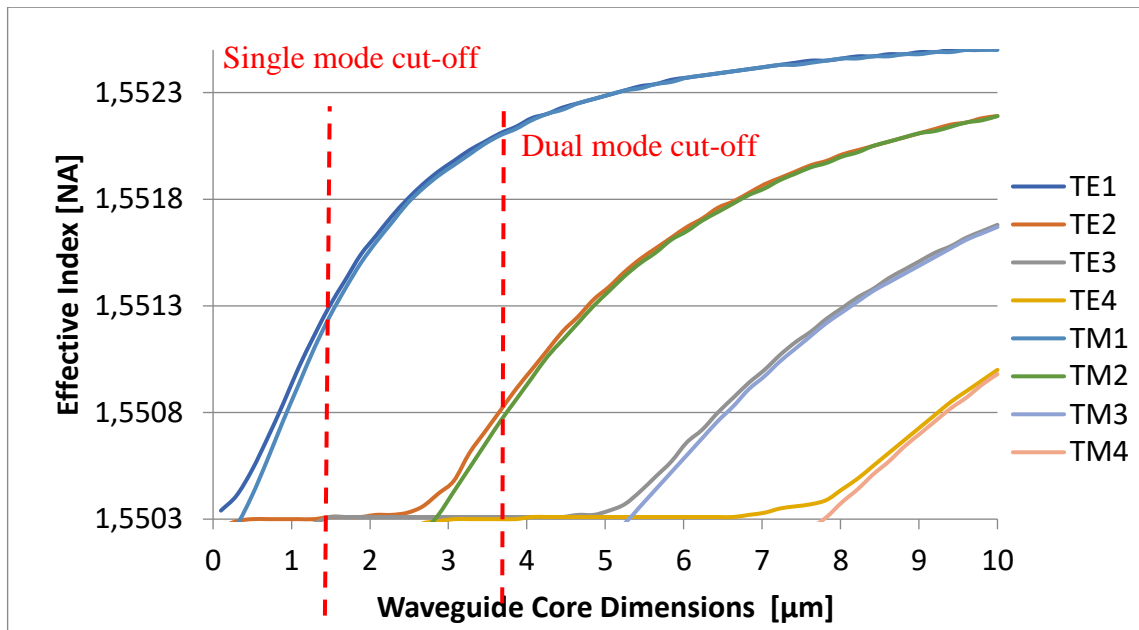


Figure 3.3- Effective index calculations for modes emerging (from cladding RI) as waveguide dimensions increased

The waveguide permits only one mode to propagate until the dimensions are greater than 2  $\mu\text{m}$  in width and thickness. Both transverse electric and magnetic modes ( $\text{TE}_1$  &  $\text{TM}_1$ ) have good field confinement ( $\Gamma_A$ ) at 70 and 71 percent (calculated by FIMMWAVE), while the 2<sup>nd</sup> order modes have minimal present in the guiding core with less than 1 percent. Fig. 3.4 shows the evolution of mode confinement within the waveguide core as its dimension increased. Simulation results the same values for TM modes, therefore only TE is shown.

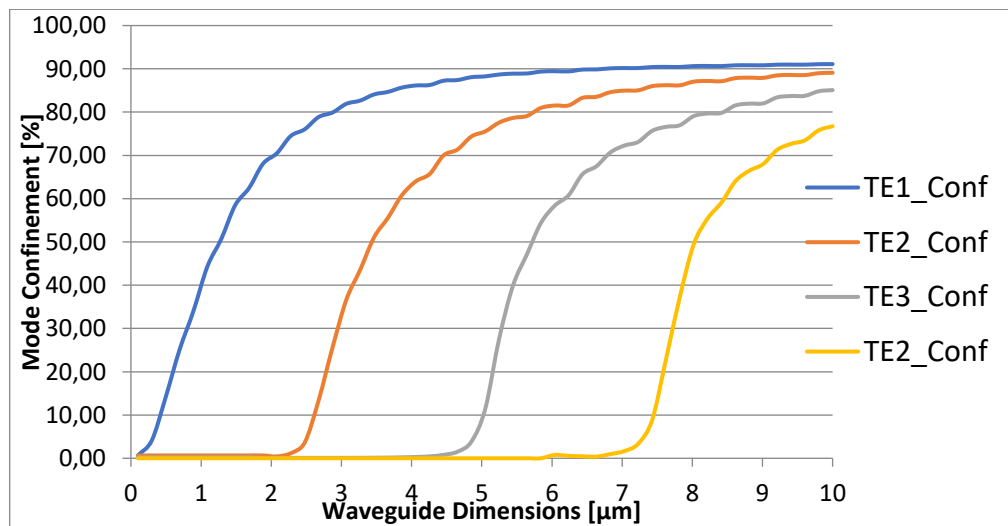


Figure 3.4 – Mode confinement for TE modes as a function of waveguide core dimension

Mode confinement factor can be used to estimate model loss due to material absorption in a given region.

$$\alpha_{mode} = \Gamma_A \alpha_m \quad (3.1)$$

Where  $\Gamma_A$  is the confinement factor for a region A of the waveguide with material absorption coefficient  $\alpha_m$ . The confinement factor is the modal energy density confined within a region of a waveguide (in the above case within the core). It can be calculated as:

$$\Gamma = \frac{\int P_{mode} dA}{\int P_{total} dA} \quad (3.1)$$

The field profile of the two modes are below.

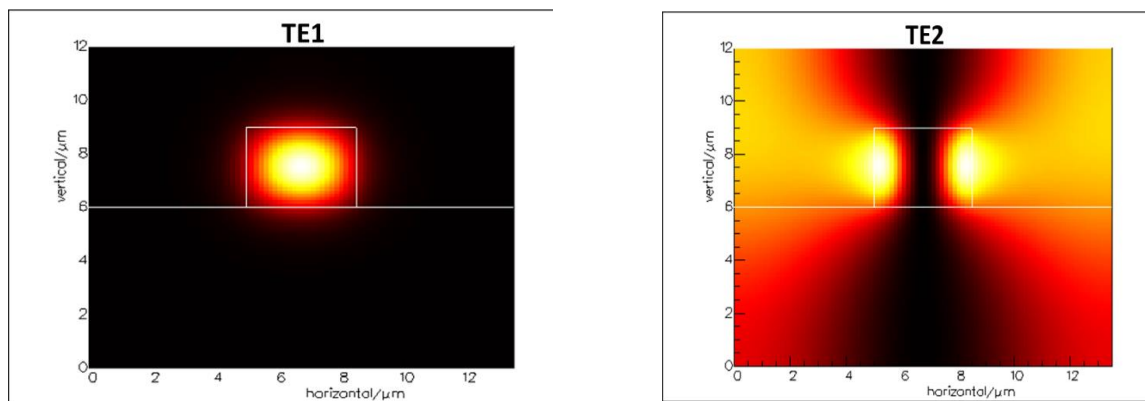


Figure 3.4 – Field profile images in the waveguide cross section for TE<sub>1</sub> and TE<sub>2</sub> modes

In general, strong confinement in the core is essential in most cases in order to maximise coupling efficiency and minimise scattering loss. However, with such a small core index difference it is difficult to achieve. Making the coupling section of the sensor from a different material than the sensing section would increase fabrication complexity as well as increase significant light scattering between the two sections due to the abrupt change in index profile. On the other hand, weakly guiding polymers have the advantage of larger than usual evanescent penetration, which can be very attractive for sensing applications.

### Evanescent Field Penetration

Evanescent field sensors are based on the principle of effective index changes due changes in adlayer ( $t_{ad}$ ) thickness, waveguide core ( $n_{core}$ ) and or index changes due to cover layer ( $n_s$ ) (recognition layer or sensing layer) [3.22]. In this thesis neither core index or adlayer thickness changes are considered as they are outside of the scope of this work.

$$\Delta n_{eff} = \left( \frac{\partial n_{eff}}{\partial t_{ad}} \right) \Delta t_{ad} + \left( \frac{\partial n_{eff}}{\partial n_s} \right) \Delta n_s + \left( \frac{\partial n_{eff}}{\partial n_{core}} \right) \Delta n_{core} \quad (3.2)$$

Based on equation 2.41 and 3.2, a relationship between sensor sensitivity and sensing layer refractive index changes can be derived for a three layered planar waveguide [3.22]. The effective waveguide thickness can be expressed as:

$$d_{eff} = d + \Delta z_{cs} + \Delta z_{sc} \quad (3.3)$$

Which states that the total core thickness is the sum of the penetration of the field into the sensing layer, substrate in addition to the core itself.

$$\Delta z_{cs} = \frac{\lambda}{2\pi} \sqrt{n_{eff}^2 - n_s^2} \left[ \left( \frac{n_{eff}}{n_{core}} \right)^2 + \left( \frac{n_{eff}}{n_s} \right)^2 - 1 \right]^\sigma \quad (3.4)$$

$$\Delta z_{sc} = \frac{\lambda}{2\pi} \sqrt{n_{eff}^2 - n_{clad}^2} \left[ \left( \frac{n_{eff}}{n_{core}} \right)^2 + \left( \frac{n_{eff}}{n_{clad}} \right)^2 - 1 \right]^\sigma \quad (3.5)$$

Where  $\sigma=0$  for TE and  $\sigma=1$  for TM. The well-known sensitivity to refractive index changes to sensing layer can be expressed as:

$$\frac{\partial n_{eff}}{\partial n_s} = \left( \frac{n_s}{n_{eff}} \right) \left( \frac{n_{core}^2 - n_{eff}^2}{n_{core}^2 - n_s^2} \right) \left( \frac{\Delta z_{cs}}{d_{eff}} \right) \left[ 2 \left( \frac{n_{eff}}{n_{core}} \right)^2 - 1 \right]^\sigma \quad (3.6)$$

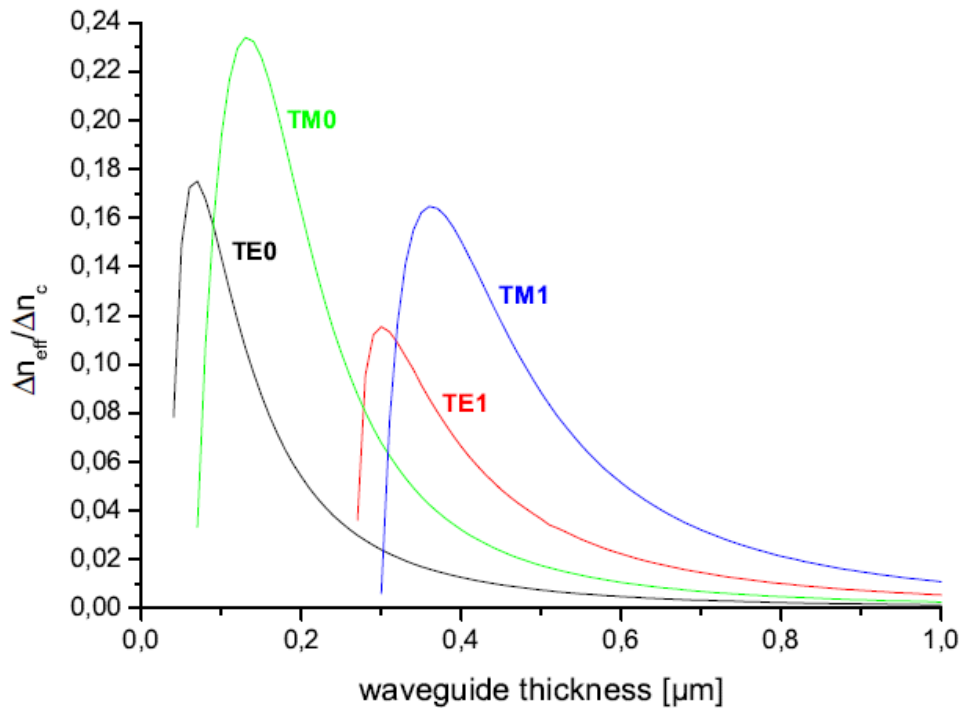
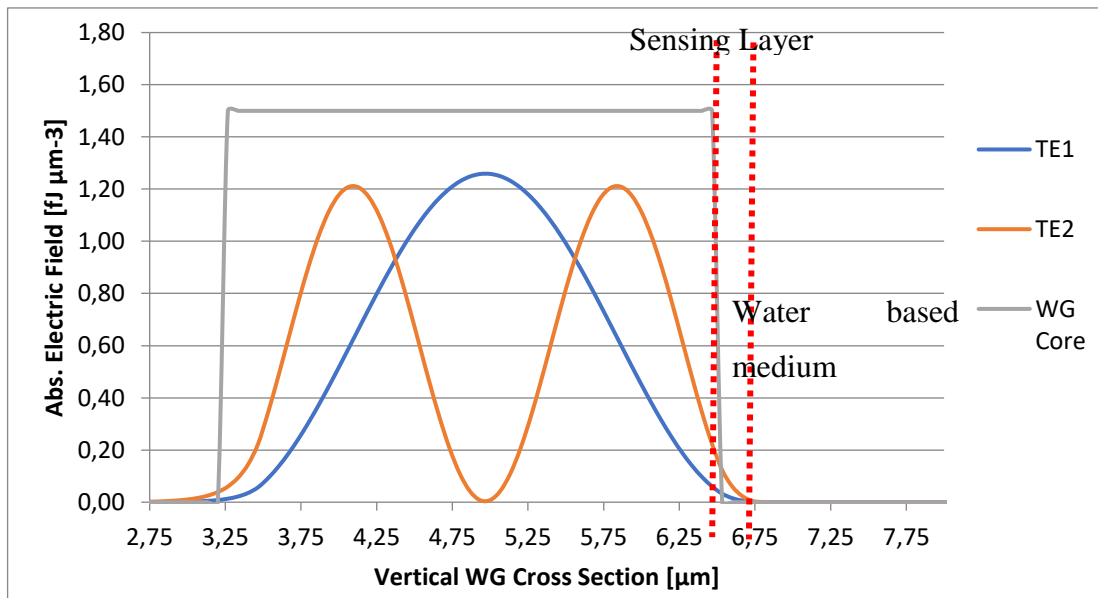


Figure 3.5 – Theoretical sensitivity of waveguide to sensing layer refractive index change for multiple modes as function of waveguide thickness,  $n_{core}=1.52$ ,  $n_s=1.33$  at 675nm wavelength [3.23]

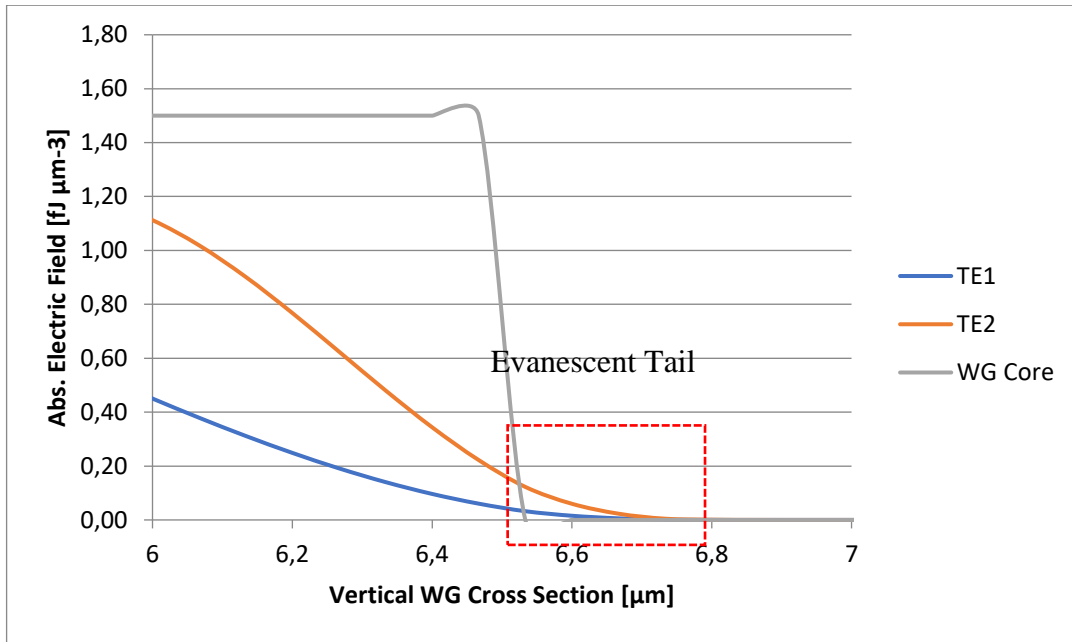
Fig 3.5 shows the theoretical sensitivities of different modes as the core thickness of the waveguide changes. It clearly shows how different mode propagating within the waveguide core will have different sensitivities. These theoretical relationships provide a good understanding of the issues and trade-offs for evanescent field sensing, but Fimmwave provides the capabilities to analyse this in 3D as it is shown in the following chapters. Moreover, equation 3.3-3.6 shows one advantage of siloxane polymer having a low refractive index difference between the core, cladding allowing higher penetration depth.

The siloxane polymer material originally developed and supplied by Dow Corning has 0.003 difference in the refractive index between the core and cladding. It allows relatively large waveguide structures to be realised. Fig 3.6 illustrates the importance of this parameter, where an industry standard material is compared with Dow Corning siloxane polymer. The UV curable Ormocore material has refractive index 1.58 and 1.56 for core and cladding respectively. The single mode cut off dimensions for Ormocore is  $1.24 \times 0.6 \mu\text{m}$  –as its refractive index difference in 0.02.

The field intensity distribution of TE1 and TE2 within the waveguide cross section are illustrated on Fig. 3.6. In the model a 200 nm sensing layer is introduced with refractive index of 1.45. In addition, a water medium (RI=1.33) is also present on the top of the sensing layer as it would be present in any water based biochemical sensor.



(a)



(b)

Figure 3.6 – Field intensity profile on (a) waveguide cross section showing the evanescent field penetration depth (b) into cladding for Ormocore polymer materials at 420nm wavelength based on 1.24x3μm cross section core

The light confinement is extremely low due to the abrupt change in refractive index at the interface of waveguide core, sensing layer and liquid medium. This topic is discussed in the detail in the following chapters.

Table 3.2- Simulation results comparing Ormocore and Siloxane polymer materials in terms of light confinement and penetration in sensing layer.

	<b>Ormocore</b>	<b>Siloxane</b>
Dimensions	1.24x0.5μm	2x3μm
Penetration	~0.2μm	~1μm
Confinement Factor	0.2%	1%

Larger dimensions allow better optical power coupling efficiency for the waveguides and relaxed alignment tolerances for the sensor chip. Both evanescent penetration and electric field confinement is significantly better for the siloxane material due to its small refractive index difference. The effects of misalignment tolerance on sensing performance in discussed in Chapter 4.6.

The standard waveguide structure has a top cladding which increases the confinement in the waveguiding core. It has a symmetric refractive index profile, where both top and bottom claddings have matching refractive index. However, in case of evanescent field sensing this is not appropriate as evanescent field decay length is only a few 100s of nanometres, ultimately limiting its sensitivity and applications. As a result, symmetrical waveguide structures (Fig. 3.7) are normally used in the coupling section of the sensing chips, where good strong light confinement is required.

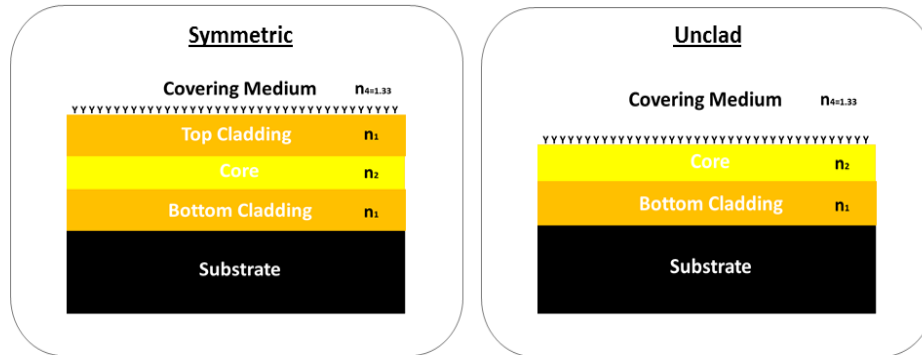


Figure 3.7 – Symmetric and unclad waveguide structures

The coupling structures are usually followed by the unclad section, where the light guided in the core has direct contact with the covering medium – where the recognition layer is deposited – allowing the evanescent field to propagate through the covering medium/core interface. It results in a highly leaky behaviour with strong light scattering. Moreover, the low index (1.33) of the typically aqueous covering medium pushes the field profile away from the interface, reducing the sensitivity. In the case of absorption-based interrogation, the sensitivity is linearly proportional to the light confinement in the recognition layer. Therefore, various novel structures have been proposed to increase the light confinement in the sensing layer.

### 3.2.2 Optical field localisation for sensitivity enhancement

Different composite waveguide structures have been proposed [3.24], which aims to manipulate the optical field profile distribution in the waveguides. The introduction of a high index layer (such as Ta<sub>2</sub>O<sub>5</sub>) or a low index metal layer (Aluminium) below the core in the sensing section can compensate for the optical field shift created by the low index liquid medium in the sensing section. Slot waveguides have also attracted considerable attention. However, it was not possible to design these with such a low refractive index difference between the core and the cladding. Fig. 3.8 illustrates the issue with the abrupt change in the refractive index profile as well as on the

evanescent field. In this chapter, a sensitivity analysis will be discussed through the introduction of composite waveguides.

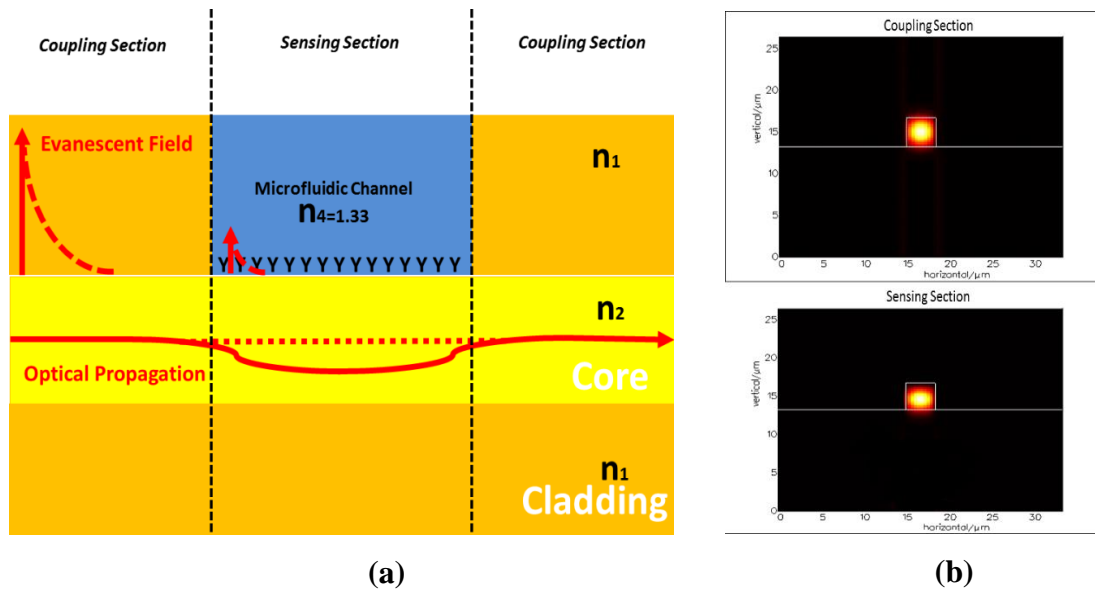


Figure 3.8 – Schematic showing the refractive index profile of the coupling (a) and sending section with the light propagating through the structure and (b) its effect on field profile

Inorganic composite waveguides based on Ta<sub>2</sub>O<sub>5</sub> have shown promising results in compensating field profile shift due to ambient refractive index shifts (water molecules near unclad sensing section) as well as enhancing sensor sensitivity [3.24]. High quality ultra-thin layers of Ta<sub>2</sub>O<sub>5</sub> can be formed by standard plasma sputtering [3.25]. Plasma deposition allows high degree of control over the thin film thickness (down to a few nanometers).

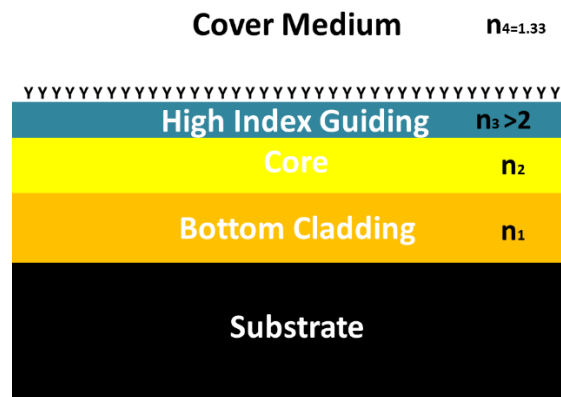


Figure 3.9. – Structure of metal-cladded leaky waveguides

The introduction of a high index (RI=2.22 at 420nm) Ta<sub>2</sub>O<sub>5</sub> layer on the top of the core layer can compensate the optical field profile shift as represented on Fig. 3.10 (a). The optical confinement

in the core reaches a maximum of 74 percent at 18 nm of Ta<sub>2</sub>O<sub>5</sub> thickness. At the same time the sensing layer confinement may be increased up to 14 percent. However, the optical waveguide mode becomes fully coupled into the thin film above 18 nm. A fully coupled slab-like waveguide mode would result in an abrupt profile change at the end of the sensing layer resulting in significant losses. An optimal point is reached at 15 nm Ta<sub>2</sub>O<sub>5</sub> thickness as shown on Fig. 3.10 (a), when the sensing layer confinement is 4 percent and the light is still mainly guided in the waveguide core.

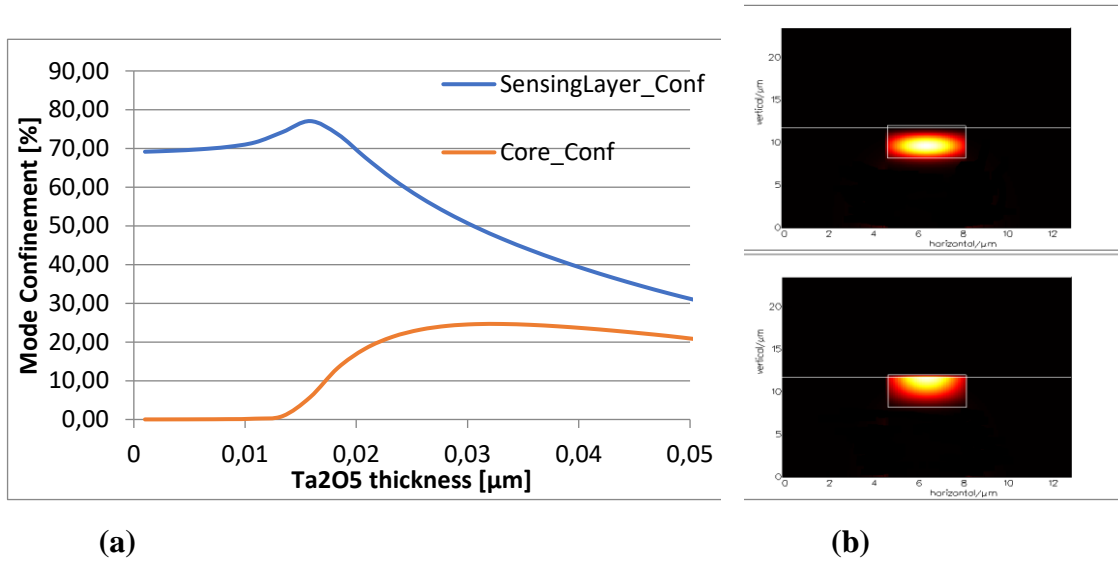


Figure 3.10 – Simulation results showing how core confinement increase (a) with Ta<sub>2</sub>O<sub>5</sub> and its (b) corresponding optical field shift at 0 and 15 nm

In the case of evanescent field sensing the sensitivity can be scaled up by simply increasing the interaction length between the recognition layer and the wave guiding film. However, it is important to carry out the required estimation through the appropriate analysis.

In the case of bulk absorption sensing, the optical power  $P_0$  propagating through a waveguide with length of  $l$  can be expressed as

$$P_l = P_0 e^{-\frac{4\pi}{\lambda} n_{eff} l} \quad (3.7)$$

Where  $\lambda$  is the operating wavelength and  $n_{eff}$  is the complex effective index. Every waveguide contains a constant part of the imaginary part of the refractive index due to material absorption (scattering losses). In our case it is not incorporated as it is negligible compared to the absorption of the actual sensing interaction. The *complex effective refractive index of the propagating mode* ( $n_{eff}$ ) is given by the expression:

$$n_{eff} = n_{eff}^r - jK \quad (3.8)$$

where  $n_{eff}^r$  is the real part of the effective refractive index which depends on the waveguide parameters and light wavelength, while  $K$  is the imaginary refractive index that depends on the absorption of the sensing layer and outer medium.

$$Absorption = \log\left(\frac{P_l}{P_0}\right) = \log\left(e^{\frac{4\pi}{\lambda} K l}\right) \quad (3.9)$$

The imaginary refractive index  $K$  can be evaluated using the absorption coefficient of the glucose at a given wavelength and its concentration based on equation (4.3). A change in analyte concentration translates into changes in the absorption coefficient of the waveguide modes [3.26]. The *molar extinction coefficient* ( $\epsilon$ ) can be used to describe absorption lines or bands and their typical values can be calculated from published data. The value of  $\epsilon$  is  $10^5 \text{ mol}^{-1}\text{cm}^{-1}$  at 420 nm (at 1 mM concentration) for a porphyrin dye [Porphyrin Ref]. By using this parameter together with Lambert-Beer's law, the imaginary part ( $K$ ) of the complex modal refractive index can be calculated. It changes as a function of glucose concentration, but the deviation in magnitude of  $n_{eff}^r$  is negligible compared to the change in  $K$  [26].

By using Beer-Lambert relationship, the following relationship can be expressed, where the  $l$  is the length of the path and  $C$  is the concentration in moles.

$$A = 0.4343 \frac{4\pi}{\lambda} K l = \epsilon C l \quad (3.10)$$

$$K = \frac{\epsilon C \lambda}{4\pi \cdot 0.4343} \quad (3.11)$$

$$K = \frac{\epsilon C \lambda}{4\pi \cdot 0.4343} \quad (3.12)$$

$$K = 0.18323 \epsilon C \lambda \quad (3.13)$$

This expression of  $K$  would be true if all the light would be coupled into the sensing layer. However, only part of the optical field is propagating in the sensing layer and as a result, the absorption experienced by the optical field is scaled by the confinement factor ( $\Gamma$ ) of the optical power within the sensing layer. This allows the calculation of the effective imaginary refractive  $K'$  of the optical mode which is given by:

$$K' = \Gamma K = 0.18323 \epsilon C \lambda \Gamma \quad (3.14)$$

Fimmwave calculates  $K'$  by taking the overlap integral of the field profile in the sensing layer region where the absorption coefficient is defined by  $\alpha_m = \frac{\epsilon C}{0.4343}$

The effective waveguide loss due to the absorption in the sensing layer can be calculated by Fimmwave and is expressed as,

$$\alpha'_m = \Gamma \frac{\epsilon C}{0.4343} \quad (3.15)$$

As an example, glucose concentration between 0-5.4 mM is equal to a material absorption coefficient ( $\alpha_m$ ) between 0 and 500 cm<sup>-1</sup> when the optical power confinement is 4%. Table x. shows the relationship between the material absorption parameter and corresponding modal absorption parameter calculated by FIMMWAVE. The model is good agreement with the equations derived above.

Table 3.3. – Calculated modal absorption parameters and their relationship with confinement

$\alpha_m$	$\Gamma_1$	$\Gamma_2$	$\alpha_1$	$\alpha_2$	$\alpha_{m1}/\Gamma_1$	$\alpha_{m2}/\Gamma_2$
0	4.02E-03	1.04E-03	-1.01E-26	1.04E-27	0.0	0.0
100	4.01E-03	1.04E-03	0.396838	0.102757	98.8	98.9
200	0.004014	0.001038	0.793588	0.205468	197.7	197.9
300	0.004014	0.001038	1.19016	0.308083	296.5	296.8
400	0.004013	0.001037	1.58647	0.410558	395.4	395.7
500	0.004011	0.001037	1.98242	0.512843	494.2	494.7

The sensor response is shown Fig. 3.11, where the optical power decreased as the glucose concentration increased. An inverted waveguide structure was used in this case, as it was in [3.24] in order to minimise the scattering effects resulting from the very high index change. Enhancement in sensitivity due to surface field localisation is significant. The uncoated waveguide sensor showed minimal response even at 1mM glucose concentration, while the composite waveguide sensor showed significant change in optical power.

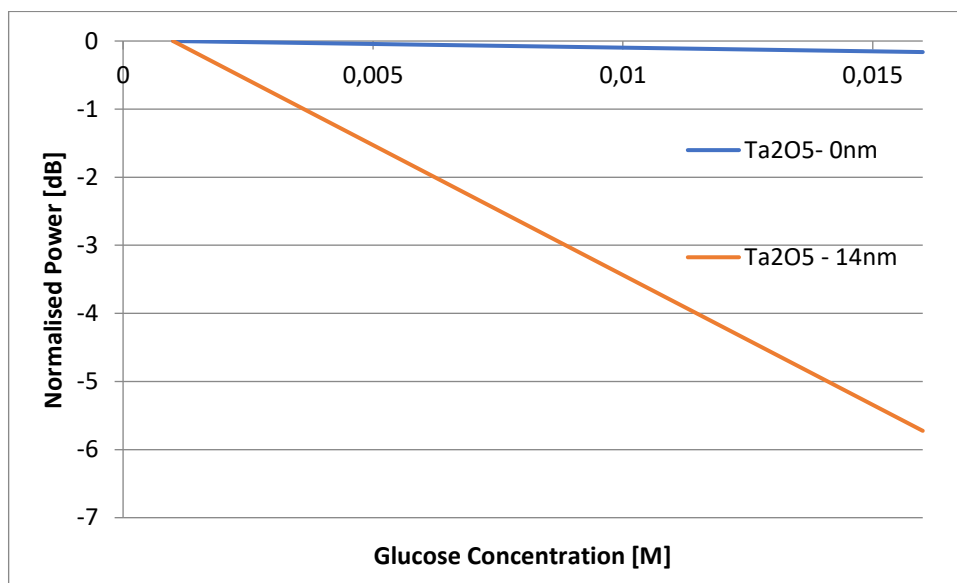


Figure 3.11 – Simulation results showing how optical power absorption (normalised) changes with glucose concentration increase at different Ta<sub>2</sub>O<sub>5</sub> thickness

Previously it was mentioned that the sensitivity is linearly proportional to optical light confinement, which is the proportion of light confined within the sensing layers, relative to the core. The following simulation shown on Fig 3.12 monitored the slope of the sensitivity curves for different thin film thicknesses in order to find the optimal thickness at which the sensitivity is maximised (dB/M). The trend is similar to what was expected from the 2D analytical results shown on Fig 3.5 where the sensitivity of the modal absorption showed an optimum point for effective core thickness.

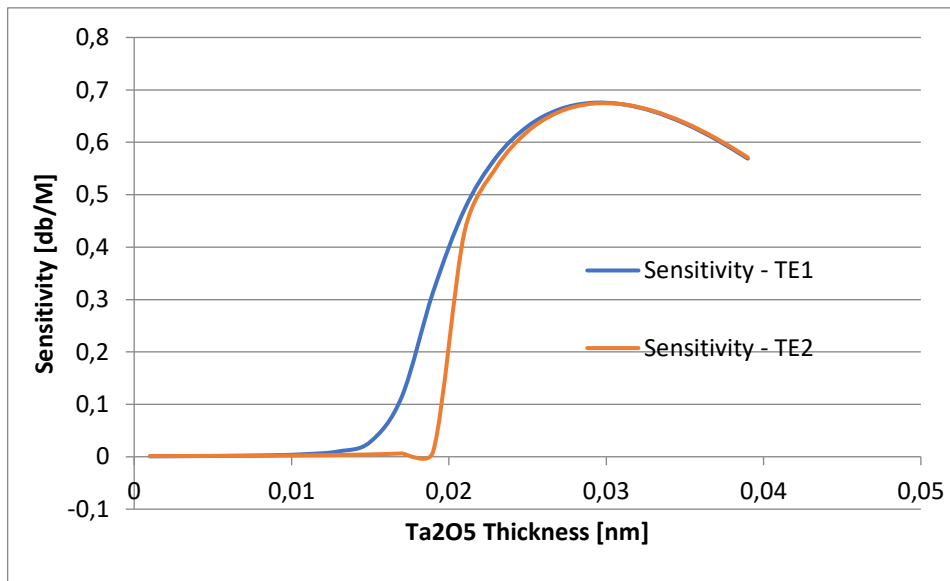


Figure 3.12 – Sensor sensitivity optimisation for Ta<sub>2</sub>O<sub>5</sub> thickness for TE1 and TE2 modes at 1mM glucose concentration

The sensor sensitivity is maximised just before 16 nm of thickness, where the light confinement in the sensing layer is maximised as well. Beyond this point, the thin film becomes guiding and therefore becomes a slab waveguide itself, which is not ideal from the point of light coupling. The optical interrogation is performed by the evanescent field with a limited penetration depth into the recognition layer. As a result, the sensitivity is also dependent on recognition layer thickness. Fig. 3.13 below shows how this can affect the sensitivity.

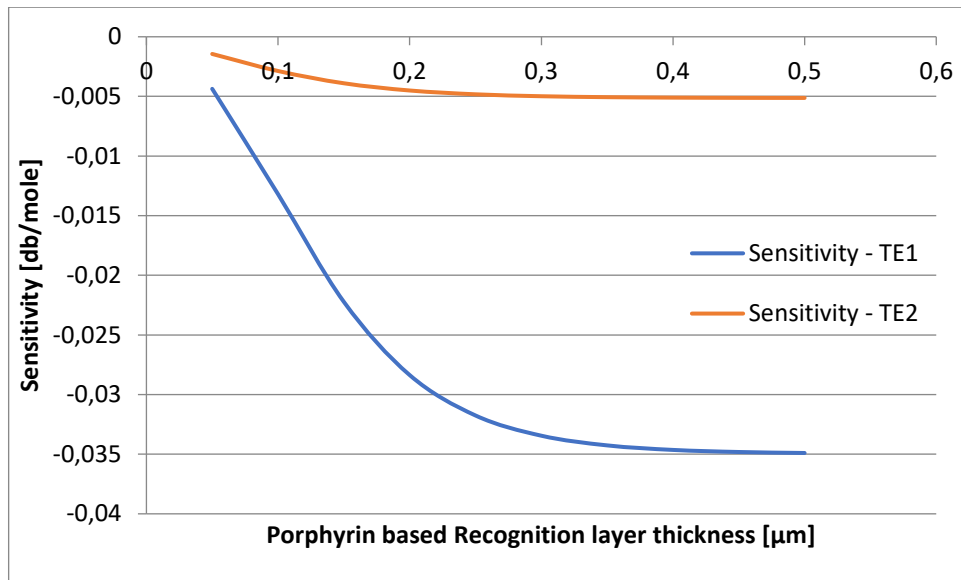


Figure 3.13 – Sensor Sensitivity dependence on porphyrin-based recognition layer thickness at 16nm of  $\text{Ta}_2\text{O}_5$  at 1mM glucose concentration

The designed inverted waveguide supports only one mode, which has a limited penetration. The higher the optical field overlap with the recognition layer, the higher the sensor sensitivity. It is clear from the results that for over 400 nm of thickness the sensing layer is thicker than the penetration depth of the evanescent field yielding no further enhancement in sensitivity. In general, thicker sensitivity layer leads to higher sensing performance. However, in terms of binding dynamics it also leads to longer response time. Optimising the recognition layer thickness is generally more difficult than adapting the dielectric layers thicknesses as it usually involves complex biochemical reactions that can be difficult to fully control. More on this will be discussed later in this thesis.

### 3.3 Conclusion

This chapter introduced the reader to the fundamental of siloxane waveguide technology from both the data communication and sensing point of view. It provided a brief overview of the key material properties as well its benefits. Low index transparent polymer-based sensors generally exhibit low optical material absorption in the visible range. By extending the usual working window of integrated sensors, it can enable the adoption of this technology, therefore the fabrication of simple and cost-effective devices. They allow much greater chemical flexibility than their silicon based high index counterparts. Optical polymers can be surface functionalised with a number of chemicals using well established techniques. Siloxane polymer material has an extremely small refractive index difference between the core and its cladding material. This has several advantages that can be utilised in various sensing applications. Increased evanescent field penetration can yield

higher sensor sensitivities and allow large structures to be realised using Dow Corning siloxane polymer waveguides. Large optical structures have better optical coupling efficiencies and relaxed fabrication tolerances, which may lead to faster industry adoption.

Sensitivity analysis was performed for composite inverted optical waveguides. Simulation were presented showcasing how sensor operation can be affected in the present of a liquid cover medium. Optical field profile shifts can seriously degrade the sensing performance of biochemical sensors.

An inorganic inverted composite waveguide was designed, where a high index (2.22 at 420nm) Ta<sub>2</sub>O<sub>5</sub> thin film was introduced into the top of the core layer. This high index material was able to compensate the abrupt refractive index profile change in the sensing layer and increase the optical confinement. The designed waveguide structure showed promising results between 0-5.4 M glucose concentrations with an interaction length of 5mm. The introduction of this thin film layer has significantly increased the performance.

The sensitivity analysis has introduced the reader to the fundamental limitations of evanescent field sensing. The limited penetration depth is limiting the future applications for this technology. Careful optimisation is required for all dielectric layers in order to maximised sensitivity, however it is difficult to optimise the optical overlap with the recognition layer. Moreover, these simulations assumed no other chemical compounds are present in the microfluidic channel, which is not the case in any practical applications. These issues are addressed in the following chapter, where more advanced optical interrogation techniques will be discussed along with novel methods to overcome these problems.

### 3.4 References

- 3.1. C. Berger, "Optical links for printed circuit boards", IEEE LEOS Conf. Proceedings, Vol. 1-2, pp. 61-62, 2003.
- 3.2. R. Dangel, et al. "Prospects of a polymer waveguide based board-level optical interconnect technology", IEEE Workshop on Signal Propagation on Interconnects, pp. 131-134, 2007.
- 3.3. N. Bamiedakis, "PCB-Integrated Gas Sensor", in IEEE Photonics Conference, paper ThEE.1 (invited), 2011.
- 3.4. J. W. Goodman, et al. "Optical Interconnections for VLSI systems", Proceedings of IEEE, vol. 72. pp. 850-866, 1984.
- 3.5. E. Griese et al. "Reducing EMC problems through an electrical/optical interconnect technology", IEEE Transactions on Electromagnetic Compatibility, vol. 41, pp. 502-509, 1999.
- 3.6. T. Sakamoto, H. Tsuda, M. Hikita, T. Kagawa, K. Tateno, and C. Amano, "Optical interconnection using VCSELs and polymeric waveguide circuits, Journal of Lightwave Technology, vol. 18, no. 11, pp. 1487-1492, 2000.
- 3.7. D. Zauner, A. M. Jorgensen, T. Anhoj, and J. Hübner, "High-density multimode integrated polymer optics", Journal of Optics A: Pure and Applied Optics, vol. 7, no. 9, pp. 445-450, 2005.
- 3.8. E. Griese, "Optical Interconnections on printed circuit boards," Optics in Computing, vol. 4089, pp. 60-71, 2000.
- 3.9. L. A. Eldada, "Polymer integrated optics: promise versus practicality", Proceedings of SPIE, vol. 4642, pp. 11-22, 2002.
- 3.10. W. Norris, "High reliability of silicone materials for use as polymer waveguides", Proceedings of SPIE, vol. 5212, pp. 76-82, 2003.
- 3.11. M. Zhou, "Low-loss polymeric materials for passive waveguides components in fiber optical telecommunications", Optical Engineering, vol. 41., pp. 1631-1643, 2002.
- 3.12. M. Immonen, M. Karppinen, and J. Kivilahti, "Investigation of environmental reliability of optical polymer waveguides embedded on printed circuit boards", Microelectronics Reliability, vol. 47, no. 2-3, pp. 363-371, 2007.
- 3.13. J. Kobayashi, T. Matsuura, Y. Hida, S. Sasaki, and T. Maruno, "Fluorinated polyimide waveguides with low polarization-dependent loss and their applications to thermo-optic switches", Journal of Lightwave Technology, vol. 16, no. 6, pp. 1024-1029, Jun. 1998.

- 3.14. C. F. Kane and R. R. Krchnavek, "Benzocyclobutene optical waveguides", IEEE Photonics Technology Letters, vol. 7, no. 5, pp. 535-537, 1995.
- 3.15. D. Bosc, a Maalouf, F. Henrio, and S. Haesaert, "Strengthened poly(methacrylate) materials for optical waveguides and integrated functions", Optical Materials, vol. 30, no. 10, pp. 1514-1520, 2008.
- 3.16. Ying Hao, "Design, fabrication and characterisation of polymer-based wavelength-division multiplexing filters for fibre to the home application", Doctoral Thesis, University of Cambridge, 2011.
- 3.17. K. Su, "Siloxane materials for optical applications", Proceedings of SPIE, vol. 6029, 2006.
- 3.18. J. Wang, S. Lee, "Ge-Photodetectors for Si-based Optoelectronic Integration", Sensors, 2011, vol. 11, pp. 696-718, 2011.
- 3.19. R. T. Chen, "Fully embedded board-level guided-wave optoelectronic interconnects", Proceedings of the IEEE, vol. 88, pp. 780-793, 2000.
- 3.20. Z. Xiao, X. Luo, P. Huei Lim, P. Prabhathan, S. T. H. Silalahi, T. Liow, J. Zhang, F. Luan, "Ultra-compact low loss polarization insensitive silicon waveguide splitter", Optics Express, Vol. 21 , Issue 14 , pp. 16331, 2013.
- 3.21. G. B. Hocker and W. K. Burns, "Mode dispersion in diffused channel waveguides by the effective index method", Applied Optics, Vol. 16, Issue 1, pp 113-118, 1977.
- 3.22. K. Tiefenthaler, W Lukosz, "Sensitivity of grating couplers as integrated-optical chemical sensors", Journal of Optical Society of America, vol. 6, 1989.
- 3.23. K. Schmitt, "A new waveguide interferometer for label free detection of biomolecules", Doctoral Thesis, University of Louis Pasteur, 2006.
- 3.24. J. Hiltunen, S. Uusitalo, P. Karioja, S. Pearce, M. Charlton, "Manipulation of optical field distribution in layered composite polymericinorganic Waveguides", Appl. Phys. vol. 98, p. 3, 2011.
- 3.25. S. Shibata, "Dielectric constants of Ta<sub>2</sub>O<sub>5</sub> thin films deposited by r.f. sputtering", Thin Solid Films, vol. 277, pp. 1-4, 1996.
- 3.26. G. Stewart, B. Culshaw, "Optical waveguide modelling and design for evanescent field chemical sensors," Optical and Quantum Electronics, vol. 26, 1993.
- 3.27. R. Giovannetti, J. Uddin, "The use of spectrophotometry UV-VIS for the study of Porphyrins", Macro to Nano, ISBN: 978-953-51-0664-7, InTech, Available from:

<http://www.intechopen.com/books/macro-to-nano-spectroscopy/the-use-of-spectrophotometry-uv-vis-for-the-study-of-porphyrins>

# Chapter 4- Advanced optical interrogation technique based on mode duplex sensing

## 4.1 Introduction

Recent developments in data communications towards achieving higher-capacity optical links have created a renewed interest in mode-multiplexed optical waveguide systems, where different modes carry different streams of information [4.1]. Asymmetric waveguide Y-junctions have been proposed to be used both at the receiver and transmitter end in order to multiplex and demultiplex the different propagating modes and efficiently recover the different data streams [4.2]. Recently mode duplex optical transmission has attracted some attention in the sensing field as well. Several papers have been published for mainly modal interferometric applications [4.3-4.5]. The previous chapter summarized some of the most well-known waveguide structures that are available for evanescent field sensing. All of them can be used to realise a highly sensitive integrated optical lab-on-chip sensor. In Chapter 2, several different well-established evanescent field-based sensing techniques were presented. However, all of them were prone to the same issues: the sensor sensitivity and response time is highly dependent on sensing layer thickness. There is a fundamental trade-off between thickness of the sensing layer and response time [4.6]. In addition to that, interferences in the liquid cover medium (microfluidic channel) may affect the recognition layer, therefore introducing unwanted signal changes.

In the context of optical sensors, this chapter summarises a novel sensor concept. Asymmetric Y-junctions are used in multimode evanescent-wave absorption sensors in order to overcome the spurious effects due to absorption changes in the outer medium and improve their operation and reliability. The proposed sensor device maintains the fundamental simplicity of multimode absorption sensors while overcoming this common issue with such devices. In the sections that follow –after a short overview of Y-junction theory, where the design of the proposed waveguide sensor is presented and its operating principle is described (section 4.3). Simulation results are

reported in Chapter 4.3 demonstrating that the device can efficiently detect the analyte of interest with an accuracy better than 99 %, even in the case of a highly-absorbing outer medium with an absorption 80 times greater than that of the sensing layer. Finally, section 4.4 concludes the chapter.

## 4.2 Asymmetric Y-junctions

Y-junctions unlike most optical devices rely purely on geometry for their functionality. Based on the geometry, they can be either symmetric or asymmetric. Symmetric junctions are widely used for equal power splitting [4.7-4.10], while asymmetric junctions, can be used for polarisation splitting, mode-combining, wavelength multiplexing or as variable power splitters [4.11-4.12]. Recently, it was proposed that they can be used for spatial mode multiplexing of a few mode fibre. [4.13.] The slow cross-sectional variation of these devices allows adiabatic propagation of modes through the junction. The study of this optical waveguide architecture could lead to further improvements in both sensing and optical communications.

### 4.2.1 Types of Y-Junctions

A symmetric single-mode Y-junction is wavelength independent and acts as an equal 3dB splitter. These have been studied extensively in the past [4.13-4.17]. Their operation can be described by considering normal local even and odd supermodes in arm A and B, as shown on Fig. 4.1.

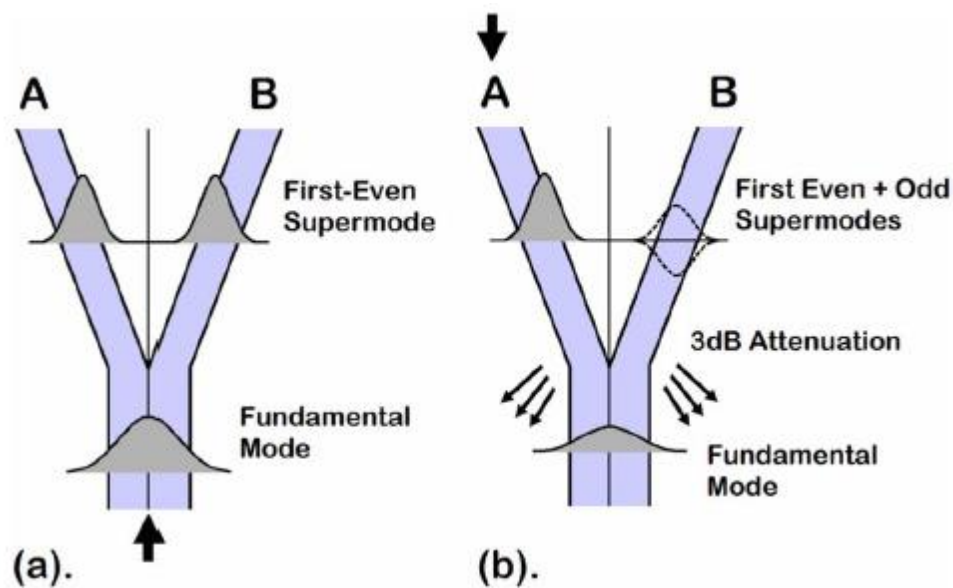


Figure 4.1 - (a) Forward and (b) backward modal propagation through a symmetric, single-mode Y-junction [4.13.]

When the branching angle is sufficiently small ( $\ll 1^\circ$ ), the power of the fundamental mode (FM) in the stem will split between the FMs of the output arms equally. It can be also interpreted as the excitation of the first-even supermode across the output arms. In the other direction, exciting the FM in arms A or B is equivalent to exciting a superposition of both the first even and first odd supermodes with equal amplitudes. [4.12.] The single mode stem only allows the even supermode from the arms to evolve into the FM of the stem, whereas the odd supermode becomes the first or second higher order mode in the stem. Since the stem is single mode, all higher order modes are radiated out. As a result, if two FMs which are of in-phase and equal amplitudes are injected into both arms it is equivalent to the excitation of only the first- even supermode and hence only the FM is excited in the stem.

#### Few-Mode Symmetric Y-Junctions

The same concept can be extended into few mode symmetric junctions. In this case, the power of second mode (first-odd) mode in the stem is equally split into two equal amplitude fundamental mode (FM) in the output arms, but with a  $180^\circ$  degree phase difference as shown on Fig. 4.2.

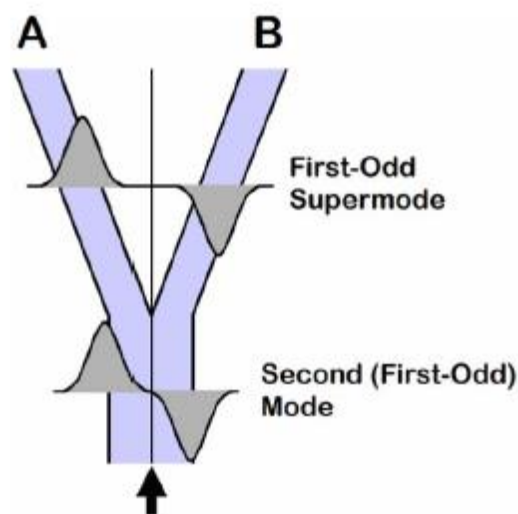


Figure 4.2 – Evolution of the second mode into the arms of a few mode symmetric junction [4.13]

If both FMs are excited in the stem equally, the output power in each arm will depend on the accumulated relative phase difference between the modes in traversing the Y-Junction. Therefore the power at the output arms can vary from 0-100%. The power of the third mode (second even) splits equally into identical second (first odd) modes in the arms, as shown below on Fig. 4.3 (a).

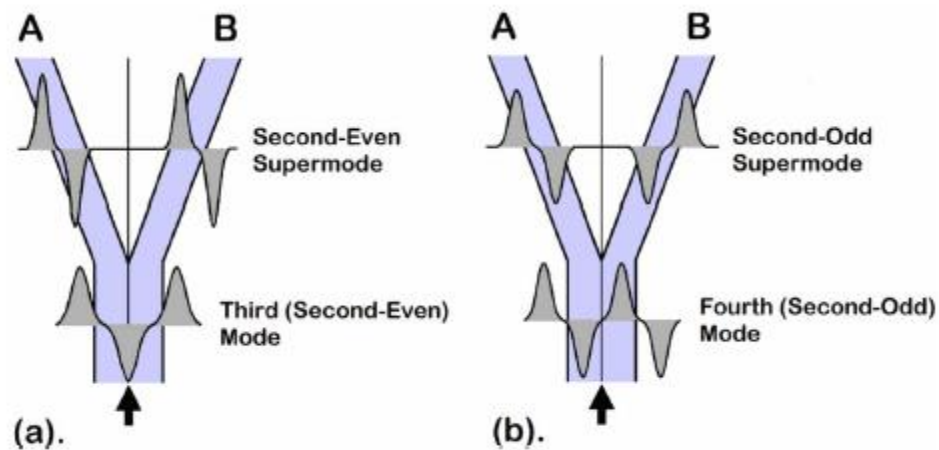


Figure 4.3 - Evolution of (a) the third mode and (b) the fourth mode, from the stem through a few-mode Y-junction [4.13]

As shown in Fig 4.3 (b), the fourth mode (second odd) splits equally into the same second (first odd) modes of the arms, however with a phase difference of  $180^0$  degrees. “The behaviour of the junction depends on the phase difference between the same order pairs of even and odd supermodes (or between the corresponding pairs of stem modes).” [4.7,4.13].

### Multimode Symmetric Y-Junctions

In this case, power splitting depends on the phase difference between the stem modes that correspond to same-order pairs of supermodes across the output arms, while all other pairs of modes split equally since they are independent of phase. [4.13] The phase difference approaches a continuum as the number of modes becomes very high, therefore essentially creating a 3 dB splitter, which is independent of mode number, wavelength or index contrast. It is also called a reciprocal device, because if all N modes are excited in one of the arms of an N-mode junction, only the first N/2 modes can stay in the stem, while the rest are radiated away.

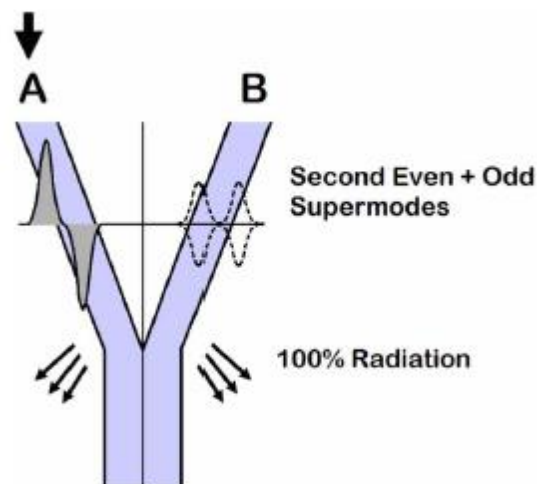


Figure 4.4 – Evolution of 2<sup>nd</sup> mode in arm A through a two mode Y-junction [4.13]

### Single-Mode Asymmetric Y-Junctions

As mentioned in [4.12], it is possible to create an asymmetric Y-junction that is capable of mode sorting if the two arms differ sufficiently in either their width or refractive indices. The first even and first odd local supermode fields simplify and become the FM fields of the wider and narrower arms respectively. As the FM in the single mode stem travels through the junction it becomes the FM of the wider arm providing that their effective index is closely matched. In the other direction, the FM of the wider arm becomes the FM of the stem, while the FM of the narrower arm evolves into the unguided 1<sup>st</sup> order mode, which is then radiated away.

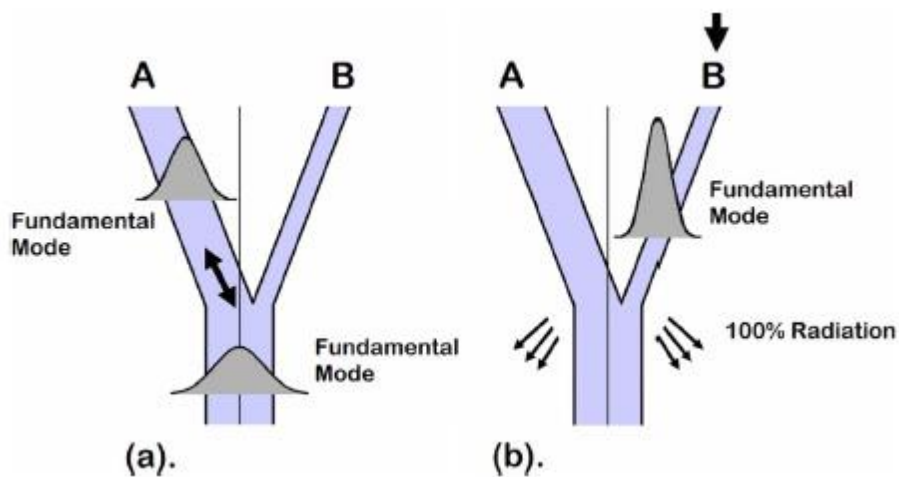


Figure 4.5 – Evolution of FM modes between (a) the wider arm and (b) the narrower arm of a asymmetric single mode junction [4.13]

### Few-Mode Asymmetric Y-junctions

The most interesting case of the asymmetric Y-junction is when the stem can support two modes, while the arms can support only one mode in each arm. As shown below, the FM of the stem exits in the wider arms and the 1<sup>st</sup>-order modes transforms into the FM of the narrower arm, providing that the effective index of each of the modes in the stem is closely matched to the effective index of the FM in the two arms. This process can be optimised to operate without any loss of power and it can also work in both directions. [4.14-4.15]

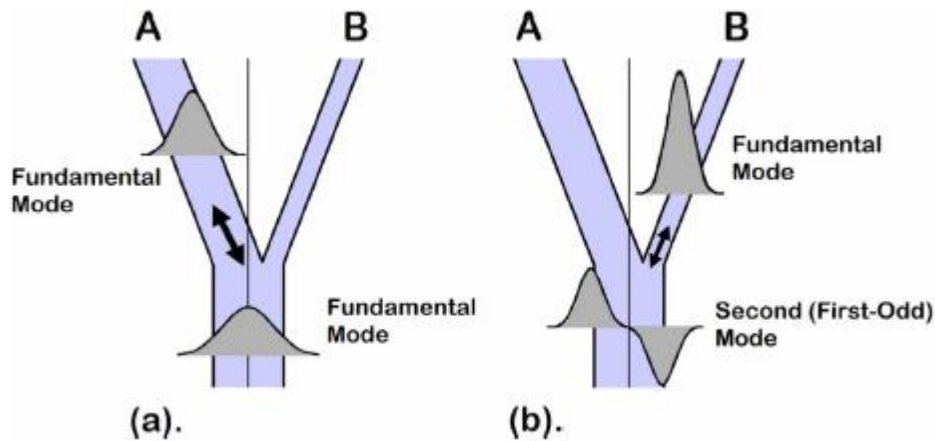


Figure 4.6 - Evolution of (a) the FM and (b) the second (first-odd) mode between the stem and arms A and B of the asymmetric two-mode Y-junction, respectively [4.13]

### Multimode Asymmetric Y-Junctions

The behaviour of the asymmetric junctions is independent of the phase of each individual mode if the transition is adiabatic and the asymmetry is high. This mode sorting behaviour is based on the requirement of closely matching the effective indices of each modes. However it is very difficult in the case of a multimode junction. If the junction is highly multi moded, the asymmetry can be tailored to provide arbitrary tap-off fractions [4.12]. The ability of combining and separating modes by using these asymmetric Y-junctions is very promising and makes them a highly attractive area of research.

#### 4.2.2 Design of asymmetric Y-junctions and simulation results

In the case of a two-mode asymmetric junction with two output arms, the fundamental mode (FM) in the stem exits as the FM of the wider arm, while the higher order mode exits as the FM of the narrower arm. As described earlier, this is a result of matching of the effective modal indices, as the FM has the largest effective index of all modes in the stem and the wider stem has the closest match to it from the two arms. In other words, as a mode propagates through a Y-junction, it evolves into the mode of the output arm with the closest effective mode index. This

can only occur if the cross-sectional variations at the junction are sufficiently small, providing approximately adiabatic behaviour. The branching/divergence angle ( $\theta_D$ , Fig 4.7) and the width of the individual arms have to be precisely designed so that there is no higher order mode present in the output arms.

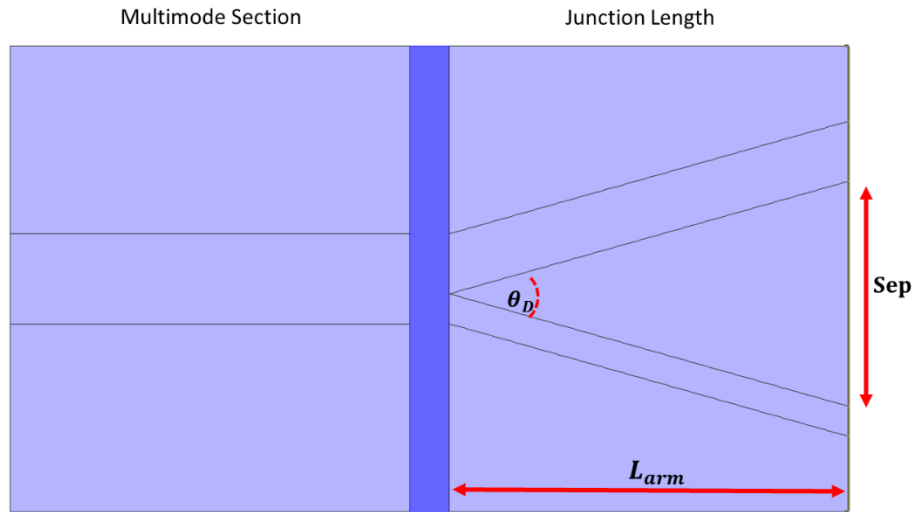


Figure 4.7 – 2 arm asymmetric waveguide junction structure

$$\theta_D = 2 * \tan^{-1} \left( \frac{Sep}{2L_{arm}} \right) \quad (4.1)$$

The mode conversion can be described quantitatively by the Mode Conversion Factor (MCF), which was first described by Burns and Milton [4.10]. It is based on mode analysis and coupled mode theory and is a measure of Y-junction asymmetry. As the asymmetry increases, the mode separation becomes better as well in the case of the two stem modes in terms of modal effective index. Unlike power splitters, in this case the smaller the divergence angle the better ( $\theta_D \ll 1^\circ$ ) due to the fact the radiation loss is larger as the divergence angle increases. The MCF is defined by:

$$MCF = \frac{|\beta_A - \beta_B|}{\theta_D \gamma} \quad (4.2)$$

Where,  $\beta_A$  and  $\beta_B$  are the propagation constants of the modes in arm A and B,  $\theta_D$  is the divergence angle between the arms and  $\gamma$  is the gamma factor defined as:

$$\gamma = 0.5 \sqrt{[(\beta_A - \beta_B)^2 - (2k n_{cl})^2]} \quad (4.3)$$

Where  $n_{cl}$  is the refractive index of the cladding between the two arms and “k” is the free space wavenumber. As described in [4.10], the gamma factor together with MCF governs the transition boundary between a mode splitter and a power divider. The first requirement for mode sorting is

that MCF has to be greater than 0.43, providing a transition boundary between mode-separation and power-splitting [4.10]. The MCF depends on the difference of the propagation constants of the fundamental modes between the arms. It assumes that no higher-order modes are present in the output arms.

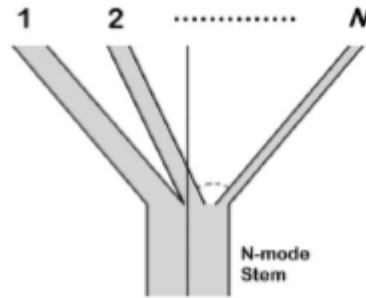


Figure 4.8 – N-Stem Asymmetric Y-Junction [4.13]

The same theory can be extended to multimode multi-arm junctions (Fig. 4.8), if the output arms are assumed to be single moded. The behaviour of a multi-arm junction can be described by applying the same set of rules for all pairs of arms, which is an appropriate assumption considering it is a linear device operating purely on phase matching. [4.12,4.11]

The MCF and the gamma factor of a specific pair output arms  $i$  and  $j$  is then given by:

$$MCF_{ij} = \frac{1}{\theta_{ij}\gamma_{ij}} \left| \frac{\beta_i - \beta_j}{i - j} \right| \quad (4.4)$$

$$\gamma_{ij} = 0.5 \sqrt{[(\beta_i - \beta_j)^2 - (2kn_{cl})^2]} \quad (4.5)$$

Where  $i$  and  $j$  denote the two output arms and  $\theta_{ij}$  is the divergence angle between them, which is assumed to be constant between consecutives arms. A two dimensional N-arm Y-junction can be modelled as a statistical combination of the MCF, which is called the Multiple Output Factor (MOF) [4.13,4.18].

$$MOF = \theta \sum_{i \neq j, j > i}^N \left| \frac{i - j}{\beta_i - \beta_j} \right| \gamma_{ij} \quad (4.6)$$

As an example, a perfect power splitter should have an infinite MOF, whilst for a perfect mode-sorter it should be zero. As a result, the first design criterion is to minimise the MOF for a given angle.

The second design criterion assumes that the output arms are single mode waveguides. The propagation constant of each stem mode should closely match the FM mode of the arms and be as far away from the unwanted higher order mode as possible. N. Riesen used the model

parameters from [4.19, 4.12-4.13] and Beam propagating methods [4.20] to find the value for the propagation constants.

A matching waveguide model was created at 420nm in FIMMWAVE/FIMMPROP based on the simulation parameters described in Chapter 3. The design process described by Riesen earlier is perfectly applicable for 2D models, however not quite useful for the fully 3D models which are required to analyse sensing mechanisms. Although, the fundamental design rules remain the same, by using FIMMWAVE/FIMMPROP in conjunction with MATLAB was used to find the optical three dimensional geometries that had the maximum mode coupling coefficients.

#### FIMMPROP Modelling

The theory describing Maxwell's equation and its general solutions is described in Chapter 3. The general solution to the wave equations is:

$$\Psi_{(x,y)} e^{j\beta_i z} \quad 4.7$$

Assuming single wavelength and a time dependence in the form of  $e^{-j\omega t}$ . These solutions called the modes of the cross section. From the mathematical point of view the mode profile  $\Psi_{(x,y)}$  and the propagation constant ( $\beta_i$ ) are the eigenfunction and the eigenvalue of the solution. In our typical few moded waveguides are assumed, however there are an infinite number of radiation modes present as well. These radiation modes will carry away optical power from the waveguide. As it is not possible to deal with an infinite number of radiation mode, in order to model efficiently the structure is surrounded by reflective boundaries which will cause the radiation modes to become a discrete set.

The guided modes and the discretised radiation modes together form a complete bases set. Essentially, the solution of Maxwell's equations in the region of the waveguide are expressed as the superposition of forward and backward propagating modes. This technique is called the Eigen Mode Expansion method (EME). As a result, the field ( $\Psi$ ) can be written as a linear combination of the 2D eigenmodes ( $\Psi_i$ ) with corresponding propagation constants ( $\beta_i$ ) found by FIMMWAVE's mode solvers:

$$\Psi_{(x,y,z)} = \sum_{i=1}^N (C_i^f \Psi_{(x,y)} e^{j\beta_i z} + C_i^b \Psi_{(x,y)} e^{-j\beta_i z}) \quad 4.8$$

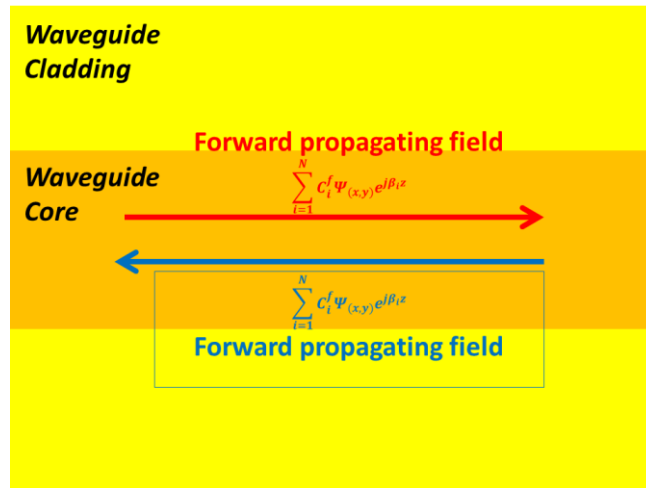


Figure 4.9 – Modes represented in FIMMPROP within the waveguide section

If the number of waveguide are sufficiently high, then the representation of EME performed by FIMMPROP becomes accurate. Once the eigenmodes are known the field is completely determined by the field coefficients ( $C_i^f, C_i^b$ ).

FIMMPROP propagates the electromagnetic fields by calculating the field coefficients in each section. If multiple section are used the joint scattering matrix is found by matrix multiplications. The basic cross section elements, Fig. 4.10, consist of a single mode and a multi-mode (in this case a 2 moded) structure.

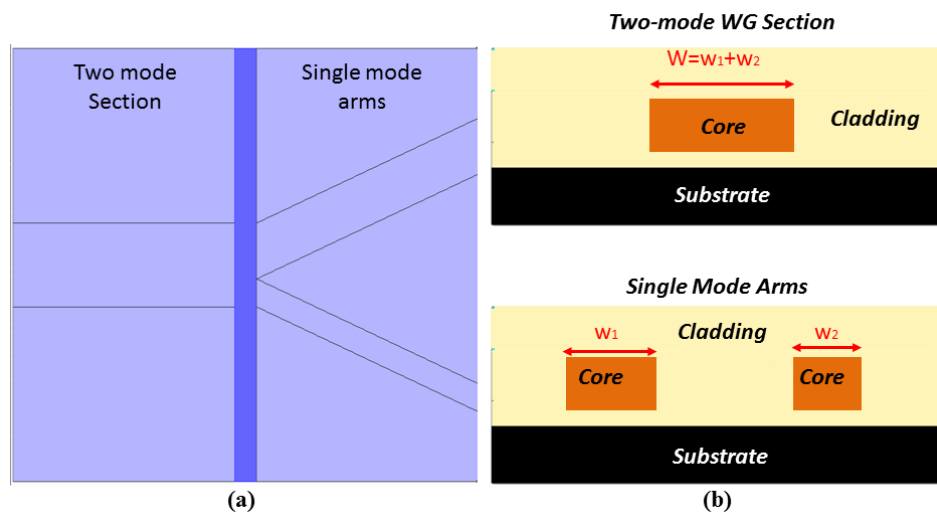


Figure 4.10 – Asymmetric waveguide junction (a) schematic in FIMMPROP and it corresponding (b) waveguide cross sections.

The thickness was 2  $\mu\text{m}$  for the whole structure, while the width was matched the cut-off dimensions to ensure the appropriate number of modes. Waveguide dimensions for the two moded section were found using the same process described before in the previous chapter. The

effective index calculations showed a cut-off dimension at 5  $\mu\text{m}$  width, at which the siloxane polymer-based waveguide still supports only two modes at 420 nm. The separation between the two single mode waveguides need to be large enough to isolate them. Any cross coupling between them would affect the adiabatic mode separation process. An effective index approximation was used to estimate the required single mode waveguide separation. Based on these results, illustrated on Fig 4.11(a), 4  $\mu\text{m}$  was chosen as an ideal separation for the two sections. As the separation increased between the two single mode arms the effective index of the transverse electric modes (TE) become unaffected above 10  $\mu\text{m}$ . All the simulations presented here are for TE modes, as the negligible difference was observed between behaviour of transverse electric and transverse magnetic modes.

The junction length was estimated by again calculating the coupling coefficients ( $CC_{ji}$ ) between the modes and the output arms. Where  $j$  denotes the mode number and  $i$  is the output arm.  $C_{11}$  represents the overall coupling coefficient from both the fundamental mode and the 1<sup>st</sup> order mode into arm 1. The length of the junction was increased and the coupling coefficient was observed to find the optimal length (Fig. 4.11(b)), while the single mode waveguide separation was kept constant at 4  $\mu\text{m}$ . The minimum junction length for an adiabatic transition is 2 mm, which is the point at which the coupling was maximised. The junction arms followed and S function shape to maximise adiabatic transition. The resulting branching angle is  $0.11^\circ$  calculated using equation 4.1.

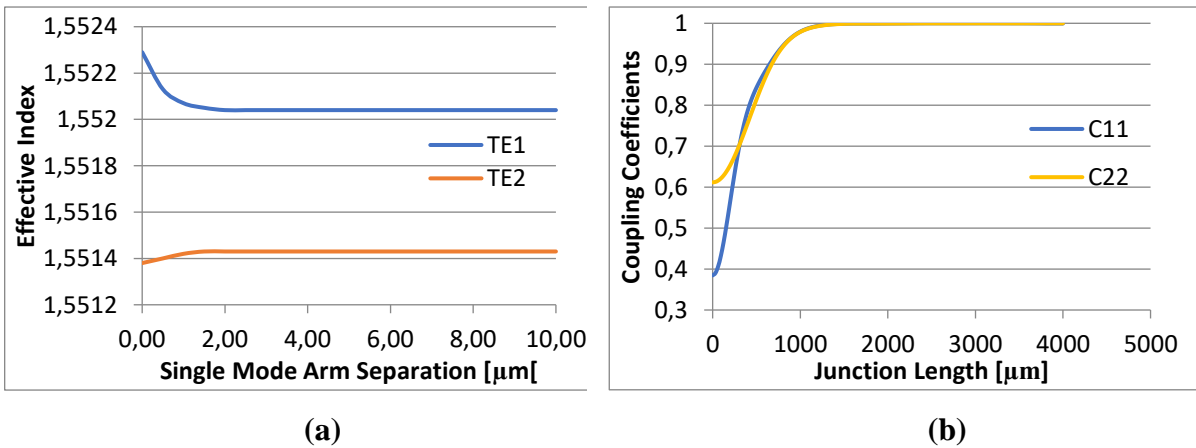


Figure 4.11 – Numerical Approximations for (a) modal effective indices at the single mode section as the waveguide separation is increased and (b) minimum junction length for maximum coupling coefficient for S-function shaped arms.

The next step is to find the optimal ratio of single mode arms that supports only single mode behaviour and the mode coupling efficiency is maximised. In Chapter 3.2, it was established that siloxane polymer-based waveguides operated at 420nm should not exceed  $2.5\mu\text{m}$  as multimode behaviour would result in decreasing mode coupling efficiency. The total width of the two arms should remain  $5\mu\text{m}$  for dual mode behaviour while their individual arms should remain single moded. The numerical simulations shown on Fig. 4.12, shows how the modal coupling coefficient between the input and output of the asymmetric junction changes as the ratio of the two waveguide widths were changed (at fixed height of  $2\mu\text{m}$ ) in the single mode section.

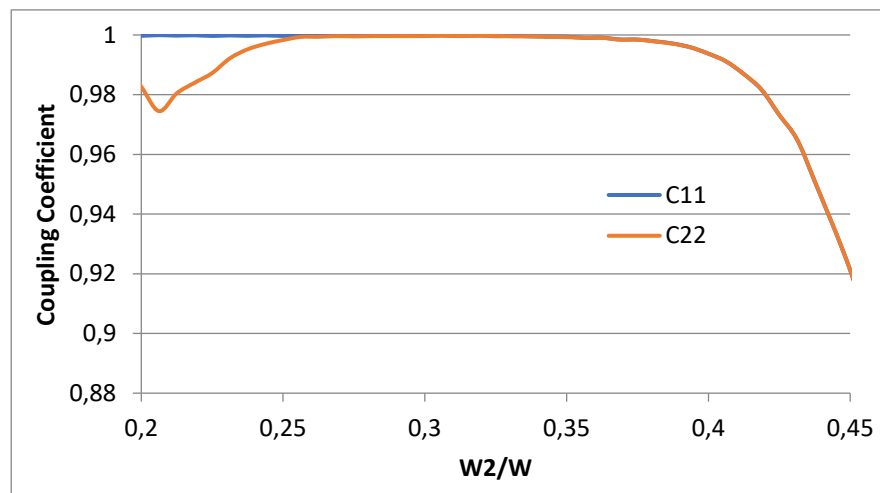


Figure 4.12 – Mode coupling efficiencies to the single mode arms as the ratio of single mode arms ( $W_1, W_2$ ) change in respect to total arm width ( $W$ )

The smaller arm starts to guide the higher order mode above the ratio of 0.28 ( $W_2=1.4\mu\text{m}$ ), its coupling efficiency increases. As the ratio of the single mode arms becoming less asymmetric the modes start to cross-couple. When the two arm are equal in width ( $W_2/W=0.5$ ) the junction essentially behaves as a power splitter, where the two modes power are split equally between the two arms. The optimal ratio for the single mode waveguides for efficient mode separation is between 0.28-0.35. The smaller arm accommodates the previously higher order mode when its dimensions are in the range of  $1.4\text{-}1.75\mu\text{m}$ , what means that in turn the wider arm needs to be kept between  $3.25\text{-}3.6\mu\text{m}$ . A third mode in the wider arm appeared on the simulation, however it was too weakly guided to affect the simulation. High asymmetry between the two waveguide arms is required to achieve high coupling efficiency. Fig 4.13 below shows the intensity field profile view of the junctions at different arm width ratios for different input mode excitation (it is almost identical for TM modes).

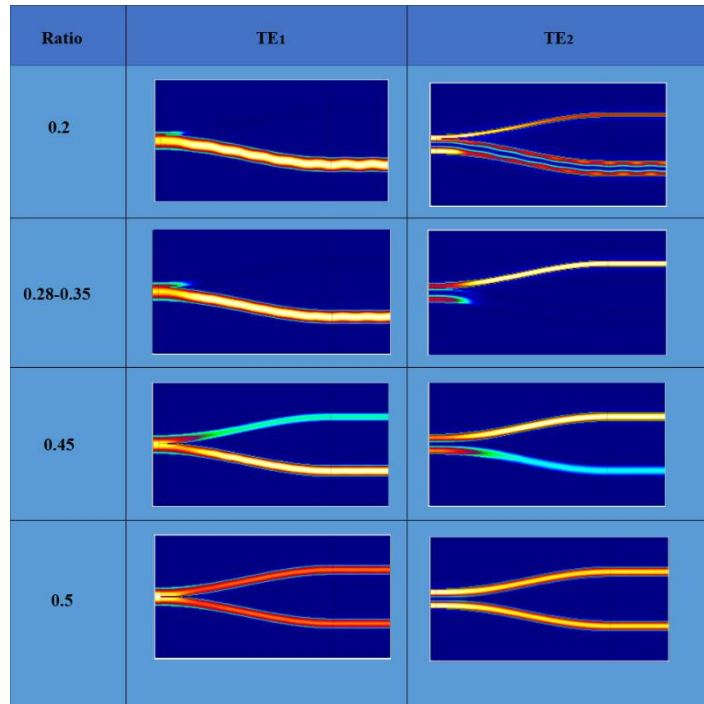


Figure 4.13 - Intensity Field Profile of the junctions (top view) at different level of asymmetry.

The number of waveguide modes that are employed in the device can be increased by using higher order asymmetric Y-junctions. Such higher-order multimode devices enable the use of larger waveguide dimensions at the device input and can therefore offer improved coupling efficiencies and alignment tolerances. As it will be shown in the next chapter, more reliable sensor operation can be achieved due to the simultaneous monitoring of a larger number of interrogating modes. Examples of some higher-order asymmetric Y-junctions are shown on Fig. 4.14.

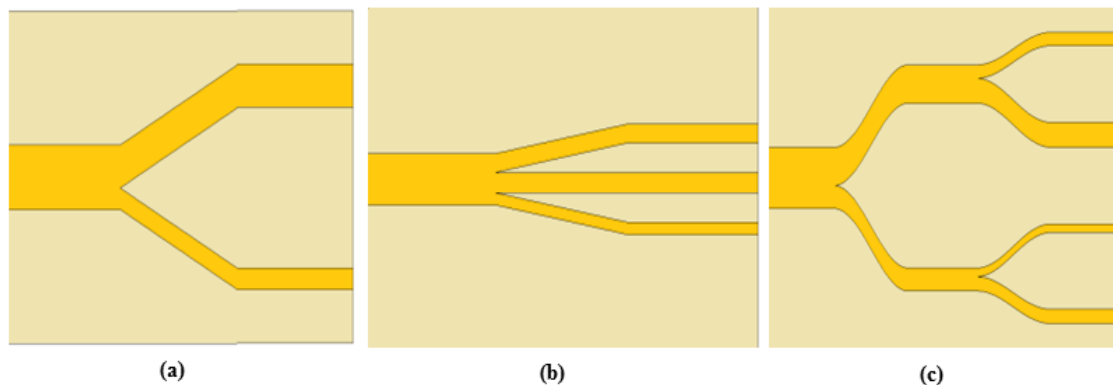


Figure 4.14 Mode Sorting Y-junctions for: (a) a 2-moded and (b) a 3- moded device as well as (c) a 4-moded device employing cascaded 2-arm junctions.

The design of such high-order mode junctions is a non-trivial process, as it requires precise matching of the effective indices of the waveguide modes in the input multimode section to the output single mode waveguides and an adiabatic transition between the two sections [4.15-4.17]. Moreover, practical considerations restrict the use of such devices to few-moded junctions.

The design process of the three arm junction was done in a manner similar to the 2 arm junctions by building the 3D waveguide junction structure in FIMMWAVE/FIMMPROP. The structural dimensions were altered and the modal coupling coefficients were numerically calculated using the effective index method or the finite difference method. The optimal dimensions were found by controlling FIMMWAVE/FIMMPROP in Matlab and optimising the modal coupling efficiencies. In the case of 3 arm junction, the multi-mode part should be kept at  $9\mu\text{m}$  in order to support 3 modes (both TE and TM). The single mode waveguides widths should not exceed this value and the optimal distribution ( $R_1=W_1/W$  and  $R_2=W_2/W$ ) needs to be found.

The modal coupling efficiencies is ideal ( $> 0.99$ ) when  $R_1$  is between 0.4-0.42 and  $R_2$  is between 0.31-0.33. Fig. 4.15 shows the numerical calculations for the smallest arm, which is appeared to be the most sensitive to width deviations.

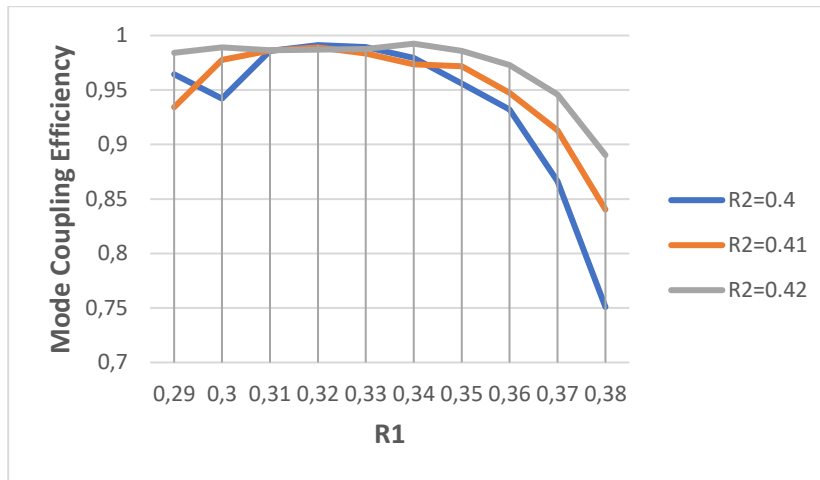


Figure 4.15 – Numerical calculation showing how the distribution of total width (W) between the arm widths effect the coupling efficiency

The field intensity profile of the designed 3 arm junction is illustrated on Fig. 4.16 at different input mode excitation. Only transverse electric polarisation is shown, as it is identical for transverse magnetic.

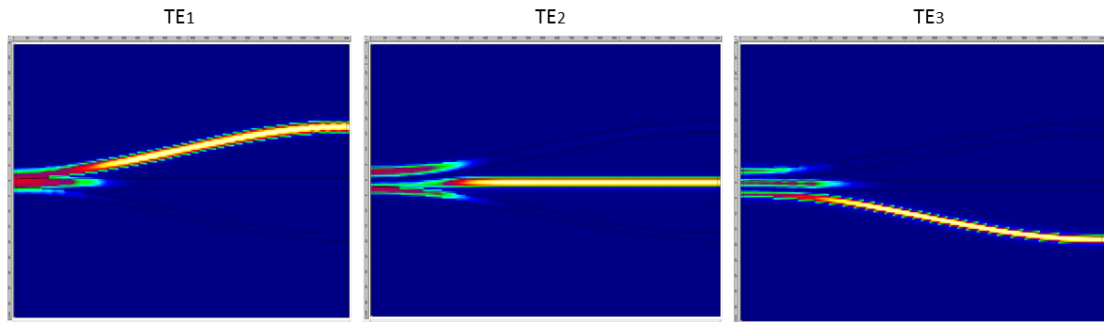


Figure 4.16 – Field intensity profiles for TE modes at different input mode excitation

The minimum junction length required for adiabatic mode transition in the Y-junction dramatically increases with the number of arms, resulting in impractically long devices [4.12-4.13]. The minimum length for the junction is 12mm, which is 4 times longer than it was for the 2-arm junction. In addition to that, numerical calculation showed the fabrication tolerances for higher-order junctions also become very stringent as the number of arms increases. The results of the fabrication analysis is detailed in the next chapter.

More practical way of achieving higher-order devices consists of cascading feasible 2-moded Y-junctions [4.21]. Fig 4.17 illustrates a 4-moded device implemented with two stages of 2-moded Y-junctions.

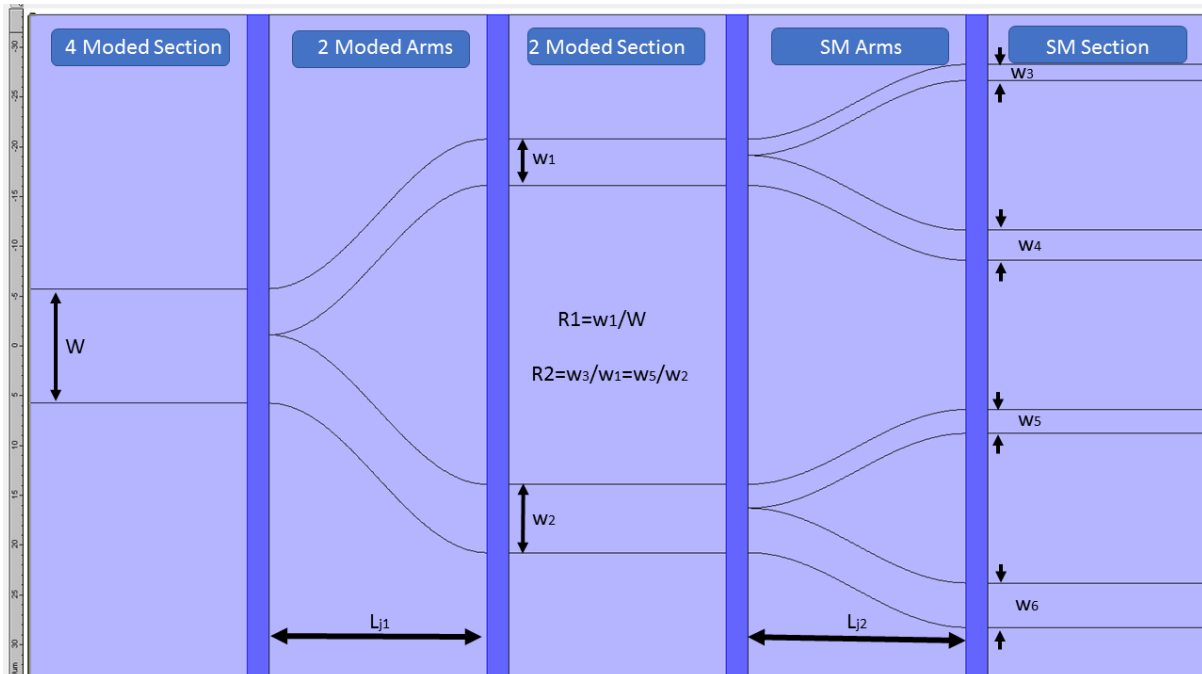


Figure 4.17 – Schematic structure (top view) of cascaded asymmetric junction model in Fimmprop

The structure consists of a 4 moded coupling structure followed by an asymmetric multimode junction, a 2 moded section feeding the light into another two arm asymmetric junction sorting the two modes into the single mode section at the output. The design rules remained the same for the 2 arm junctions. Keeping  $R_2$  in the range of 0.28-0.35 allows modal coupling efficiency above 0.99 regardless of the fact that their input arms widths ( $W_1, W_2$ ) are different. The minimum junction length required was the same as before (3mm).

The key structure is the 4 to 2 mode sorting section, which guides the modes to the correct output arm when the ratio ( $R_1$ ) is kept between 0.37-0.4. Fig 4.18 shows the evolution of mode sorting for the 4 to 2 mode junction as  $R_1$  changes. The length of this junction is 10mm, while the total length is 12 mm with the addition of the 2 to 1 mode sorting junction.

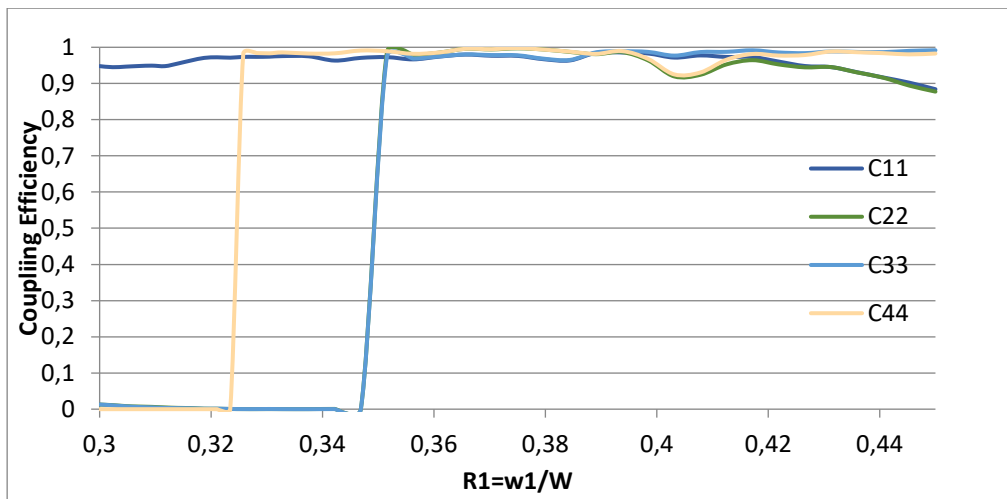


Figure 4.18 – Numerical Calculation showing the modal coupling efficiency changes in the 4 to 2 mode sorter junction at different output arm widths

The sensor is only 12mm long and is capable of separating 4 modes by cascading three 2-arm junctions. The separation between the arms were kept at  $15\mu\text{m}$  for all the output arms. Fig. 4.19 shows the field intensity profile of the modes as they pass through the designed device and fed into different output arms showing a good mode sorting performance. Again, the result is identical for both polarisation, and therefore only one is shown.

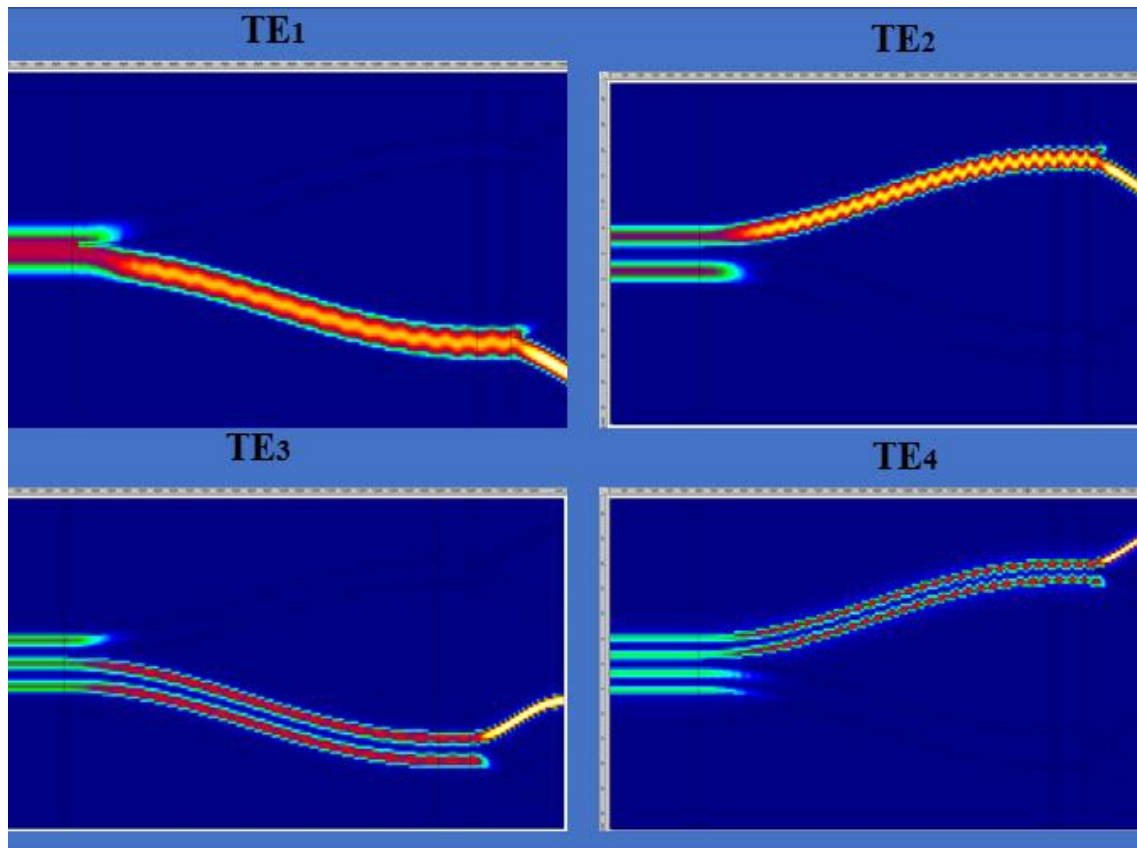


Figure 4.19 -Field intensity profiles for TE modes at different input mode excitations

The next chapter investigates the fabrication sensitivities of these structures in order to find an optimal technology for fabrication.

### 4.2.3 Fabrication sensitivity

To assess the tolerances for the fabrication of such devices, a basic analysis has been carried out. The mode sorting efficiency of a 2- , 3- and a cascaded Y-junction is calculated when the width of one arm of the junction is offset by a small amount  $\Delta$  with respect to its ideal value (Fig. 4.20). The offset  $\Delta$  is introduced in the narrowest arm for the 2 and 3-arm devices as its mode coupling performance is more susceptible to width changes.

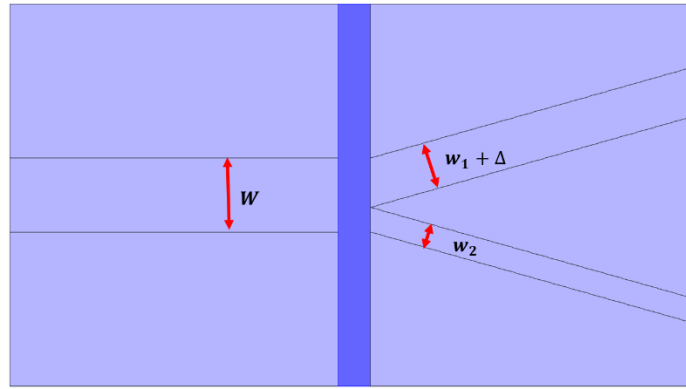


Figure 4.20 – Structure dimension increment by  $\Delta$

While in the case of the cascaded junction it was the 4 to 2 mode sorting junction that was the most susceptible. The results shown on Fig. 4.21, demonstrate that the use of cascaded Y-junctions can enable the formation of higher order mode sorters with more relaxed fabrication tolerances than large asymmetric Y-junctions. The mode coupling efficiency was more resilient to waveguide width deviations in comparison to the 3-arm junction.

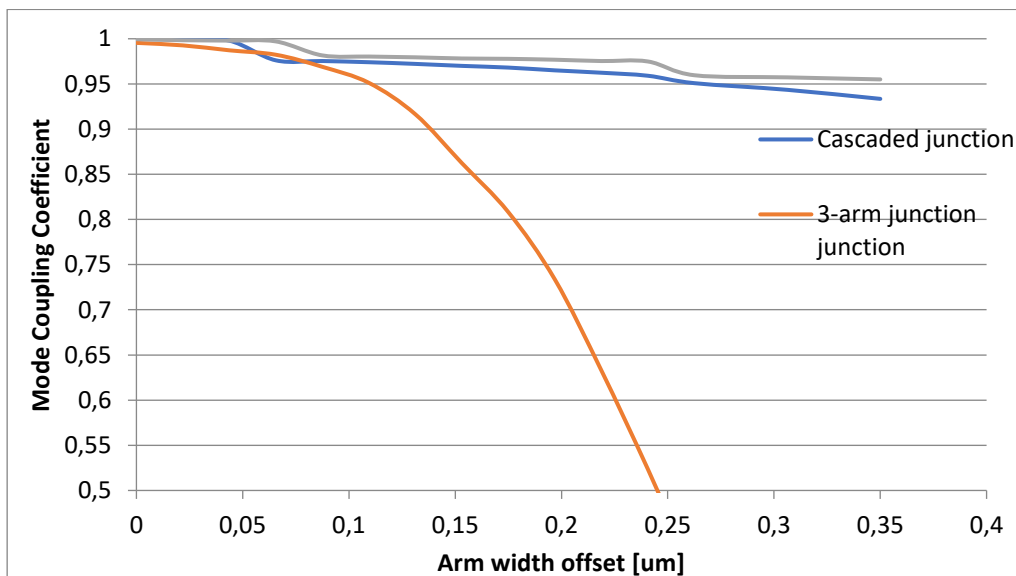


Fig. 4.21– Summary of fabrication sensitivity analysis, where mode coupling efficiency changes with arm widths for each device

The fabrication tolerances of both cascaded and 2-moded junction can be achieved with standard fabrication methods, while the 3-arm junction requires complex fabrication techniques to be used. More on this will be discussed in Chapter 5, focusing on different high-resolution fabrication technologies appropriate for siloxane polymer waveguide technology.

### 4.3 Mode selective sensor based of asymmetric Y-junctions

In the last decade, optical sensing has seen a rapid growth as it offers great advantages over other sensing technologies, such as immunity to electromagnetic interference, high selectivity and sensitivity [4.22]. In particular, lab-on-a-chip optical sensors have attracted considerable interest from the medical industry targeting the development of highly-sensitive but low-cost portable devices. Thus, the integration of optical waveguide technologies with sensing elements and microfluidics onto low-cost platforms has received significant attention [4.23]. Several successful optical detection schemes have been implemented with such integrated waveguide sensors, based on different detection principles such as absorption [4.22], interferometry [4.23], spectroscopy [4.24] and plasmonics [4.25].

Absorption-based waveguide sensors are the most widely used devices as they are inherently simpler to fabricate and require low-cost light sources and detectors. Such sensors, unlike other common sensing elements such as Mach-Zehnder interferometers, microrings and gratings, do not require the fabrication of complex optical structures, which, in turn, require high-resolution fabrication processes and stringent alignment tolerances in the device assembly and packaging. Despite their simplicity, an important issue regarding the operation of evanescent-wave sensors is the fundamental trade-off between the thickness of the sensing layer and the measurement sensitivity. Relatively thick sensing layers (membranes, typically  $\sim 1 \mu\text{m}$  in thickness) exhibit increased sensitivity due to the large overlap of the evanescent field and the sensing area. However, they suffer from slow response and recovery times due to the increased diffusion time of the measurand molecules from the carrier medium (outer medium) into the membrane. In comparison, thinner sensing layers, such as self-assembled monolayers ( $\sim 10\text{-}100 \text{ nm}$  in thickness), exhibit very fast responses but can suffer from spurious effects due to the presence of other chemical species in the carrier medium, as the evanescent field extends outside the sensing layer and interacts with these as well as the sensing layer (Fig. 4.22).

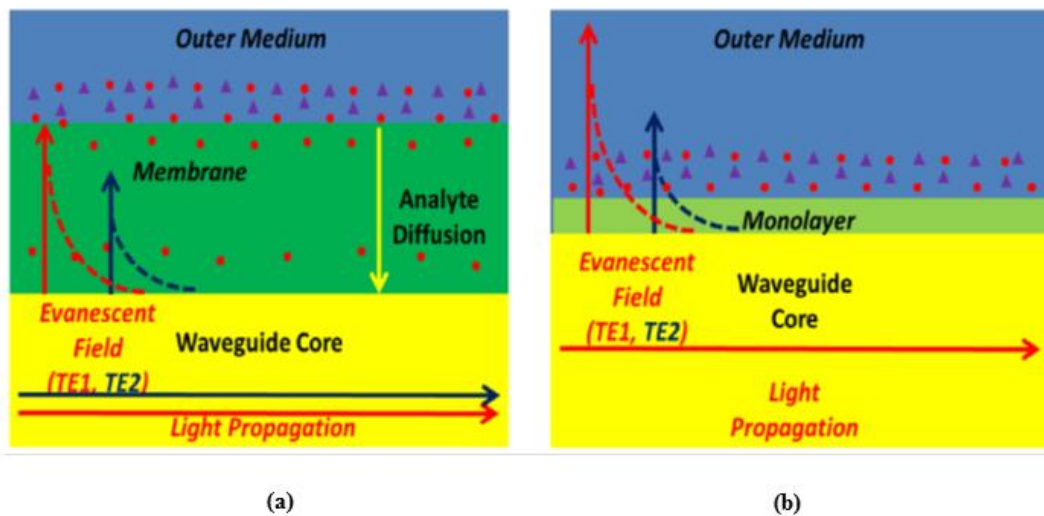


Fig. 4.22 – Illustration of the problem regarding the optimisation of sensing layer, evanescent field penetration and interference between target analyte (red dots) and other absorbing chemical species (purple triangles) for both (a) membrane with relatively large thickness ( $\sim 1 \mu\text{m}$ ) and (b) monolayer with depth of order 10s of nanometres

It has been shown that the absorption changes in the outer medium can be as large as 50 times higher than the absorption changes in the sensing layer due to the presence of other (non-specific) chemical species in the outer medium, therefore causing serious degradation in the evanescent-wave sensor operation [4.26]. As a result, reference waveguides are typically deployed to overcome this issue, such as in interferometric sensors, in order to distinguish real from spurious sensor response. Here, we propose a novel method of tackling this issue in absorption waveguide sensors using asymmetric mode-selective Y-junctions.

### 4.3.1 Sensor operation

The schematic of the proposed absorption-based multimode waveguide sensor is shown in Fig. 4.22 for a 2-moded interrogation. It comprises 3 sections: the input coupling section, the sensing section and the asymmetric Y-junction section. Similar devices enabling interrogation of larger number of waveguide modes can be implemented by deploying a larger-order Y-junction and are discussed later. The input section comprises a multimode waveguide which offers higher coupling efficiency and larger alignment tolerances at the device input than the commonly-used single mode waveguides. The sensing section comprises the multimode waveguide functionalised with a sensing layer and includes the microfluidic channels that deliver the target analyte to the sensing area. The different waveguide modes propagating in the sensing section

have an evanescent tail, which differs in probing depth and extends to a different degree in the sensing layer and outer medium. As a result, different waveguide modes exhibit a different sensitivity to absorption changes in the sensing layer and outer medium. Lower order modes, due to their increased confinement in the waveguide core, exhibit larger sensitivity to changes in the sensing layer, while higher order modes are more sensitive to absorption changes in the outer medium than lower order modes. The asymmetric Y-junction is appropriately designed to separate the waveguide modes at the corresponding waveguide outputs by matching the effective refractive indices of the guided modes in the transition area [4.21]. By monitoring the variation of the output power at the different output waveguides, the sensor response due to changes in the sensing layer and the outer medium can be de-correlated. The proposed sensing structure is shown on Fig. 4.23.

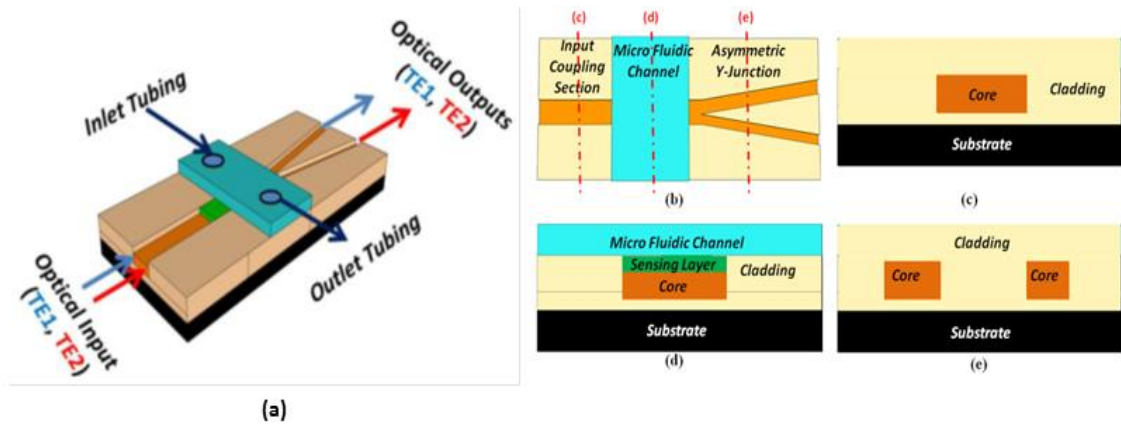


Figure 4.23 – Schematic of the proposed optical waveguide sensor: (a) planar view and (b) top view, and cross section of the device at its different segments: (c) multimode input section, (d) sensing section and (e) output section.

### 4.3.2 Sensitivity analysis

A matching waveguide model is produced in FIMMWAVE/FIMMPROP for each of the studied sensor devices (structures in Fig. 4.14 a, b and c). The waveguide core and cladding refractive indices are assumed to be 1.55 and 1.553 respectively at 420 nm, matching siloxane polymer materials [4.23]. The sensing section length is kept constant at 5 mm for all the simulations, while the sensing layer thickness is chosen to be 200 nm, unless stated otherwise. The refractive index of the outer medium is 1.33 (water-based solution), while that of the sensing layer is 1.45 (typical for a protein recognition layer). The penetration depth of the evanescent field of the 2<sup>nd</sup> order

mode in the sensing section is found to be  $\sim 0.5 \mu\text{m}$  due the small refractive index difference  $\Delta n$  of  $3 \times 10^{-3}$  between core and cladding materials. The absorption of the sensing layer  $\alpha_m$  depends on the analyte concentration which in turn changed the material absorption. While the outer medium is assumed to have an additional absorption coefficient  $\beta$  that can be varied between 0 to  $100 \times \alpha_m$ . The case  $\beta=0$  represents the ideal case where the outer medium does not exhibit any spurious absorption at the wavelength of interest and, therefore does not interfere with the sensor operation. On the other hand, the case  $\beta = 100 \times \alpha_m$  corresponds to a “worst-case” scenario which can cause serious interference with the analyte concentration estimation. For each device studied, the waveguide modes are found using the Fimmwave mode solver and their corresponding propagation loss due to the absorption in the two layers is derived for the different values of  $\alpha_m$  and  $\beta$ .

The total power at the output arms can be expressed as:

$$P_{arm1} = 10\log((C_{11} + C_{21}) * e^{-\frac{2\pi L}{\lambda}(\Gamma_\alpha \alpha_m + \Gamma_\beta \beta)}) \quad (4.9)$$

Where  $C_{11}$  is the coupling of mode 1 to mode 2 and  $C_{21}$  is the coupling from mode 2 to mode 1.  $\Gamma_\alpha, \Gamma_\beta$  represent the mode confinements within the sensing layer and outer medium, respectively affected by absorption coefficients ( $\alpha_m, \beta$ ) or each medium.

Fig. 4.23 shows the variation of the output power for the two output arms of a 2-moded sensor as the function of the absorption coefficients of the sensing layer ( $\alpha_m$ ) and the outer medium ( $\beta$ ). It can be seen that the lower order mode is slightly more sensitive to absorption changes in the sensing layer (larger slope) whereas the 2<sup>nd</sup> order mode is much more sensitive to the absorption changes in the outer medium.

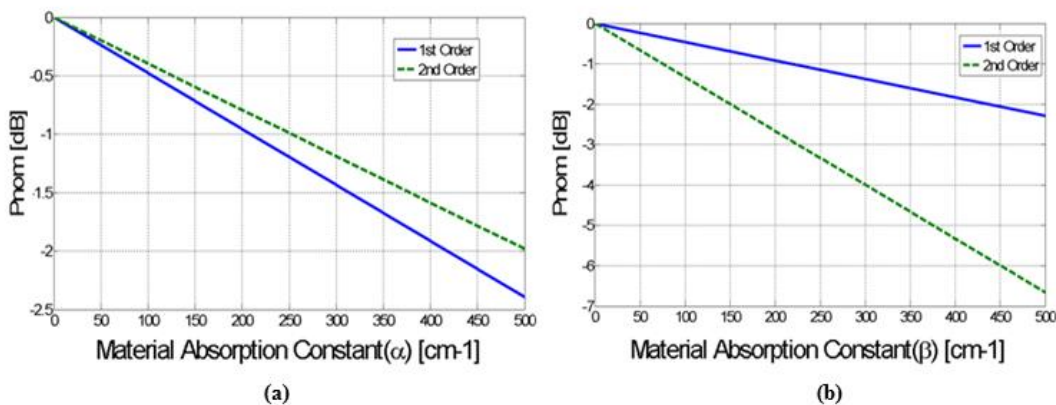


Fig. 4.24 Mode Sensitivity for absorption changes in (a) the sensing layer and (b) the outer medium for each mode

From Fig. 4.24, it can be observed that the power of each mode depends has and exponential decay to the absorption coefficients  $\alpha$  and  $\beta$  of the sensing layer and outer medium respectively. For analysis purposes, the results are represented in logarithmic form resulting in a straight line. As a result, the power of each waveguide mode (normalised) at the sensor output can be easily expressed with simultaneous equations.

In case of a mode duplex waveguide sensor, the modal sensitivity of can be expressed for each of the two-layer as:

$$S_{11} = \left. \frac{dP_{arm1}}{d\alpha} \right|_{\beta=0} \quad S_{12} = \left. \frac{dP_{arm1}}{d\beta} \right|_{\alpha=0} \quad S_{21} = \left. \frac{dP_{arm2}}{d\alpha} \right|_{\beta=0} \quad S_{22} = \left. \frac{dP_{arm2}}{d\beta} \right|_{\alpha=0} \quad (4.10)$$

Each mode is effected by both the sensing layer and outer medium absorption.

$$A_1 = S_{11} * \alpha + S_{12} * \beta \quad (4.11)$$

$$A_2 = S_{21} * \alpha + S_{22} * \beta \quad (4.12)$$

Using the asymmetric waveguide junction, the optical power of each waveguide mode can be efficiently monitored, while the optical loss of each mode can be expressed as:

$$\begin{bmatrix} A_1 \\ A_2 \end{bmatrix} = \begin{bmatrix} S_{11} & S_{12} \\ S_{21} & S_{22} \end{bmatrix} \begin{bmatrix} \alpha \\ \beta \end{bmatrix} \quad (4.13)$$

Where  $A_i$  is the total loss (in dB) of mode  $i$ , and  $S_{1i}$  and  $S_{2i}$  are the slope of absorption of mode  $i$  to absorption changes in the sensing layer and the outer medium respectively.

By measuring the power of each waveguide mode before and after the injection of the analyte, the mode loss  $A_i$  can be found and therefore, by solving equation (4.14), we can obtain the unknown absorption coefficients  $\alpha$  and  $\beta$  of a particular sample by finding the least-squares solution of:

$$\begin{bmatrix} \hat{\alpha} \\ \hat{\beta} \end{bmatrix} = \begin{bmatrix} S_{11} & S_{12} \\ S_{21} & S_{22} \end{bmatrix}^{-1} \begin{bmatrix} A_1 \\ A_2 \end{bmatrix} \quad (4.14)$$

The described analysis can be extended for higher-order sensor devices. The increase in the number of interrogating modes can further improve the detection process by increasing the size of the sensitivity matrix  $S$ . Equations (4.15) and (4.16) show the equations to be solved for the 3

and 4-moded sensors. The least-square solution for equations (4.15-16) can be easily derived with common linear algebra methods.

$$\begin{bmatrix} S_{11} & S_{12} \\ S_{21} & S_{22} \\ S_{31} & S_{32} \end{bmatrix} \begin{bmatrix} \hat{a} \\ \hat{b} \end{bmatrix} = \begin{bmatrix} A_1 \\ A_2 \end{bmatrix} \quad \begin{bmatrix} S_{11} & S_{12} \\ S_{21} & S_{22} \\ S_{31} & S_{32} \\ S_{41} & S_{42} \end{bmatrix} \begin{bmatrix} \hat{a} \\ \hat{b} \end{bmatrix} = \begin{bmatrix} A_1 \\ A_2 \end{bmatrix} \quad (4.15-16)$$

In order to evaluate the accuracy of the estimation method, the simulation model is run for different values of  $\alpha_m$  and  $\beta$  for the three devices. As an example, the material absorption was change as it would before a quinamine dye reacts with glucose (0-5.4mM). The concentration of glucose at the sensing layer is assumed to be constant at 0.5 mM, while the thickness of the sensing layer is varied between 50 and 200 nm. The outer medium absorption  $\beta$  is assumed to be a multiple  $M$  of the sensing layer absorption coefficient  $\alpha_m$ , ranging from  $M=0$  which represents the ideal case of a non-absorbing carrier, to  $M=100$  which represents the extreme case of a very highly-absorbing medium. For such a highly-absorbing outer medium the spurious response of the sensor is expected to be very large. The simulation is carried out for each sensor device for each combination of the  $(\alpha_m, \beta)$  parameters and the corresponding mode loss values  $A_1$  and  $A_2$  for each combination of  $(\alpha_m, \beta)$  are obtained from the simulations.

$$\beta = M * \alpha_m \quad (4.17)$$

The obtained  $A_1$  and  $A_2$  values are fed into the sensor analysis method described above, providing the estimated  $\hat{a}$  and  $\hat{b}$  values for the sensing layer and outer medium respectively. Fig. 4.25 shows the relative error  $\varepsilon_1$  in the estimation of actual values of  $\alpha_m$  obtained with the model for the 2-moded sensor device for the different values of the absorption multiplier ( $M$ ):

$$\varepsilon_1 = \left| 1 - \frac{\hat{a}}{\alpha} \right| \quad (4.18)$$

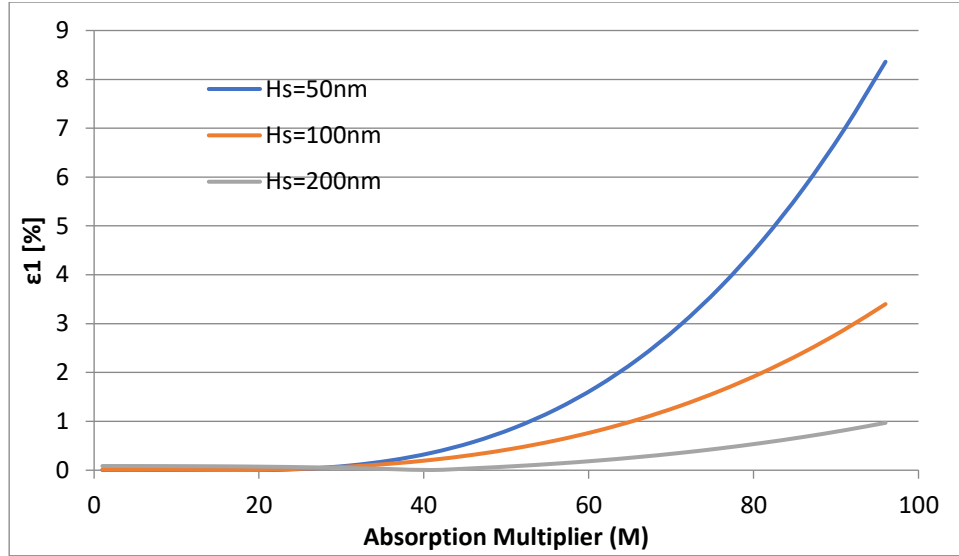


Fig. 4.25 Relative error in the estimation of the sensing layer absorption  $\alpha_m$  obtained with the proposed mode selective sensor as a function of the spurious absorption of the outer medium for a range of sensing layer thicknesses.

For most physical system, a concentration estimation error of 5% of the total dynamic range is considered acceptable. As shown in Fig. 4.25, The relative error for  $\alpha_m$  is below 1% even in the case of a highly-absorptive outer medium with an absorption coefficient over 96 times larger than that of the sensing layer for thicknesses larger than 200 nm. For a thinner sensing layer, such as in a self-assembled monolayer (~10s of nanometers), this threshold is reached value of M is above 65. Overall, the simulation results indicate a considerable estimation robustness for all the thicknesses studied. The immunity of the proposed sensor to spurious response due to absorption changes in the outer medium, even in the extreme case of presence of highly-absorbing species. For comparison, the operation of the multimode absorption sensor device without the mode-sorting junction is also studied. The structure of such a device is shown in Fig. 4.26 and it comprises only the input, output and sensing waveguide sections. For such a device, only the total power at the output of the device can be monitored due to the absence of the mode-sorting junction. As a result, the effect of the outer medium on the measurement cannot be distinguished. The absorption of the sensing layer  $\hat{a}$  is estimated based only on the absorption coefficients  $S_{ji}$  of each waveguide mode to the changes in the sensing layer. For a two-moded device

$$A_{tot}=A_1+A_2=S_{11} * \hat{a} + S_{12} * \hat{a} \quad (4.19)$$

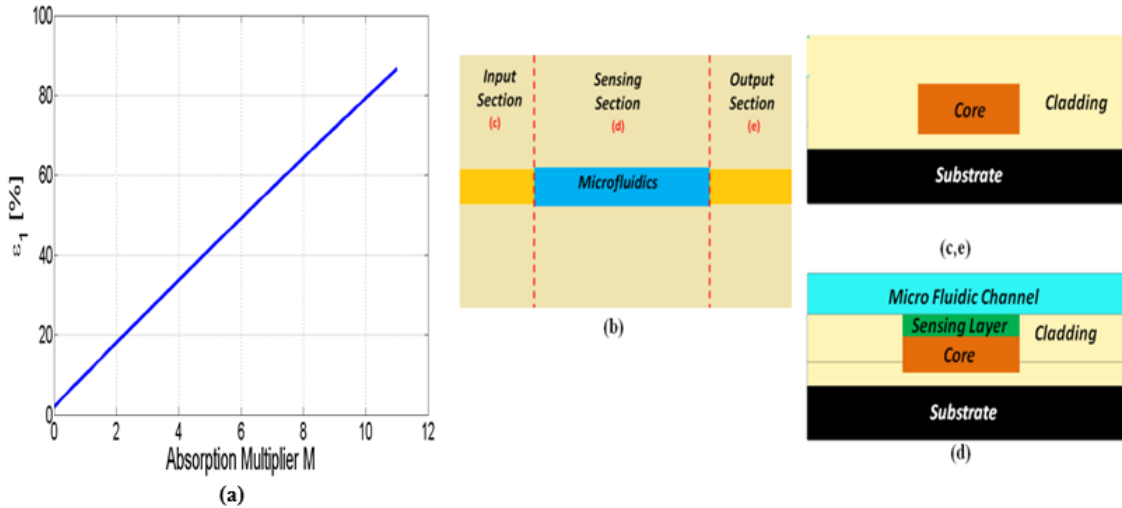


Figure 4.26 Relative error in the estimation of the sensing layer absorption  $\alpha_m$  for different absorption multipliers of the outer medium for the multimode waveguide without the use of asymmetric junctions (structure (b) and cross section (c-d)).

Fig. 4.26a shows the error in the estimation of the absorption coefficient  $\alpha$  due to the absorption of the outer medium. The plot indicates a much larger error in the absorption estimation demonstrating the benefits of the use of the mode-sorting junction in the sensor device. As, it was mentioned earlier, the sensing layer is 200 nm thick for all the simulations, unless stated otherwise.

An error estimation analysis similar to the one carried out for the 2-moded sensor, is performed for the 3 and 4-moded sensor devices shown in Fig. 4.27. It is expected that the use of larger sensitivity matrices in the absorption estimation (eq. (4.12) and eq. (4.13)) should provide an improved sensor performance for a larger number of interrogating modes. Fig. 4.26 shows the relative error in the estimation of the absorption coefficient  $\alpha_m$  as a function of absorption multiplier  $M$  for the different number of interrogating modes in the device. As expected, the higher-order devices offer an improved performance. The error in the concentration estimation drops from 0.85% to 0.35-0.1% for  $M=100$  (highly-absorbing outer medium), as the number of interrogating modes was increased from 2 to 4. It has to be noted however, that if the spurious absorption of the outer medium does not exceed  $\sim 40$  times the absorption change in the sensing layer, similar quality low-error detection can be achieved with the 2-moded device which is simpler to fabricate.

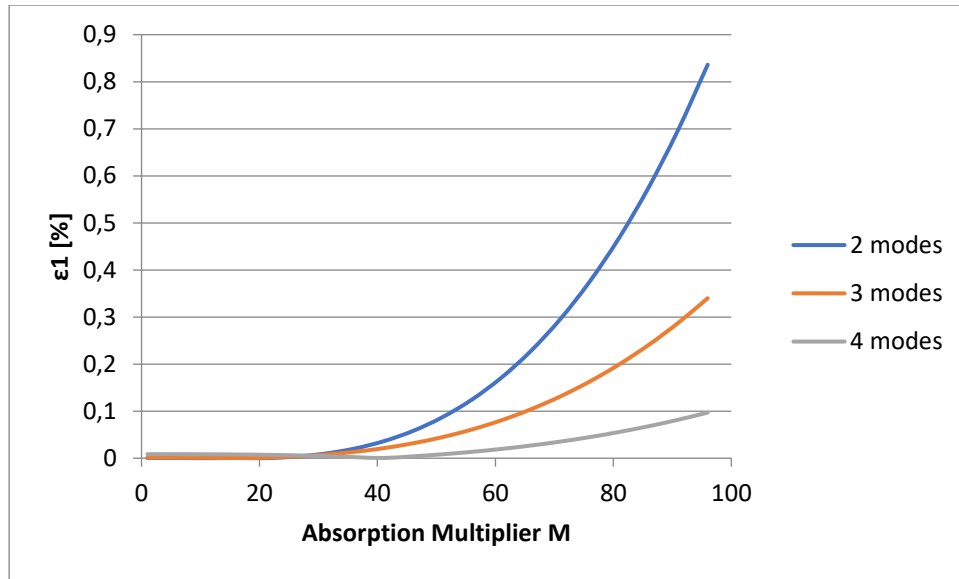


Figure 4.27 Relative error in the estimation of the sensing layer absorption  $\alpha$  for different absorption multipliers of the outer medium for the three different mode-selective sensors.

Finally, the sensor enables the estimation of the material absorption coefficient  $\hat{b}$  of the outer medium following the same process. The error in the outer medium concentration estimation can be described as:

$$\varepsilon_2 = \left| 1 - \frac{\hat{b}}{\beta} \right| \quad (4.20)$$

It can be noticed (Fig. 4.28) that the estimation of the outer medium absorption is very accurate even for large absorption multipliers, while similar good results are obtained from all types of devices.

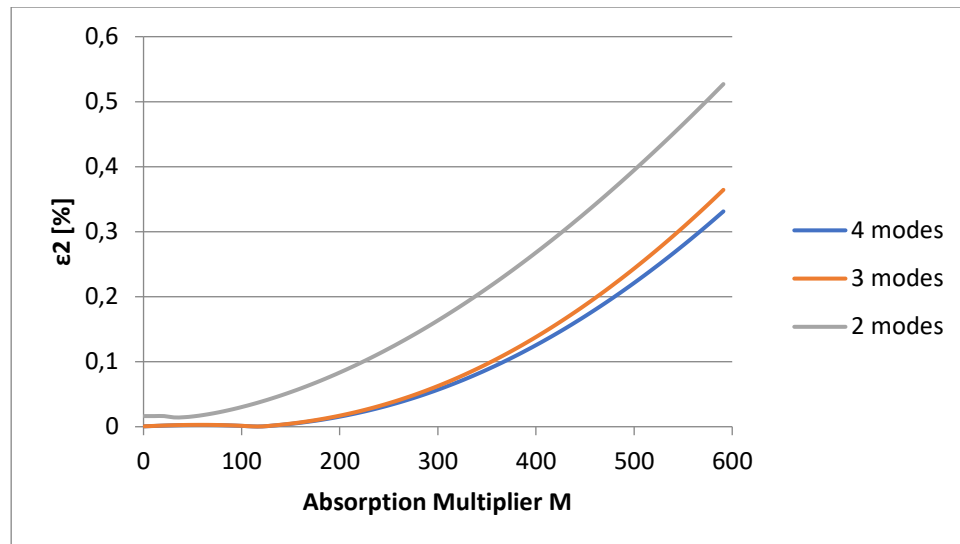


Figure 4.28 – Relative error in the estimation of the outer medium absorption  $\beta$  obtained with the proposed mode selective sensor for a different number of interrogating modes in the device.

### 5.3.3 Modal Injection effects on sensor performance

Optical sensors based on planar waveguides inhibit high sensitivity and compact size, however there are two main issues. Misalignment tolerance is a great issue, where the input light coupling section is small such as a slot waveguide or even a single mode waveguide sensor. Typically, a single mode waveguide with cross section around 4-5  $\mu\text{m}$  for visible light (e.g. Corning® RGB 400 by Thorlabs), it requires an alignment tolerance lower than  $\pm 1\mu\text{m}$ . The cost of a sensor is highly dependent on assembly tolerance as it defines the technology at which it requires to assemble the chip with the light coupling section and light source.

The simulation results based on the models described in the previous section are shown on Fig. 4.29. It illustrates how misalignment affects the mode coupling efficiency for a two-arm junction as two standard core diameter of input coupling fibre was used for an input waveguide of 5  $\mu\text{m}$ . The results show the clear advantage of having a larger waveguide core at the input of the sensor on the misalignment tolerance of the sensor. The single mode waveguide core has a very limited misalignment and it cannot excite the correct modes regardless of the alignment, in contrast the 62.5 $\mu\text{m}$  fibre with more relaxed tolerance of 4  $\mu\text{m}$ .

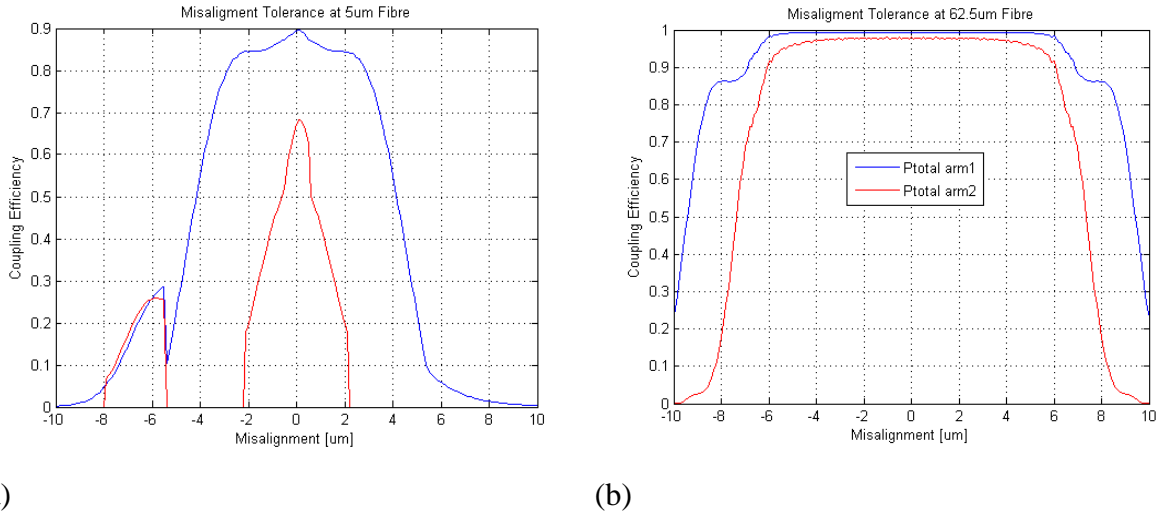
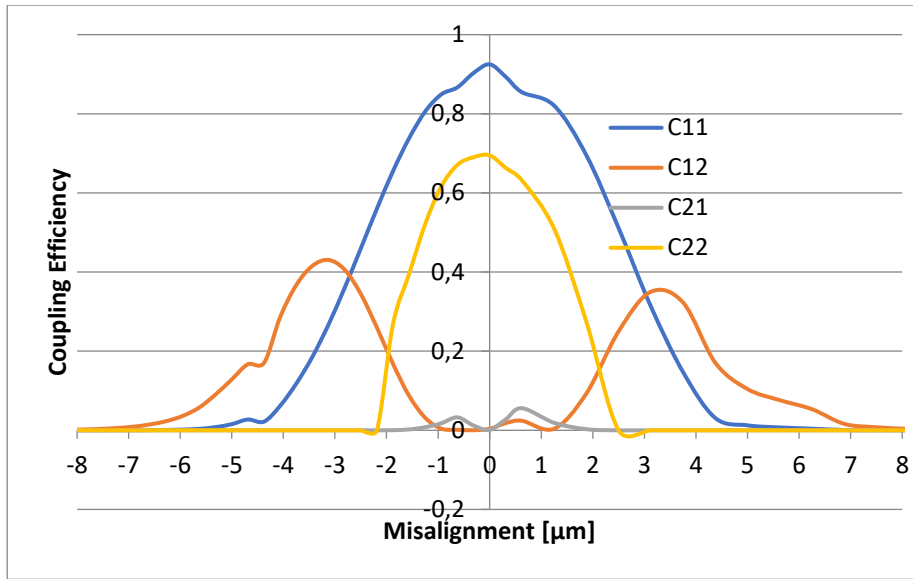
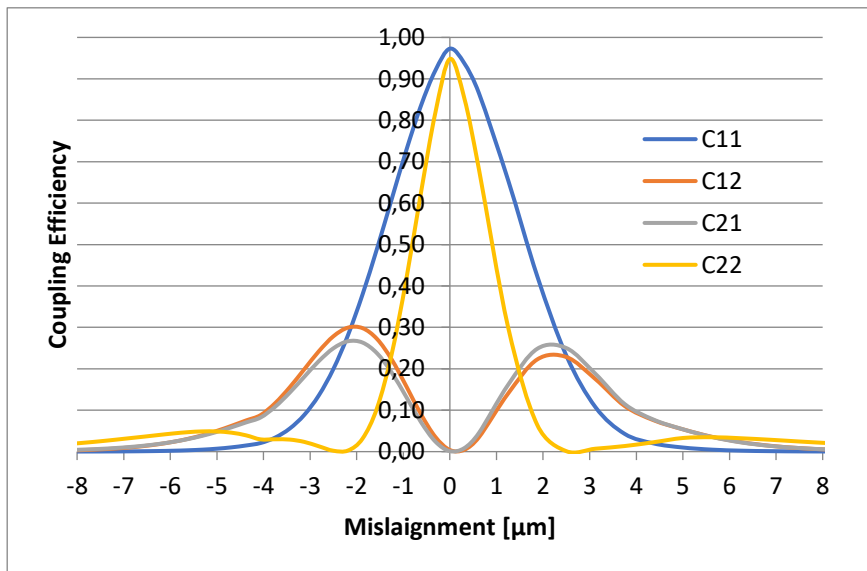


Figure 4.29 – Misalignment tolerance of a 2-arm junction with (a) 5  $\mu\text{m}$  and (b) 62.5  $\mu\text{m}$  coupling core width

Mode duplex sensor operation is highly dependent on our ability of exciting the designated modes within the input coupling section. Its sensitivity is dependent on the mode power within the sensing layer. Each mode will exhibit different sensitivity based on both their penetration depth and their modal power. Fig 4.30 shows the difference in mode coupling coefficients when a 5  $\mu\text{m}$  and a 62.5  $\mu\text{m}$  fibre is used for exciting the modes a 2-arm junction sensor. The 5 $\mu\text{m}$  core cannot evenly excite the modes within the waveguide which is an important factor for the mode duplex sensor, whereas for the 62.5  $\mu\text{m}$  core can excite them all evenly with a relaxed alignment tolerance of 3 $\mu\text{m}$ . Based on the results presented on Fig. 4.30, the sensor performance discussed in the previous chapters are achievable if the alignment tolerance is kept within 2  $\mu\text{m}$  for a large core multimode fibre such as a 62.5  $\mu\text{m}$ .



(a)



(b)

Figure 4.30 – Mode sorting performance of a 2-arm junction sensor with a  $5 \times 2 \mu\text{m}$  cross section input waveguide, excited by a (a)  $5 \mu\text{m}$  and a (b)  $62.5 \mu\text{m}$  input core.

Misalignment tolerance effects the measurement accuracy as the modal excitation changes. Fig 4.31 shows the concentration estimation on 2 moded sensor for different coupling core widths and its misalignment performance. The use of large multimode fibres are important in order to excite the modes appropriately as well as achieving relaxed misalignment tolerance.

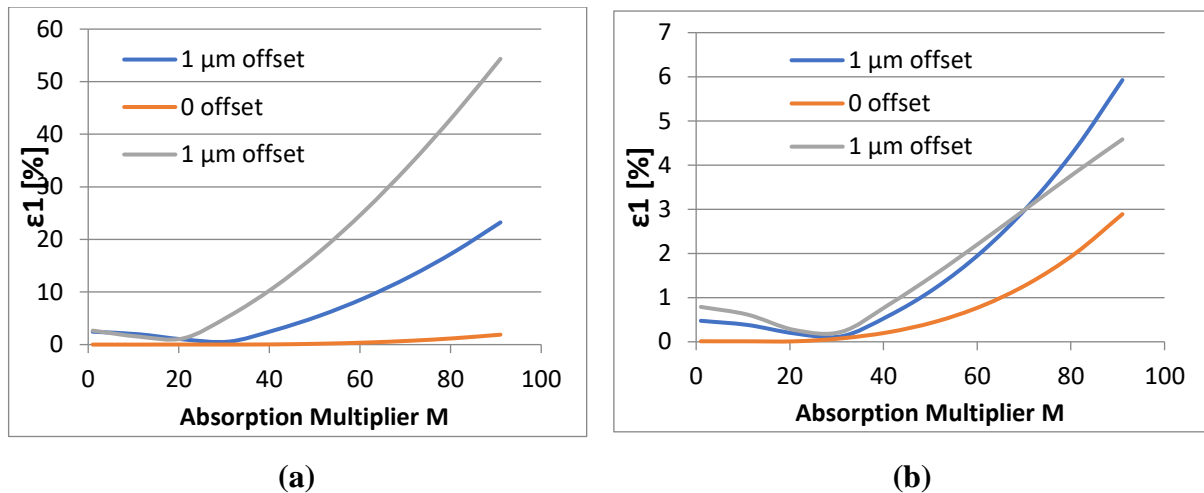


Figure 4.31. - Relative error in the estimation of the sensing layer absorption  $\alpha$  for different absorption multipliers of the outer medium as a function of fibre offset, (a) 5  $\mu\text{m}$  and (b) 62.5  $\mu\text{m}$  coupling core width

## 4.4 Conclusion

In this chapter, the reader was introduced to the fundamentals of Y-junctions, with specific attention paid to asymmetric Y-junctions and their mode sorting capabilities. Two, three and four mode sorter junctions were designed based on siloxane polymer waveguides at 420nm wavelength. A short overview of various design trade-offs has been discussed.

A novel multimode evanescent-wave absorption sensor based asymmetric Y-junction was proposed. The sensing layer is interrogated by more than one waveguide mode, which can then be separated to different waveguide output arms using an appropriately designed asymmetric Y-junction. The device offers immunity to the common problem of evanescent-wave absorption sensors due to the spurious absorption of the outer medium. By monitoring the behaviour of the different waveguide modes, it enables decorrelation of the real from the spurious absorption.

Simulation studies were carried out on the basic waveguide sensor to demonstrate that the device can accurately estimate the absorption changes in the sensing layer, even in the extreme case of a highly-absorbing outer medium. Estimation error of material absorption below 1% are obtained for absorption coefficients of the outer medium which are up to 96 times larger than that of the sensing layer. The sensing layer parameters were based on porphyrin-based dye, where the material absorption was the same as used in Chapter 3 for glucose concentrations up to 5.4 mM. The sensor performance is compared to the performance obtained from a reference absorption

waveguide sensor without the asymmetric waveguide junction demonstrating the benefits brought by the proposed sensor structure. The detection accuracy is improved for higher-order sensor devices due to the larger number of monitored waveguide modes but at the increased cost of device length and reduced fabrication tolerances. Having larger input coupling waveguide sections supporting multimode behaviour has its trade-offs. Misalignment tolerance is usually in the range of 1  $\mu\text{m}$  for a single mode waveguide sensor, whereas the 2-moded duplex sensor it was around 2  $\mu\text{m}$ , which is considerable difference. However, the well-known issue for multimode sensors is the dependence of sensitivity on launching conditions. The modal sensitivity within the sensing section will be dependent on the modal power distribution, which is a function of launching conditions. Based on the results shown in Chapter 4.3.3, even modal distribution at the multimode section can be achieved by using launching fibre with larger core diameter.

## 4.5 References

- 4.1 J. D. Love, A. Ankiewicz, "Purely geometrical coarse wavelength multiplexer/demultiplexer," *Electron. Lett.*, vol. 39, pp. 1385–1386, 2003.
- 4.2 R. G. H. van Uden, R. A. Correa, E. A. Lopez, F. M. Huijskens, C. Xia, G. Li, A. Schülzgen, H. de Waardt, A. M. J. Koonen & C. M. Okonkwo, "Ultra-high-density spatial division multiplexing with a few-mode multicore fibre", *Nature Photonics*, vol. 8, pp. 865–870, 2014.
- 4.3 K. Chen, H. P. Chan, F. Chen, W. Y. Chan, B. Sun, "An accurate analysis for two-mode interferometer based Mach-Zehnder interferometer interleaver", *Optics Communications*, vol. 283, pp. 4639-4644, 2010.
- 4.4 K. Zinoviev, L. M. Lechuga, C. Dominguez, "Interferometer and sensor based on bimodal optical waveguide and sensing method", Patent No.: Patent EP2017602A1
- 4.5 R. Bruck, R. Hainberger., "Sensitivity and design of grating-assisted bimodal interferometers for integrated optical biosensing", *Optica Express*, Vol. 22, No 26, 2014
- 4.6 T. Koster and P. Lambeck, "An integrated optical platform for absorptive sensing of chemical concentrations using chemo optical monolayers", *Meas. Sci. Technol.*, vol. 13, pp. 1230-1238, 2002.
- 4.7 H. Sasaki and I. Anderson, "Theoretical and experimental studies on active Y-junctions in optical-waveguides," *J. Quantum Electron.*, vol. 14, pp. 883–892, 1978.

- 4.8 A.G. Medoks, "The theory of symmetric waveguide Y-junction," *Radio Engineering and Electronic Physics-USSR* 13, vol. 106, 1968.
- 4.9 M. Izutsu, Y. Nakai, and T. Sueta, "Operation mechanism of the single-mode optical-waveguide-Y junction," *Opt. Lett.*, vol. 7, pp. 136–138, 1982.
- 4.10 W. K. Burns and A. F. Milton, "Mode conversion in planar dielectric separating waveguides," *J. Quantum. Electron.*, vol.11, pp. 32–39, 1975.
- 4.11 W. M. Henry and J.D. Love, "Asymmetric multimode Y-junction splitters," *Opt. Quantum Electron.*, vol. 29, pp. 379–392, 1997.
- 4.12 W. Y. Hung, H. P. Chan, and P. S. Chung, "Novel design of wide-angle single-mode symmetric Y-junctions," *Electron. Lett.*, vol. 24, pp. 1184–1185, 1988.
- 4.13 N. Riesen, J.D. Love, and J.W. Arkwright, "Few-mode elliptical core fiber data transmission," *IEEE Photon. Technol. Lett.*, vol. 24, pp. 344–346, 2012.
- 4.14 J. D. Love, R. W. C. Vance, and A. Joblin, "Asymmetric, adiabatic multipronged planar splitters," *Opt. Quantum Electron.*, vol. 28, no. 4, pp. 353–369, 1996.
- 4.15 H. Sasaki and I. Anderson, "Theoretical and experimental studies on active Y-junctions in optical-waveguides," *IEEE J. Quantum Electron.*, vol. 14, no. 11, pp. 883–892, 1978.
- 4.16 A. G. Medoks, "Theory of symmetric waveguide Y-junction," *Radio Eng. Electron. P.*, vol. 13, no. 1, p. 106, 1968.
- 4.17 M. Izutsu, Y. Nakai, and T. Sueta, "Operation mechanism of the single-mode optical-waveguide-Y junction," *Opt. Lett.*, vol. 7, no. 3, pp. 136–138, 1982.
- 4.18 J. D. Love and N. Riesen, "Single-, few-, and multimode Y-junctions," *J. Lightwave Technol.*, vol. 30, pp. 304–309, 2012.
- 4.19 Snyder and John D. Love, "Optical Waveguide Theory", 1<sup>st</sup> Edition, Springer US., 1984.
- 4.20 F. Barnes, "Optical waveguide analysis using beam propagation method", Term paper, pp. 1-20, 2006.
- 4.21 A. M. Bratkovskaya, J. B. Khurgin, E. Ponizovskaya, W. V. Sorina, M. R.T. Tana, "Mode division multiplexed (MDM) waveguide link scheme with cascaded Y-junctions", *Optical Communications*, vol. 309, pp. 85-89, 2013.
- 4.22 N. Bamiedakis, T. Hutter, R. V. Penty, I. H. White, and S. R. Elliott, "PCB-Integrated Optical Waveguide Sensors: An Ammonia Gas Sensor," *Journal of Lightwave Technology*, vol. 31, no. 10, pp. 1628-1635, 2013.

- 4.23 B. J. Luff , J. S. Wilkinson, J. Piehler, U. Hollenbach, J. Ingenhoff and N. Fabricius, “Integrated optical Mach–Zehnder biosensor”, *Journal of Lightwave Technology*, vol. 16, no. 4, pp. 583–589, 1998.
- 4.24 M. Ramuz, D. Leuenberger, and L. Bürgi, “Optical biosensors based on integrated polymer light source and polymer photodiode,” *J. Polymer Sci. Part B: Polymer Phys.*, vol. 49, pp. 80–87, 2010
- 4.25 T. M. Chinowsky, “Portable 24-analyte surface plasmon resonance instruments for rapid, versatile biodetection”, *Biosens. Bioelectron.*, vol. 22, pp. 2268–2275, 2007.
- 4.26 Riesen and J. D. Love, “Design of mode-sorting asymmetric Y-junctions,” *Applied Optics*, Vol. 51, Issue 15, pp. 2778-2783, 2012.

# Chapter 5 – Device fabrication and experimental results

## 5.1 Introduction

Most of the sensor structures and novel sensing methods described in the previous chapter were not possible to be fabricated with standard fabrication processes. Siloxane waveguide technology emerged in the early 2000s specifically designed for the application of low cost optical interconnects, where relaxed alignment and fabrication tolerances are required. Novel interconnect structures were developed based on large waveguide core structures (typically  $50 \times 50 \mu\text{m}$ ), which allowed simple and low-cost fabrication technology based on UV photo lithography. However, recent advances in the CPS group towards optical sensing techniques required a new method of fabrication. The standard fabrication processes for  $50 \times 50 \mu\text{m}$  siloxane waveguide structures operated at 850 nm for optical interconnect application have a resolution of  $5 \mu\text{m}$ . Most of the robust recognition layers that allow high sensor selectivity are operated in the visible range and the sensor sensitivity required either single mode or few moded operation for planar optical waveguides-based sensors structures. The smallest features in the designed waveguides structures were  $1.5\text{-}1.7 \mu\text{m}$  (at 420nm) with a resolution of better than 100 nm required. This section provides a brief introduction to the techniques available for polymer-based nanofabrication that might be suitable for the siloxane polymer-based waveguide technology.

Realising a siloxane-based polymer lab-on-chip sensor required a large improvement in fabrication technology such as higher resolution and the ability of attaching microfluidic channel to guide the target enzymes and analytes to the sensing region of the sensor in a continuous manner at very low volume flows.

In Section 5.4, the brain fluid sensor project is discussed aimed to investigate the applicability of siloxane waveguide technology to biomedical applications. Section 1.2 provided a brief introduction to the issue of continuously measuring brain microdialysates. A state of art

technology review was carried (Appendix) at the start of the project in order to identify possible research directions for implementing a siloxane polymer-based lab-on-chip sensor for this application.

The technology review summarised the most widely used recognition elements and optical interrogation techniques currently available for glucose, lactate and pyruvate. The recognition elements of the aforementioned optical sensors were mainly based on monitoring redox enzymatic processes using oxygen or change in a pH as an indicator. Generally optical interrogation is carried out by either light absorption, interferometry, fluorescence intensity or life time quenched by molecular oxygen. The corresponding state of art research for each technique are summarised in the Table 7.1-3.

Decacyclene complexes of Pt(II), Pd(II) with porphyrins, Ru(phen), Ru(bpy) and Ru(dpp) were the most popular dyes because they can be used for fluorescence by exciting the sensing layer or simple absorption using visible light. Metal complexes are preferred because they display a large Stokes shift with relatively long decay times along with a good photostability [5.1]. Mostly, these compounds have been immobilised with glucose oxidase as an oxygen sensitive indicator, and then are excited by blue light with photo emission in the wavelength range between 500-600nm. Response times are usually in the range of 1-6 minutes, which can be further enhanced at the expense of their dynamic range [5.1-3]. As the literature suggests [5.4], glucose oxidase in combination with porphyrins is identified as a good candidate for analysing brain microdialysates because of its high sensitivity, reversibility and fast response time. Moreover, lactate and pyruvate oxidase are widely available and it share the similar attributes to glucose oxidase. Therefore, it was thought highly likely that it would be possible to fabricate a multiplexed sensor based on these recognition elements that can be used to detect all three analytes of interest. The development of this recognition layer and the corresponding sensor measurements are discussed in Chapter 5.4.

### Overview of Fabrication Technologies

There are various different methods available for polymer waveguide fabrication, each having its own advantages and disadvantages. Selecting the most suitable fabrication process depends on various factors, such as the type of the polymer, production cost and volume, ease of fabrication and required resolution. The most commonly used methods in optical waveguide fabrication are based on lithography, laser direct writing and soft-lithography (moulding).

Embossing is an indirect technique, which requires an embossing plate to be fabricated before

the polymer can be processed. [5.5] It is often applied to relative large core dimensions (above 100 $\mu\text{m}$ ) or when complex structures such as optical splitters need to be fabricated. Embossing is appropriate for mass production due to low-cost, however the master module is very expensive.

Nano-imprint lithography is a promising new fabrication method. Recently, several submicron core sized sensor structures were showcased based on this fabrication technology [5.6-7]. It is very similar to embossing, however curing can be done either thermally or by UV exposure. The master stamp is generally a patterned silicon wafer with an anti-adhesion coating. The purpose of the coating is to enhance the quality of stamp release following the curing stage. This technique will be discussed in greater detail later in this chapter.

Optical photolithography is a commonly used technique [5.8-9] because it can provide very fast and cheap mass production. This simple technique is based on a special optically transparent material called photoresist. This special polymer material withers and becomes soluble (positive resist) or insoluble (negative resist) when exposed to UV radiation due to cross-linking of molecules. The last step of the process is to apply the solvent, which washes away any unwanted photoresist areas. The only problem is that it can be only applied to a limited number of polymers and requires a new mask for each waveguide design.

Electron Beam Lithography is a very attractive technique, mainly because it does not require any mask and provides high resolution but at the expense of being slow, expensive, and this generally not suitable for mass production. This technique is based on the practice of scanning a beam of electrons in a patterned way across the surface covered with a film (resist), then selectively removing either exposed or non-exposed regions of the resist. By using this technique, nano-scale features can be created in the resist that can subsequently be transferred to the substrate material. Direct laser writing is very similar to photolithography. The structures are created by illuminating negative-tone or positive-tone photoresist via light at a particular wavelength. The structural pattern is written in to the photosensitive photoresist by precise positioning of the laser focal point. The unsolidified remainder of the resist is then washed away by a solvent, leaving only the required structure. [5.10] One of the main advantages of this technique is that it does not require a mask. Moreover, it also allows for the creation of discrete 3D features without disturbing other regions. The laser ablation technique is based on irradiating the polymer material with a high intensity laser beam. As a result, the unwanted features are removed. This is a commonly used method in PCB

manufacturing for drilling in high density boards and trimming embedded resistors. Generally, 3 different types of laser are used, excimer ( $\lambda=248\text{nm}$ ), UV Nd: YAG ( $\lambda=355\text{nm}$ ) or CO<sub>2</sub> ( $\lambda=10.6\ \mu\text{m}$ ) [5.11]. The 248nm excimer laser is particularly suitable for this application due to the UV absorption properties of the polymer materials [5.11]. By using this technique, rapid prototyping is possible as opposed to mask based techniques. Moreover, it also allows for creating ablated features within restricted regions of a sample without affecting the surrounding regions and suitable for large production with 3D capability [5.12].

The advantages and disadvantages of the different methods are summarised in Table 5.1.

*Table 5.1. – Summary of different fabrication methods*

Fabrication Technique	Advantages	Disadvantages
Embossing	<ul style="list-style-type: none"> <li>• Suitable for core size above 100 <math>\mu\text{m}</math></li> <li>• Good for mass production</li> </ul>	<ul style="list-style-type: none"> <li>• Heating may change some properties of the material</li> <li>• Not suitable for all polymers</li> <li>• Embossing plate needs</li> </ul>
Nano-imprint Lithography	<ul style="list-style-type: none"> <li>• Submicron features</li> <li>• Good for mass production</li> </ul>	<ul style="list-style-type: none"> <li>• Limited high volumes instrumentation</li> <li>• Heating may change RI</li> <li>• Master stamp required</li> </ul>
Optical Lithography	<ul style="list-style-type: none"> <li>• Good for mass production</li> <li>• Good core feature quality</li> </ul>	<ul style="list-style-type: none"> <li>• New mask required for each design</li> <li>• Slow process</li> <li>• Not available for all polymers</li> </ul>
Electron Beam Lithography	<ul style="list-style-type: none"> <li>• No mask is required in advance</li> <li>• High resolution</li> <li>• Good for nm scale patterns</li> </ul>	<ul style="list-style-type: none"> <li>• Not suitable for mass production</li> <li>• Slow process</li> <li>• Not available for all polymers</li> <li>• Min. feature size: 5nm</li> </ul>
Direct Laser Writing	<ul style="list-style-type: none"> <li>• No mask is required</li> <li>• Rapid Prototyping</li> </ul>	<ul style="list-style-type: none"> <li>• High intensity laser beam might change the property of the material</li> </ul>
Laser Ablation	<ul style="list-style-type: none"> <li>• Milling Technology</li> <li>• No mask is required</li> </ul>	<ul style="list-style-type: none"> <li>• 3D capability</li> <li>• Thermal damage creating rough surface</li> </ul>

Each of the fabrication technologies have their own benefits and limitations. Advanced optical structures, such as Mach-Zehnder interferometers or sensors based on directional

couplers require great accuracy, whilst maintaining low cost and ease of mass manufacturability. Generally mask (or stamp) based techniques have a limited flexibility in terms of rapid prototyping, as a new mask is required for every design, whilst providing fast and easy production comparable to UV photolithography. Direct patterning techniques are usually more expensive and much slower. As a result, they are normally used for rapid prototyping as they provide a significant degree of flexibility, as they do not require a new mask every time the design is changed. In addition, recent advances in 3D printing of large core Ormocore waveguides [5.13] have created a new tool for 3D integration of photonic structures for electro-optic PCBs. However, it is still not applicable for high volume manufacturing.

Considering all the factors for the application, nano-imprint lithography is a good candidate for mass manufacturing chip scale photonic sensors. In the last decade it has been shown that it can provide high resolution patterning allowing the formation of advanced optical structures for both sensing and communication applications. A major part of this work reported here was to investigate, whether this fabrication method is applicable for siloxane polymer waveguide technology. In this chapter, the reader is guided through the development of nano-imprint technology for siloxane polymer material allowing ultra-high resolution fabrication, therefore the realisation of advanced photonic waveguide structures.

## 5.2 Standard fabrication technology for Siloxane waveguides based on UV photolithography

Polymer based integrated optics has been intensely researched due to its desirable properties. Cost-effective and functional optical devices can be realised suitable for mass production. Compared to silicon-based photonics, they provide higher flexibility and ease in terms of fabrication with their tailor made properties. Polymer materials have no restriction on the choice of substrate material, therefore complex integrated optical devices can be realised on any type of surface with ease.

Siloxane polymer materials for both core (OE 4140) and cladding (OE 4141) were supplied by Dow Corning. Traditionally optical waveguides based on Siloxane have been fabricated by UV photolithography. The fabrication process has been in development for a decade and have allowed the formation of several novel devices from PCB interconnects [5.14] to integrated gas sensors [5.15]. All of the designed devices were based on simple large core (50x50  $\mu\text{m}$ ) structures such as 90° bends, crossings, symmetric Y-splitters. Ying Hao worked

[5.8] on the development of single mode waveguide for 1550nm applications with limited success as her structures pushed the ultimate limitations of this fabrication technology based on photolithography. At the current state of development the process that is described in this chapter allows the formation of planar waveguide structures from 10  $\mu\text{m}$  to 100  $\mu\text{m}$  with a resolution of 5  $\mu\text{m}$ . This chapter section the basic principle of this process as well as how it was used to fabricate some larger structures for the application of microfluidic wells.

The process of patterning the photo sensitive siloxane resist is illustrated on Fig. 5.1. A standard 3 layered buried structure can be formed by the following process. The bottom cladding is created by first spin coating the cladding material on the substrate. The spin rate and time defines the thickness of the bottom cladding layer, while the viscosity of the polymer limits the maximum possible thickness. For all the processes described here the same 40% Toluene-Siloxane mixture was used. Increasing the concentration of Toluene in the mixture can yield lower viscosity and therefore thinner thin film thicknesses can be achieved. Following spinning, the toluene is evaporated by preheating the sample for 2 minutes at 110 degrees. After 3 minutes resting the sample is placed in the mask aligner for flood exposure. The length of the exposure is dependent on the film thickness and the strength of the UV lamp (typically 5-10 seconds). Following the UV exposure, the sample is hard baked (at 150 degrees) and rested again for 3 minutes. Once the bottom cladding is formed, the core material is spin coated and soft-baked. After 3 minutes of resting time, this is then followed by the UV exposure, where the necessary optical alignment is performed. After 5 minutes of resting, the sample is post baked for 1 minute at 110 degrees and place into a mesithylene bath for development for a few seconds. The solvent removes all unlinked material, leaving only the exposed features behind. After development and the necessary hard baking at 150 degrees for 30 minutes. The top cladding is deposited using the same process as the bottom cladding. Once all the layers are formed, then the sample is hard baked for an hour at 150 degrees.

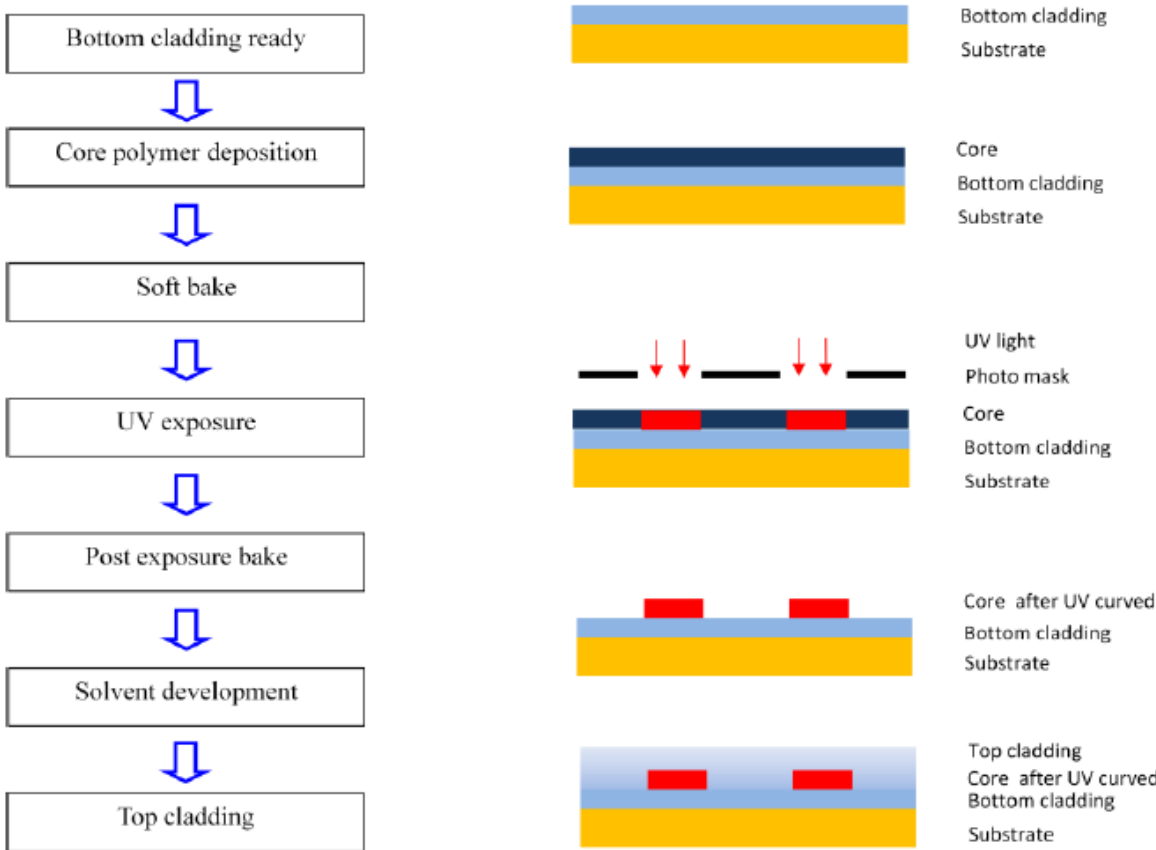


Figure 5.1 – Polymer Waveguide fabrication process using Optical Photolithography. [5.8]

Each step described above need to be optimised for different feature sizes and applications. As an example, the UV exposure time and development time are the most dominant factors, which needs to be adjusted for different dimensions. Fig. 5.2 shows the effects of overexposure and development. Overexposure can lead to a degraded verticality in the sidewalls, therefore increasing the overall cross section. Alternatively, leaving the sample in the development fluid for too long can result in a removal of material on the topside of the core.

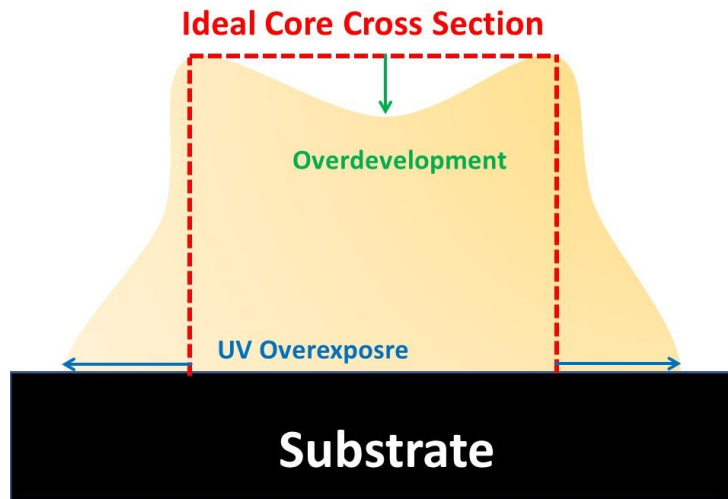


Figure 5.2 – Fabrication process non-idealities affecting the core cross section

This fabrication process has been very successful realising large core optical waveguides, where fabrication tolerance is a few microns. However, biochemical sensors operating in the visible range require features in the range of a few microns. For structures below  $10\ \mu\text{m}$  a very small proximity gap is required between the sample and the photomask. Moreover, the edge bead problem is also an issue as Ying described it in her thesis [5.8], as it is a result of surface tension while spinning.

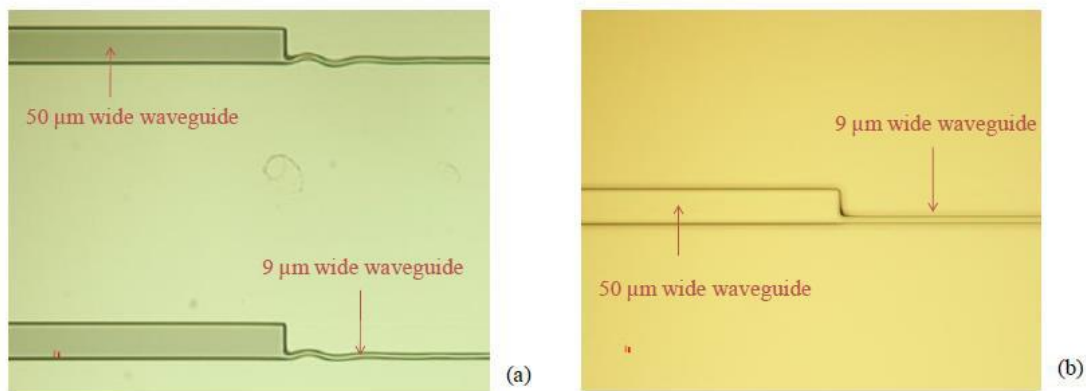


Figure 5.3 – Size comparison of standard large core structure with single mode at 1550 for (a)  $50\ \mu\text{m}$  and (b)  $20\ \mu\text{m}$  of proximity gap. [5.8]

Ying Hao [5.8] attempted to fabricate directional couplers for a Mach Zehnder interferometer with a  $9 \times 9\ \mu\text{m}$  single mode structure with a  $14\ \mu\text{m}$  coupling gap left between the arms. Fig.

5.4 clearly shows the ultimate limitation of this fabrication method, where the residual layer is left between the coupling waveguides.

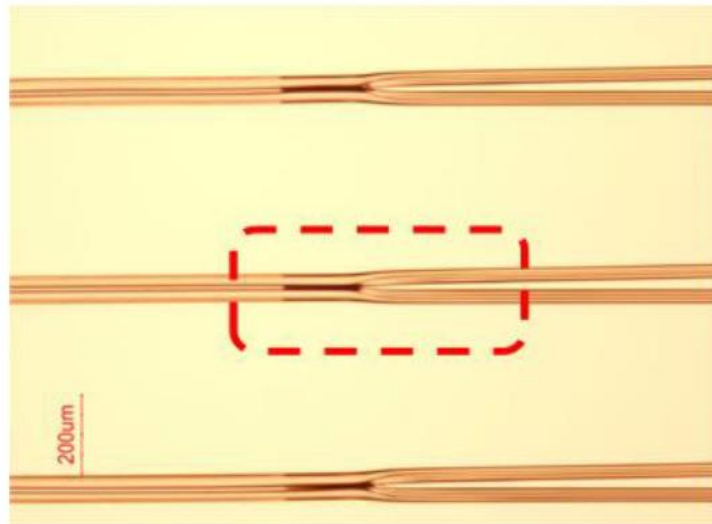


Figure 5.4 – Directional Couplers fabricated by Ying Hao illustrating the fabrication limitation for features below  $10\mu\text{m}$  for 3dB couplers [5.8]

However, photolithography is suitable for fabricating the large feature components on the lab-on-chip sensor such as the microfluidic channels and wells. Fig 5.5 shows the microfluidic wells that were formed on the sensor chip. The top cladding was patterned using a simple aluminium sheet as a mask. More details on this sensor will be discussed later in this chapter.

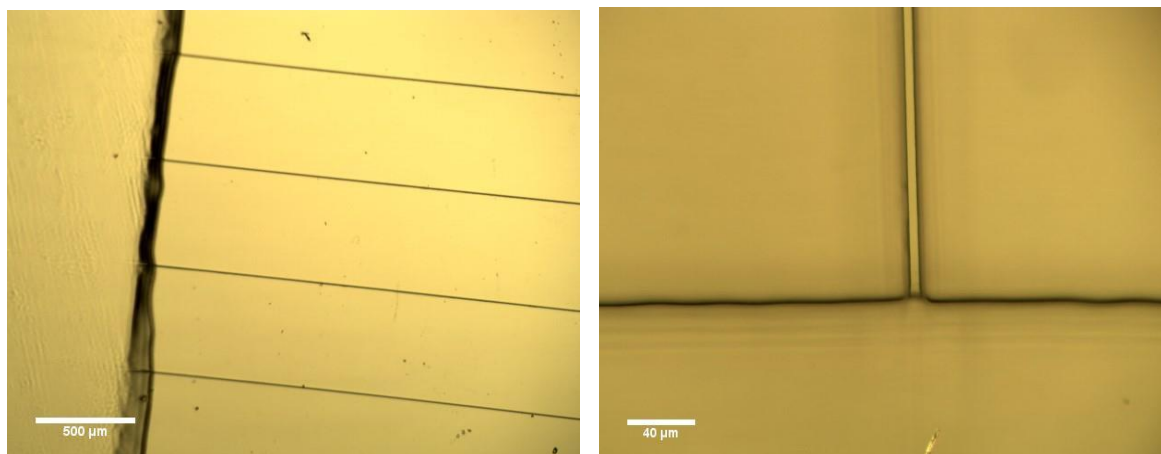


Figure 5.5 – Microscope image of siloxane based microfluidic wells over an array of optical waveguide cores made for brain fluid analyser project

Realising optical sensors based on single mode operation requires much higher fabrication resolution with features sizes between  $1\text{-}5\mu\text{m}$ . As a result, a new fabrication method had to

be adopted for the siloxane waveguide technology in order to realise the highly sensitive biochemical sensor designs.

### 5.3 Nano-imprint Lithography

Several lithographic techniques were discussed in the previous sections such as embossing or optical lithography. Nano-imprint lithography (NIL) has shown promising results in fabricating micro- and nano-structures in polymer thin-films. The basic process of imprinting waveguide structures is illustrated on Fig. 5.6.

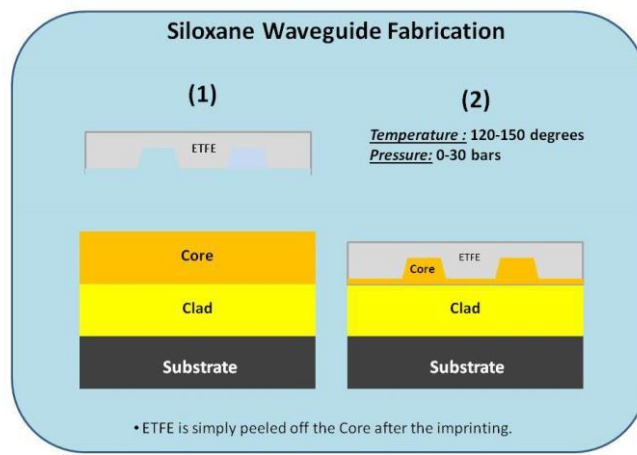


Figure 5.6 – Process of fabricating siloxane polymer waveguides using nano-imprint lithography

The bottom cladding is formed by standard photo lithography, while the core layer is formed by stamping to master mould (hard stamp) into the spin coated siloxane resist.

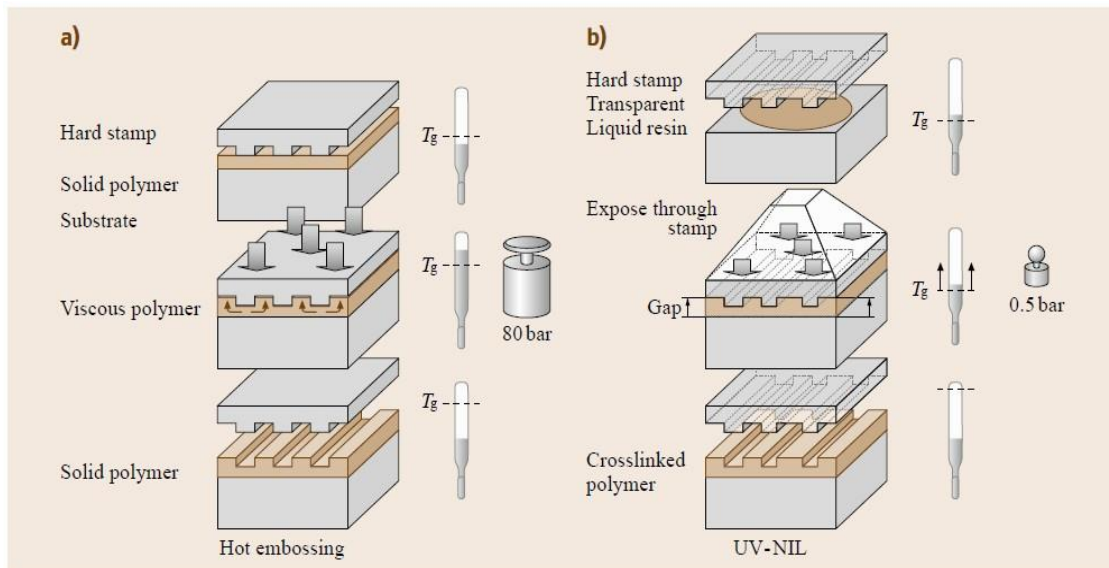


Figure 5.7 – Comparison between (a) Thermal and (b) UV NIL techniques illustrating the latter does not require high pressure or elevated temperature [5.16]

There are two main types of NIL processes depending on how the polymer is cured, as illustrated on Fig. 5.7. Thermal NIL is performed by heating up the polymer sample to its glass transition temperature ( $T_g$ ) and by applying pressure to emboss (or imprint) the patterns from the silicon or quartz hard mould. In the case of UV NIL, the curing is carried out by exposing the sample to UV light and therefore no heating is necessary. As a result, UV NIL is generally faster and does not require high pressure in contrast to thermal NIL, which may be important for some applications. On the other hand, the selection of available UV curable polymers is less [5.16]. Nevertheless, compact disks, magnetic disks and optical detectors have all been realized by both techniques.

The fabrication accuracy and quality is highly dependent on the material properties of the mould (or stamp), which needs to be mechanically, chemically and thermally stable. It has to retain its pattern structure at elevated temperatures up to 170 degrees and in some cases up to 10s of bar of pressure. Moulds are normally made of silicon, quartz glass or nickel, for which a high resolution patterning methods are available. NIL is a promising tool to transfer high resolution patterns from an expensive material onto to low cost and easily mass producible one. Inorganic stamps possess good mechanical stability, also inherently limit the efficiency of the pattern transfer. Hard moulds tend to break during demoulding as a result of the elevated temperatures and pressure damaging the polymer patterns. As result, Barbero [5.17] has proposed an interesting process, where Ethylen- Tetrafluorethylen (ETFE) is used as intermediate stamp. High resolution pattern transfer was achieved

due to the mould's mechanical stability and resistance to distortion at high pressure and high temperatures. The ETFE mould provided low surface energy and flexibility, which resulted in clean and easy mould release without deformation, which is often not the case with PDMS [5.17]. This mould is also reusable allowing simple and inexpensive reproduction providing an economical alternative to the current standard silicon based stamps. As a result, all the master stamps used in this work was based on ETFE material.

### 5.3.1 Master Fabrication

Nano-imprint technology allows high resolution pattern transfer from a master stamp onto an appropriate resist material. The patterns on the master stamp are usually produced by electron-beam lithography, allowing the formation of ultra-high resolution patterns followed by an etching process. The etching process is dependent on vertical feature dimensions, and generally either wet or dry etching is used. In the case of dry etching, normal reactive ion etching is often used for vertical features less than  $1\mu\text{m}$ , while deep reactive ion etching is required for anything greater than that. The optical waveguide features that were described in Chapter 3 and 4 were around  $3\mu\text{m}$  and therefore DRIE was the only option for creating good quality vertical structures. This technology allowed the formation of large trenches even up to 100s of micrometers in depth with an etch rate of  $3\mu\text{m}$  per minute. However, the speed and quality of the etching rate is highly dependent on the selectivity of mask, profile control and wafer-level uniformity. The target substrate is usually a silicon wafer. However newer etching tools are capable of etching polymer and quartz glass substrates.

The process used is based on the standard Bosch process, originally developed and patented by Robert Bosch. It is based on alternating etch and passivation cycles. The basic principle is showed on Fig. 5.8.

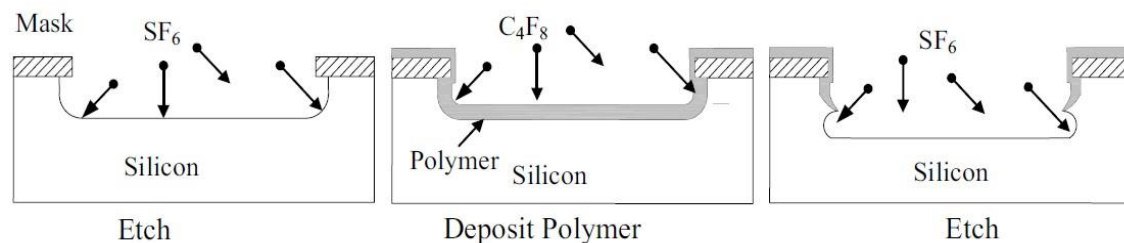


Figure 5.8. – Principle of Deep reactive ion etching process [5.18]

The first cycle is an ion-assisted etching of the silicon substrate by an etching gas ( $\text{SF}_6$ )

and the second is a sidewall passivation step using a polymer-producing gas (C<sub>4</sub>F<sub>8</sub>). The passivation cycle is necessary to coat the sidewall in order to prevent lateral expansion. In successive etching steps, both SF<sub>6</sub> and O<sub>2</sub> gas is used, where oxygen ions etch the bottom polymer while fluoride ions etch silicon at the bottom. As a result, the sidewalls remain protected by the polymer. The continuous repetition of this cycle is capable of achieving highly anisotropic through-hole etching.

Silicon Master Stamp Fabrication for the NIL process

The designed optical waveguide features were between 1.5-12µm wide and 3 µm high. This limited the patterning process to electron beam lithography as features below 3µm were difficult to achieve with high accuracy otherwise. The standard etching recipe (Fig. 5.10) created a very rough sidewall surface, resulting in increased light scattering in the transferred polymer structures. Thus, the etching recipe had to be tuned to maximise the feature quality in order to minimize surface roughness on the sidewalls and maximise verticality.

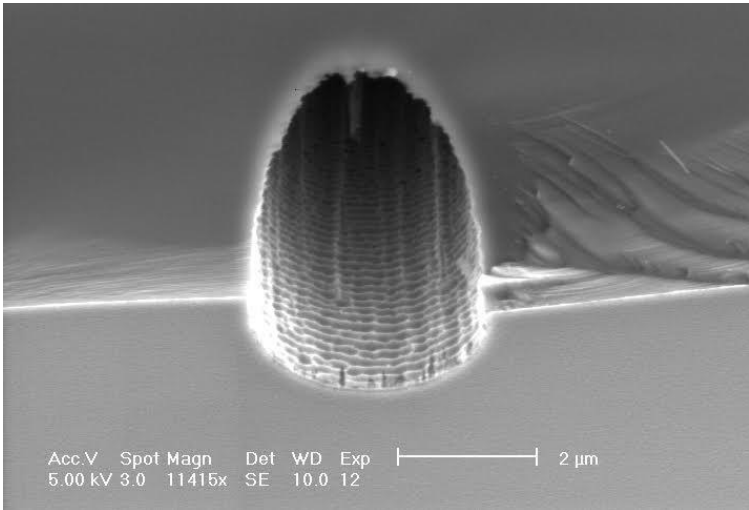
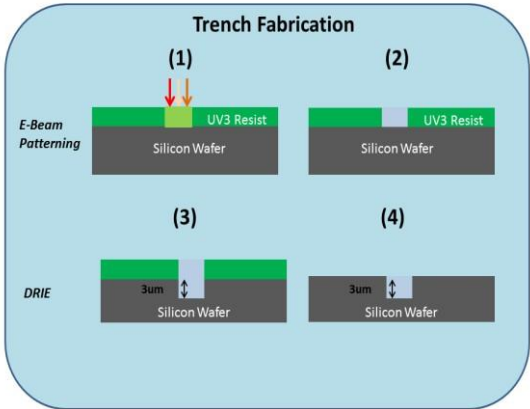


Figure 5.9. – SEM image showing rough cake layered sidewall

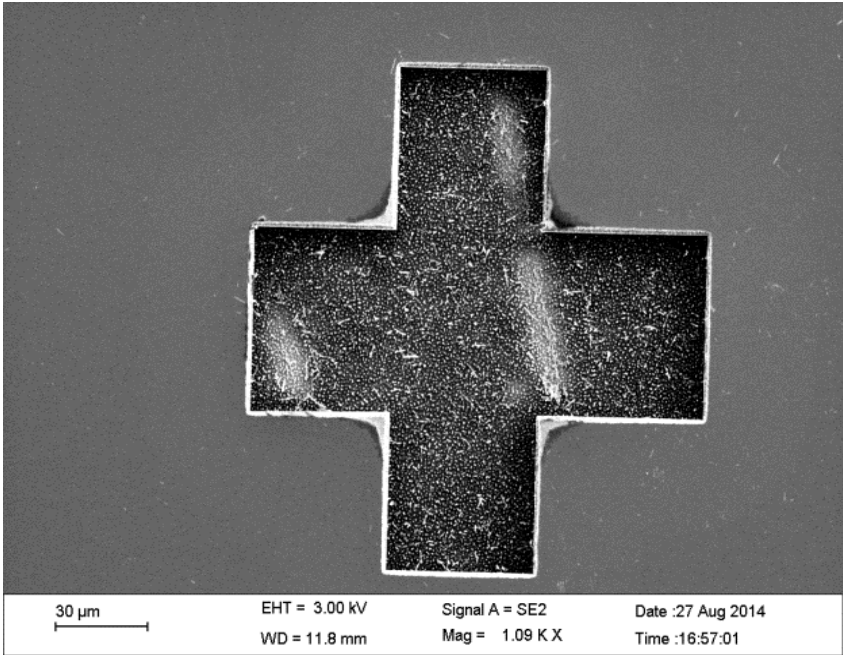
Table 5.2 - Standard Bosch Recipe

	SF <sub>6</sub>	C <sub>4</sub> F <sub>8</sub>	O <sub>2</sub>
Platen Power [W]	1500	1500	1500
Gas Flow [scm]	250	200	200
Temperature [Celsius]	10	10	10
Pulse Length [s]	3	2	2

Fig. 5.10 below shows the standard etching trial sample, a cross with 50 $\mu$ m arm widths and around 3 $\mu$ m depth.



(a)



(b)

Figure 5.10 – Silicon trench fabrication using standard Bosch recipe (a) and the fabricated sample (b)

For the recipe development, the silicon was first patterned by UV photolithography using AZ5214 negative resist, which has a selectivity of 1:4. The resist did not manage to withstand the etching process with good quality even though its selectivity should have been sufficient. The corners were badly damaged and highlighted the need for the deposition of a

hard mask with higher selectivity. A modified Bosch process was developed for ridge etching based on an Aluminium hard mask (Fig. 5.11). The silicon wafer was patterned by the EBL process based on a UV3 resist. Afterwards, 150nm of Aluminium was sputtered on the substrate using DC reactive magnetron sputtering followed by lift-off. During the lift-off process, the sample was placed in an acoustic resonator, where the polymer layer was gently peeled-off leaving the designed features on the wafer made of Aluminium. This way the desired features remained as ridges instead of trenches, however it also can be fabricated (inverted waveguide structures) by using an inverse resist, which was not available at the time.

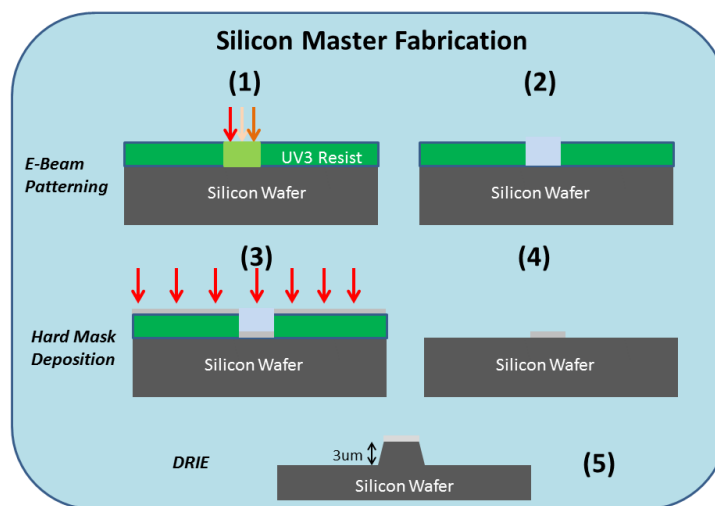


Figure 5.11 – Silicon master stamp fabrication based on (1-2) Electron beam lithography using UV3 resist followed by hard mask deposition (Aluminium) then (4) lift-off and (5) deep reactive ion etching.

The different gas exposure parameters were altered until sufficient quality was achieved. The etching rate had to be slowed down, in order to get sufficiently smooth sidewalls by reducing the platen power for SF<sub>6</sub> and shortening the pulse time. Fig 5.12 (a) shows the original recipe with rough sidewalls and (b) with the slow etching rate. Careful calibration of the C<sub>4</sub>F<sub>8</sub> and O<sub>2</sub> pulse time was required to adjust the sidewall steepness (~90°) and depth (3µm) to the application. The sidewall smoothness can be adjusted by increasing the C<sub>4</sub>F<sub>8</sub> and O<sub>2</sub> flow rates from 200 sccm to 250 sccm and reducing the SF<sub>6</sub> rate

to 200 sccm.

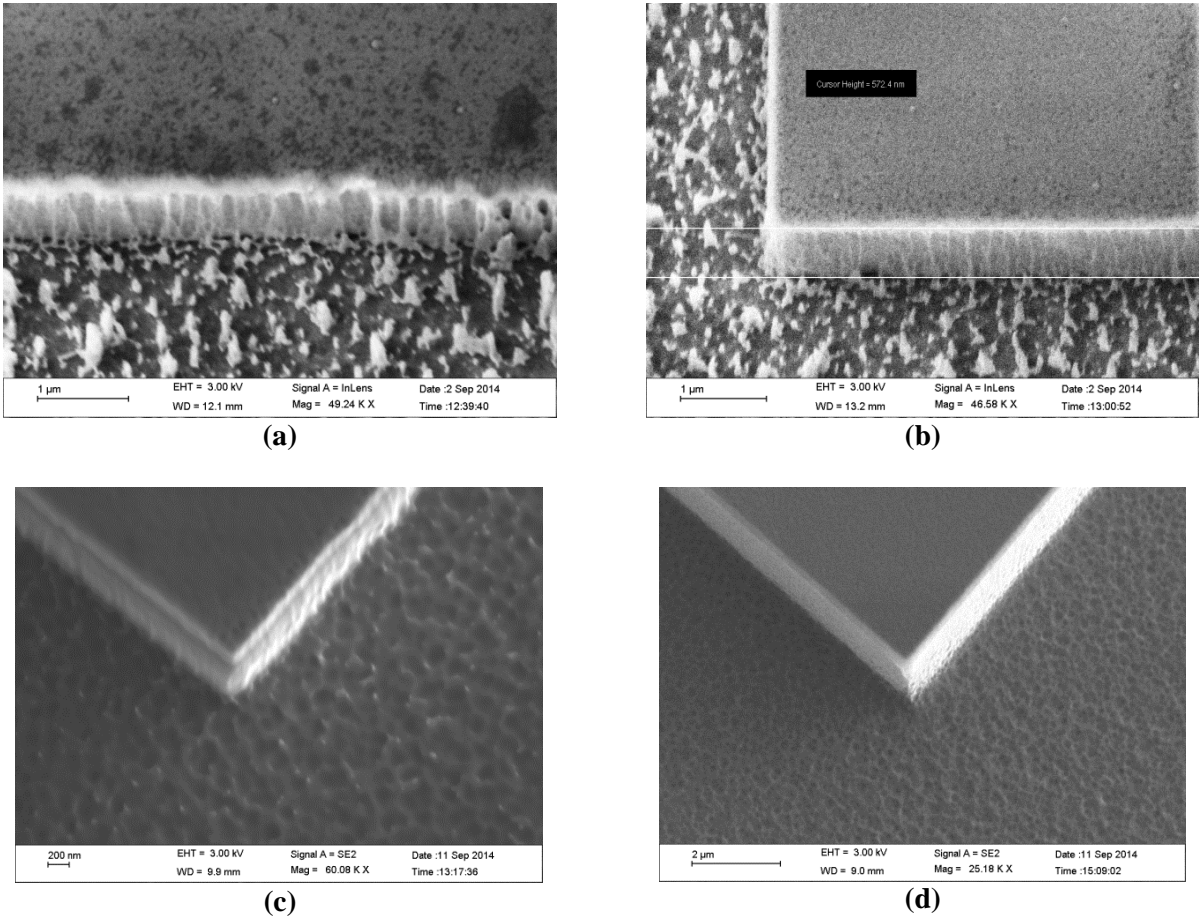


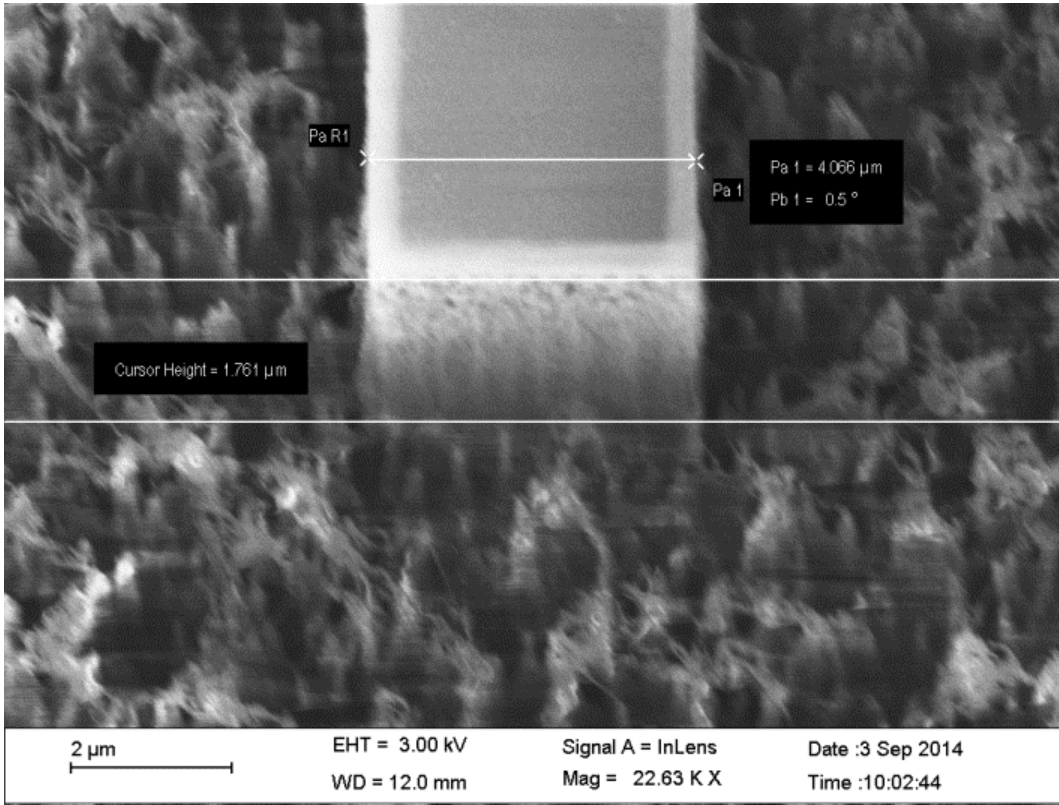
Figure 5.12 – Sidewall quality optimisation by adjusting flow rate (a,b) and pulse time (c,d)

The standard pulse time (3 seconds) for 3 μm per minute etching left distinct layered structures. The pulses had to be shortened significantly in order to achieve an acceptable sidewall quality. Another important parameters was the process temperature, which can affect both etching rate and limit the maximum achievable depth as it can significantly reduce the metal selectivity.

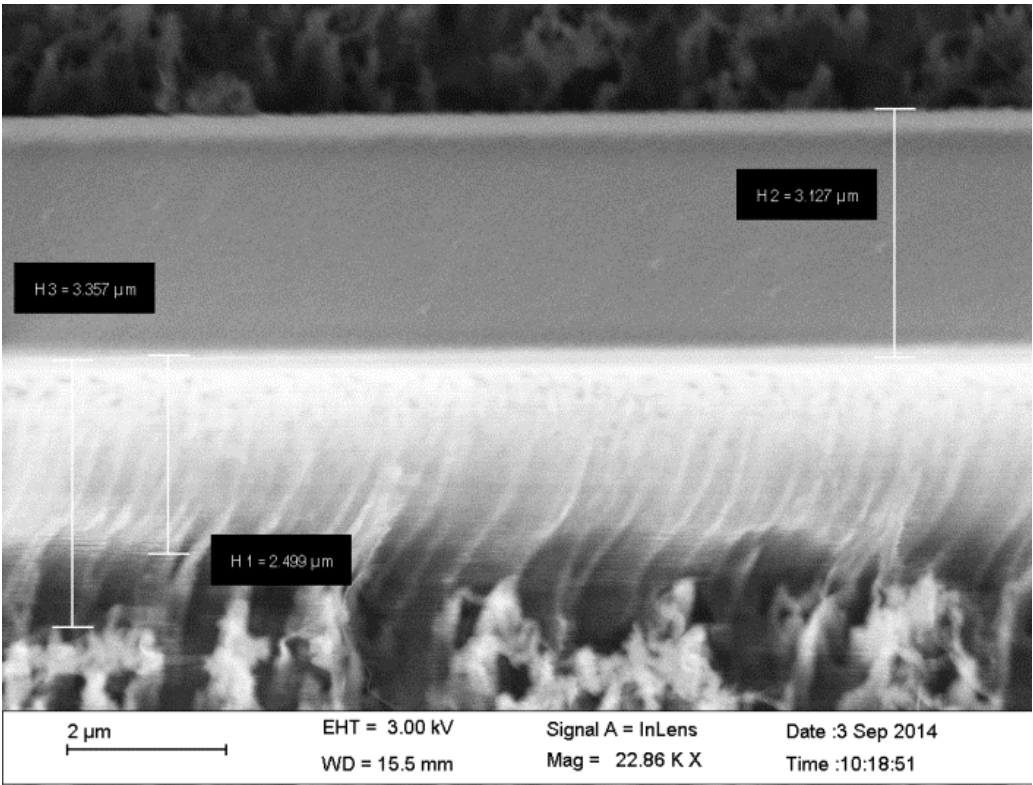
The optimal etching rate was found to be 600 nm per minute using the etching formula described in Table 5.3 below. The final process produced features good quality waveguide feature and corners remained sharp and the sidewall verticality was almost perfect at 89° (Fig. 5.13).

Table 5.3 – DRIE etching recipe

	SF <sub>6</sub>	C <sub>4</sub> F <sub>8</sub>	O <sub>2</sub>
Platen Power [W]	1100	1100	1100
Gas Flow [scm]	200	200	200
Temperature [Celsius]	10	10	10
Pulse Length [s]	1	1.5	1.5



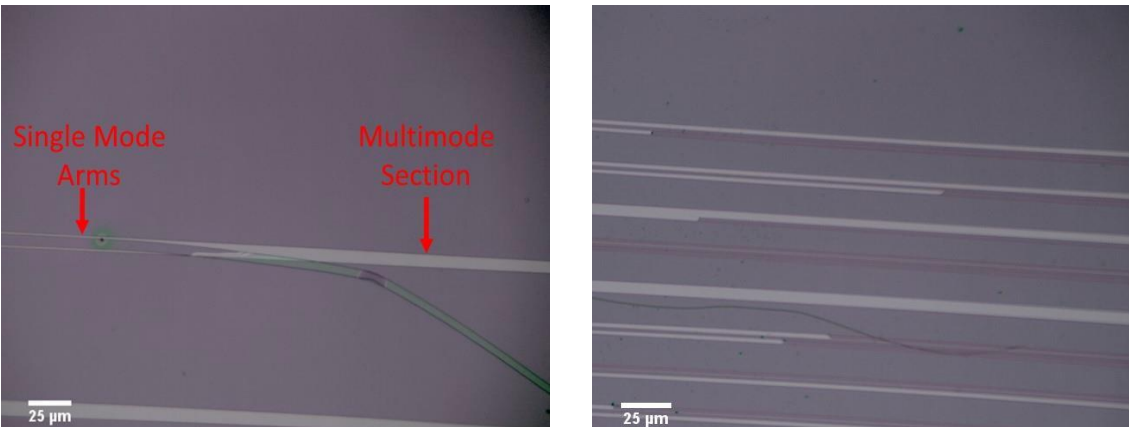
(a)



(b)

Figure 5.13 – Single mode optical waveguide features patterned on silicon substrate, (a) cross section view, (b) sideview

The fabrication of the designed asymmetric junctions were more difficult as the previously used recipe for the EBL did not manage to create the desired junction quality (Fig. 5.14).



(a)

(b)

Figure 5.14 – Microscope images of damaged asymmetric Y-junctions patterns on silicon, (a) broken arm at the tip of the junction, (b) resulting damaged waveguide junction array

Unfortunately, the features were damaged following the development process. The tip of the junctions, where the two arms join together, peeled off the surface at every trial. The most likely cause was the low adhesion of the UV3 resist to the silicon substrate. Another attempt was made using UV photolithography and AZ5214 resist. Fig. 5.15 showing the quality of the Aluminium patterns following the lift-off process.

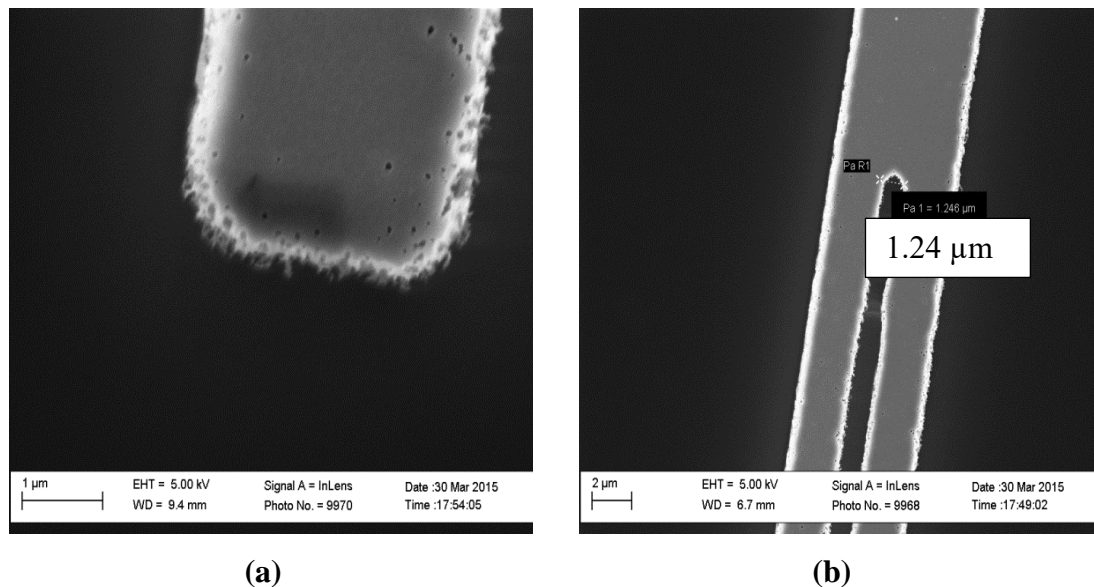


Figure 5.15 – SEM images of asymmetric Y-junctions patterned into silicon substrate, (a) tip of the junction, (b) rough waveguide edges

This time most of the tip of the junctions remained. However, they were much thicker than originally designed. Moreover, the edge of the aluminium was torn creating a very rough surface around the edge of the features. Such a rough sidewall would have translated into a very rough sidewall quality following the DRIE process. These non-idealities would have also got transferred into the polymer and result in significant light scattering in the waveguide and very poor mode coupling performance. Therefore, until the source of this issue is found no further progress could be made.

### 5.3.1 Siloxane polymer based single mode waveguides fabrication and characterisation

The final aim of the fabrication development was to increase the polymer waveguide fabrication resolution by using the NIL process. The previously discussed waveguide structures such as single mode ridge and inverted structures, were patterned onto silicon wafers. The previous section discussed the process development as well as the technology. In order to use the patterned silicon samples as master stamps, it was necessary to carry out

silanisation [5.19]. The purpose of this step is to reduce the surface energy of the silicon sample and allow ultra-high resolution pattern transfer. The overall process is shown on Fig. 5.16, where the silicon patterns are transferred from silicon to an intermediate fluoropolymer.

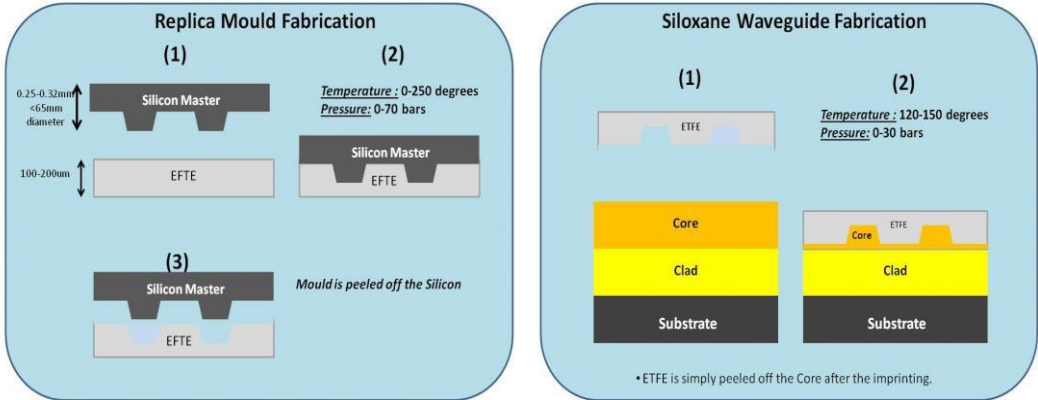


Figure 5.16 – Schematics of polymer waveguide fabrication based on NIL using ETFE replica mould

Replica Mould Fabrication Process

The intermediate polymer can be any soft polymer, which has a higher glass transition temperature than the target polymer. In the case of UV NIL, this requirement is not an issue. ETFE was the first choice of material, as it was shown to have superior material properties compared to PDMS [5.17]. The glass transition temperature of ETFE was 150 °C, while it is 110 °C and 130 °C for the cladding and core siloxane polymer material respectively. The process phases are described on Fig. 5.17, following where the sample is placed in the Obducat Nano Imprint Lithography system.

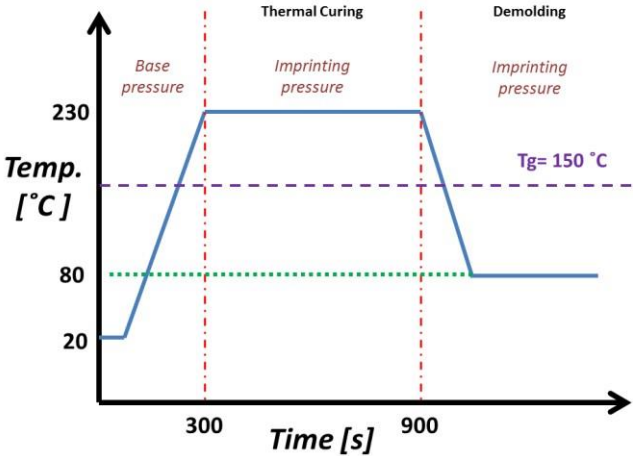


Figure 5.17 – Silicon to ETFE pattern transfer based on Thermal NIL process

The ETFE thin film is cut and placed on the silicon sample. The area of the ETFE has to be less than the silicon, otherwise the ETFE film will bend downwards at the edge of the silicon stamp and therefore upwards in the middle of the area where the patterns are, thus introducing an uneven patterning. A guard period has to be introduced, which should be greater than 5mm from the edge of the stamp in order to maintain high quality pattern transfer. Before placing the ETFE thin film in the silicon stamp both surfaces have to be cleaned by water and IPA in order to remove any dust particles. Once they are placed in the imprinting machine, the temperature is increased to 230 °C while the pressure is kept at base (2-5 bars). Once the set temperature is reached the pressure is increased to 30 bars for 600 minutes, which are the required conditions for the ETFE to take on the shape of the silicon stamp. Following the imprinting phase (Fig. 5.7) the sample is slowly cooled down to the demoulding temperature, at which point the sample is removed and cooled down further to ambient temperature before being peeled off the silicon stamp. Fig. 5.18 shows the SEM image of the master silicon stamp and the resulting patterns on ETFE.

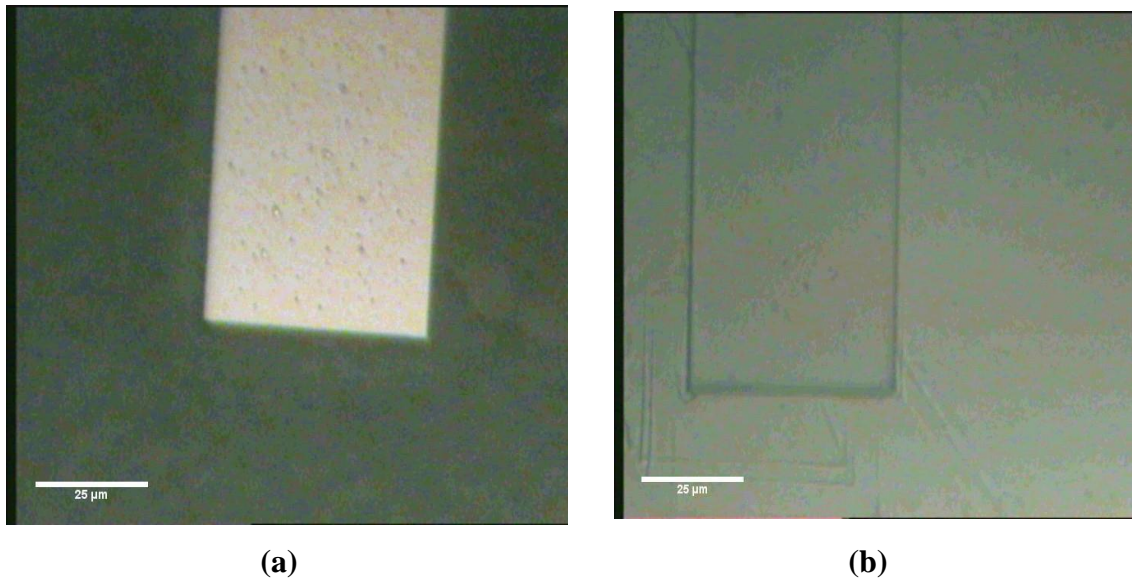


Figure 5.18 – Waveguide feature transfer from (a) silicon to (b) ETFE thin film

The SEM images on Fig. 5.19 illustrate the result of process development. Fig. 5.19 (a) showcases the quality of trenches at the beginning of the project, where the imprinting pressure and temperature was not optimised. The second image (b) shows an improved rectangular cross section with distinctive vertical sidewalls, matching the original 4 μm dimensions.

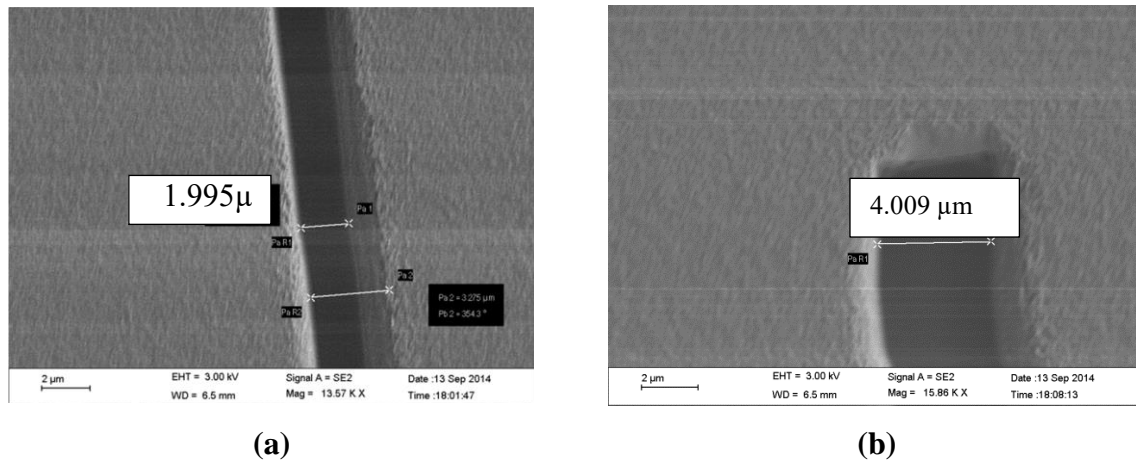


Figure 5.19 – Replica mould process development showcasing (a) before and (b) after images

### Siloxane Waveguide Formation

Once the patterns are transferred to the ETFE thin film, it can be used multiple times as a stamp for the polymer transfer phase. As it was described in [5.17], low viscosity polymers

do not require high pressure or elevated temperature (in case of UV curing). This is due to the fact that resistance to flow increases with the viscosity of the polymer, which can be compensated by increasing the embossing temperature. Also due to the micron size features it can take longer for the polymer material to fill in the ETFE cavities compared to standard nano imprinting recipes [5.20]. Therefore the fabrication development of single mode optical waveguide structures were carried out in two different ways.

The used substrate in each case was a 2” Dow Corning quartz glass, which was coated with the bottom cladding material using the same recipe described earlier forming an approximately 20µm thick cladding layer. The single mode siloxane core material was coated at 2000 RPM followed by prebaking at 110 °C for 2 minutes.

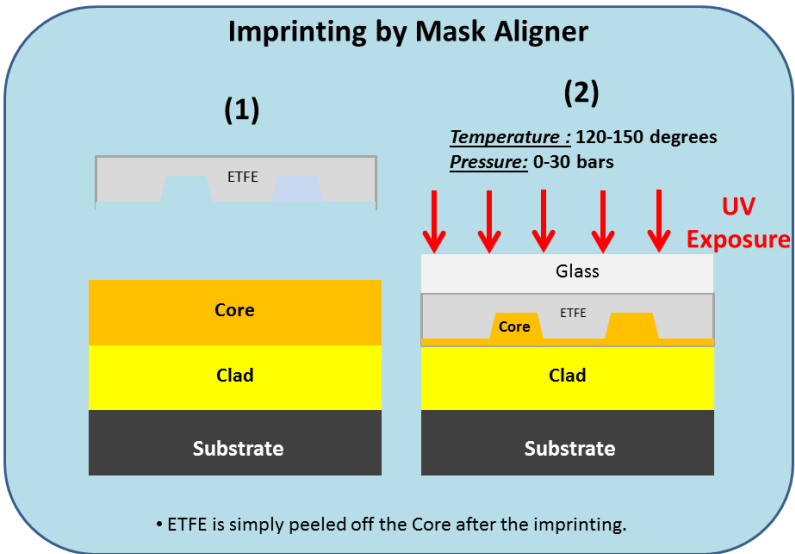


Figure 5.20 – Imprinting process by mask aligner

First the imprinting was performed by a mask aligner (MJB4) in hard contact mode, which allowed fast UV curing of the samples. Pre-processing was required in order to evaporate all the solvent from the resist (Toluene), which would otherwise happen during thermal curing forming bubbles in the polymer as gas molecules would be trapped between the mould and the resist (Fig. 5.21 (a)).

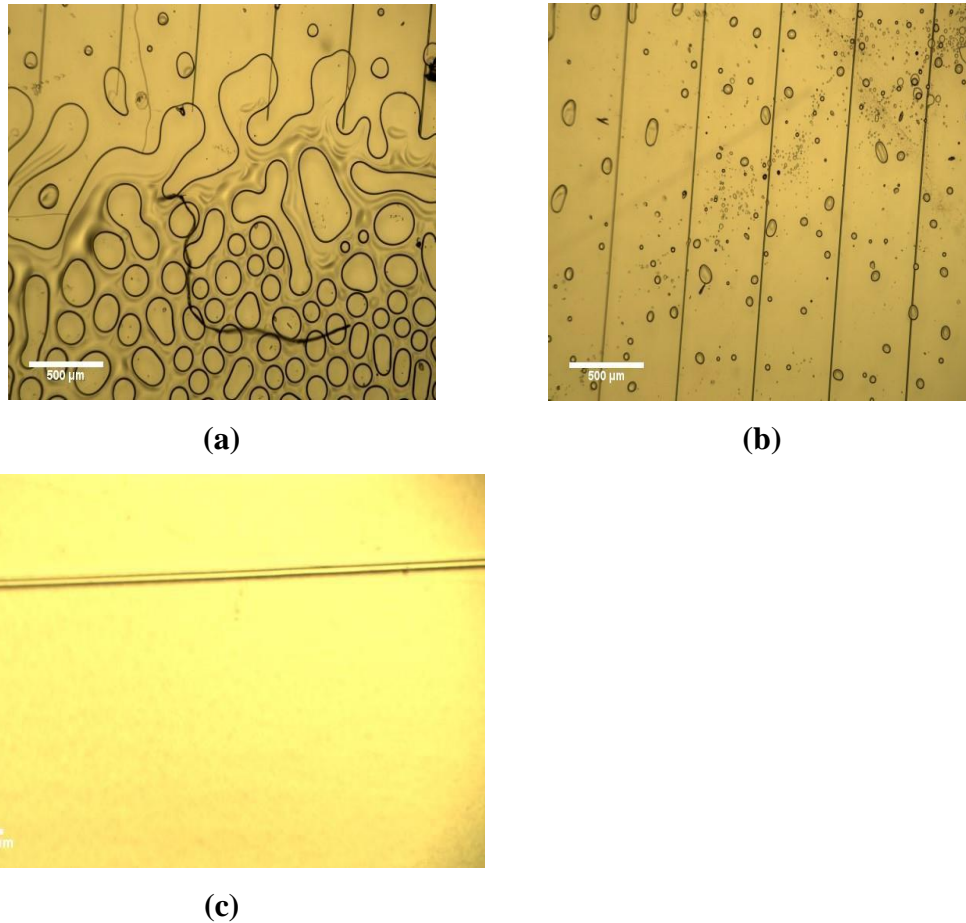


Figure 5.21 –Imprinting process development, (a) gas bubbles due to non-ideal curing, (b) shorter curing time, (c) fully developed sample after vacuum treatment

Vacuum treatment was necessary in order to pull out all the oxygen bubbles trapped between the mould and the resist as the attachment was done manually. This issue was resolved by placing the sample in a vacuum chamber or desiccator and applying a strong vacuum using a turbo pump several times. However, still some microscopic bubbles remained (Fig. 5.21 (b)) as a result of degassing of the resist during the UV exposure. These gases normally left the material during UV photolithography as no enclosure was containing them in the materials, however in our case the mould almost completely enclosed the resist material. By appropriate prebaking and optimised short UV exposure this effect was minimised (Fig. 5.21 (c)).

However, the actual pressure control was not precise and allowed limited dynamic range. The field profile image is shown on Fig. 5.22, it illustrates the problem when low pressure is applied. As the pressure is not sufficient, a residual layer is formed below the core decreasing the light confinement.

The rectangular ridge waveguide core turned into a slab waveguide. Therefore, it was necessary to employ thermal NIL by using the Obducat Nano-imprint instrument.

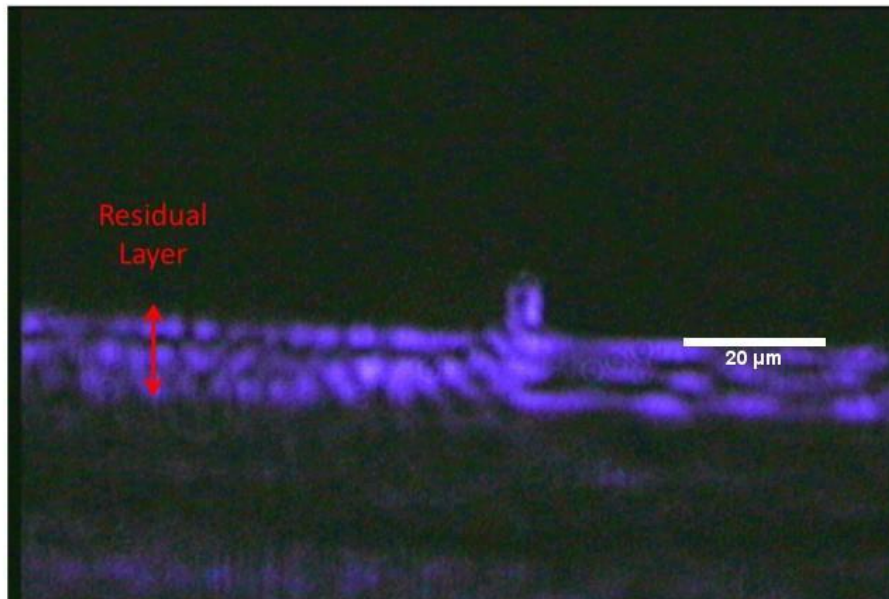


Figure 5.22 – Intensity field profile of siloxane waveguide core fabricated by UV NIL using a mask aligner (MJB4) indicating large residual layer

This allows precise pressure and temperature control over a wide range, between 1-50 bars and 20- 250 °C, respectively. The embossing recipe was developed by varying both temperature and pressure as well as the pre-processing conditions for the polymer resist.

Fig. 5.23 shows the embossing process graph of the imprinting.

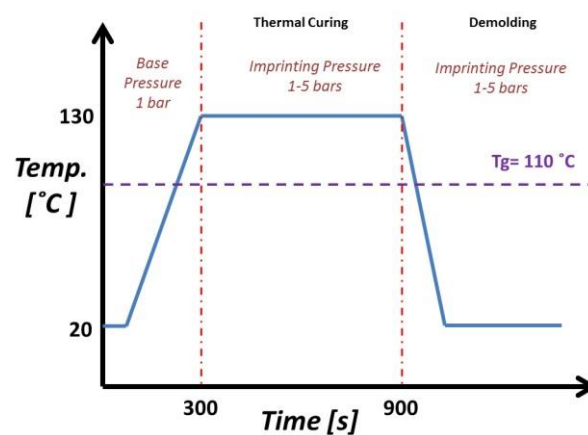
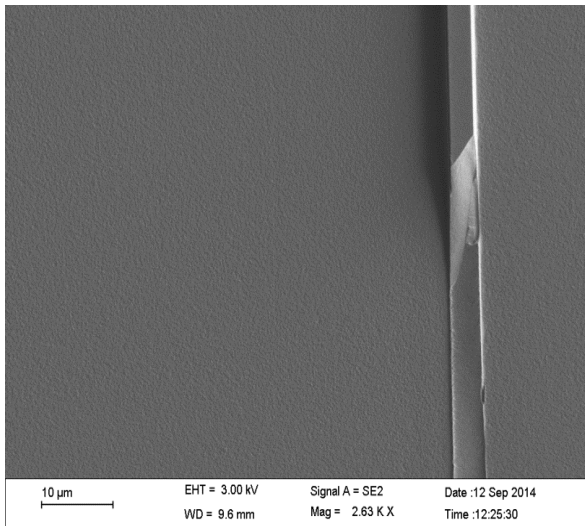
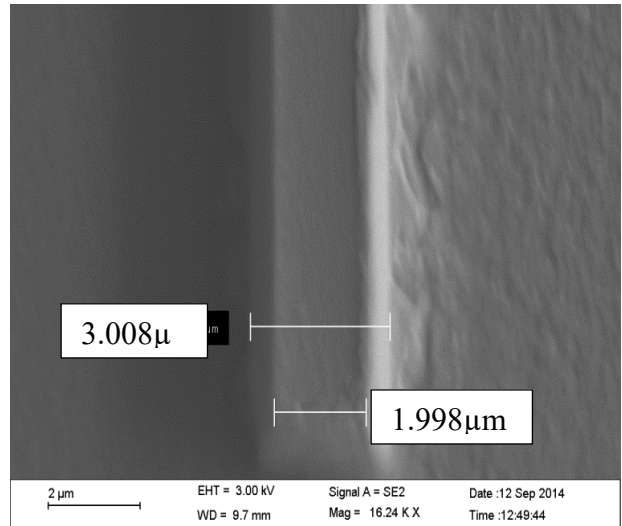


Figure 5.23 – ETFE to siloxane polymer imprinting process

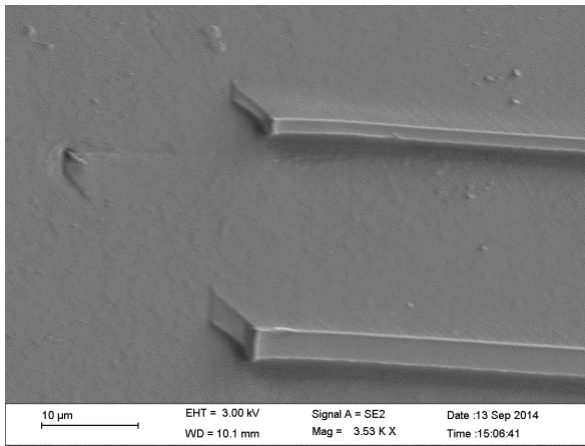
The polymer is kept at base pressure until the imprinting pressure is reached at 130 °C. The length of the thermal curing was tested between 180-600 seconds in order to find the shortest required embossing time. Demoulding too early results in feature distortion (Fig. 5.24) and often breaks the features off the substrate.



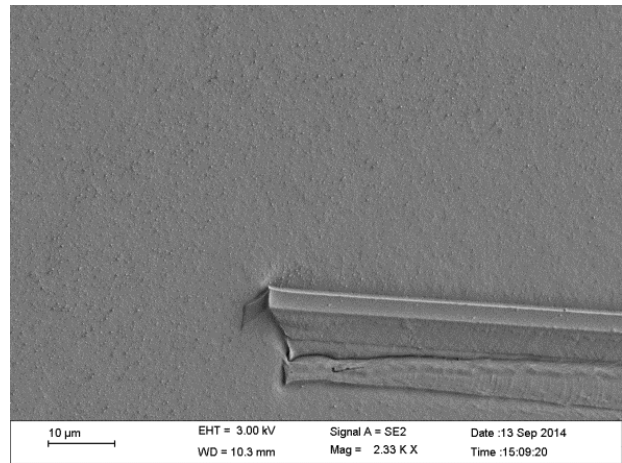
(a)



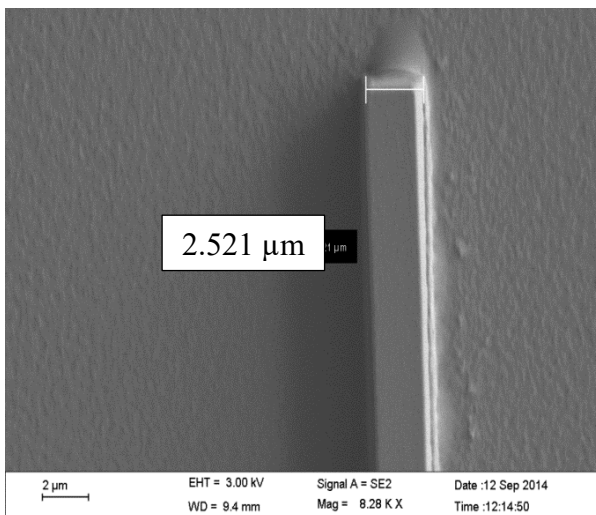
(b)



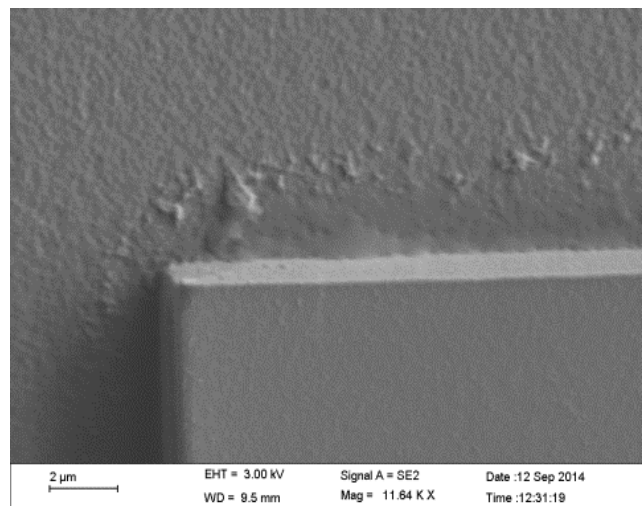
(c)



(d)



(e)



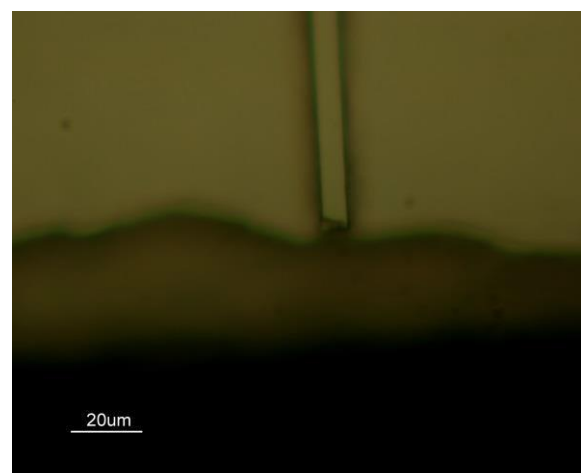
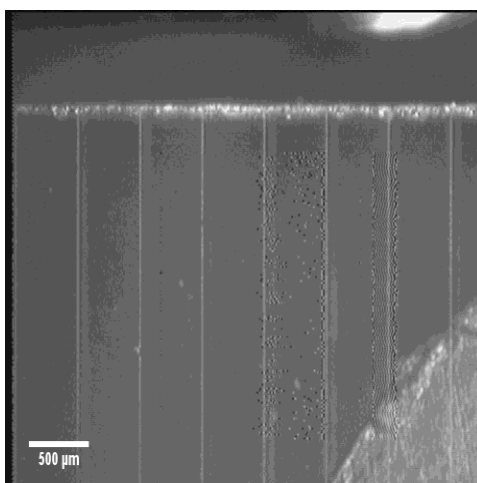
(d)

Figure 5.24 – Images illustrating issues with (a) early demolding and (b) deformation of features, while

(c-d) show issues with mould mechanical instability, (e-f) shows the samples with ideal recipe

The polymer waveguide features were often distorted until the recipe was optimized, especially the waveguide ends and corner structures. The ETFE mould appeared to be resilient to mechanical pressure only if its thickness was optimal for the particular structure. Most of the waveguide features were  $3\mu\text{m}$  deep and it was found that the minimum ETFE thickness required for reliable pattern transfer was  $250\mu\text{m}$ . Fig 5.24(c-d) shows the features when a  $200\mu\text{m}$  thick mould was used which could not withstand the mechanical pressure that was applied. The optimal temperature for curing the siloxane polymer was  $130\text{ }^\circ\text{C}$  at 1.8 bars for 600 seconds. Fig 5.24. (e-f) shows (SEM images angled point of view) the final waveguide features with high quality corners and high resolution pattern transfer. The quality of fabrication these feature sizes was significantly better than the standard UV photolithography process.

One of the main issues with the characterisation of the fabricated waveguides were the lack of an appropriate dicing tool. Normally dicing was carried out by a MircoRace Series 3 dicing saw. Due to the built-in microscope in the instrument, it allowed both buried and ridge waveguide features to be clearly seen as well as the dicing markings. A diamond blade was used for dicing the silicon or glass wafer along the dicing markings. However, limited access to the instrument did not allow proper process optimisation for these samples. Therefore, only the standard recipes could be used which were normally used for the large waveguide core samples. Fig. 5.25 (a) shows a waveguide array following dicing leaving a very rough end facet. Ying [5.8] performed a polishing after the dicing which improved the quality but not sufficiently. For edge-fire coupling the facet of the waveguide has to be as smooth as possible and have vertical sidewalls in order to minimize the coupling loss. However, the dicing saw often broke off the polymer layer Fig. 5.25 (b-c) and damaged the waveguide core.



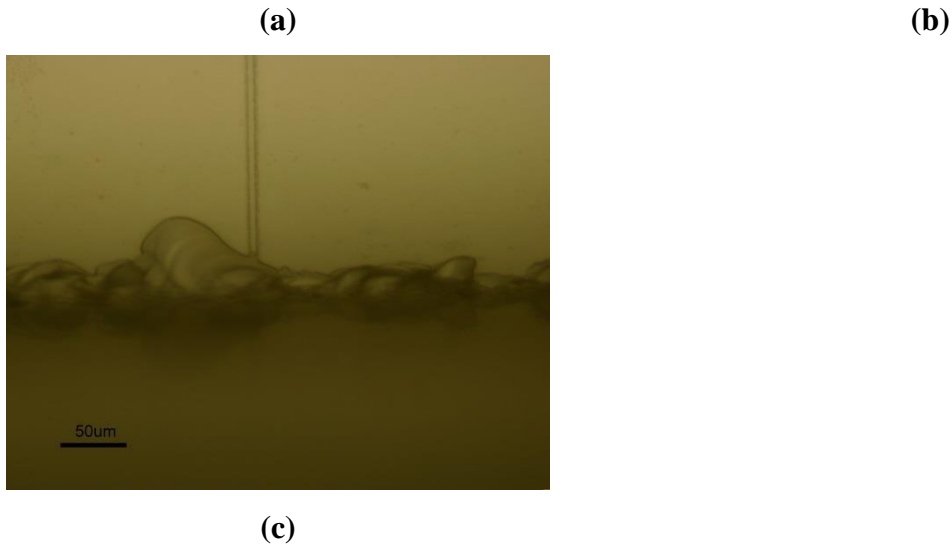


Figure 5.25 – Microscope images (top view) of the waveguides (a-c) following the standard dicing procedure using Microrace Series 3 dicing saw.

The low-quality end facet resulted in significant coupling losses and light scattering, ultimately limiting the quantitative characterisation methods. Dicing method optimisation was not an option as the instrument had limited accessibility and it was out of order for several months. As a result, an alternative method was required to dice the polymer waveguides.

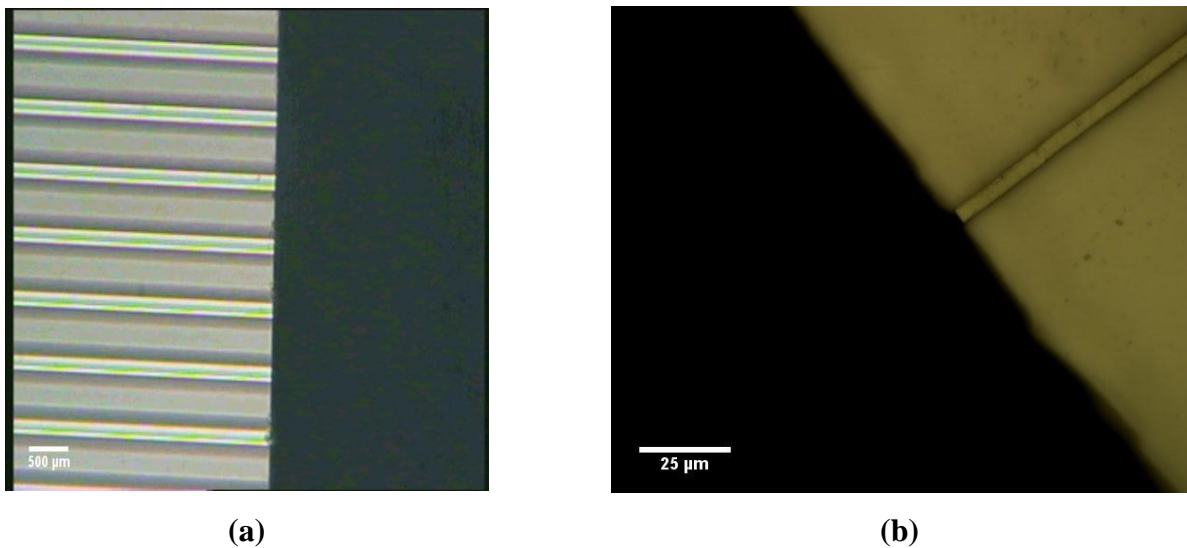


Figure 5.26 – Microscope Images showing the polymer waveguide samples cleaved by hand using a diamond cutter.

In order to overcome this issue, the polymer waveguide features were transferred onto a silicon substrate with 100 orientation, which allowed it to be cleaved by hand using a diamond cutter. The wafers were carefully cracked at two opposing straight end parallel to each other and the crack was guided through the surface snapping the whole wafer. Through observation, it was concluded that the

total polymer layer thickness have to be less than  $100\mu\text{m}$  in order to be snapped successfully at a reasonable quality. On Fig. 5.26 (a-b), the resulting waveguides can be seen illustrating the difference between the two methods. Unfortunately, it was still difficult to cut the features perpendicular to the straight waveguide, often leaving an angled end facet.

### 5.3.2 Siloxane polymer waveguide measurements

The fabricated optical waveguides and its light confinement characteristics were inspected by field profile measurements (Fig. 5.27). Light was coupled into the waveguides using edge-fire coupling. Single mode fibre was used for coupling the light from a GaN laser diode operated at  $425\text{nm}$ . The light is collected by an objective lens with  $50\times$  magnification followed by a CCD camera to observe the intensity profile image at the end facet of the waveguide. In the case of the light absorption measurement the camera was replaced by a multimode fibre before connected to the light power meter.

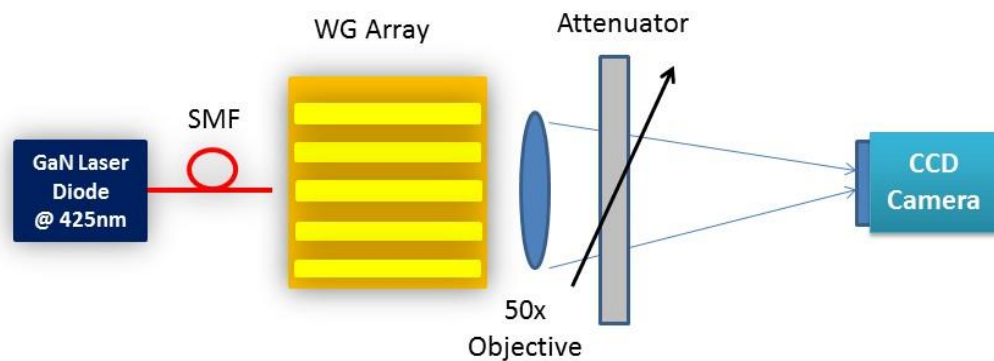


Figure 5.27 – Experimental Setup for intensity profile measurement

The field profile images are shown on Fig. 5.28, field intensity profile (Fig. 5.28 (b)) at the end facet of a  $2.5\times 3\mu\text{m}$  waveguide.



Figure 5.28 – Intensity field profile of (a) 2.5x3 and (b) 3x3  $\mu\text{m}$  siloxane ridge waveguide captured on a CCD camera at 50x magnification

The nearfield 3D intensity plot of Fig. 5.28 (b) is shown on Fig 5.29, where both horizontal and vertical intensity is plotted in respect to the centre of the waveguide. The curves are not clearly Gaussian as there are artefacts present that might be due to poor quality dicing as well as some higher order modes still being present.

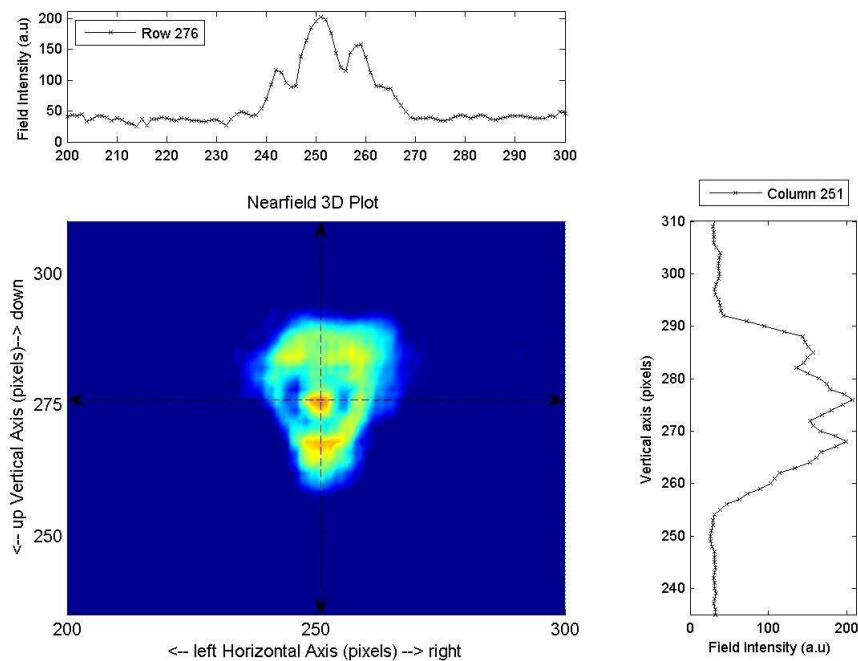


Figure 5.29 – Nearfield 3D intensity plot of the light intensity captured at the end facet of single mode waveguide

The received power level levels on a 2 cm long waveguide array with 3  $\mu\text{m}$  height and 2.5-5  $\mu\text{m}$

width waveguides are represented on Fig. 5.25. The GaN laser diode coupled -5 dBm into the waveguides via the single mode optical fiber. The optical power for each of the waveguides in the array were measured (Fig. 5.30). Waveguides with the largest cross section (5x3  $\mu\text{m}$ ) had 27 dBm power loss, while the 3x3  $\mu\text{m}$  waveguide had a significant power loss of -43 dBm. The smallest waveguide having the cross section of 2.5x3  $\mu\text{m}$  had the lowest optical power very close to the background signal level at -56dBm, therefore it was hardly guiding any light.

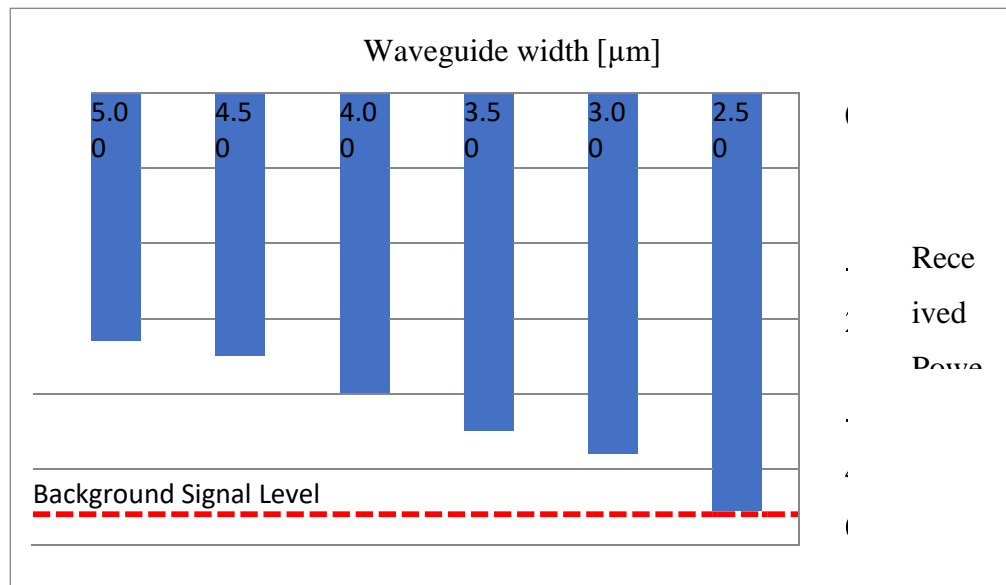


Figure 5.30 –Waveguide transmission measurement for an array of siloxane waveguide (2.5-5 $\mu\text{m}$  wide and 3 $\mu\text{m}$  high)

This section of the chapter has summarised the development process of a novel fabrication technology for siloxane waveguide technology allowing the implementation of single moded waveguides. The designed optical waveguide patterns were fabricated acceptable accuracy and good sidewall quality. The rest of chapter describes how these siloxane-based waveguides were used for monitoring biochemical reactions in a lab-on-chip architecture.

## 5.4 Investigation of siloxane polymer waveguide technology for brain fluid analysis

The main goal of presented work in this chapter is to investigate the possibility of using siloxane polymer based optical waveguides for biochemical sensing. The aim of this pilot project was to develop an optical sensor capable of measuring glucose, lactate and pyruvate concentration in an aqueous environment native in the brain. First, the development of a novel porphyrin-based recognition layer will be discussed. The reader is guided through the investigation of different

chemical reactions tested for all the analyte of interest. At the beginning of the project a literature review was carried out in order to identify the most applicable sensing technology and dye compound for each of the target analyte. The summary of this review can be found in the Appendix (Chapter 6).

A lot of the mentioned sensor designs were based on high refractive index materials such as silicon. Group III-V material-based sensors have also played a major role in the development of integrated photonic sensor systems. This is mainly due to their high optical confinement and extremely small dimensions, allowing highly sensitive and compact devices to be realised. Low index materials based on polymer materials are becoming an attractive choice due to their low production and development cost as well as favourable loss characteristics compared to silicon in the visible optical range. Low index materials also provide higher chemical flexibility as they can be easily functionalised for different binding agents. Fabricating materials and structures based on polymers are cheaper and more available than their silicon counterparts as simple photolithography and nano-imprinting can be used with matching accuracy. Not to mention the fact that polymer materials are more environmentally friendly and require smaller efforts in their disposal.

The technology review in the Appendix provided an insight into the most frequently used recognition elements for all the three analytes. A short literature is provided in order to gain insight into the most promising glucose, lactate and pyruvate sensors highlighting the lack of attention paid to pyruvate and lactate sensing. Oxidase and Decacyclene complexes, such as Pt(II), Pt(II), Ruthium dyes are the most widely used for both fluorescence and absorption sensing, but require the sensors to be operated in the visible range for both excitation and detection. Porphyrin based recognition layer have showed promising results [5.21] with a fast reaction time operating at 420nm wavelength.

The choice of recognition element defines the required operating wavelength, which in turn also defines the required (and available) light source. Almost all the siloxane-based waveguides have been developed for optical interconnect technology with large dimensions around 50x50  $\mu\text{m}$  cross section operated at 850nm wavelength. There even the simplest structures such as junctions have to be developed and designed specifically sensor operating wavelength, which in this case is 425nm. It would require tremendous amount of work and time, therefore the described research in this thesis have focused on making simple single mode waveguide structures and enhance their sensitivity to the required level by developing advanced surface functionalization and using some of the mentioned features such as slot waveguides or using high index materials as a substrate. Moreover, developing high quality recognition element was the most important part of the development process as it is discussed in the next chapter.

### 5.4.1 Introduction to Porphyrins

The word porphyrin is derived from the Greek word of *'porphura'*, which mean *'purple'* as most of the porphyrin materials have a strong purple colour. These molecules are abundant in nature and have essential functionalities in life [5.22-23]. Metalloporphyrins, in particular can be found in various biological systems, where they play essential roles. For example, in nature they provide active sites for numerous proteins for oxygen transport and storage (haemoglobin, myoglobin) or electron transfer (cytochrome c or oxidase) to energy conversion (chlorophyll) [5.24]. As a results these remarkable materials have been actively researched since the 60's in order to gain a better understanding of their properties and how they can be utilised for science. This in turn attracted research interest form several disciplines *i.e.* materials to medical science.

Porphyrin molecules are considered as good sensing materials due to several features such as the ability to make different conformers of their molecular 3D structure and their unique optical properties with respect to each conformer. Further, their capability to adsorb and/or release gases and to act as an active centre in catalytic reactions has attracted considerable attention. Porphyrin based thin films on metal and semiconductor surfaces have been tested in various applications. As an example, metalloporphyrins have been actively used to detect volatile toxic gasses such as ammonia, and nitrogen dioxide *etc.* [5.25]. Besides sensing, recently they have proposed to increase the efficiency of dye-sensitized solar cells [5.26].

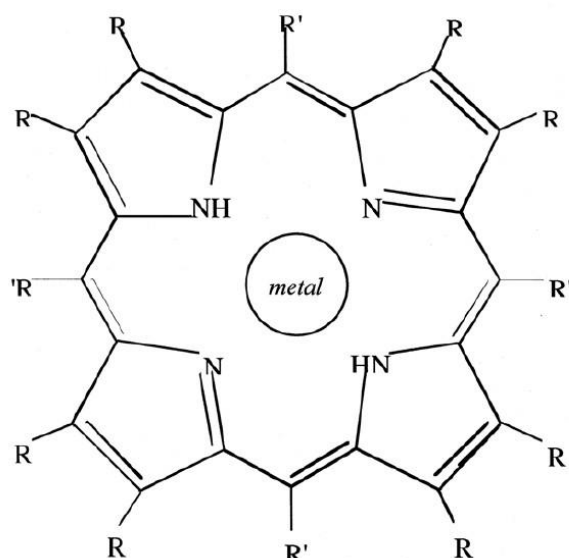


Figure 5.31 – Molecular Structure of Porphyrin, where the metal in the centre acts as a host for any of the D-Block elements [5.25].

Porphyrin is made of 4 pyrrole rings (Fig. 5.31) with p-bond conjugation joined together by a methylene bridge with two hydrogen atoms bonded to two of the central nitrogen atoms. Most of the transition element from the d-block of the periodic table can be entrapped inside the ring, by carefully choosing the peripheral substituents. Following entrapment, the molecular structure deprotonates forming a dianionic ligand, where the ions behave as Lewis acids accepting lone pairs of electrons from the dianionic Porphyrin ligand. As opposed to most metal complexes the resulting colour change is due to absorption within the ligand involving excitation of electrons from  $\pi$ - $\pi^*$  Porphyrin ring orbitals [5.24]. Fig 5.32 shows the two step process of ZnTPP to  $\text{NO}_2$ . In the first step  $\text{NO}_2$  oxidises the complex. This oxidised complex can react with another  $\text{NO}_2$  molecule, which is covalently bound to one phenyl ring. The second reaction leads to visible colour change, while the first can be only observed in the infrared

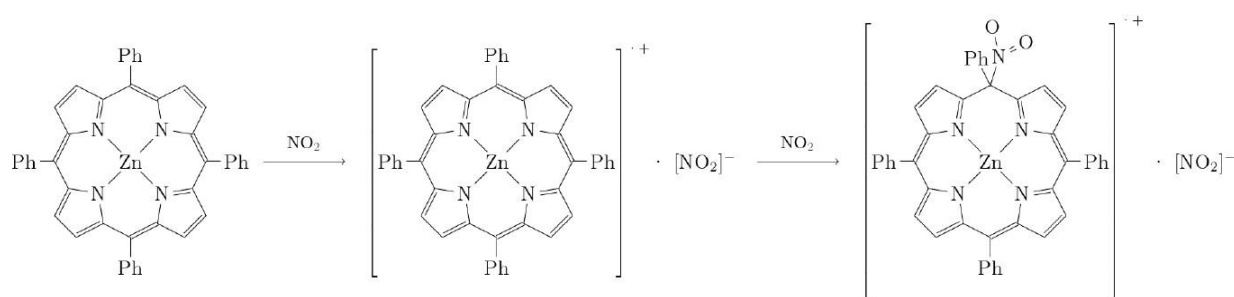


Figure 5.32 Two step reaction mechanism of ZnTPP to  $\text{NO}_2$  [5.24]

Porphyrins show significant solvatochromic effects with a range of vapours such as alcohols, amines, phosphines, which can result in indistinguishable colour effects that can have a negative effect on the measurement [5.27-29]. However, the adsorption properties of this material is characterised by large sensitivities due to its extremely large extinction coefficient and wide selectivity. The wide selectivity is generally contributed to weak interactions such as van der Waals force and hydrogen bonding, but the p-bond conjugation aids  $\pi$ - $\pi$  interactions between e.g. aromatic systems of porphyrins and aromatic analytes. This particular property makes this compound very attractive for gas sensing. Consequently, in the past it has been mostly researched for this application. The most important property of porphyrin is tenability, as it is possible to attach other sensitive chemical species (dyes), which contain metallic compounds therefore tuning its sensitivity to other analytes of interest [5.21]. One example was mentioned in the previous chapter, where a porphyrin based heterostructure was used in order to measure glucose [5.21]. Together all these features of porphyrin and the paper [5.21] describing the glucose measurements indicated an interesting research direction that would allow us to measure lactate and pyruvate as well.

Absorption Band of porphyrin

Electrons in atoms or ions occupy a set of discrete energy levels separated by forbidden energy gaps. Transition can only occur between these levels. When the energy level of the incoming photon matches the bandgap energy. There are only a limited number of combinations of these bandgaps, therefore the absorption band can be made of a limited set of photon energies. The optical feature of Porphyrin can be attributed the mixing of transitions between the two highest and lowest occupied orbital levels. This allows the creation of the Soret band with absorption maximum at 420nm and a much weaker visible Q-band (Fig. 5.33) with several absorption peaks at 524, 555 and 590nm. The absorption maximum is defined by the energy difference between the highest and lowest occupied electron orbitals.

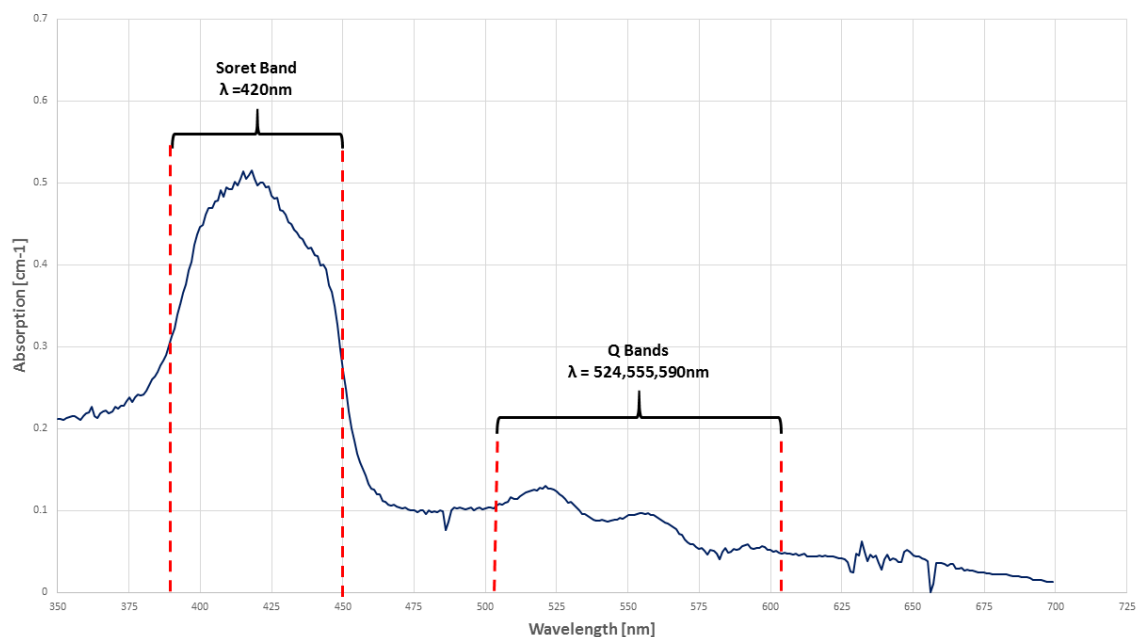


Figure 5.33. – Absorption Spectrum of porphyrin

The fine adjustments in the peripheral substituents on the porphyrin ring can result in minor changes the absorption bands. For example, protonation of the two of the inner nitrogen atoms or the insertion/change of metal atoms into the macrocycle can strongly change the visible absorption spectrum [5.28]. These optical phenomena attracted the attention of several researchers in various fields and allowed the development of novel applications in optoelectronics[5.30], data storage [31], solar cells [5.26] and chemical sensing [5.33].

#### 5.4.2 Deposition techniques

Porphyrin based sensors have attracted considerable attention due to their stability, chemical sensitivity, reproducibility and therefore various designs have been implemented [5.34-37]. For

## Chapter 5 – Device fabrication and experimental results

sensing purposes, porphyrin has to be deposited in a solid thin film form onto an appropriate

substrate. There are several different techniques available. However, optimising the process to a particular target substrate takes time in order to achieve good adsorption and sensitivity. Traditionally thin film deposition of porphyrin is carried out by “*solvent casting*” [5.38] Porphyrin is usually dissolved in an organic solvent, such as chloroform or ethanol allowing to control the specific amount of solution with a known quantity. The dissolved solution is deposited onto the target surface by either simply injecting a known amount by a micro pipette (drop coating) or just dipping the substrate onto the solution itself (dip coating). The main drawbacks of this technique are poor reproducibility and the lack of control over the thickness of the thin film, which is crucial for most of the optical interrogation techniques such as evanescent field sensing.

**Langmuir-Blodgett** is a well-established technique usually used to obtain thin films of organic compounds by molecular interaction. Most gas sensors are based on recognition layers deposited by LB [5.28]

**Self-Assembled Monolayers** are based on predefined and functionalised surfaces by adsorption of organic molecules onto inorganic substrates. This technique opened a promising way for surface functionalization in a highly controlled manner at the molecular level [5.31]. The main benefit of using this technique is the extremely low thickness achievable in the range of 10`s of nanometers. Another useful approach is **Electro Polymerisation**, where the molecular complexes are deposited by electric excitation on the target substrate. Promising results were reported in [5.39], especially as most sensors use various conductive metal surfaces as a substrate for the recognition layer, which plays a pivotal role in the interrogation mechanism.

Less attention has been paid to physical techniques such as spin coating or vacuum evaporation. Spin coating is a simple technique, providing good control over the thin film thickness. However it suffers from limited sensitivity and reproducibility [5.38]. Vacuum deposition has several benefits over other techniques, such as thin film purity. Porphyrin thin films can be produced without using any extraneous compound, therefore achieving much higher purity compared to any other techniques, where chemical solvents are needed. As a drawback, porphyrin is considered a “messy” material, therefore it makes it difficult to clean the vacuum chambers after deposition making it difficult for any process development. A novel physical deposition has been proposed by M. Tonazzo in [5.34], where cobalt 5,10,15,20 meso-tetraphenyl porphyrin (CoTPP) is deposited by glow-discharge sublimation and provided a good comparison between each technique.

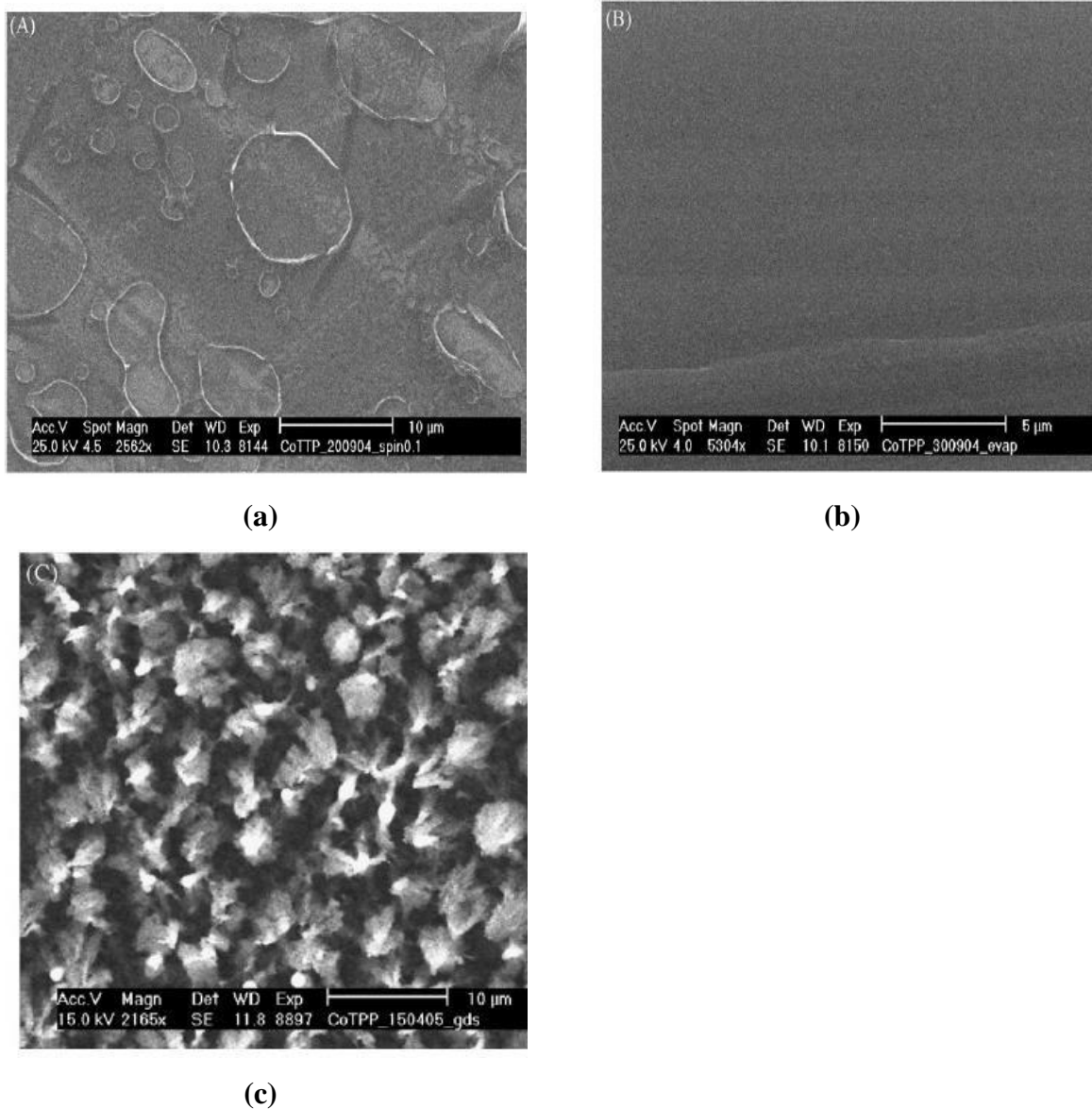


Figure 5.34 – SEM images of (a) SPIN coating (b) VE (c) GDS films of CoTPP [5.38]

As the SEM images on Fig. 5.34 illustrate, the main difference between the techniques is the surface morphology. Spin coating creates a porphyrin thin film filled with craters as a result of solvent evaporation. GDS on the other hand creates a very rough surface in micro meter range. Vacuum evaporation appears to result in a flat surface, which is ideal for creating recognition layers based on heterostructures, where multiple biochemical layers have to be formed in a well-ordered manner. The UV-VIS absorption spectrum of the aforementioned samples are shown below, where minor differences can be observed between the techniques as a result of different intermolecular arrangements affecting the optical transmission of the thin films. The overall optical absorption of GDS was higher as a result of the high surface roughness (Fig. 5.35), but the absorption peaks are less defined as well. Having well defined band structure is important for optical sensing. The Soret absorption peaks are the most defined when VE was used. This can be linked to the high purity of

the material as well as the flat natures of the thin films.

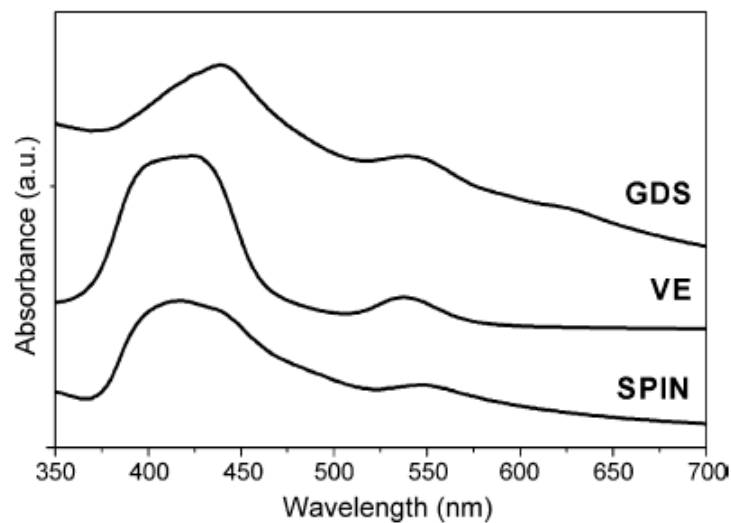
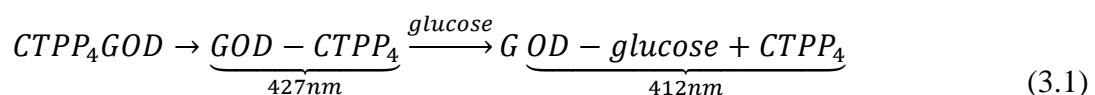


Figure 5.35 UV-VIS Absorption Spectrum of porphyrin thin film deposited by Spin Coating Vacuum Evaporation and Glow-discharge Sublimation [5.38]

The adsorption of target analytes onto a recognition layer based on porphyrin can give rise to changes in mass, work function and most importantly optical absorption. Each quantity can be translated into an electrical or optical signal by choosing the appropriate transduction mechanism. Mass and conductivity measurements have faced several disadvantages in terms of limited sensitivity, slow response time and complicated data analysis. On the other hand, optical sensing techniques based on monitoring the change in the optical properties of the thin films have been proven to be a promising approach [5.40].

### 5.4.3 Recognition layer development

The development of the porphyrin based recognition layer for analysis of brain micro dialysates began in 2012 based on the paper of [5.21], where the author successfully carried out reversible glucose reactions in a matter of seconds. Meso-tetra(4-carboxyphenyl) porphine (CTPP<sub>4</sub>) binds immobilised glucose oxidase giving two absorbance peaks at 412 nm (Soret band) and 427 nm (Q band). The immobilised complex resulted in an absorbance loss at 427nm due to the disassociation of CTPP<sub>4</sub> from GOD as described below.



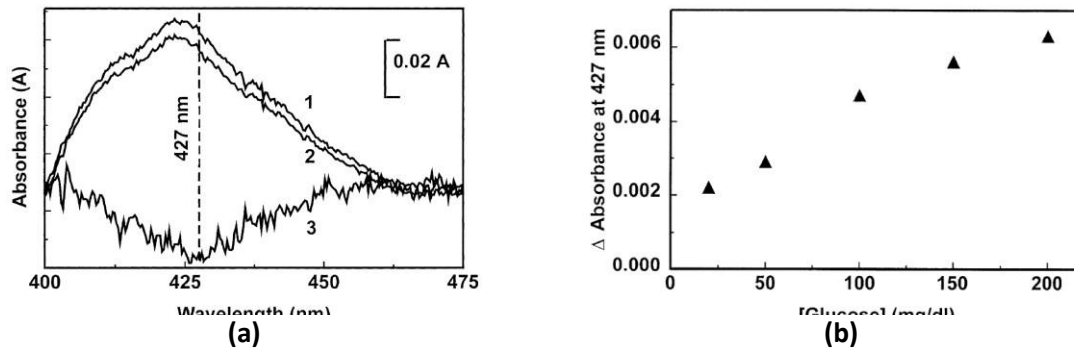


Figure 5.36 Absorbance Spectra of (a) before (1) and after exposure (2) to 50mg/dl glucose solution. The dynamic range of GOD-<sub>4</sub> complex is shown on (b) [5.21]

The paper did not state clearly whether the complex was reversible. However the speed of reaction and dynamic range were promising (Fig. 5.36) for the application of brain microdialysate analysis. The first step in the development process was to investigate whether this complex can be used for pyruvate and lactate by using their corresponding oxidase complexes. As a result the glucose, pyruvate and lactate oxidase was tested in a liquid form using a HP 8453 UV Spectrometer and a cuvette. The basic description and operation of the device is given in the following section. The subsequent section presents the results along with discussion.

### Conceptual Test of CTPP-oxidase complex for analysing glucose, lactate and pyruvate in a aqueous environment

The first phase of the recognition layer development was to verify the previously described chemical reaction (eqs. 3.1) works for all the target analytes in question. This section describes the first experiments that provided the first insight into this chemical reaction. It was the first crucial step towards the development of the first recognition layer, aiming to create the means of continuously measuring all the three analytes in the cerebellum fluid required to monitor brain metabolism.

#### Experimental Setup

The optical system of the spectrophotometer is shown in Figure 5.37 Its radiation source is a combination of a deuterium-discharge lamp for the ultraviolet (UV) wavelength range and a tungsten lamp for the visible (VIS) and short wave near-infrared (SWNIR) wavelength range. The image of the filament of the tungsten lamp is focused on the discharge aperture of the deuterium lamp by means of a special rear-access lamp design which allows both light sources to be optically combined and share a common axis to the source lens. The source lens forms a single, collimated beam of light. The beam passes through the shutter/stray-light correction filter area then through

the sample to the spectrograph lens and slit. In a standard absorption spectrometer, a monochromator is used to limit the range of wavelength at which passes through the sample cuvette. However in the spectrometer, light is dispersed onto the diode array by a holographic grating. This allows simultaneous measurement of all wavelength information. The result is a fundamental increase in the rate at which spectra can be acquired.

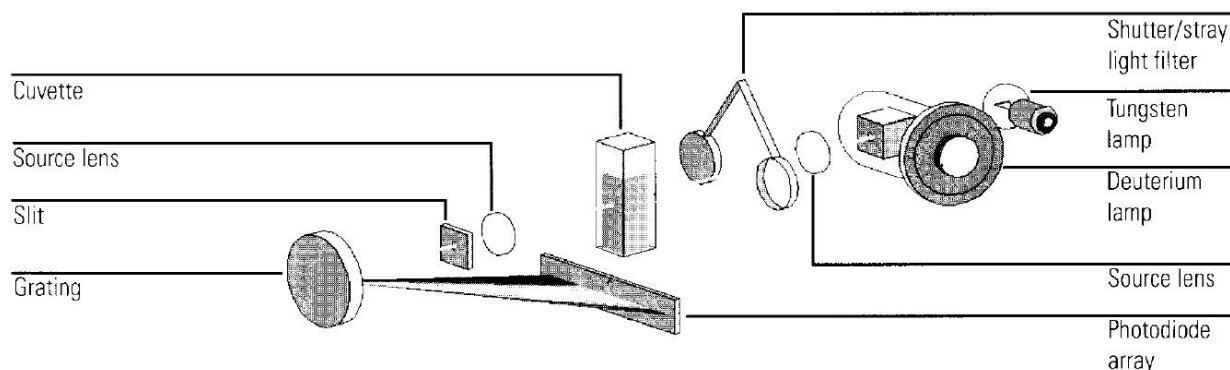


Figure 5.37 - Schematic of the optical System for HP 8453 UV-Visible Spectrometer

### Measurement Process

At the beginning of the experiment a reference measurement is taken with a water solution that is used in all subsequent sample measurements. Following the reference measurement, the baseline spectrum is measured and displayed on the PC. The reference absorbance values are subtracted from sample absorbance values.

In a spectrophotometer, monochromatic plane-parallel light enters a sample at right angles to the plane-surface of the sample. In these conditions, the light intensity is linearly dependent on the molar concentration ( $C$ ) and molar absorptivity ( $\epsilon$ ), while exponentially dependent on the light path length in centimetres ( $L$ ).

$$I(\lambda) = e^{\epsilon CL} \quad (5.2)$$

Beer's Law states that molar absorptivity is a material constant and the absorbance is linearly proportional to concentration for a given substance dissolved in each solute and measured at a given wavelength. Accordingly, molar absorptivities are commonly called molar extinction coefficients. Since transmittance and absorbance are unit less, the units for molar absorptivity must cancel the units of concentration and light path. Accordingly, molar absorptivities have units of  $M^{-1} \text{ cm}^{-1}$ . Standard laboratory spectrophotometers are fitted for use with 1 cm width sample cuvettes; hence, the path length is generally assumed to be equal to one centimetre and the term is dropped altogether in most calculations.

$$A_{\text{measured}}(\lambda) = I_{\text{sample}}(\lambda) - I_{\text{reference}}(\lambda) \quad (5.3)$$

The measured absorption values are arbitrary units (AU) as well as the ratio of the received and

incident power (or current). The received powers measured at the array of photodiodes are referenced to the reference measurements.

### Liquid Solution Measurements

1mg of porphyrin was dissolved in 100  $\mu\text{L}$  of Ethanol, then diluted with 25mL of DI Water. Each analyte was tested separately and so the same amount of glucose, pyruvate and lactate oxidase powder were dissolved (1mg) in 25mL of DI water in separate solutions. The corresponding three target analytes were prepared in different eppendorf tubes as well by dissolving 1mg of glucose, lactate and pyruvate sodium in water. Following the reference measurement the porphyrin and glucose oxidase were added to the water solution in the cuvette and the spectrometer returned the well-known porphyrin absorption spectra, illustrated on Fig. 5.38.

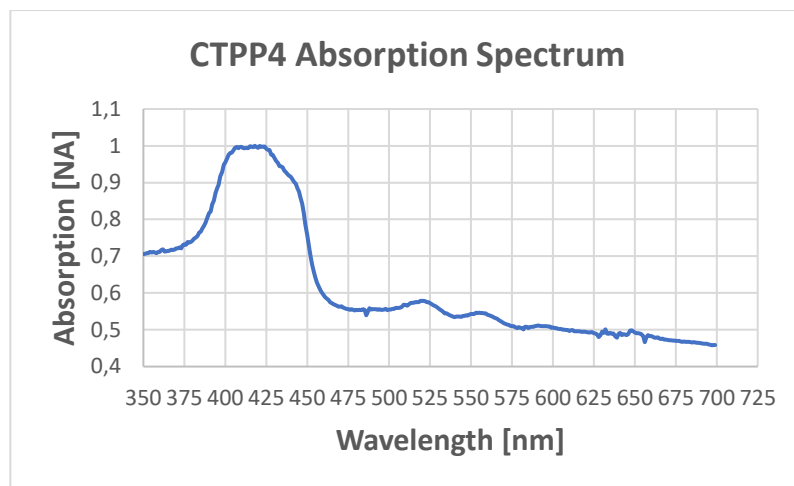


Figure 5.38 – Measured optical absorption spectrum of the CTPP<sub>4</sub> solution

The absorption spectrum of the CTPP<sub>4</sub> solution clearly shows the Soret band at 420nm and three Q bands at 524, 555 and 590nm. An artefact was present at 490nm on all the absorption curves, which is assumed to originate from the instrument. The next step was the addition of the glucose oxidase and glucose solution, which resulted in an absorption increase in the Soret band illustrated on Fig. 5.39.

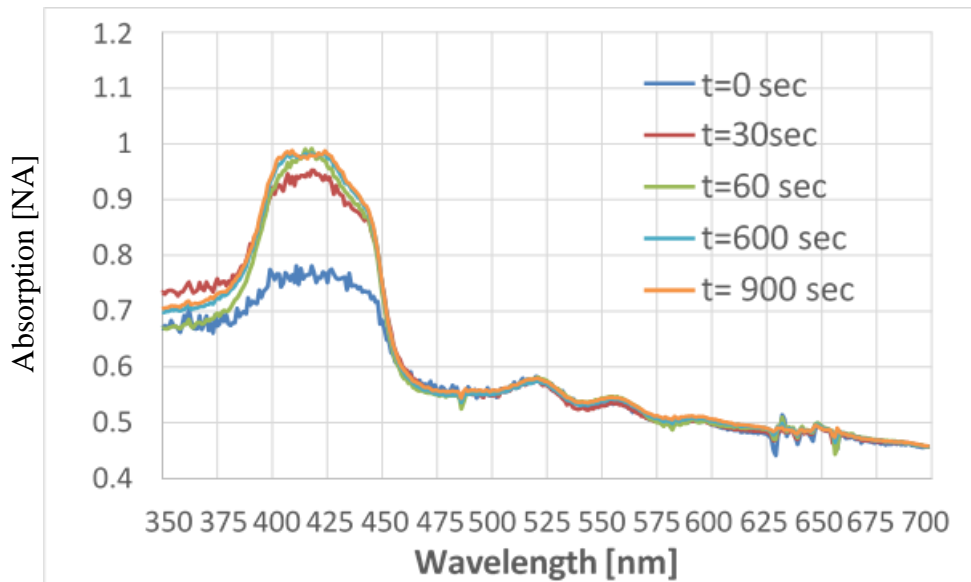


Figure 5.39 – Evolution of CTPP4-GOX complex in the optical spectrum as it reacts with 20mM/L of glucose

The ratio of CTPP4 and GOX solution was 1:1, which resulted in a clearly distinguishable absorption increase at 425nm. Several measurement points were taken up to 900 seconds in order to monitor how the chemical reaction evolves with time. The absorption values for all the absorption peaks are listed in Table 5.3 Based on the measurement points, it can be clearly concluded that the wavelength of interest for the CTPP4-GOX complex will be at 420nm, where the absorption increase was significantly higher from 0.75 to 0.977. Moreover, the reaction reached 99,53% of its settled value after 60 seconds.

Table 5.4 – Measured absorption [AU] at different peaks with time, resolution 0.0002 AU and accuracy of 0.005 AU

t [sec]	0	30	60	300	600	900
A(420nm)	0.7516	0.9447	0.9724	1.0011	0.9775	0.9771
A(512nm)	0.5640	0.5644	0.5694	0.5767	0.5650	0.5696
A(555nm)	0.5337	0.5354	0.5473	0.5523	0.5434	0.5456
A(590nm)	0.5040	0.5054	0.5052	0.5133	0.5089	0.5123

Continuous monitoring of brain microdialysates requires the opto-chemical reaction to finish within a minute in order to achieve near continuous online monitoring of patients. The concentration of glucose was 20 mM/L and the reaction finished (99,5% , Fig. 53) after 60 seconds, which is acceptable given the physiological range for glucose is between 0.1-5mM.

The next step was to find out how the ratio of CTPP4 and GOX affects the reaction time for the same concentration of analyte (20mM). The distribution of CTPP4 and GOX was changed, while

the same concentration of analyte was applied. The results of the kinetic tests are summarised in Table 5.4. The ideal ratio for CTPP4/GOX solution was found at 1:1 as the reaction finishes within 60 seconds.

*Table 5.5 – Reaction time changes with CTPP4/GOX ratio*

CTPP4/GOX Ratio	0.5	1	2
Reaction Time [s]	20	60	130

When the ratio of CTPP4/GOX concentration was 1:1 and the concentration of glucose was changed between 1-20 mM/L a linear increase in reaction time was observed (Fig 5.40). At 1:1 ratio between the two compound the chemical reaction was finished below 60 seconds given the concentration of glucose was below 20mM/L, while at 100mM/L reaction took over in 4 minutes.

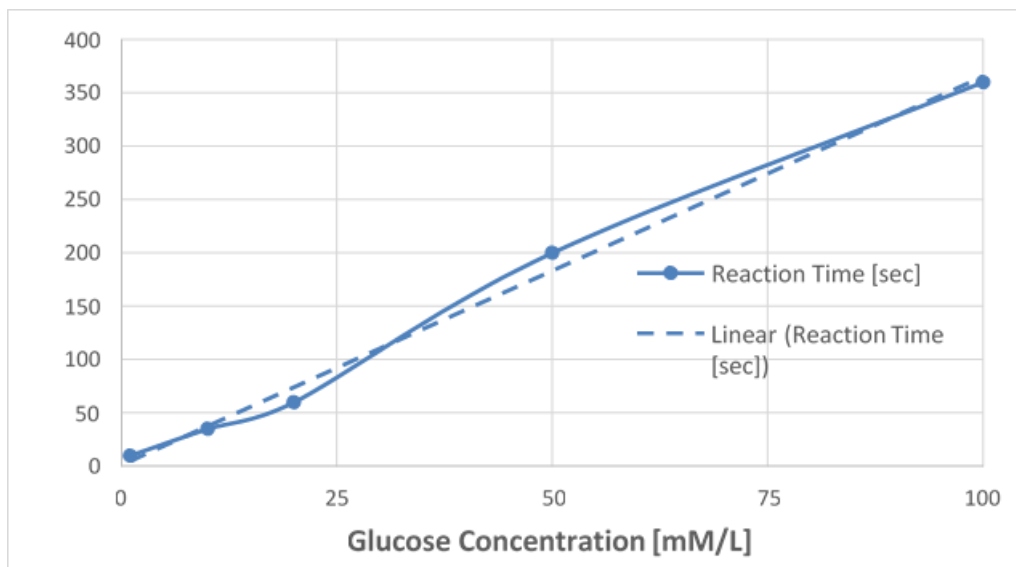


Figure 5.40 – Change in reaction time as a function of glucose concentration

As the physiological range for glucose is 0.1-5mM/L within the cerebellum, the optimal ratio of the two compound can be established at 1:1. The experiment showed fast and clear reaction for glucose and similar reaction times were observed during the tests carried out for pyruvate and lactate.

The final question that remained is how other interferants within the cerebellum can affect the measurement. Brain fluid extracted from the cerebellum will contain all three analytes of interest, which could potentially affect the measurement process. The CTPP4-GOX compound with ratio of 1:1 with the same process as before, then 1mM/L of pyruvate and lactate was applied as shown on Fig. 5.41.

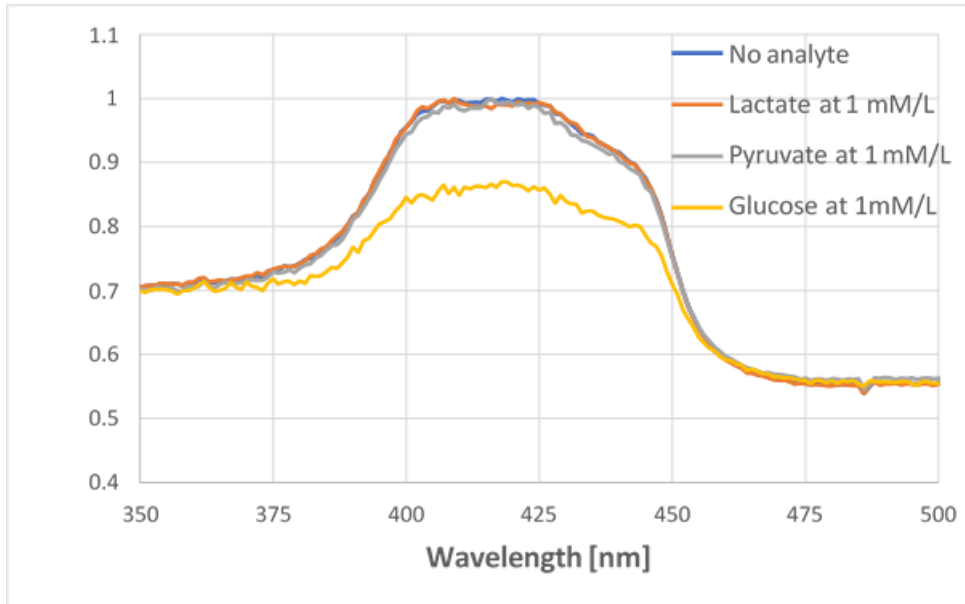


Figure 5.41 – Evolution of CTPP4-GOX complex in the optical spectrum as it reacts with 20mM/L of glucose, while not reacting to the other substances

The change in absorption was 0.6% for lactate and 0.21% for pyruvate, which is negligible compared to the absorption change when glucose was applied.

Table 5.6 – Absorption change of CTPP4-GOX compound at 420nm for 1mM/L pyruvate and lactate

	No analyte	Lactate at 1 mM	Pyruvate at 1 mM	Glucose at 1 mM
A(420nm)	0.9943	0.9884	0.9921	0.8635
Percentage of change	0	0.59	-0.21	-15.14

The CTPP4-GOX reaction showed promising results in a liquid form. The absorption spectrum analysis showed a significant optical absorption increase at 420 nm wavelength for glucose, pyruvate and lactate. The chemical reaction finished within 60 seconds between 1-20 mM/L, which is matching the physiological range for glucose in the cerebellum [5.41]. Moreover, the selectivity test also showed negligible reaction for CTPP4-GOX to lactate and pyruvate compounds.

#### 5.4.3.1 Reversible recognition layer development for brain microdialysates

The next step was to develop a deposition process for the CTPP4-GOX recognition layer and investigate whether it is possible to reverse the reaction using a buffer fluid as it was reported in [5.21], which required for the sensor to be reusable. For this purpose, the same VIS-Spectrometer was used with a different mount as before that can hold a microscope glass instead a cuvette.

The standard glucose determination methods based on glucose oxidase are based on monitoring

H<sub>2</sub>O<sub>2</sub> or O<sub>2</sub> production. For example, in [5.42] a potentiometric sensor is used, that is based on a coupled reaction, by monitoring the oxidation of an indicator compound. Such methods are prone to interferents, such as other oxidising agents, ascorbate and L-cysteine as well as others. As a result, increasing specificity by employing coupled enzyme systems has been a focus of recent research [5.21]. By using permeable polymer layers over the enzyme surface some improvement can be made. However, this is sensitive to cracks or peeling allowing penetration of the interferents into the enzyme surface.

In [5.21], a multi-layered recognition layer was presented (Fig. 5.41), which showed promising reversible reaction within seconds. The next series of experiments was intending to reproduce the results and prove the fact that CTPP4 based dye can be used for lactate and pyruvate as well.

A microscope slide is functionalised by Aldehyde (from Sigma-Aldrich, 10µL in 500µL DI water) in order to make it less hydrophobic. Followed by the activation of PAMAM dendrimer 4<sup>th</sup> generation (from Sigma-Aldrich), where 10µL of PAMAM was diluted in 500µL DI water. This serves as an intermediate layer that functionalises the surface by increasing the adhesion between the layers deposited afterwards. The porphyrin layer (made of 1mg in 500 µL DI Water and 20µL Ethanol) was deposited onto the PAMAM, followed by the GOX layer (1mg in 500µL DI Water). Each layer was deposited by solvent casting, which is simply placing a droplet of 20µl of the solution on the target area, then soft baked at 80 degrees for 60-90 minutes. Following the soft baking, the sample was rinsed with 25mM of Phosphate buffer (from Sigma-Aldrich) to remove the excess material. The overall dye structure is illustrated on Fig. 5.42, showing the adhesion of glucose molecules and its optical interrogation normal to the microscope slide surface. Because of the binding molecules to the CTPP4-GOX layer, the extinction coefficient changes resulting in a large change of optical absorption. Once the chemical reaction is over, the sample is rinsed with Phosphate Buffer (at pH 7) removing the analyte from the surface and therefore reversing the process.

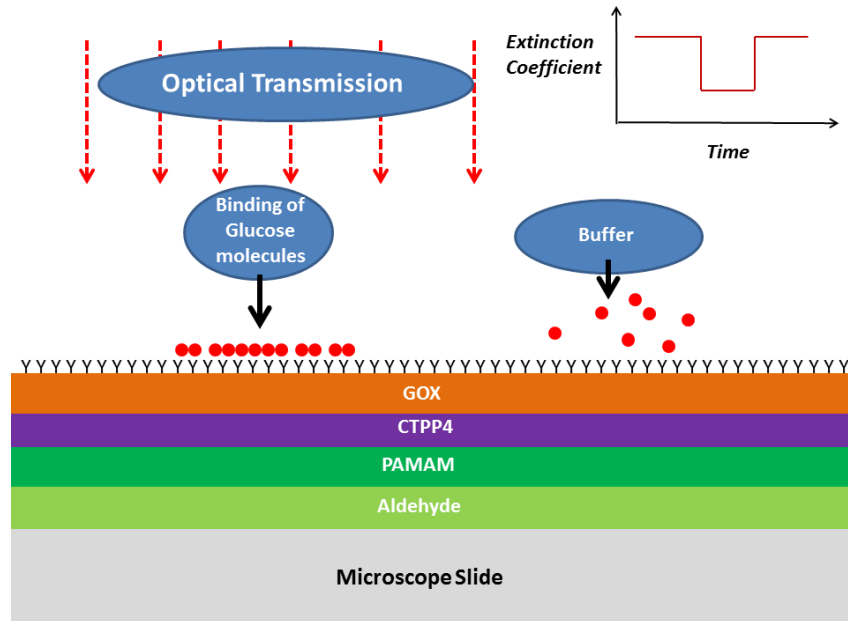


Figure 5.42 – Multi-layered recognition layer illustrating the binding reaction with glucose molecules and the use of a Phosphate buffer for reaction reversal

The same process described in [5.21] was carried out and tested for glucose, lactate and pyruvate. The binding reaction resulted in a decrease (Fig. 5.43) in optical absorption at 420nm and finished within 10 seconds. The reaction time was shorter than the practically possible shortest measurement time. The red line represents the finished reaction curve after 10 seconds, following that the 25mM/L buffer fluid was applied.

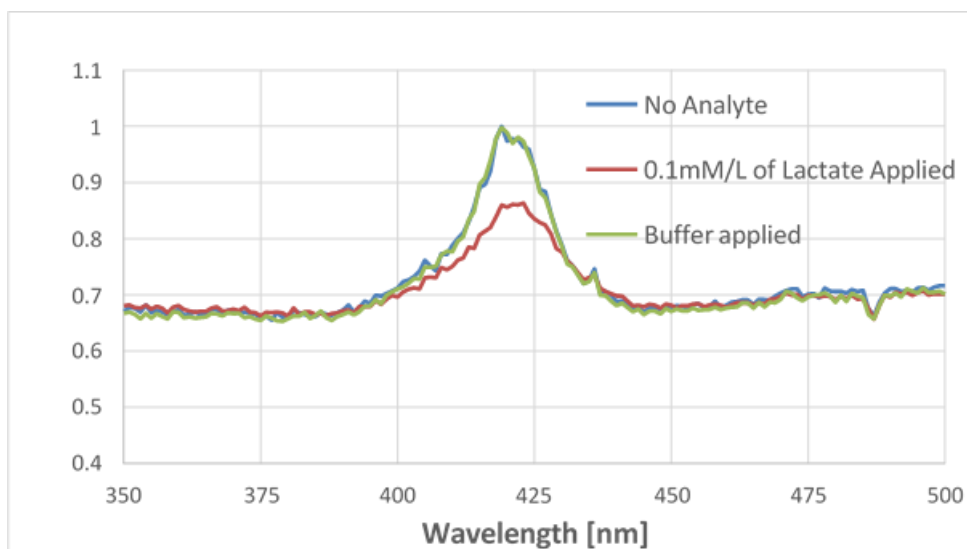


Figure 5.43 – CTPP4-LOX compound reaction when 0.1mM/L of lactate applied and reversed when 25mM/L Phosphate buffer was applied

The Phosphate buffer reversed the reaction resulted an absorption returned to 98,5% of its original value compared to the value when no analyte was present (Table 5.6). The same

glass slide measurement was carried out for pyruvate with similar results (Fig 5.44, Table 5.7). The absorption decreased in both cases with 13,7% for lactate and 46,2% for pyruvate.

Table 5.7 – Absorption change [AU] of CTPP4-LOX compound at 420nm for 0.1mM of lactate

	No Analyte	0.1mM of Lactate Applied	Buffer applied
A(420nm)	0.9733	0.8564	0.9885
Percentage of change	0	-13.7	1.5

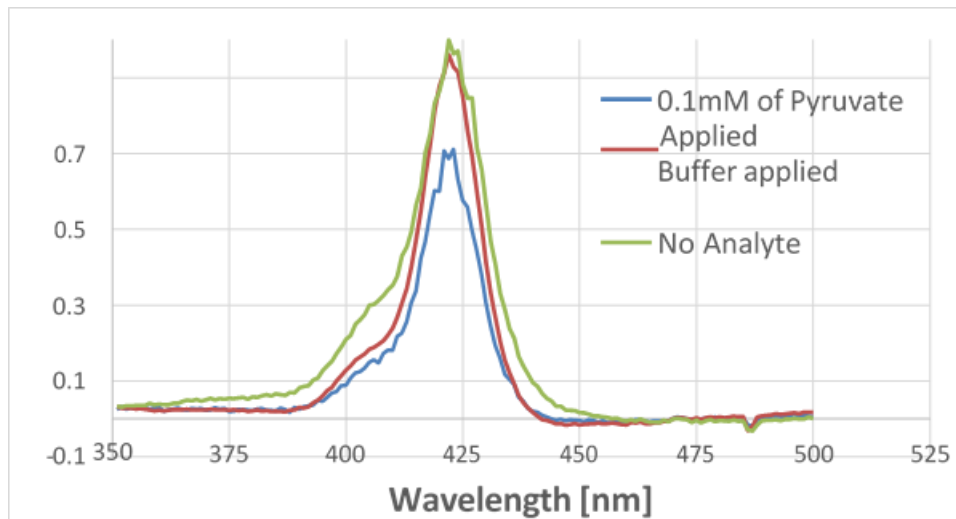


Figure 5.44 – CTPP4-POX compound reaction when 0.1mM of pyruvate applied and reversed when 25mM/L Phosphate buffer was applied

Table 5.8 – Absorption change of CTPP4-POX compound at 420nm for 0.1mM/L of pyruvate

	No Analyte	0.1mM/L of Pyruvate Applied	Buffer applied
A(420nm)	0.8780	0.6008	0.8645
Percentage of change	0	-46.2	-1.5

The addition of 25mM Phosphate buffer reversed the reaction, however in some occasions the LOX/POX layer was removed as well the analyte, highlighting the need to further improvement of the deposition method. Both the reaction and the reversal took place within a few seconds. It was difficult to measure the exact value due to practical constrains, but it was below 10 seconds.

The absorption maxima for all the analytes were at 420nm, which means the same wavelength of light can be used for optical interrogation, simplifying the sensor structure as well as lowering the

cost of the device. The concentration of lactate and pyruvate was kept low in order to achieve fast response times. Lactate and pyruvate oxidase compounds were significantly more expensive than glucose limiting the in-depth investigation. However, these measurements proved that the CTPP<sub>4</sub> based dye in conjunction with the three oxidase compounds capable to produce reversible reactions for three analyte of interest.

#### Recognition layer attachment to Siloxane polymer samples

The previous experiments showed compatibility of CTPP<sub>4</sub> for all the oxidase solutions and therefore proved that all three of the target analytes can be monitored in a reversible manner. Moreover, all reactions were finished within a few seconds at a 0.1 mM/L concentration of glucose and the Phosphate buffer resulted in complete reaction reversal in a similar time frame.

The next step in the development process was the addition of a polymer layer as a substrate made of siloxane core material. At this point it was essential to determine whether this method can be integrated onto the siloxane polymer waveguide technology. The deposition of CTPP<sub>4</sub> appeared to be more difficult as the polymer was very hydrophobic and the buffer fluid removed all the layers from the polymer in a matter of minutes. Further deposition refinements were required in order to match PAMAM-CTPP<sub>4</sub> layers and enhance their adhesion to the polymer material. The thickness of CTPP<sub>4</sub> layer was not conform and often aggregated (clump together) (Fig. 5.45(a)), which made it difficult to make consecutive measurements.

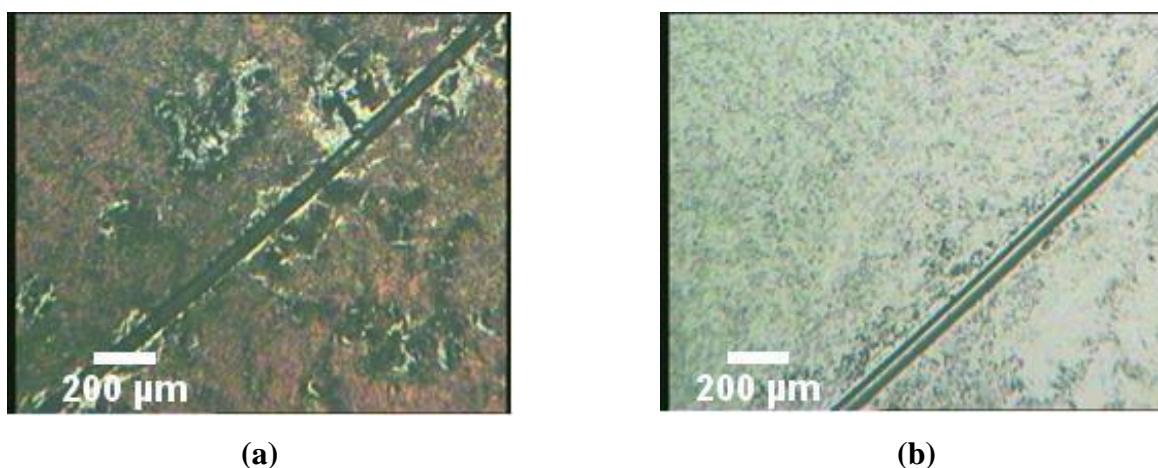


Figure 5.45 – CTPP<sub>4</sub> Deposited onto (1) siloxane polymer waveguide samples (2) after exposition to Phosphate Buffer at 50mM/l concentration

The high degree of surface roughness and uneven dye thickness incorporated errors into the measurements as it changed the optical path of the sample. Moreover, refractive index changes

## Chapter 5 – Device fabrication and experimental results

occurred as a result of water molecules infiltrating into the polymer material. An insulating layer

made of graphene was introduced to prevent this effect, which later turned out also highly beneficial for the quality of deposition.

The introduction of a graphene layer to the GTPP<sub>4</sub>-GOD complex

Graphene is a one-atom-thick planar sheet consisting of sp<sup>2</sup> carbon atoms in a form of densely populated honeycomb crystal lattice [5.43]. It has attracted significant interest due to its high surface area and electronic conductivity, high Young modulus, thermal conductivity, and optical transmittance [5.44-45].

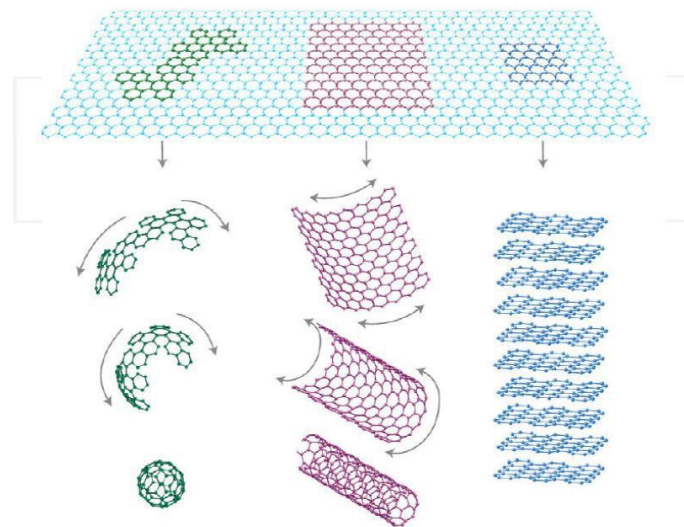


Figure 5.46 – Schematic diagrams of graphene structures in 0D,1D and 3D [5.46]

Graphene has two oxidation states: graphene oxide (GO) and reduced graphene oxide (rGO). rGO has good conductivity and poor solubility in water, while GO has low electronic conductivity and excellent water solubility [5.47-48]. This is primarily due to its rich oxygen-containing and hydrophobic groups such as hydroxyl, epoxide, carboxyl and carboxylic. As a result, GO will then be converted into a  $\pi$ -conjugation-rich graphene, which makes it a good combination with porphyrin.

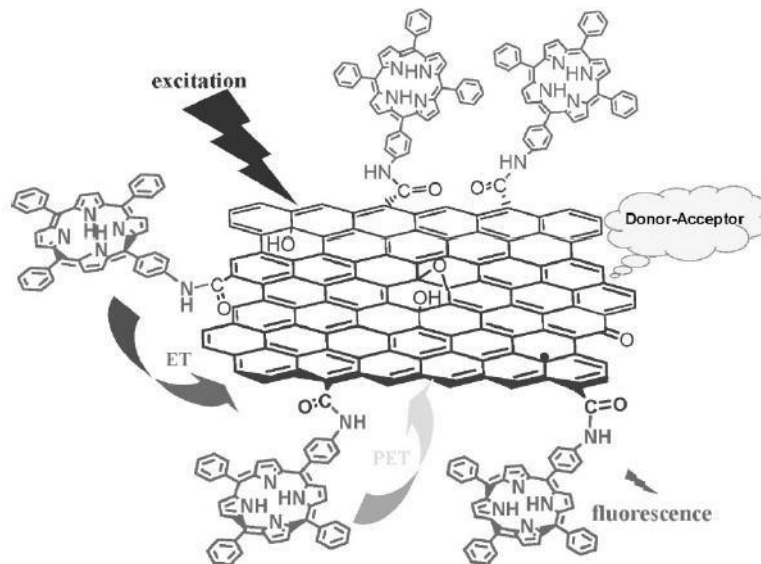


Figure 5.47 – Schematic Representation of covalently bonded GO and TPP [5.48]

The porphyrin-modified acceptor nanoparticles along with the 2D (Fig. 5.46-47) 18  $\pi$ -electron porphyrins exhibit good optoelectronic properties [5.49-55]. Therefore, as expected the 2D nanometer scale graphene with the optoelectronically active porphyrin molecules can lead to interesting applications in the field of optical sensing.

The creation of this GO-CTPP4 hybrid layer required a new graphene transfer methodology as the standard process [5.55-56] involving PMMA and polymer etching by ethyl-acetate (or acetone) would also affect the siloxane polymer. The developed process is illustrated on the Fig. 5.48.

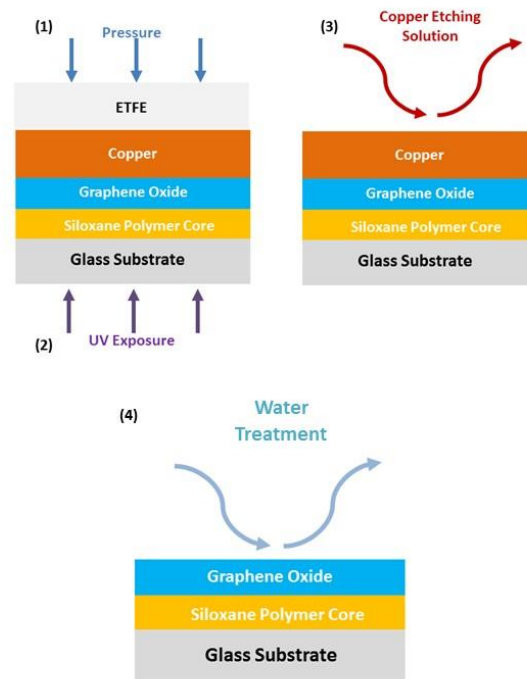
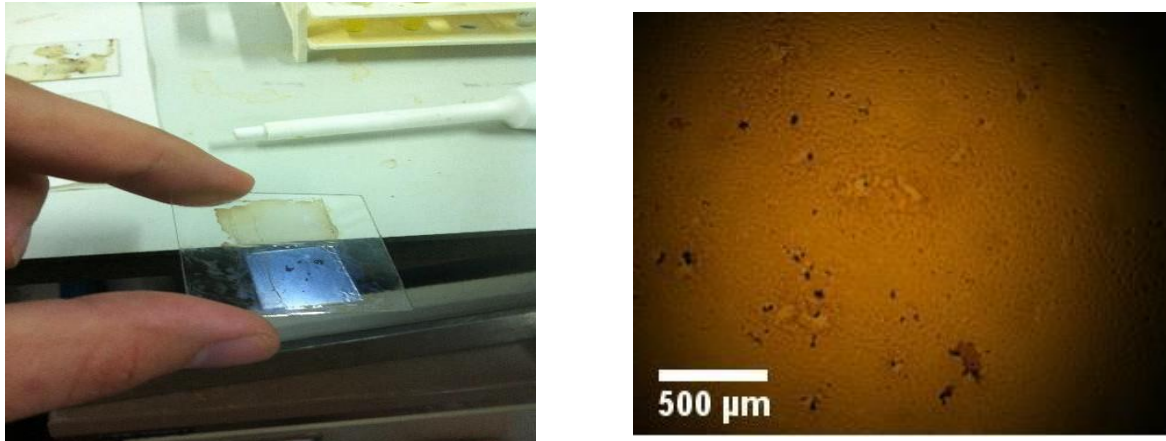


Figure 5.48– Schematic describing the deposition of graphene oxide on siloxane polymer coated glass substrate, (1) Imprinting, (2) UV exposure, (3) ETFE peel off and Copper Etching, (4) Water treatment

The glass slides were spin coated with siloxane polymer core material (~20  $\mu\text{m}$ , 2000 RPM for 45s). The copper sheets containing multi layered GO (was provided by CMMPE group) on both sides were placed on the sample and it was placed in a desiccator for 2 hours in order to remove the oxygen bubbles. Afterwards, the sample was placed in the Obducat Nano Imprint Lithography System (covered with a soft transparent fluoropolymer, called ETFE), which applied pressure (10 bar for 300 seconds) and partly cured the polymer and flattened the copper/polymer sheet (also removing any remaining bubbles). A 10 second long UV exposure (Step 2) was required to finish curing the polymer and therefore create a covalent bonding between the graphene oxide and siloxane polymer materials. The ETFE sheet was then peeled off and the copper was etched away using Iron III Chloride solution. The sample was mounted on the sidewall of a glass beaker filled with the etching solution (34mg Iron II Chloride dissolved in 250 mL DI water). The beaker was placed on a magnetic stirring plate, thereby creating a constant flow of the etchant over the copper sample, enhancing the etching process as well as removing the etched copper residue. The final stage was to repeat the same process by replacing the Ferro-chloride solution with DI water. Leaving it overnight removed all the remaining of the copper from the graphene oxide layer.

The final step of creating a hybrid GO-CTPP<sub>4</sub> layer was to deposit the porphyrin layer on the surface of the graphene via solvent casting. The CTPP<sub>4</sub> solution was prepared by dissolving 1mg of CTPP<sub>4</sub> in 500  $\mu$ L of Ethanol (99%) and shaken for 30 minutes, followed by dilution in water based on the required concentration for the corresponding glucose oxidase solution. Once the porphyrin solution was sufficiently dissolved 10 $\mu$ L was applied to the graphene coated siloxane polymer sample. The porphyrin solution instantly spread evenly out where the graphene oxide was present creating an even coating (Fig. 5.49). Once the ethanol evaporated, it was soft baked for 90 minutes then placed in a water bath overnight.



(a)

(b)

Figure 5.49 – Images of the GO-CTPP<sub>4</sub> layer deposited onto a (a) siloxane polymer coated glass slide and its surface image shown on microscope (b)

A small microfluidic chamber made of PDMS was installed on the top of the sensing region in order to maintain the optical path and limit the evaporation of the fluids from the sample. A microfluidic chamber, with a volume of 2  $\mu$ L, was fabricated by SU8 based soft lithography. Before the microfluidic chamber was attached to the porphyrin coated siloxane sample, both samples were exposed to oxygen plasma in order to create free radicals on the surface (except the sensing region) and therefore covalent bonding took place when they came in contact. The final sensor sample with the attached microfluidic well is illustrated on Fig. 5.50. Inlet and outlet tubing was inserted into the PDMS in order to have the ability to inject and flush out the microfluidic wells between measurements.

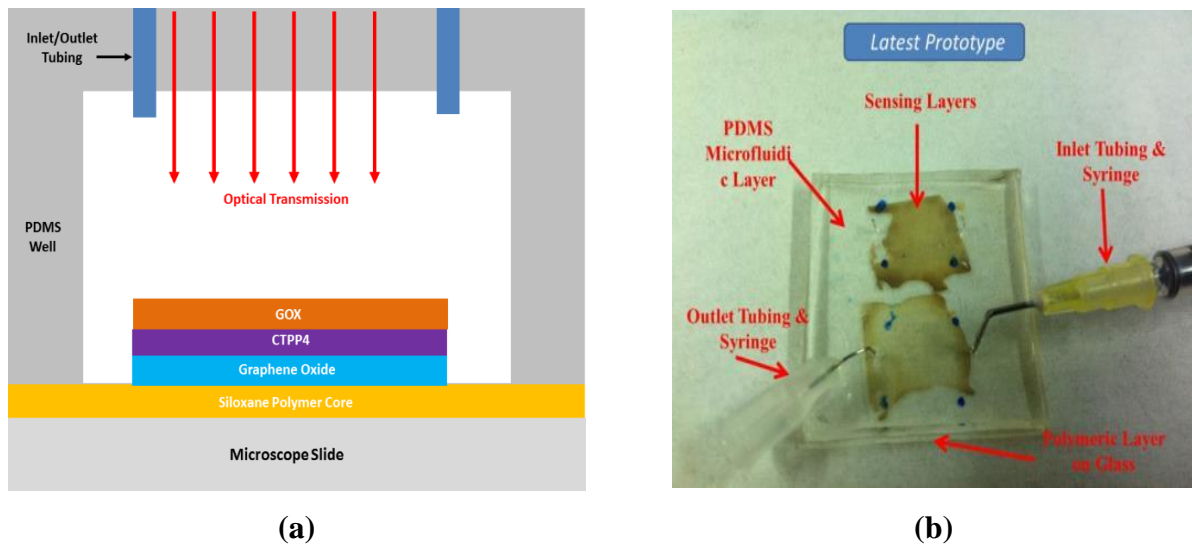


Figure 5.50 – Schematic showing the (a) hybrid GO-CTPP4 layer with the PDMS (2 $\mu$ L) well attached, (b) photo of the test sample

Unfortunately, the sensing region could not be completely covered and therefore some of the deposited regions were exposed resulting in lower reaction intensity. Moreover, the PDMS layer also limited the optical detection as it increased the optical path and therefore scattering effects. The experiment was carried out using test analytes synthesized by researchers at NCCU. The analytes provided were made of several interferents that can be present in an actual brain fluid. The glucose solution was prepared in CNS perfusion fluid and its components are listed in Table 5.8.

Table 5.9 – List of components in the analyte under test

Content	Concentration [mM/L]
NaCl	147
KCL	2.7
CaCL2	1.2
MgCl2	0.85
Glucose Sodium	5

The blank measurement was taken with CNS perfusion fluid (blue line on Fig. 5.45) in order to avoid any errors in the measurements as a result of pH changes. Afterwards, the previously described analyte was injected containing 5mM/L glucose solution. As illustrated in Fig. 5.51, a strong reaction occurred at the 420nm when the analytes were injected into the system, resulting in a decrease in absorption in the Soret band, with hardly any changes in the Q-band peaks.

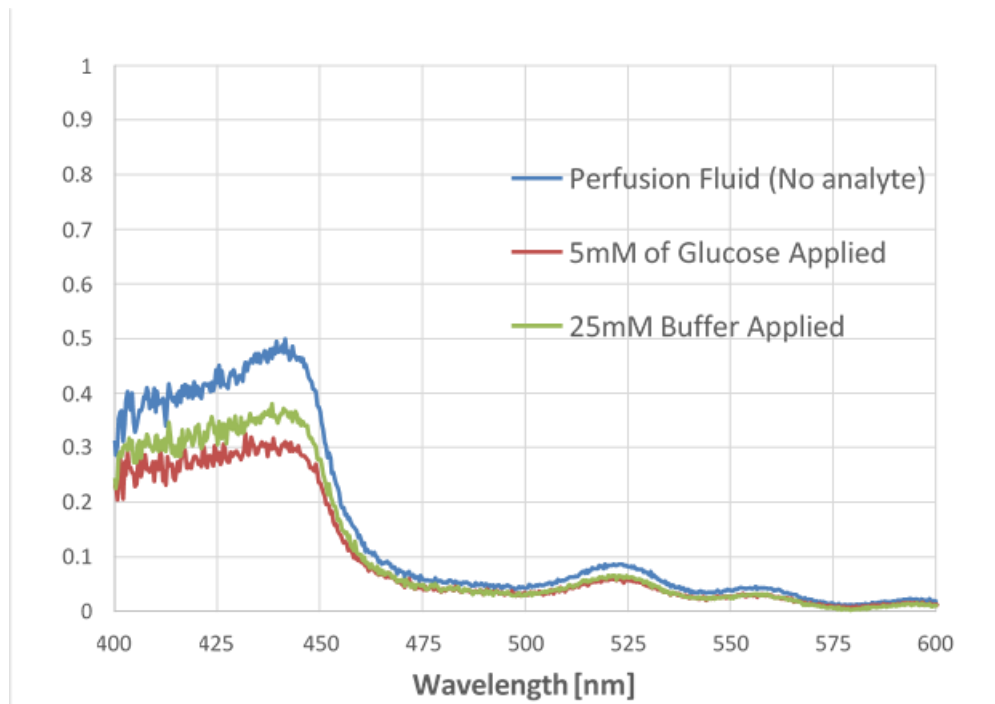


Figure 5.51 – Absorption Spectrum of siloxane polymer sample functionalised with CTPP4-GOX and exposed to artificial brain fluid containing 5mM/L of glucose.

Table 5.10 Absorption change of CTPP4-GOX functionalised on siloxane polymer at 420nm

	Perfusion Fluid (No analyte)	5mM/L of Glucose Applied	25mM/L Buffer Applied
A(420nm)	0.413	0.28	0.331
Percentage of change	0	-47.50	-24.77

Unfortunately, the reaction was only partly reversible as the microfluidic channel detached from the polymer layer. There could have been several reasons, one is the partial remain of the original analytes as well as the optical path change due to pressure build up in the well. Moreover, it is also possible that the buffer fluid concentration was too high resulting in additional dye removal from the substrate. As a result, consecutive measurements were not possible in the way of quantitative analysis.

#### 5.4.4 Waveguide Measurements

The optimal optical interrogation was established at a wavelength of 425nm, where the binding event results in a significant optical absorption change. During the experiments the main issue was to overcome the water effects due to pressure changes in the microfluidic channel. As the analyte or buffer fluid was injected into the sensing well, the PDMS based microfluidic channel extended

## Chapter 5 – Device fabrication and experimental results

as the pressure increased in the well thus changing the optical path. The sensing reaction was interrogated using a VIS spectrometer, where the light propagated through the sensing layer normal to the surface through the PDMS layer. It leads to the conclusion that the only way to overcome this issue is to interrogate the sensing layer evanescently.

In Chapter 5.3 a new fabrication process based on the Thermal NIL technique is described for siloxane polymer. Based on the analysis in Chapter 3 and Chapter 4, fabrication with such a high precision at this feature size would allow the formation of a highly sensitive optical waveguide based on single mode waveguide structures leading the way towards the realization of photonic lab-on-chip sensors. The previously described hybrid GO-CTPP<sub>4</sub> recognition layer can only be formed if inverted waveguide structures are used. Therefore, the sensor development started by fabricating the highly sensitive inverted waveguides as discussed in section 5.3.2 using direct imprint lithography. However, even after trying several different silanisation recipes [5.19] – in order to reduce the natural adhesion of the silicon mould – the siloxane material was stuck to the mould resulting in the destruction of the hard mould. The microscope images shown on Fig. 5.46 show the patterned cladding layer following the demoulding. The sidewalls of the trenches formed in the cladding material were of poor quality (Fig. 5.52) due to the rough demolding. The sidewalls were often damaged and the quality of the trenches varied.

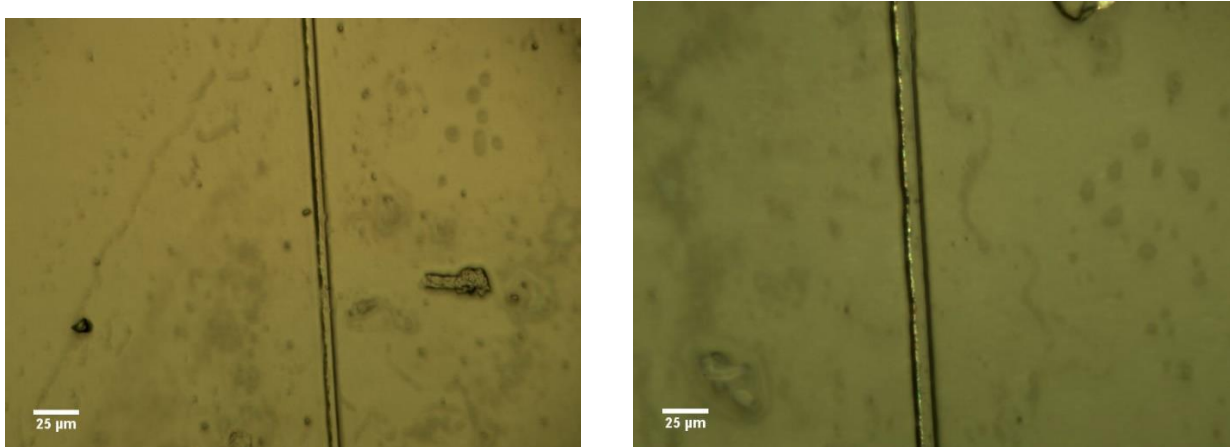


Figure 5.52 – Inverted waveguide pattern formed by direct imprinting

The standard process for depositing graphene was also attempted [5.56] on ridge waveguides. The graphene coated copper sheets were coated with either PMMA or polystyrene by spin coating. The samples are left to dry overnight followed by copper etching (Iron Chloride solution described earlier). The samples are placed in water bath for couple of hours, before imprinted on the waveguides at 110 °C temperature and pressure (at 2 bar). The intermediate polymer had to be etched away using ethylacetate or acetone. The polymer etching trials either resulted in damaging the waveguide core or leaving a residual polymer layer as illustrated below.

## Chapter 5 – Device fabrication and experimental results

An alternative method is the standard process [5.55], where the graphene coated polymer is simply placed on the top of the waveguide features following the water bath. The samples are left to dry overnight, before etched away using the Iron Chloride solution. However, neither of these processes were successful as the graphene did not bond with the siloxane waveguide core properly. Fig. 5.53 (b) shows the residual layer (shaded areas) remained, where the PMMA remained on the top of the graphene layer. In contrast, Fig 5.49 the graphene layer shows clear image of the top of the siloxane layer. It has been concluded that the graphene can only bond with the siloxane polymer material if it is cured while in contact with the graphene. In Chapter 5.4.3.3, the graphene was deposited on the flat siloxane material by directly imprinting the copper sheet into a spin coated substrate. The sample was cured either thermally or by UV exposure enabling covalent bonding between the two material. In these cases, this bonding did not occur therefore the graphene was usually washed (Fig. 5.53 (b)) away with the intermediate polymer during the polymer etching.

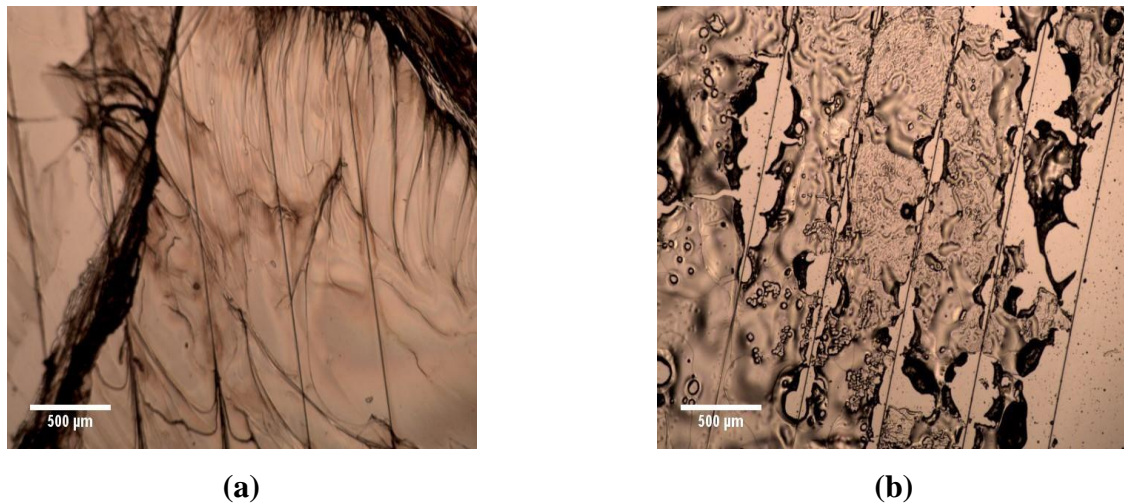


Figure 5.53 – Microscope images showing the waveguide array after the graphene transfer trials by (a) imprinting PMMA resulting in a residual layer (shaded area) and the standard process, (b) unbonded graphene washed away

As a result, the original multi-layered dye recipe was used (Fig. 5.54) for the waveguide experiments based on the techniques described in Chapter 5.4.3. The schematic below illustrates the sensing layer structure consists of Aldehyde/PAMAM/CTPP4/GOX, where the biochemical reaction is interrogated using evanescent field sensing.

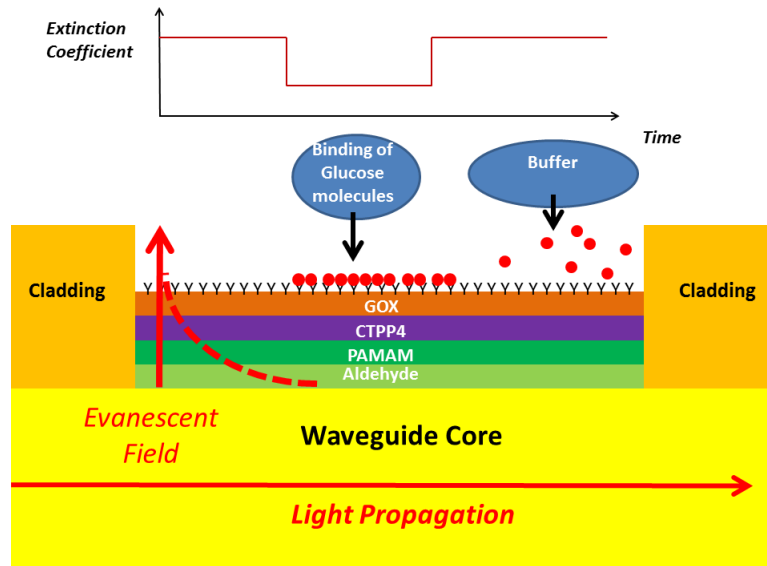


Figure 5.54– CTPP4-GOX recognition layer structure deposited on the waveguide core and interrogated evanescently

Once the siloxane waveguides were fabricated, a microfluidic well was formed in the cladding using UV Photolithography (Fig. 5.55). The deposited cladding material at the beginning and the end of the waveguide provides better input and output coupling efficiency, reduces light scattering. Moreover, the PDMS layer can be simply placed on the top of the cladding layer enclosing the well around the sensing layer.

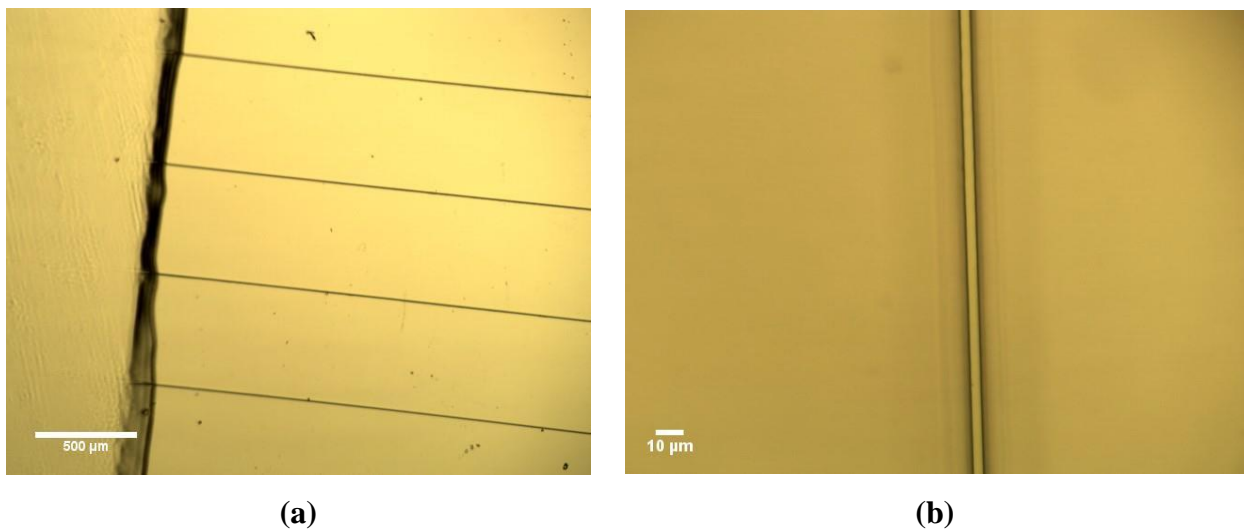


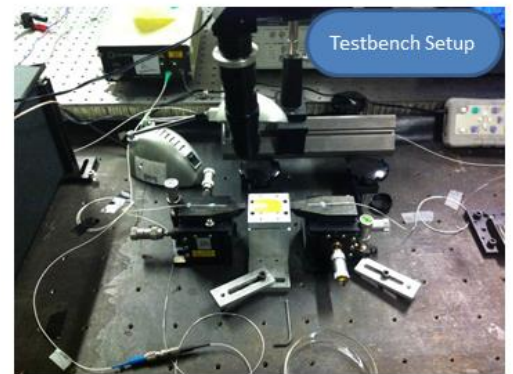
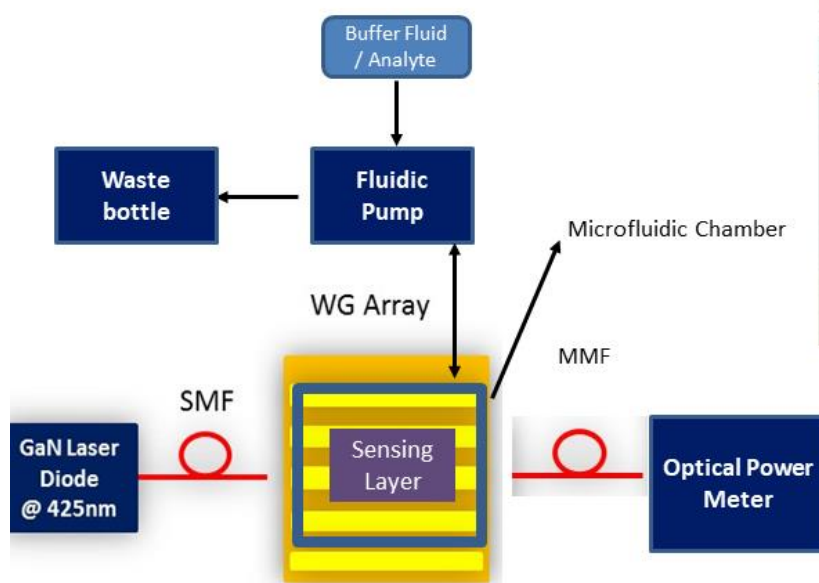
Figure 5.55 – Fabricated high quality siloxane waveguide arrays (2.5-5 μm wide and 3μm high) (b) with microfluidic well (a) formed by the patterned cladding

The only difficulty assembling the sensor chip is the attachment of the PDMS layer with strong adhesion. The standard procedure for attaching the PDMS layer is to expose both surfaces to oxygen plasma. However, it also effected the recognition layer as it removed some part of the CTPP4 and GOX layers. While the glucose oxidase were completely removed, the CTPP<sub>4</sub> remained

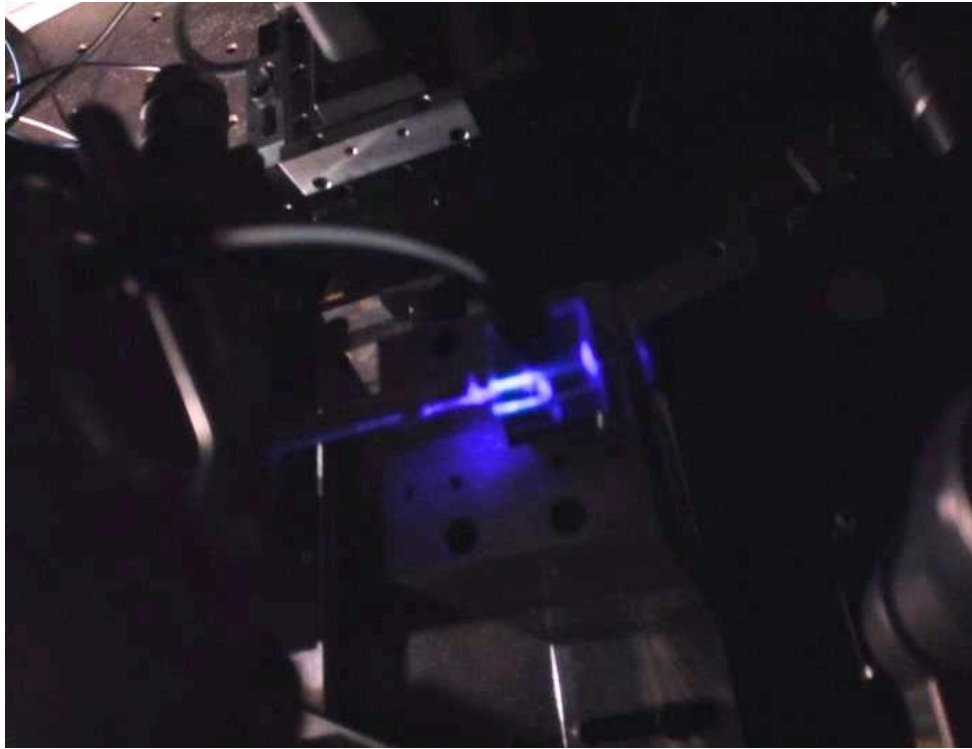
## Chapter 5 – Device fabrication and experimental results

on the surface. For this reason the glucose oxidase had to be deposited after the enclosure is placed on the sensing well. The GOX solution was injected into the well by a syringe and activated over 2 hours as was originally done in [5.21]. Following the activation step, the GOX solution was flushed out by water using a syringe pump. This process was verified by replicating a waveguide sample on a Dow Corning quartz glass and performing this deposition process. As both the glass and the siloxane polymer were transparent the chemical reaction was tested on the previously described (Chapter 5.4.3.3) experimental setup in order to verify that the CTPP4-GOX reaction is possible even after the CTPP4 layer is exposed to oxygen plasma.

On Fig. 5.56 the experimental setup is shown with the attached PDMS layer on the optical bench.



(a)



(b)

Figure 5.56 – Experimental Setup (a) of Optical lab-on-chip sensing with sensing layer, optical waveguide sensor and microfluidic channels attached, (b) image of sensor unit during measurement with inlet tubes pumping fluids into the microfluidic chamber

The first experiments highlighted an issue, where the optical power drifted away from the optimal point. As a result, the power decreased on a 0.2-0.5 dB/min rate due to mechanical drift causing misalignment in the launch conditions. It made reliable consecutive measurements impossible. Also, the presence of water molecules at the vicinity of the siloxane polymer core created a strong noise component in the measured signal due to the significant change in refractive index profile. Water molecules diffusing into the polymer core also contributed to the random absorption changes as well as the power loss and scattering effects.

This was somewhat mitigated when larger waveguide were fabricated with a height of  $4\mu\text{m}$  and with the deposition of a 5nm  $\text{Ta}_2\text{O}_5$  layer over the core material. As it was described in Chapter 4, the two main advantage of depositing a  $\text{Ta}_2\text{O}_5$  layer on the polymer core are compensating water effects (RI profile shifts) and enhanced sensitivity. However even at this point only proof of concept measurements were possible. Fig. 5.57 shows the result of an experiment, where the optical sensing was coated with the CTPP4-GOX complex and microfluidic channels were attached. The measured power on the  $\text{Ta}_2\text{O}_5$  coated waveguide core before the dye deposition was -50 dBm on the  $4\times 4\mu\text{m}$  core waveguide and the highly absorbing dye added a -25 dB absorption into the system. The maximum allowed dynamic range of the sensor was 25

## Chapter 5 – Device fabrication and experimental results

dB. The expected reaction was an absorption decrease as this is what was observed previously in the glass slide measurements.

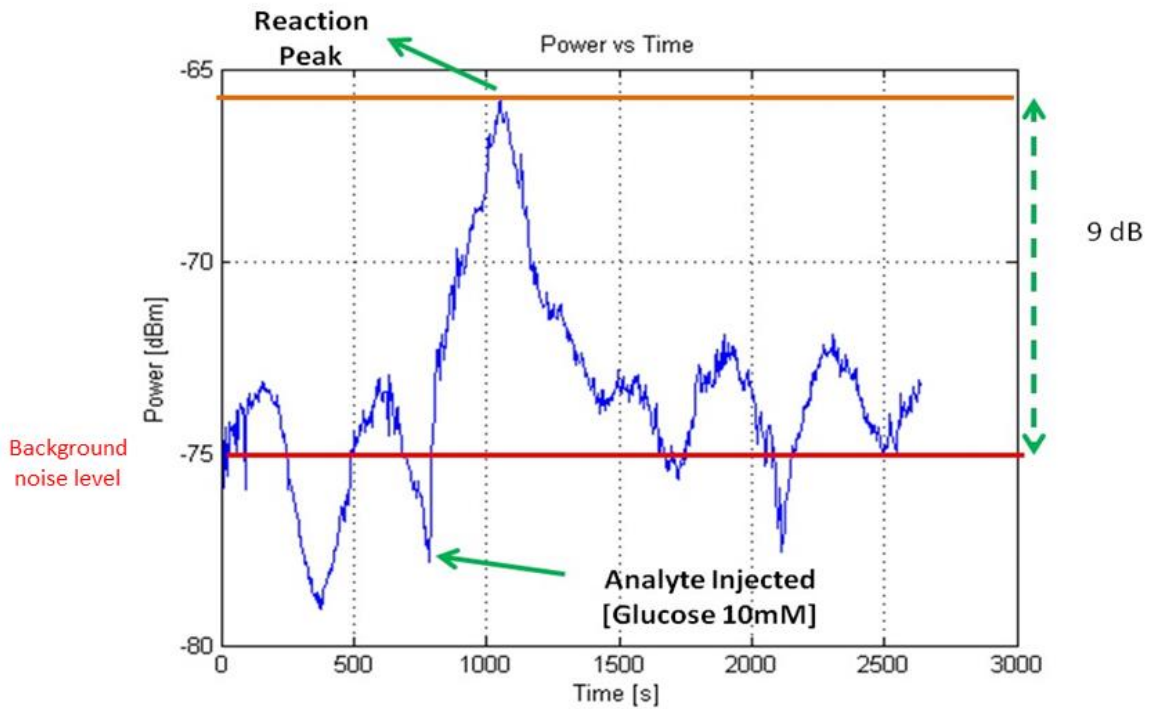


Figure 5.57 – Optical sensing experiment with glucose at 10mM/L concentration (noise

There was a 3dB signal swing present in the system, however the glucose reaction was clearly visible. The absorption decreased to -65dBm, when the glucose was injected and naturally reversed once the reaction finished. Unfortunately, as it was often the case with the glass slide measurements the PDMS layer detached, thus it was difficult to flush out the fluids from the well following the first reaction, making it difficult to make consecutive measurements, which would allow the estimation of the dynamic range. There was a gradual drift present in the measurement along with the previously mentioned signal swing. The swing was probably due to the movement of air within the lab moving the tip of the fibers in the setup responsible for light coupling. Even though air conditioning was turned off it was still present. The drift could have been due to the misalignment of the alignment stage that gradually moved which was probably due to mechanical vibration from the environment. The change in background noise level is probably due to different ambient lighting. During this experiment the light in the lab was turned off, while in the previous waveguide measurements shown on Fig. 5.30. the lights were left on.

## 5.5 Conclusion

This chapter summarised the development of a novel fabrication technique of siloxane polymer waveguide technology and illustrated its potential in the formation of optical lab-on-chip sensors. The adoption of Nano-imprint Lithography was essential in order to extend our fabrication capability. This technique has already been adopted by other members of the Photonic Research Group and will allow the realization of more advanced photonic waveguide structures. Along with this fabrication method, the standard technique was briefly introduced providing a good comparison between the two technologies.

The development of the fabrication has spanned over a year until the very last months of the PhD limiting the realization of all the mentioned sensor structures such as the asymmetric Y-junction. Some issues with silicon patterning mentioned were not investigated further due to the time limit in the clean room as well as the outages of the EBL system, where most of the work was carried out. The formation of single mode waveguide junctions were successful, however highlighted the need for a new technique for light coupling. The standard edge-fire light coupling technique based on fiber coupling has been sufficient for the large core siloxane waveguides, as misalignment tolerances for these features were tolerable using the alignment stages available. However, during the experiments, it became clear that in the case of single mode waveguides with cross sections below  $4 \times 4 \mu\text{m}$  the misalignment tolerance has become an issue. Performing measurements where high sensitivity is required became impractical as the power levels often drifted away due to mechanical vibration from the environment.

The previously discussed CTPP4-GOX recognition layer have been tested on a conceptual level using glass slides and proved that with further work more robust sensors can be realised. The sensor chip has been assembled and tested, however some questions remained. It has been proved that the new dye can react for all three analytes, but only showed convincing reversible reaction on glass slides.

The deposition technique of the recognition layer has been adjusted successfully for siloxane polymer based waveguides, however the buffer fluid removed the dye when it contacted with buffer fluid following the first measurements. Another issue that needs to be addressed is the improvement of PDMS-siloxane polymer adhesion. The standard technique of attaching microfluidic channels to sensor chips is based on the use of oxygen plasma exposure in order to create free radicals on both surfaces. Afterwards, the two surfaces are attached creating a covalent bonding between the sensor chip and PDMS based microfluidics. During our experiments, it became clear that this process was

## Chapter 5 – Device fabrication and experimental results

not necessarily sufficient. The two surfaces often detached during the experiments, which means the two materials were either not compatible or further recipe refinement is necessary.

Regardless, the Ta<sub>2</sub>O<sub>5</sub> coated waveguides with GO-CTPP<sub>4</sub> recognition layer showed a strong reaction. The optical power increased by 9 dB when 10mM/L of glucose was applied. The reaction time was longer than expected around 300 seconds, however this can be attributed to increased diffusion time of glucose molecules into the sensing layer. The recognition layer thickness was greater than the evanescent penetration depth therefore molecular diffusion time might be an issue. Further adjustments to the sensing layer deposition can certainly reduce the reaction time as the glass slide measurements proved the chemical reaction itself is fast.

Based on the result that are presented here, it can be concluded the functionalization of siloxane polymer waveguide have a great potential in realising biochemical sensors in the future. The new fabrication technique will allow the formation of more robust and complex lab-on-chip sensors based on this material.

## 5.6 References

- 5.1. Mark-Steven Steiner, Axel Duerkop and Otto S. Wolfbeis, “Optical methods for sensing glucose”, Chem. Soc. Rev., Vol. 40, pp. 4805–4839, 2011.
- 5.2. A. N. Ovchinnikov, V. I. Ogurtsov, W. Trettnak, D. B. Papkovsky, “Enzymatic Flow-Injection Analysis of Metabolites using new type of oxygen sensor membranes and Phosphorescence phase measurements”, Anal. Lett., Vol. 32, pp. 701-716, 1999.
- 5.3. D. B. Papovsky, “Luminescent porphyrins as probes for optical (bio) sensors”, Sens. Actuators, B, Vol. 11, pp. 293-300, 1993.
- 5.4. T.C. Collins, C. Munkholm, R.E. Slovacek, Bayer Corp., “Optical oxidase enzyme based sensors”, WO Patent No: 2000 011205
- 5.5. M. J. Rooks, H. V. Roussell, and L. M. Johnson, “Polyimide optical waveguides fabricated with electron beam lithography”, Applied Optics, Vol. 29, No. 27, pp. 3880-3882, 1990.
- 5.6. M. V. Foguel, X.-Anh Ton, M. V.B. Zanoni, M.a Del Pilar T. Sotomayor, K. Haupt, B. Tse Sum Bui, “A molecularly imprinted polymer-based evanescent wave fiber optic sensor for the detection of basic red 9 dye”, Sens. and Act. B: Chemical, Volume 218, No. 31, pp. 222-228, 2015.
- 5.7. S. Jiang, Y. Peng, B. Ning, J. Bai, Y. Liu, N. Zhang, Z. Gao, “Surface plasmon resonance sensor based on molecularly imprinted polymer film for detection of histamine”, Sens. and Act. B: Chemical, Vol. 221, Issue 31, pp. 15-21, 2015.
- 5.8. Ying Hao et al. “Design, fabrication and characterisation of polymer based wavelength - division-multiplexing filters for fibre-to-home application”, University of Cambridge, Thesis, 2011.
- 5.9. S.A. Campbell,” The science and engineering of microelectronic fabrication”, 1<sup>st</sup> Edition, 1996
- 5.10. Femtosecond laser multiphoton polymerization, 2011. [Online], Available: <http://www.wophotonics.com>
- 5.11. ACTMOST, “Technology portfolio prototyping mastering and replication”, 2010. [Online]. Available: <http://www.actmost.eu/Access-Units/Prototyping-mastering-replication>.
- 5.12. G. VanSteenberge, “MT-Compatible Laser-Ablated Interconnections for Optical Printed Circuit Boards”, J.T.L., Vol. 22, No. 9, pp. 2083-2090, 2004.
- 5.13. Suganuma D, Ishigure T., “Fan-in/out polymer optical waveguide for a multicore fiber fabricated using the mosquito method”, Opt Express Vol. 26, No. 23, Issue 2, pp. 1585-93, 2015.

- 5.14. Nikos Bamiedakis, Kevin A. Williams, Richard V. Penty, Ian H. White, “Optical Fiber Telecommunications VIA”, 1<sup>st</sup> Edition, Elsevier, 2013.
- 5.15. N. Bamiedakis et al., “Low-cost PCB-integrated Polymer Waveguide Sensor for Gas Detection”, Conference paper on Lasers and Electro-Optics (CLEO), 2011.
- 5.16. H. Schiff, A. Kristensen, “Handbook of Nanotechnology”, Springer, 3<sup>rd</sup> Edition, 2010
- 5.17. D. R. Barbero, M. S. M. Saifullah, P. Hoffmann, H. Jörg Mathieu, D. Anderson, G. A. C. Jones, M. E. Welland, U. Steiner, “High Resolution Nano-imprinting with a Robust and Reusable Polymer Mold”, *Adv. Funct. Mater.*, Vol. 17, pp. 2419–2425, 2007.
- 5.18. P. Dixit, J. Miao, „Effect of SF6 flow rate on the etched surface profile and bottom grass formation in deep reactive ion etching process”, *Journal of Physics: Conference Series* 34, pp. 577–582, 2006.
- 5.19. S. Gilles, “Chemical Modification of Silicon Surfaces for Application in Soft Lithography”, Forschungszentrum, Jülich, Thesis, 2012.
- 5.20. H. D. Rowland, A. C. Sun, P. R. Schunk, W. P. King, J., “Impact of polymer film thickness and cavity size on polymer flow during embossing: toward process design rules for nano-imprint lithography”, *Micromech. Microeng.*, Vol. 15, p. 2414, 2005.
- 5.21. B. J. White and H. J. Harmon, “Novel optical solid-state glucose sensor using immobilized glucose oxidase”, *Biochem. Biophys. Res. Commun.*, Vol. 296, pp. 1069–1071., 2002.
- 5.22. D. Dolphin Ed, “The Porphyrins”, Vol. 6, Part A, Academic Press, New York, 1978.
- 5.23. D. Dolphin Ed, “The Porphyrins”, Vol. 7, Part B, Academic Press, New York, 1978.
- 5.24. C. Peter, K. Schmidt, M. Schiel, J. Wollenstein, “Metallo-porphyrins as gas sensing material for colorimetric gas sensors on planar optical waveguides”, *Proc. Of SPIE*, Vol. 8066, 2011.
- 5.25. R. Bernini, M. TOnezzer, F. Mottola, L. Zeni, A. Quaranta, G. Maggioni, S. Carturan, G. Della Mea, “Volatile organic compounds detection using porphyrin-based metal-cladding leaky waveguides”, *Sens. & Actuators B*, Vol 12, pp. 231-236, 2007.
- 5.26. S. Mathew, A. Yella, P. Gao, R. Humphry-Baker, B. F. E. Curchod, N. Ashari-Astani, I. Tavernelli, U. Rothlisberger, Md. K. Nazeeruddin, M. Grätzel, “Dye-sensitized solar cells with 13% efficiency achieved through the molecular engineering of porphyrin sensitizers”, *Nature Chemistry*, Vol. 6, pp. 242–247, 2014.
- 5.27. N.A. Rakow, K. S. Suslick, “A colorimetric sensor array for odour visualization”, *Lett. Nat.*, Vol 406, pp. 710-713, 2000.
- 5.28. Y. Sunao, K. Kotaro, Y Hiroaki, M. Taku, “Second order non-linear properties of amphiphilic porphyrins in Langmuir Blodgett monolayer assemblies”, *J. Photochem. Photobiol. A, Chem.*,

Vol 87, pp. 115-119, 1995.

- 5.29. S.M. Borisov, V.V. Vasilev, “New optical sensors for oxygen based on photophosrecent cationic water-soluble Pd(II), Pr(II) and Ru(III) porphyrins”, *J. Anal. Chem.*, Vol. 59, pp. 155-159, 2004.
- 5.30. K. Sendhil, C. Vijayan, M.P. Kothiyal, “Nonlinear optical properties of a porphyrin derivative incorporated in Nafion polymer”, *Optical Materials*, Vol. 27, Issue 10, pp. 1606–1609, 2005.
- 5.31. Chao Li, James Ly, Bo Lei, Wendy Fan, Daihua Zhang, Jie Han, M. Meyyappan, Mark Thompson, Chongwu Zhou, “Data Storage Studies on Nanowire Transistors with Self- Assembled Porphyrin Molecules”, *J. Phys. Chem. B*, Vol. 108, Issue 28, pp 9646–9649, 2010
- 5.32. J.H. Fuhrhop, D. Dolphin Ed., “The Porphyrins”, Academic Press, New York, Vol II. 1978.
- 5.33. C. Di Natale, A. Macagnano, G. Repole, G. Saggio, A. D’Amico, R. Paolesse, T. Boschi, “The exploitation of metalloporphyrins as chemically interactive material in chemical sensors”, *Mat. Sci. and Eng.*, Vol. 5, pp. 209-215, 1998.
- 5.34. M. Tonzzer, G. Maggioni, A. Quaranta, S. Carturan, G. Della Mea, “Optical sensing properties of CoTTP thin films deposited by glow discharge induced sublimation”, *Sens. Actuators B*, Vol 122, pp. 613-619, 2007.
- 5.35. J.A.J. Brunik, C. Di Natale, V. Campo dall’Orto, A. Macagnano, A. Angelaccio, A. Sgarlata, J. Hurst, I. Rezzano, M. Mascini, A. D’Amico, Porphyrin thin films coated quartz microalances prepared by electropolymerization techniques, *Thin Solid Films*, Vol. 354, pp. 245–250, 1999.
- 5.36. C. Di Natale, D. Salimbeni, R. Paolesse, A. Macagnano, A. D’Amico, “Porphyrins-based opto- electronic nose for volatile compounds detection”, *Sens. Actuators B*, Vol. 65, pp. 220–226, 2000.
- 5.37. M. Andersson, M. Holmberg, I. Lundstrom, A. Lloyd-Spetz, P. Martensson, R. Paolesse, C. Falconi, E. Proietti, C. Di Natale, A. D’Amico, “Development of a ChemFET sensor with molecular films of porphyrins as sensitive layer”, *Sens. Actuators B*, Vol. 77, pp. 567–571, 2001.
- 5.38. M. Tonzzer, A. Quaranta, G. Maggioni, S. Carturan, G. Della Mea, “Optical sensing responses of tetraphenyl porphyrins toward alcohol vapours: A comparison between vacuum evaporated and spin-coated thin films”, *Sens. Actuators B*, Vol 122, pp. 620-626, 2007.

- 5.39. K.A. Macor, T. G. Spiro, “Porphyrin electrode films prepared by electrooxidation of metalloporphyrins”, *J. Am. Chem. Soc.*, Vol 105, pp. 5601-5607, 1983.
- 5.40. Akrajas, M.M. Salleh, M. Yahaya, “Enriching the selectivity of metalloporphyrins chemical sensors by means of optical technique”, *Sens. Actuators B*, Vol 85, pp. 191-196, 2002.
- 5.41. I. Timofeev, K.L. H. Carpenter, J. Nortje, P. G. Al-Rawi, M. T. O’Connell, M. Czosnyka, P. Smielewski, J. D. Pickard, D. K. Menon, P. J. Kirkpatrick, A.K. Gupta, P. J. Hutchinson, “Cerebral extracellular chemistry and outcome following traumatic brain injury: a microdialysis study of 223 patients”, *Brain*, Vol. 134, pp. 484–494, 2011.
- 5.42. S. M. Usman Ali, O. Nur, M. Willander and B. Danielsson, “A fast and sensitive potentiometric glucose microsensor based on glucose oxidase coated ZnO nanowires grown on a thin silver wire”, *Sens. Actuators B*, Vol. 145, pp. 869–874, 2010.
- 5.43. Novoselov K, Geim A, Morozov S, J. D, Zhang Y, Dubonos S, Grigorieva I, Firsov A.” Electric field effect in atomically thin carbon films”, *Science*, Vol. 306, Issue 10, pp. 666-669. 2004
- 5.44. A. M, Tung V, Kaner B. “Honeycomb carbon: a review of graphene”, *Chemical Reviews*, Vol 110, Issue 1, pp. 132-145, 2010.
- 5.45. Dutta S, Pati S., “Novel properties of graphene nanoribbons: a review”, *Journal of Materials Chemistry*, Vol. 20, Issue 8, pp. 8207-8223, 2010.
- 5.46. Y. Hu, X. Sun, “Chemically Functionalized Graphene and their applications in electrochemical energy conversion and storage”, *Adv. in Graphene Sci*, 1<sup>st</sup> Edition, 2013.
- 5.47. A. K. Geim, K. S. Novoselov,” The rise of graphene”, *Nature Materials*, Vol 6, pp. 183 - 191, 2007.
- 5.48. Y. Xu, Z. Liu Zhang, Y. Wang, J. Tian, Y. Huang, Y. Ma, X. Yhang, Y. Chen, “A graphene hybrid material covalently functionalized with porphyrin: Synthesis and optical limiting property”, *Adv. Mater.*, Vol 21, pp. 1275-1279, 2009.
- 5.49. A. C. Ferrari, F. Bonaccorso, V. Fal’ko, K. S. Novoselov, S. Roche, P. Bøggild, S. Borini, Frank, H. L. Koppens, V. Palermo, N. Pugno, J. A. Garrido, R. Sordan, A. Bianco, L. Ballerini, M. Prato, E. Lidorikis, J. Kivioja, C. Marinelli, T. Ryhänen, A. Morpurgo, J. N. Coleman, V. Nicolosi, L. Colombo, A. Fert, M.Garcia-Hernandez, A. Bachtold, G. F. Schneider, F. Guinea, C. Dekker, M. Barbone, Z. Sun, C. Galiotis, A. N. Grigorenko, G. Konstantatos, A. Kis, M.l Katsnelson, L. Vandersypen, A. Loiseau, V. Morandi, D. Neumaier, E. Treossi, V. Pellegrini, M. Polini, A. Tredicucci, G. M. Williams, B. Hee Hong,

- J.-Hyun Ahn, J. Min Kim, H. Zirath, Bart J. van Wees, H. van der Zant, L. Occhipinti, A. Di Matteo, I. A. Kinloch, T. Seyller, E., Quesnel, X. Feng, K. Teo, N. Rupesinghe, P. Hakonen, S. R. T. Neil, Q. Tannock, T. Löfwander, J. Kinaret, “Science and technology roadmap for graphene, related two- dimensional crystals, and hybrid systems”, *Nanoscale*, Vol 7,p. 4598, 2015.
- 5.50. Guo B, Liu A, Chen E., “Controllable N-doping of graphene”, *Nano Letters*, Vol 10, Issue 12, pp. 4975-4980, 2010.
- 5.51. Li N, Wang Z, Zhao K “Large scale synthesis of N-doped multi-layered graphene sheets by simple arc-discharge method”, *Carbon*, Vol 48, Issue 1, pp. 255-259, 2010.
- 5.52. Panchokarla L, Subrahmanyam K, Saha S.,” Synthesis, structure and properties of boron and nitrogen doped graphene”, *Advanced Materials*, Vol 21, Issue 46, p. 4726, 2009.
- 5.53. Kim H, Kim H.” Preparation of carbon nanotubes by DC arc discharge process under reduced pressure in an air atmosphere”, *Materials Science and Engineering B*, Vol 133, Issue 1-3, pp. 241-244, 2006.
- 5.54. Wang X, Li X, Zhang L., “N-doping of graphene through electrothermal reactions with ammonia.”, *Science*, Vol 324, Issue 5928, pp. 768-771. 2009.
- 5.55. G. B. Barin, Y. Song, I. Gimenez, A. G. S. Filho, L. S. Barreto, J. Kong, “Optimized graphene transfer: Influence of polymethylmethacrylate (PMMA) layer concentration and baking time on graphene final performance”, *Carbon*, Vol. 84, pp. 82-90, 2015.
- 5.56. M. Hera, R. Beamsa, L. Novotny, “Graphene transfer with reduced residue”, *Physics Letters A*, Vol. 377, Issues 21–22, pp. 1455–1458, 2013.

## Chapter 6 - Appendix

### 6.1 Review of optical sensing techniques for brain microdialysis

The editors of the Lancet Neurology journal have described traumatic brain injury as a silent epidemic [6.1] as result of the recent revelations in the annual US incidence reports [6.2]. According to them, TBI related incidences are higher than breast cancer by almost 4 fold and cost and estimated \$60 billion in 2000 [6.1]. These incidences include intracerebral haemorrhage, cerebral contusion or axonal injury. Following an accident, the injured area becomes “ischemic” due to loss of blood flow. As a result, biochemical changes occur in the brain metabolism that can serve as a good indicator to monitor the outcome of patients. Approximately 40% of TBI patients deteriorate in the day following their injury, while treated in intensive care units.

By monitoring the cerebral extracellular biochemistry using microdialysis, researchers at NCCU have identified the metabolic derangements associated with such events. Their study [6.2] assessed the distribution of glucose, lactate and pyruvate changes in the first 72 hours following a brain injury in various different patient groups over a six-month period. Samples were collected every hour and analysed by the previously mentioned ISCUS flex microdialysis analyser. It was concluded that the main indicator is the lactate/pyruvate ratio as the most persistent predictor for patient outcome. The lactate/pyruvate ratio can discriminate between favourable and unfavourable outcomes in addition to mortality. Other groups have verified the lactate to pyruvate ratio (L/P) and lactate to glucose ratios (L/G) as being the most prominent predictors [6.3] as well as providing a comparison between biochemical changes occurring in the arterial blood and brain fluid. “Cerebral microdialysis is important for detailed insight into cerebral metabolic alterations, which are missed by simply investigating the impact of insulin on changes in arterial blood glucose levels” [6.4]. The majority of the research is focusing on blood glucose. However, the range at which glucose needs to be monitored is much higher (3-50mM) than is required for brain microdialysis (0-5 mM). Moreover, sample volumes for brain microdialysate analysis are very low (nanoliters) for continuous monitoring as the maximum brain fluid extraction rate from

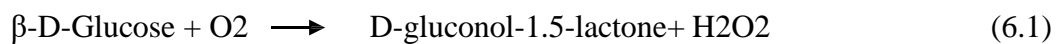
the cerebral is 0.3  $\mu\text{L}/\text{min}$ . Faster flow rates may perturb the local biochemistry in the microenvironment around the catheter tip. The rest of this chapter is aimed at providing an overview of different optical sensor technologies used in conjunction with various biochemical recognition elements relevant to this application.

### 6.1.1 Glucose Sensing Review

There are approximately 150 million people around the world currently suffering from diabetes. This number is estimated to double by 2025 according to a study in [6.4]. The glucose sensor industry is probably the biggest single one in the diagnostic field, estimated to be 30 billion Euros per year. The demand for continuous online blood glucose monitors has dramatically increased as it often requires insulin administration several times a day. Fortunately, there are dozens of low cost commercially available devices available, most of them based on electric transduction. Optical sensing schemes have not had the success of electrochemical schemes. However, they are a matter of active research. Methods such as absorptiometry, reflectometry, fluorescence, and surface plasmon resonance had the greatest success. However, almost all reversible continuous sensors are based on either fluorescence or surface plasmon resonance (SPR). No reflectometric or interferometric method is known that could enable continuous reversible sensing either in blood or in brain fluid [6.5].

Sensor Classification based on method of recognition

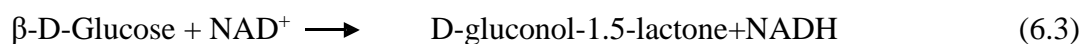
Selection recognition or metabolism in the case of enzymes is the main prerequisite for glucose sensing. There have been several proposed methods with different limitations in terms of dynamic range, reversibility, lifetime and sensitivity. The first continuous sensing schemes were based on detection of oxygen consumption [7.6] according to equation (7.1) that catalyzed by glucose oxidase (GOX). Alternatively, the  $\text{H}_2\text{O}_2$  generation can be monitored as well.



Another option is to monitor the formation of protons (i.e. via the decrease in pH) e.g. in equation 6.2.



Another enzyme glucose dehydrogenase reaction is also used to sense glucose by monitoring the glucose to gluconolactone according to equation (6.3).



## Chapter 6 - Appendix

One way of monitoring the NADH formed is to excite the dye at 340nm, which results in fluorescence at 460nm [6.7]. Unfortunately, the NADH monitoring is irreversible, therefore cannot be used for this application.

Another enzymatic procedure to monitor glucose levels by sensing cofactor FAD, a yellow coenzyme with a strong intrinsic green fluorescence, is converted into its reduced form (FADH<sub>2</sub>) before being converted back by molecular oxygen. [6.8]



The ISCUS device is using an old-fashioned irreversible dye based on the GOD-POD method, Glucose is oxidized by glucose oxidase (GOD) to produce gluconate and hydrogen peroxide. The hydrogen peroxide is then oxidatively coupled with 4-amino-antipyrene (4-AAP) and phenol in the presence of peroxidase (POD) to yield a red quinoneimine dye (eq. 6.6) that is measured at wavelength of 505nm. The absorbance at 505 nm is proportional to the concentration of glucose in the sample. It is not applicable for continuous sensing. Moreover, it also requires elevated temperature. The enzymatic activity is most efficient at 37 degrees, which means it requires temperature control.



There are five main methods for the recognition of glucose, their main features are summarized in Table 6.1.

1. ***Kinematic Enzymatic Assays:*** The recognition of glucose by certain enzymes (or coenzymes) that subsequently undergo changes in their intrinsic absorption and/or fluorescence, or carry a (fluorescent) label placed near the site of interaction. Enzymes such as glucose oxidase (GOX), glucose dehydrogenase or glucokinase.
2. ***Affinity binding of glucose:*** Measurement of formation or consumption of metabolites as caused by certain enzymes (such as GOX). The enzymatic factors that could be monitored: oxygen consumption, hydrogen or acid produced during the enzymatic reaction.
3. ***Organic Boronic Acids:*** These are robust molecular receptors. However, they are rarely specific for glucose, therefore interference is an issue. Therefore, it is used for blood glucose measurement, where it has a relatively high concentration compared to other substances, this is not the case for brain fluid.
4. ***Affinity binding for ConA:*** Based on affinity binding of glucose to the plant lectin concanavalin A (ConA). This utilises competitive binding and a labelled

carbohydrate such as dextran or glycosylated protein.

5. **Glucose Binding Proteins (GBP):** Specifically engineered proteins, which are capable of changing their optical properties on binding glucose. Although, they can be only detected

in the UV light regime, unless labelled with fluorophores to shift the change of optical signal towards the visible range of the spectrum. The use of a labelled protein is preferred, because it enables the optical properties of the system to be finely tuned.

*Table 6.1 – Summary of the different recognition methods*

Method of Recognition	Pros	Cons	Feasibility for clinical Application
Kinetic Enzymatic Assays using GOx	Fully Reversible, Range of 1- 20mM	Short enzymatic life time, critically time dependent	Short Enzymatic lifetime
Affinity binding of glucose to apo-GOx	Stable, Fully reversible, not time dependent	Short dynamic range (1 $\mu$ L-100 $\mu$ L), specific labelling is needed, pH dependent	Very small dynamic range
Boronic Acid	Stable	Slowly reversible, strongly pH dependent	Not applicable for continuous sensing
ConA	Dynamic Range: 1-200mM, no pH dependence	Fairly specific for glucose, slow system, ConA is toxic	Not applicable for continuous sensing
GBP	Fully reversible, fairly simple, Refractive Index change at binding, hardly pH dependent	Fairly specific for glucose, low concentrations only unless genetically engineered	Complex chemistry, only one example of GBP with refractive index change at binding

## Chapter 6 - Appendix

### Absorption based Glucose Sensors

Absorption based glucose sensors have been actively researched since the mid 80's and they are currently the most widely used lab instruments due to their simplicity and low-cost. There are a number of different strategies for designing an absorption-based optical biosensor. One is to detect the light absorption directly, which relies tracking the changes in the optical absorption lines or bands of the measure and at a convenient wavelength, at which the absorbance is directly proportional to the concentration. Indirect absorption is another method, where a secondary reagent is used to mediate the sensing, e.g pH sensors use an indicator dye whose colour/absorption characteristics change as a function of pH.

A summary of absorption based sensors is in Table 6.2. Where all the sensors use indirect sensing monitoring, usually using oxygen as an indicator. The most successful schemes are based on optrodes in conjunction with a flow injection system. The employment of such system provides higher dynamic range, but often on the expense of the detection limit. A HPLC pump was employed in order to provide chemical mixing and temperature control. For continuous sensing reversibility is crucial, however their work did not investigate it. The only waveguide-based glucose sensor [6.9] has a good dynamic range of 3.4-100mM, however the detection limit is very high compared to ISCUS, where it is 0.1mM. Horseradish peroxidase was also used with GOx for glucose immobilisation with good detection limit around 1.5 $\mu$ M, however at the expense of dynamic range. The system responded very fast to various concentrations in a few seconds. One of the most successful real online glucose sensor was [6.10], where they used Meso-tetra(4- carboxyphenyl) porphine (CTPP<sub>4</sub>) which binds reversibly to immobilized glucose oxidase (GOD), resulting in an absorbance peak for the CTPP<sub>4</sub>-GOD complex at 427 nm. The dynamic range was 1.1-10mM and it responded to glucose in 6 seconds. This immobilisation technique could be a good start for a polymer-based online waveguide system. However, further investigation is required to find out how compatible this receptor could be for lactate and pyruvate.

Table 6.2. – Summary of absorption based glucose sensor

Technology	Analytical Range	Detection Limit	Reversibility	Response Time	Laser	Benefits	Comment	Reference & Year
Polymer waveguide sensor for early diagnostic and wellness monitoring	2.78-27.78 mM	0.56mM ,	No	3min	LED, ?nm			[6.11] 2011
Planar Optical Waveguide, Absorption, K9-Glass	3.4-110 mM	3.4mM	NA	NA	488 nm,argon laser	waveguide based absorption sensor.	GOD-POD Method	[6.12] 2007
Fibre optic Optrode Sensor	2-10 mM	2mM	2-15min	10 s to 5 min	490nm	Reversible and fast	GOD-POD/ FAD, 30 C temp. control	[6.13], 1997
Reagentless flow-through sensor	1.5-55uM	1.5uM	2min	Few seconds	Working: 376/450nm	Very reversible, fast, "reagentless"	Flow Rate:0.85mL/min GOx/HRP	[6.14] 2007
Reagentless, Abs. Sensor	1.5-300 uM	1.5uM	5min	Few seconds	424nm	Very reversible, fast, "reagentless"	HRP/H2O2	[6.15], 2007
Novel optical solid-state glucose sensor	1.1-11 mM	1,1mM	Yes	6s	424nm		GOD with CTPP , reversible dye	[6.10],2002

### Fluorescence Glucose Sensors

Fluorescence based continuous glucose sensors are one of the most actively researched areas. This approach is usually based on measuring the consumption of oxygen using probes whose fluorescence is quenched by oxygen. Typical probes (summarised in Table 6.3) for oxygen include luminescent complexes of Ruthium, platinum or palladium which are strongly quenched by oxygen. These probes are usually fabricated on the top of the waveguide/fibre core with a thickness of 2-10 $\mu\text{m}$ , while the enzymes are immobilised in or on this layer. Various probes have been reported whose fluorescence or lifetime is quenched by molecular oxygen. Decacyclene complexes, such as Pt(II), Pt(II), Ruthium dyes are the most widely used, because they can be excited with visible light.

The most robust sensor architectures are usually optical optrodes [6.16-20] combined with a microfluidic flow-through cell. A flow-injection system is used to create the enzymes complex such as glucose oxidase then it is pumped through a micro cell, where it interacts with the probe. The oxygen variations are sensed by the probe, which in turn emits the light at a specific wavelength and intensity as a function of the glucose concentration. GOD displays absorption maxima in the visible region at about 380 and 450 nm and an intrinsic fluorescence emission maximum at about 530 nm with a decacyclene probe, as it was investigated in [6.16,7.18-19]. Alternatively, the GOX- FAD reaction has its absorption maxima around 470nm, while its fluorescence is monitored above 480- 520nm [6.20]. One of the earliest continuous fluorescence-based glucose sensor with FIA was done in 1989 [6.21], where they used the GOD enzyme with decacyclene as reversible oxygen indicator. They achieved a 0.01-2mM analytical range within 60 seconds. Moreover, the addition of a dialysis membrane protected the membrane from protein contamination resulting in an extended dynamic range of 1-200mM with a response time of 2-5 minutes. From the aspect of brain dialysis, probably the work in [6.19-22] provides the best starting point for the research due to their reversibility and fast response.

Almost all of the continuous sensor designs were based on optical fibre based rather than waveguides. Theoretically the pyruvate oxidase (POX) and lactate oxidase (POX) enzymatic processes can be monitored as well. An interesting research could be to combine a novel oxygen sensor architecture with a probe (Ruthium, Palladium or Platinum) to monitor glucose (Fig 6.2).

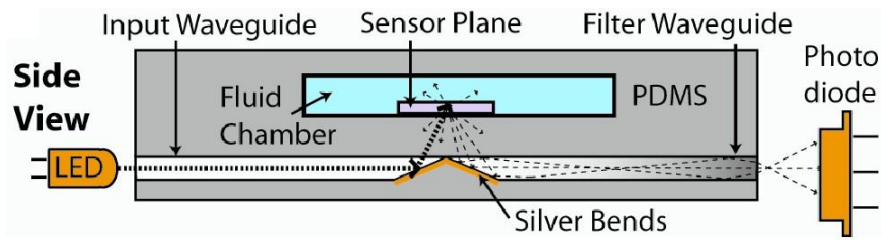


Figure 6.2 – Polymer Waveguide based oxygen sensor chip [6.28]

Table 6.3 – Summary of fluorescence based glucose sensors

Technology	Analytical Range	Detection Limit	Reversibility	Response Time	Laser Excitation/Emission	Benefits	Comment	Reference & Year
Online Oxygen Optrode with FIA	0-30mM, Glucose and Lactate	NA	NA	50-80s	410nm/495nm	Online and continuous,	Stable for 4 weeks, GOD-POD/POD, 37C temp., control	[6.22], 1990
Fibre optic Optrode Sensor	1.5-2mM	0.01mM	1-10min	2-30min	450nm/500nm		GOD-POD/Oxygen, FLU	[6.23], 1989
Fibre optic (NADH)	1.1-11mM	0.6mM	No		360nm/ 460nm			[6.24], 1989
Fast responding fibre optic optrode flow-thorough sensor	0.01-2mM (possible up to 200mM)	0.01mM	No	60s (3-5min for 200mM)	410nm/500nm	Stable up to 20 weeks	GOD based, 0.89ml/min, decacyclene probe	[6.25], 1989
FLU experiment based on GOx	2.5-20mM	2.5mM	NA	5min	278nm/340nm	GOx entrapped in membrane	GOD/FAD	[6.26], 2007
Phosphorescence (Fiber optic)	0.2-20mM	NA	Yes	2-5min range)		Compact, flow-through	Platinum dye	[6.27], 1999
Optrode based, FIA	1-80mM	1mM	NA	100s	465/610nm		2D crystalline bacterial surface layers	[6.18],1996
Optical Fibre based, Ruthium based Continuous, Optrode	0.1-30mM	0.1mM	Yes	20s	460/600nm	30 days lifetime	GOx and Ru probe, Sol-gel	[6.19], 2007

## Interferometric Sensors

Interferometric structures are very popular due to the fact that they can be easily integrated, are compact and can be highly sensitive. The interaction between the sample and the optical signal propagating in the sensor produces a change of optical mode effective index and then in its phase. The phase to amplitude conversion is done by interferometric optical architectures. One previously mentioned architecture is the Mach-Zehnder approach (Fig. 6.3), which provides high sensitivity and is widely used. The optical signal is split by a Y-junction in to two signals, one travels through the reference arm, while the other travels through the sensing arm. At the sensing arm the cladding is removed and layered with a receptor that either changes its refractive index as a function of the analyte concentration (homogeneous sensing) or changes the thickness of a molecular layer (surface sensing).

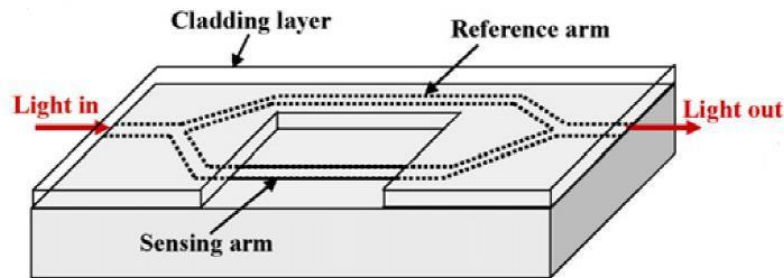


Figure 6.3. – MZM Interferometer Sensor [7.29]

A simple example for such sensor is shown on Fig 6.4 [6.30], where they used a HeNe laser at 633nm without any receptors. The relation between the concentration of sugar and the output signal from the interferometer is nearly linear in the range from 0% to 1% concentration of the sugar solution, which caused  $1.4 \times 10^{-4}$  refractive index change. As the figure below shows the concentration of sugar was much higher than what is expected in the brain fluid (0.1mM – 5.56mM), which clearly indicates the need for binding proteins or enzymes to achieve the required sensitivity.

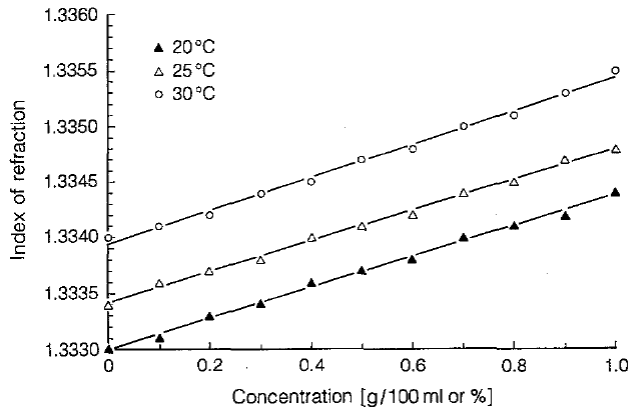


Figure 6.4. – Sensitivity of label-free MZM [6.31]

The other promising approach is based on Young Interferometry, therefore the change in refractive index is determined by the change in the interference pattern, which is captured by a CCD camera (Fig. 6.5). The change in the interference pattern is analysed by taking the FFT of the interference pattern.

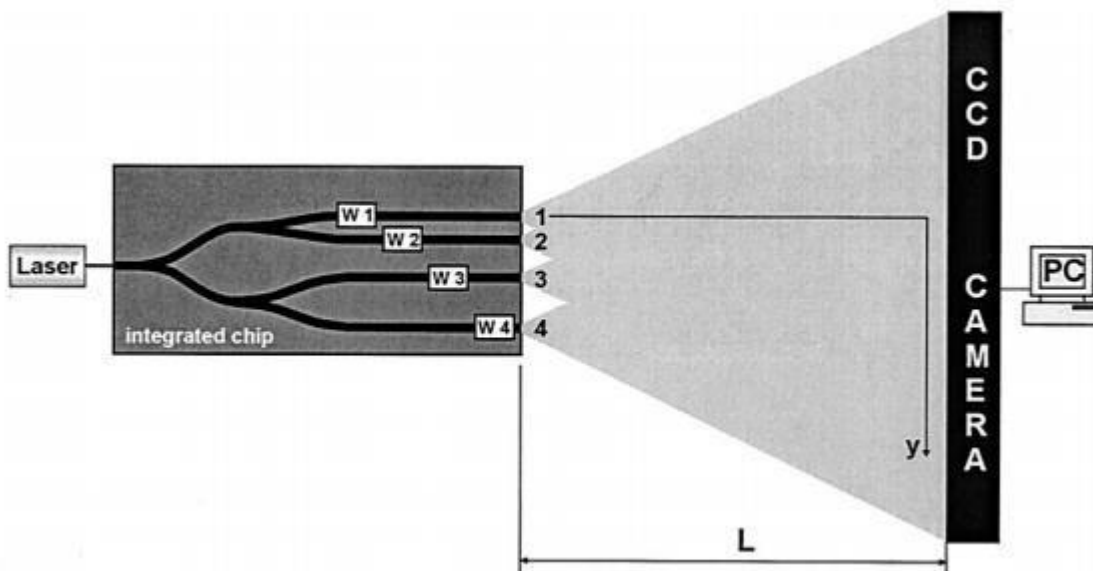


Figure 6.5 – 4-arm young interferometer [6.29]

Another type of interferometric sensor (Fig. 6.6) is based on the measurement of phase difference due to polarisation rotation. In [6.32] the linearly polarised light passes through the glucose solution and the left and right-circularly polarised light experiences different refractive index. The dynamic range of the sensor was 0-11mM with a resolution on 0.22mM, which is promising. However, the system requires a quarter-wave plate and the sample cell needs to be rotated by a motor, which makes the PCB integration questionable.

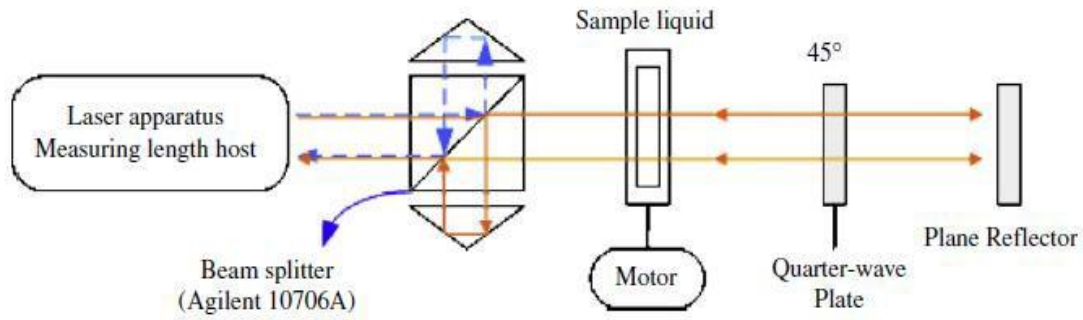


Figure 7.6 – Schematic of the High-precision optical metrology system for determining refractive index of liquid glucose solution. [6.32]

An optical fibre based heterodyne interferometer that is proposed in [6.33] shown on Fig. 6.7 was capable of rapid glucose measurements in 3 second with the dynamical range of 0.1-7.6mM.

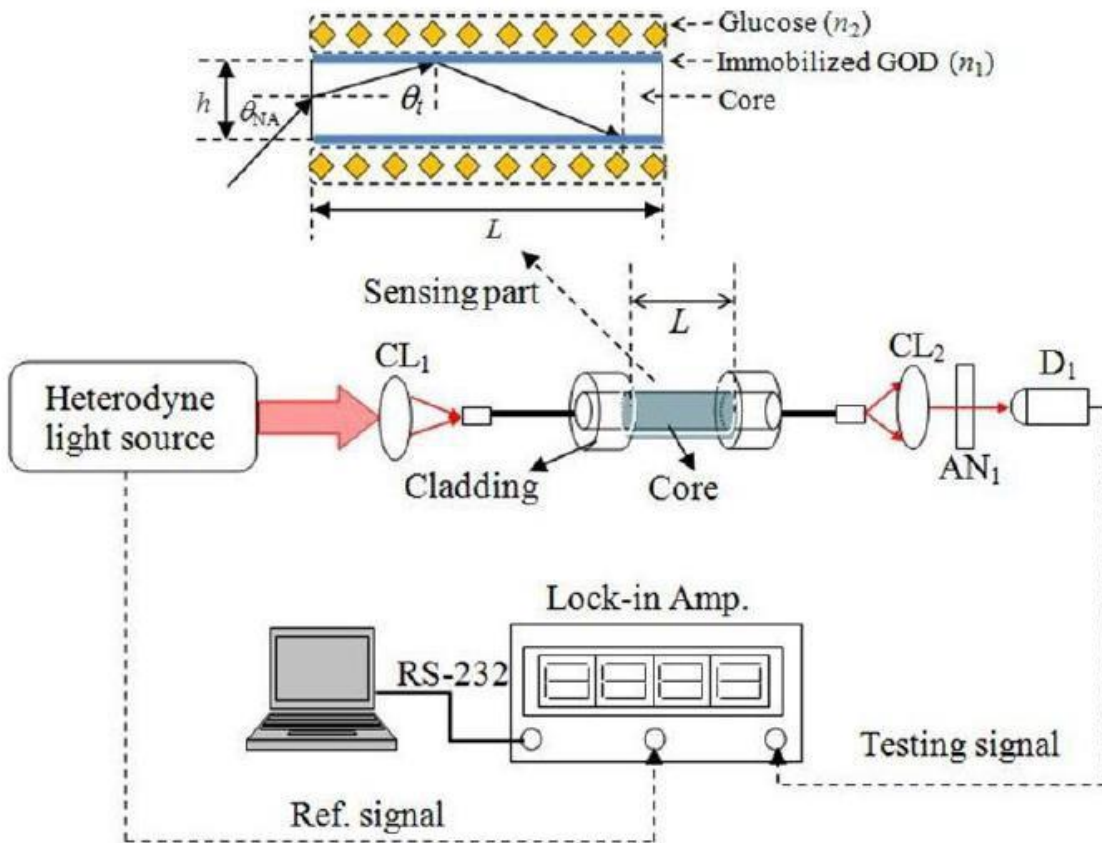


Figure 6.7 – Schematic of the heterodyne interferometer based fibre sensor [6.33]

The same group a year later in 2011 improved the system with an additional reference fibre. The sensor was reusable, while the sensitivity remained the same [6.34].

## Chapter 6 - Appendix

Based on the interferometric techniques summarised in Table 6.3, the MZM and Young architectures proved to be highly sensitive. However, they have been only implemented at the near

IR wavelength range, where recognition selectivity is limited.. The recognition elements designed for biochemical sensing are mostly designed to operate in the visible spectrum. Low-cost high quality light sources are not available for photonic integration at visible wavelengths at the moment. As a result, designing a practical low cost lab-on-chip sensor is not possible at the moment. Without the required binding agents at the longer wavelengths the sensor would have low selectivity.

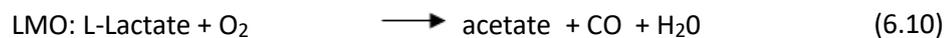
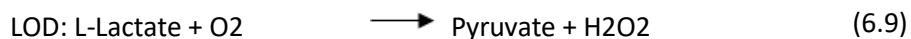
## Chapter 6 Appendix

Table 7.4. – Summary of Interferometric Glucose Sensors

Technology	Material	Detection Limit	Laser	Benefits	Comment	Reference & Year
Label-free Glucose, MZM	Pyrex glass	0.5mM,	633nm	Label-free	$\Delta n=10^{-4}$	[6.30] 1992
Periodic MZM	K9 glass	0.5mM			$\Delta n=10^{-4}$	[6.34], 1998
Broadband MZM	Silicon		(450nm-750nm)	Good Dynamic Range	Only proposed, simulation based	[6.35],2008
Integrated Young Interferometer	Silicon	1.7mM			$\Delta n=10^{-8}$ , 15mm optical path length	[6.36], 2008
Real-time measurement of glucose concentration and average refractive index using a laser interferometer	NA	NA	NA, probably HeNe	Requires optics that difficult to integrate on PCB	a polarized phase detection technique	[6.31], 2008
Fabrication of glucose fibre sensor based on immobilized GOD technique for rapid measurement	Glass fibre	1 $\mu$ M	HeNe 632nm	10uL Sample Volume, fast response below 1s, Reusable on 10x	GOX, Dye: propyl aldehyde, suberic acid bis sodiumsalt with phosphate, Response time 3s	[6.32-33], 2010, 2011

## 6.1.2 Lactate Sensing Review

Lactate sensors are essential in clinical analysis for diagnosis of lactate acidosis as a result of metabolic, respiratory, or haemodynamic disturbance. Typical fields of application are sport medicine for exercise control and the food industry. Four different kinds of enzymes are frequently used for L-lactate determination: Lactate dehydrogenase (LDH), cytochrome b2, lactate oxidase (LOD) and lactate monooxygenase (LMO). A reaction scheme of LMO is shown in the following equation:



The LDH reaction is most often used for discontinuous routine analysis in clinical laboratories. However, it is irreversible, and therefore it is not applicable for a potential continuous brain fluid analyser. Lactate sensors for continuous determination of lactate are mostly based on electrodes. Thus, lactate can be determined with an oxygen or hydrogen electrode by using the enzymes LMO or LOD. For optical sensing usually LDH, LOD and LMO are used. As the summary shows in Table 6.5, the related articles are scarce compared to glucose. Real online monitoring of lactate has only been done in [6.37] by using absorption, but it is irreversible and requires temperature control. The fastest responding sensor was in [6.38], but it is based on LDH fluorescence, which is irreversible as well. A summary of different pyruvate sensors is given in Table 6.5.

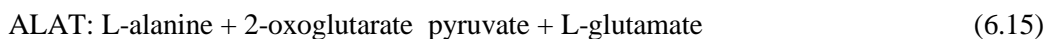
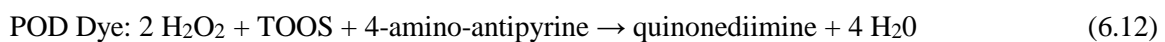
Table 6.5. – Summary of optical lactate sensors

Technology	Analytical Range	Detection Limit	Reversibility	Response Time	Laser Excitation/Emission	Benefits	Comment	Reference & Year
Absorption/ LDH based	0.2-1mM	0.2mM	No	60s	Abs: 340nm	Fast	Sol-gel immobilisation, disposable	[6.37], 2002
Fiber Optic Optrode , FIA, FLU, LMO	2-50mM , 0.3-6mM	2mM , 0.3mM	10min	2-3min, 2.5-5min	410/450nm	Reversible, Good Range	Oxygen sensor, LOD1.2ml/min, V=20uL	[6.38.], 1990
Fibre Optic Sensor, FLU, LMO	0-5mM	50µM	5min	3min	470/600nm	Resistive to Interference	Ruthium Dye, oxygen detection	[6.39], 2001
Fibre Optic Optrode, FLU, LMO	0.5-1mM , 3mM with FIA	0.5mM	10min	1-3min	410/500nm	Fully reversible	Flow rate: 1.2ml/min	[6.40], 1989
FLU sensor, fiber optic	50nm-50uM	50nM	NA	2min	315/425nm	Very low detection limit	LOX/HRP, Optrode	[6.41], 1995



### 6.1.3 Pyruvate Sensing

Pyruvate is the least researched substance out of the three analytes. The enzymatic process for the ISCUS device is the following, Pyruvate is enzymatically oxidised (PyrOx) in presence of inorganic phosphate (Pi). Peroxidase (POD) catalyses the reaction between the hydrogen peroxide formed, TOOS and 4-amino-antipyrine to form the red-violet coloured Quinonediimine. It is unfortunately irreversible and requires temperature control as it is the case for most of the previously described peroxidises-based processes.



The enzymatic processes described in equations 6.11-15 are summarised on Fig. 6.8 where the required dyes are indicated as well [6.41-43]. As table 6.6 shows, a few of the relevant existing pyruvate sensors require temperature control and are non-reversible.

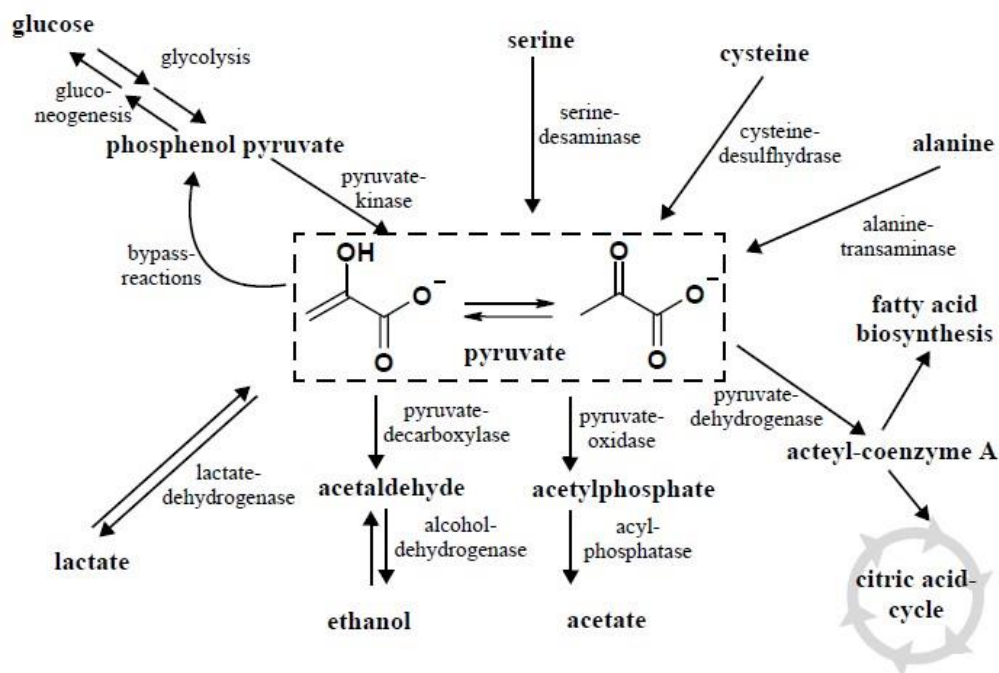


Figure 6.8. – Pyruvate is a key intermediate in the anaerobic and the aerobic metabolism of almost all living organisms [6.41]

The currently existing optical sensors are based on irreversible enzymatic recognition. An alternative way of sensing pyruvate is to use a pH sensitive dye as discussed in [6.7].

*Table 6.6 – Summary of optical pyruvate sensors*

Technology	Analytical Range	Detection Limit	Reversibility	Response Time	Laser Excitation/Emission	Benefits	Comment	Reference & Year
Spectrum Analysis of pyruvate oxidase, ABS	NA	NA	NO	7min	ABS:550nm		POD method, 37C temps control	[6.42], 1990
Dual-enzyme fiber optic biosensor for pyruvate, FLU, Optrode	0.02-1mM	0.0084 mM	No	24min	340/410nm		LDH, 30 C temp. Control,	[6.43], 1997
LDH, Sol-gel method, ABS	0-1.5mM	50uM	No	NA	ABS: 340nm		LDH,TEOS dye sol-gel films, 37C	[6.44], 1997

## 6.2 References

- 6.1 L. Edge, "Traumatic brain injury: time to end the silence." *Lancet Neurol.*, vol. 9, pp. 331., 2010.
- 6.3 Whitfield, P., Thomas, E., Summers, F., Whyte, M., and Hutchinson, P., "Head injury- a multidisciplinary approach", Cambridge University Press, 1<sup>st</sup> Edition, 2009.
- 6.4 Finkelstein, E., Corso, P., and Miller, T., "Incidence and economic burden of injuries in the United States"; Oxford University Press, 1<sup>st</sup> Edition, 2006.
- 6.5 I. Timofeev, K. L. H. Carpenter, J. Nortje, P. G. Al-Rawi, M. T. O'Connell, M. Czosnyka, P. Smielewski, J.D. Pickard, D. K. Menon, P. J. Kirkpatrick, A. K. Gupta, P. J. Hutchinson, "Cerebral extracellular chemistry and outcome following traumatic brain injury: a microdialysis study of 223 patients", *Brain*, vol. 134, pp. 484–494, 2011.
- 6.6 Roman Meierhans, Markus Béchir, Silke Ludwig, Jutta Sommerfeld, Giovanna Brandi, Christoph Haberthür, Reto Stocker and John F Stover, "Brain metabolism is significantly impaired at blood glucose below 6 mM and brain glucose below 1 mM in patients with severe traumatic brain injury", *Critical Care*, vol. 14, R13, 2010.
- 6.7 National institute of Diabetes and Digestive and Kidney Diseases, "Diabetes Overview" NIH 94-3235., 1994
- 6.8 M., S. Steiner, A. Duerkop, O. S. Wolfbeis, "Optical methods for sensing glucose", *Chem. Soc. Rev.*, vol. 40, pp. 4805–4839, 2011.
- 6.9 Maria C. Moreno-Bondi' and Otto S. Wolfbeis, "Oxygen Optrode for Use in a Fiber-optic Glucose Biosensor", *Anal. Chem.*, vol. 62 , pp. 2377-2380, 1990.
- 6.10 R.Narayanaswamy , F.Sevilla, "An optical fibre probe for determination of glucose based on immobilized glucose dehydrogenase", *Analytical Letters*, vol. 21, issue 7, pp. 1165-1175, 1988.
- 6.11 J. White and H. J. Harmon, "Novel optical solid-state glucose sensor using immobilized glucose oxidase", *Biochem. Biophys. Res. Commun.*, vol. 296, pp. 1069–1071., 2002.

- 6.12 R. Irawan, Y.H. Cheng, W.M. Ng, M.M. Aung, I.K. Lao, V. “Polymer waveguide sensor for early diagnostic and wellness monitoring”, *Biosensors and Bioelectronics*, vol. 26, pp. 3666– 3669, 2011.
- 6.13 R. Zou, B. Chen, H. Wang, X. Hu, M. Iso , “Glucose sensor based on planar optical waveguides”, *Bioinformatics and Biomedical Engineering*,. Conference Paper, 2007.
- 6.14 W. Zhang, H. Chang, G. A. Rechnitz, “Dual-enzyme fiber optic biosensor for pyruvate”, *Anal. Chim. Acta*, vol. 350, pp. 59-65, 1997.
- 6.15 V. Sanz, S. Marcos, J. Galb’an, “Direct glucose determination in blood using a reagentless optical biosensor”, *Biosensors and Bioelectronics*, vol. 22, pp. 2876–2883, 2007.
- 6.16 Vanesa Sanz, Susana de Marcos, Javier Galban, “Direct Glucose determination in blood using reagentless optical biosensor”, *Anal. Chem.*, Publisher: Biosensor and bioelectronics, 2007.
- 6.17 B.A.A. Dremela, S.-Y. Lib, R.D. Schmida ,“On-line determination of glucose and lactate concentrations in animal cell culture based on fibre optic detection of oxygen in flow-injection analysis”, *Biosensors and Bioelectronics*, vol. 7, Issue 2, pp. 133-139, 1992.
- 6.18 M. Portaccio M. L. B. D. Ventura O. Stoilova, N. Manolova, I. Rashkov D., G. Mita, “Fiber-optic glucose biosensor based on glucose oxidase immobilised in a silica gel matrix”, *Journal of Sol-Gel Science and Technology*, vol. 50, Issue 3, pp 437-448, 2009.
- 6.19 Neubauer, D. Pum, U. B. Sleytr, I. Klimant and O. S. Wolfbeis, “Fibre-optic glucose biosensor using enzymemembranes with 2-D crystalline structure”, *Biosens. Bioelectron.*, vol. 11, pp. 317–325, 1996.
- 6.20 P. J. Scully, L. Betancor, J. Bolyo, S. Dzyadevych, J. M. Guisan, R. Ferna’ ndez-Lafuente, N. Jaffrezic-Renault, G. Kuncova’ , V. Mate’ jec, B. O’Kennedy, O. Podrazky, K. Rose, L. Sasek and J. S. Young, “Optical fibre biosensors using enzymatic transducers to monitor glucose”, *Meas. Sci. Technol.*, vol. 18, pp. 3177–3186, 2007.
- 6.21 W. Trettnak, Otto S. Wolfbeis, “A fully reversible fibre optic glucose biosensor based on the intrinsic fluorescence of glucose oxidase”, *Anal. Chem. Acta*, vol. 221., pp. 195, 1989.

## Chapter 6 - Appendix

- 6.22 Bernhard P.H. Schaffar, Otto S. Wolfbeis , “A fast responding fibre optic glucose biosensor based on an oxygen optrode”, *Biosens Bioelectron.*, vol. 5, pp. 137-48., 1990.
- 6.23 B.A.A. Dremel, S.Y. Li, R.D. Schmid, “On-line determination of glucose and lactate concentrations in animal cell culture based on fibre optic detection of oxygen in flow-injection analysis”, *Biosensors and Bioelectronics*, vol. 7, issue 2, pp. 133-139, 1992.
- 6.24 W. Trettnak, O.S. Wolfbeis, “A fully reversible fibre optic glucose biosensor based on the intrinsic fluorescence of glucose oxidase”, *Anal. Chim. Acta*, vol. 221, pp. 195-203, 1989.
- 6.25 R.Narayanaswamy, F.Sevilla, “An optical fibre probe for the determination of glucose based immobilized glucose dehydrogenase”, *Analytical Letters*, vol. 21, Issue 7 , 1989.
- 6.26 B.P.H. Schaffar, O. S. Wolfbeis, “A fast responding fibre optic glucose biosensor based on an oxygen optrode”, *Biosens Bioelectron.*, vol. 5, issue 2, pp. 137-148, 1989.
- 6.27 P.Luca , M. Lepore , M. Portaccio , R. Esposito , S. Rossi , U. Bencivenga, D.G. Mita, “Glucose determination by means of steady-state and time-course UV fluorescence in free or immobilized Glucose Oxidase”, *Sensors*, vol. 7. issue 11, pp. 2612-2625, 2007.
- 6.28 D. B. Papkovsky, A. N. Ovchinnikov, V. I. Ogurtsov, G. V. Ponomarev and T. Korpela, “Biosensors on the basis of luminescent oxygen sensor: the use of microporous light-scattering support materials”, *Sens. Actuators, B*, vol. 51, pp.137–145. 1999.
- 6.29 K.S. Lee, H. L. T. Lee, R. J. Ram, “Polymer waveguide backplanes for optical sensor interfaces in microfluidics”, *Lab Chip*, vol. 7, pp. 1539–1545, 2007.
- 6.30 X. Fan, I. M. White, S. I. Shopova, H. Zhu, J. D. Suter, Y. Sun, “Sensitive optical biosensors for unlabeled targets: A review”, *Anal. Chim. Acta*, vol. 620, pp. 8–26, 2008.
- 6.31 Y. Liu, P. Hering , M. O. Scully, “An Integrated Optical Sensor for Measuring Glucose Concentration”, *Applied Physics B* , vol. 54, issue 1, pp 18-23, 1992.
- 6.32 Y.Yeh , H. Shih, Tainan, “Real-time measurement of glucose concentration and average refractive index using a laser interferometer”, *Optics and Lasers in Engineering* , vol. 46,

issue 9 , pp. 666–670, 2008.

- 6.33 T.Q. Lin, Y.L. Lu, C.C. Hsu, “Fabrication of glucose fiber sensor based on immobilized GOD technique for rapid measurement”, *Optics Express*, Vol. 18, Issue 26, 2010
- 6.34 Y.L. Lu, T.Q. Lin, S. Heng Liang, C.C. Hsu, C.Y. Yeh, “The glucose concentration in serum measured by the fiber sensor with heterodyne interferometry”, *OECC*, Conference Paper, 2011.
- 6.35 Z. Weissman, E. Brand, I. Tsimberov, D. Brooks, S. Ruschin, “Mach-Zehnder type, evanescent-wave sensor, using periodically segmented waveguide”, *Lasers and Electro-Optics Society Annual Meeting*, 1998.
- 6.36 K. M. Raptis I, Misiakos K, Makarona, “Broad-band Mach-Zehnder Interferometry as a detection principle for label-free biochemical sensing”, *IEEE Sensors*, Conference Paper, 2008.
- 6.37 M. Wang, Sa. Uusitalo, M. Maattala, R. Myllyla , M. Kansakoski, “Integrated dual-slab waveguide interferometer for glucose concentration detection in the physiological range”, *SPIE Conference Paper*, 2008.
- 6.38 C.I. Li, Y.H. Lin, C.L. Shih, J. Tsaur, L.K. Chau, “Sol–gel encapsulation of lactate dehydrogenase for optical sensing of L-lactate” *Biosensors & Bioelectronics*, Vol. 17, pp. 323– 330, 2002.
- 6.39 W. Trettnak, O. S. Wollbeis, “A Fiber Optic Lactate Biosensor with an Oxygen Optrode as the Transducer”, *Analytical Letters*, Vol 22., Issue 9, pp. 2191-2197, 1989.
- 6.40 S. G. Ignatova, J. A. Fergusonb, D. R. Waltb, “A fiber-optic lactate sensor based on bacterial cytoplasmic membranes “, *Biosensors and Bioelectronics*, vol. 16, issues 1–2, pp. 109–113, 2011.
- 6.41 W. Trettnak, Otto S. Wolfbeis, “A fully reversible optical lactate biosensor based on the intrinsic fluorescence of lactate monooxygenase”, *Analytical Division, Anal. Chem.*, vol. 334, pp. 427- 430, 1989.
- 6.42 F. Wang, F. Schubert, H. Rinnebe, “A fluorometric rate assay of hydrogen peroxide using immobilized peroxidase with a fiber-optic detector“, *Sensors and Actuators B*, vol.

Chapter 6 - Appendix

28, pp. 3-7, 1995.

- 6.43 M. Nawata, Y. Gasawara, K. Kawanabe, S. Tanabe, "Enzymatic Assay of 3-Mercaptopyruvate Sulfurtransferase Activity in Human Red Blood Cells Using Pyruvate Oxidase", *Analytical Biochemistry*, vol. 190, pp. 84-87, 1990.
- 6.44 W. Zhang, H. Chang, G. A. Rechnitz, "Dual-enzyme fiber optic biosensor for pyruvate", *Anal. Chim. Acta*, vol. 350, pp. 59-65, 1997.
- 6.45 K. Ramanathan, M.N. Amalasanan, B.D. Malothra, D.R. Pradhan, S. Chandra, "Immobilization and Characterization of Lactate Dehydrogenase on TEOS Derived Sol-Gel Films", *Journal of Sol-Gel Science and Technology*, vol. 10, pp. 309-316, 1997.